UNIVERSITA' DEGLI STUDI DI PAVIA

DIPARTIMENTO DI CHIMICA

Dottorato di Ricerca in Scienze Chimiche e Farmaceutiche

Direttore: Prof. Antonella Profumo

Operando spectroscopy for the study of reaction mechanisms in electrochemistry

Tutore:
Prof. Paolo Ghigna

Tesi di dottorato di ricerca di

Martina Fracchia

TRIENNIO ACCADEMICO 2016-2019 (XXXII CICLO)

Coordinatore: Prof. Mauro Freccero

Guardavo gonfiare le gemme in primavera, luccicare la mica nel granito, le mie stesse mani, e dicevo dentro di me "Capirò anche questo, capirò tutto, ma non come loro vogliono. Troverò una scorciatoia, mi farò un grimaldello, forzerò le porte". Era snervante, nauseante, ascoltare discorsi sul problema dell'essere e del conoscere, quando tutto intorno a noi era mistero che premeva per svelarsi: il legno vetusto dei banchi, la sfera del sole di là dai vetri e dai tetti, il volo vano dei pappi nell'aria di giugno.
[…]
Saremmo stati chimici, Enrico ed io.

Primo Levi, "Il Sistema Periodico"

Abstract

The progressive lack of fossil fuels together with the growing awareness of the environmental problems has led to an extensive research on renewable and sustainable energy sources. In this sense, electrochemistry covers a major role, considering that many processes for sustainable energy production are based on electrochemical reactions.

While much attention has been devoted to the development of new electrode materials, a comprehensive understanding of the mechanism of electrochemical reactions is still necessary to rationalize the choice of the electrodes and to design new ones, with the final aim of reaching higher efficiencies. *Operando* X-Ray absorption spectroscopy (XAS) is a powerful and versatile technique which allows information regarding the electronic and structural properties of a given material, while the material is operating under conditions of reaction. In this thesis, *operando* XAS was carried out on electrodes involved in (photo)electrocatalytic reactions. Attention was especially paid to photosystems for the photocatalytic water splitting, where *operando* XAS permitted to study the generation and the fate of the photogenerated carriers (recombination/charge transfer) and to clarify the role of the overlayer in composite electrodes.

While *operando* XAS experiments with hard X-rays (*i.e.* highly energetic X-rays) are well-established, the same cannot be said for *operando* XAS with soft X-rays, since their low penetration depth and the severe vacuum limitation have hindered a parallel development. In this work, a pioneering experiment of *operando* soft-XAS at ambient pressure was performed to study the reactivity of SnO_2 towards reducing gases.

Finally, dynamic multi-frequency analysis (DMFA) was employed in the field of electrocatalysis as a new strategy for the study of reaction mechanisms. This technique, which consists in acquiring dynamic impedance spectra while cycling the electrode under investigation, allowed information to be gained regarding the mechanism of the HER reaction on Pt and relevant kinetic parameters, through directly following their trend with the potential.

Contents

List of abbreviations

AC	Alternating current
AIROF	Anodic Iridium Oxide Film
CA	Chronoamperometry
CE	Counter Electrode
CV	Cyclic Voltammetry
DC	Direct Current
dEIS	dynamic Electrochemical Impedance Spectroscopy
DFT	Density Functional Theory
DMFA	Dynamic Multi-frequency Analysis
EC	Equivalent Circuit
EIROF	Electrodeposited Iridium Oxide Film
EIS	Electrochemical Impedance Spectroscopy
EXAFS	Extended X-ray Absorption Fine Structure
FEL	Free Electron Laser
FEXRAV	Fixed Energy X-ray Absorption Voltammetry
FMS	Full Multiple Scattering
FT	Fourier Transform
FTIR	Fourier Transform Infrared Spectroscopy
FTO	Fluorine-doped Tin Oxide
HER	Hydrogen Evolution Reaction
HERFD-XAS	High Energy Resolution Fluorescence Detected XAS
HOR	Hydrogen Oxidation Reaction
iFT	Inverse Fourier Transform
IMPS	Intensity Modulated Photocurrent Spectroscopy
IR	Infrared Spectroscopy
LED	Light Emitting Diode

LSV	Linear Sweep Voltammetry
MD	Molecular Dynamics
MS	Multiple Scattering
OCP	Open Circuit Potential
OER	Oxygen Evolution Reaction
OPD	Over Potential Deposition
ORR	Oxygen Reduction Reaction
PEC	Photoelectrochemical cell
PEM	Polymer Electrolyte Membrane
RDF	Radial Distribution Function
RE	Reference Electrode
RHE	Reversible Hydrogen Electrode
SCCM	Standard Cubic Centimetres per Minute
SIROF	Sputtered Iridium Oxide Film
SLJ	Semiconductor Liquid Junction
Soft-XAS	Soft X-rays Absorption Spectroscopy
SS	Single Scattering
STFT	Short Time Fourier Transform
TAS	Transient Absorption Spectroscopy
TEY	Total Electron Yield
TGA	Thermogravimetric Analysis
UPD	Under Potential Deposition
UV/Vis	Ultraviolet/Visible
WE	Working Electrode
XANES	X-ray Absorption Near-Edge Structure
XAS	X-ray Absorption Spectroscopy
XPS	X-ray Photoelectron Spectroscopy
XRD	X-ray Diffraction

Introduction

The growing awareness of environmental problems, the increasing energetic need of the world coupled to an uneven distribution of the resources, as well as the progressive lack of fossil fuels, have led to an urgent requirement for the creation of energy-saving programs for existing technologies and for the development of new processes based on renewable-energy sources[1]. In this sense, the field of electrochemistry is covering a major role, considering that most of the existing technologies for energy production and storage are based on electrochemical reactions[2]. As an example, extensive research is carried out in the field of batteries, where much attention is nowadays devoted to finding alternatives to lithium-ion batteries, *e.g.* sodium-ion batteries[3] or metal-air batteries[4], or to finding efficient ways for lithium-ion recovery[5]. Electrochemical reactions are also the foundation of hydrogen-based technologies, providing new sustainable ways to produce clean H_2 by exploiting solar energy (photocatalytic water splitting),[6] and to employ it for energy production (fuel cells)[7]. Furthermore, innumerable processes founded upon electrochemical reactions already exist in the field of energetics, and in recent years they have attracted increasing attention from the research community.

Much attention has been especially devoted to finding new electrode materials that may deliver better performance. In the vast majority of cases, the quest for materials and catalysts is carried out through trial-and-error procedures, rather than following a rational design. Indeed, this remains common in the field of electrochemistry and materials science, wherein serendipity often has a key role in finding the best candidates for a given process[8]. As a result, a lack of basic and fundamental understanding of the underlying mechanisms exists for most of the electrochemical reactions involved in these processes. It has, therefore, gradually been realised that there exists real need to find effective ways to investigate the mechanism of electrochemical reactions. Obviously, electrochemical reactions have been extensively studied with purely electrochemical techniques; however, a complementary view should be given with spectroscopic techniques, which can provide independent information. The key to elucidation and evaluation of the mechanism of electrochemical reactions is to investigate them through *operando* spectroscopy, *i.e.* getting the spectroscopic information while the reaction is occurring and while effectively simulating the real operating conditions of a given process. Finding a way to combine electrochemical and spectroscopic measurements whilst simultaneously re-creating effective and realistic working conditions of the process under consideration is not straightforward. Considering, for instance, a photoelectrocatalytic reaction, re-creating the exact working conditions means: i) illuminating the sample with visible light; ii) employing an electrode that shows good performance in real devices, rather than a sample specifically conceived and designed for the experiment; iii) employing a realistic cell configuration, *e.g.* with a proper amount of electrolyte and a low distance between the reference and the working electrode; and, iv) connecting the electrodes to a potentiostat to apply an external potential.

Broadly speaking, every electrochemical reaction in a given electrochemical process has its own requirements that need to be fulfilled to re-create *operando* conditions, so the ideal spectroscopic technique should not only be informative, but above all extremely versatile. Most of the well-known spectroscopic techniques employed for *ex-situ* measurements are not adequately versatile. For example, UV (Ultraviolet) spectroscopy, or IR (Infrared) and Raman spectroscopies, are severely disturbed by the presence of an electrolytic solution. X-ray Photoelectron Spectroscopy (XPS) is more selective and could be in principle highly informative as a surface sensitive technique, but it has the strong limitation that measurements should be acquired in ultra-high vacuum. Even the so-called near-ambient pressure XPS is generally carried out at pressures which are quite far from ambient[9]. Another well-known technique, X-ray Diffraction (XRD), is quite versatile but not element-selective; everything can therefore interfere with the measurements, *e.g.* the support, the current collectors and the electrolytic solution. In addition, conventional X-ray diffraction cannot be applied to nanomaterials and amorphous samples, which are frequently used in the field of electrocatalysis.

In this thesis, *operando* X-ray Absorption Spectroscopy (XAS) has been employed to investigate electrochemical reaction mechanisms by coupling of spectroscopic and electrochemical measurements. In particular, *operando* XAS has been employed to study electrochemical reactions involved in processes for sustainable energy production, with specific attention being paid to photocatalytic water splitting. XAS has shown to be particularly effective for the study of electrochemical reactions; firstly, XAS is element specific and can be applied to every kind of sample, including nanocrystalline and amorphous materials. This technique is also notably versatile and can be applied within experiments that efficiently mimic the working condition of a given process. Secondly, it should be noted that the electrode materials employed as catalysts or photoelectrocatalysts are expected to undergo changes in their electronic and structural properties as a consequence of the application of an electric potential or, in case of photoelectrocatalysts, as a consequence of illumination with visible light. XAS is particularly suited to observing and quantifying these changes, being sensitive to both electronic properties, *i.e.* oxidation state, density of the empty states, coordination geometry, and to the local structure of a given element. The comprehension of such modifications is essential to obtaining an exhaustive understanding of the fundamental processes that occur during the reaction.

This thesis will be structured as follows: the theoretical background regarding X-ray absorption spectroscopy will be given in the first Chapter, while the second Chapter contains a brief introduction on the investigated electrochemical reactions, with particular attention given to photocatalytic water splitting. In the same Chapter, the potentialities of *in situ* and *operando* XAS in electrochemistry will be also explained, followed by a consideration of the existing state of the art regarding the application of XAS in this field.

In the third Chapter, the methods and strategies adopted in this thesis to investigate the mechanism of electrochemical reactions will be presented. The first part of the Chapter focuses on *operando* XAS and explains in detail the selection of the samples, the characteristics of the spectroelectrochemical cell and the experimental methods employed in this work. The majority of this thesis is then devoted to conventional *operando* XAS, along with two alternative and innovative strategies that have been considered: i) *operando* soft-XAS at ambient pressure and ii) dynamic multi-frequency analysis (DMFA). A brief overview on these last two *operando* spectroscopies will be given in the second part of the Chapter.

The following Chapters will present the results obtained with *operando* XAS for the study of the mechanism of electrocatalytic (Chapter 4) and photoelectrocatalytic (Chapter 5-7) reactions. Finally, Chapter 8 and 9 will show the two “pilot experiments” regarding the application of soft-XAS and DMFA in the assessment of electrochemical reaction mechanisms.

1. X-ray Absorption Spectroscopy (XAS) - theory and fundamentals

X-ray Absorption Spectroscopy (XAS) represents a powerful and versatile technique for the determination of the electronic and atomic structure of matter on a local scale (*ca.* 10 Å around the element under study). In this Chapter, a brief overview on the principles of XAS will be given, starting from the generation of X-rays by synchrotron facilities, to the main aspects of the absorption process in the XANES (X-ray Absorption Near Edge Structure) and the EXAFS (Extended X-ray Absorption Fine Structure) regions.

1.1 X-ray generation: the synchrotron radiation

X-rays are that portion of the electromagnetic spectrum with a wavelength between *ca.* 0.01 nm ($1.2 \cdot 10^5$ eV) and 10 nm ($1.2 \cdot 10^2$ eV). At the laboratory scale, X-rays are usually produced with a Coolidge tube, where electrons are emitted by thermionic effect and accelerated towards a metallic target. The emission spectrum of a Coolidge tube is characterized by emission lines at energies distinctive of the target material, and by a continuous radiation in the region of X-rays, called the *Bremsstrahlung* radiation, of much lower intensity. In the late 60's, the progressive improvements of X-rays based techniques, *e.g.* spectroscopy, diffraction and imaging, demanded the use of tunable and intense radiation over the entire range of X-ray energies, as well as a higher collimation and focusing of the beam. All these conditions could be satisfied using synchrotron radiation, which was first pioneeringly employed in the field of high energy physics, and then started to become more accessible with the creation of dedicated large synchrotron facilities.

In a synchrotron, electrons are generated by thermionic effect from a tungsten wire and then accelerated until they reach a speed close to the speed of light. Only at this point, the electrons can be injected in the so-called storage ring, where their energy is kept constant. The storage ring is composed by straight sections and bending magnets, which force the particles to follow a curved trajectory. If electrons with a speed close to the speed of light are forced to change the direction of their motion (*i.e.* accelerated) under the effect of magnets, they emit radiation which is known as synchrotron radiation[10]. This radiation has a high intensity and is emitted tangentially to the storage ring with a very narrow divergence. The cut-off energy, *i.e.* the highest emitted energy in a synchrotron, is strictly connected to the radius of the storage ring. A schematic representation of a synchrotron radiation facility is shown in Fig. 1.1 a.

The X-rays emitted by a synchrotron have an intensity which is ten orders of magnitude higher than that emitted by a Coolidge tube. Moreover, the intensity of the radiation can be further enhanced using periodic magnetic structures called insertion devices. These magnets are placed in the straight part of the storage ring and can be of two kinds, namely wigglers or undulators; their alternating magnetic field structure forces the electrons to oscillate perpendicularly to the direction of their motion to cause further emission of synchrotron radiation during each individual wiggle. Depending on the number of wiggles, the intensity of the radiation may therefore be increased of many orders of magnitude (especially for undulators).

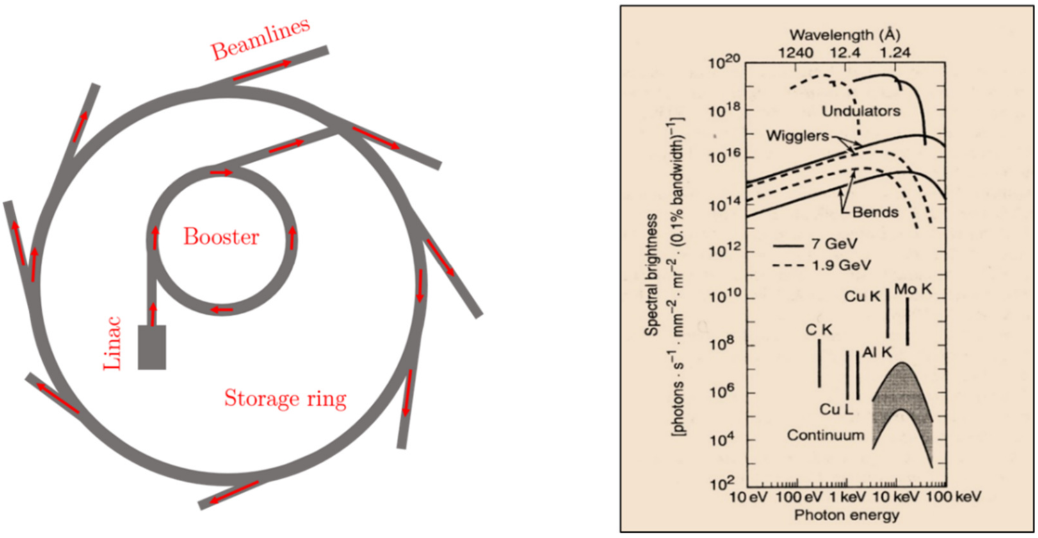

***Figure 1.1**:* (a) Schematic representation of a synchrotron radiation facility (*e.g.* ESRF, European Synchrotron Radiation Facility in Grenoble). The electrons are accelerated through a linear accelerator (LINAC) to the booster ring, where they are further accelerated until they reach a speed close to the speed of light. Only at this point they are injected into the storage ring; the synchrotron radiation is emitted tangentially to the ring. (b) Comparison of the spectral brightness for several synchrotron sources and conventional X-ray sources. The figure is reproduced from *X-Ray Data Booklet, Lawrence Berkeley National Laboratory, October 2009*[11].

An additional advantage of synchrotron radiation is that it is highly focused and collimated. To take this into account, it is convenient to introduce the concept of “brilliance”, which can be defined as:

$$B = \frac{I}{S \cdot \Omega} \tag{1.1}$$

Where I is the intensity of the beam expressed as photons per second, Ω is the solid angle and S the area of the source. In Fig. 1.1 b, the emission spectrum of the synchrotron radiation in presence of bending magnets, wigglers or undulators is compared to the emission lines coming from a Coolidge tube. Firstly, as pointed out before, it can be noted that the brilliance is much higher with respect to the Coolidge tube. Secondly, the radiation is intense over a wide range of energy (in case of bending magnets for over 1000 eV).

1.2 X-ray absorption

When X-rays of intensity I_0 are sent on a sample, they are absorbed causing the photoionization of core electrons to the *continuum*. After absorption, the X-ray intensity is attenuated to the value I according to the Beer-Lambert law:

$$I = I_0 e^{-\mu x} \tag{1.2}$$

Where μ is the linear absorption coefficient and x is the thickness of the sample. The absorption coefficient μ is strongly dependent on the atomic number of an element and decreases with energy, following the empirical Victoreen law[12]:

$$\mu \approx \frac{\rho \cdot Z^4}{A \cdot E^3} \tag{1.3}$$

Where ρ is the density of the sample, Z is the atomic number, A is the atomic mass and E is the energy. This smooth decrease of μ with energy is interrupted by sharp discontinuities, the absorption edges, as evident by Fig. 1.2. The absorption edges are located at energies corresponding to the binding energies of core electrons of the element under investigation.

When the incident X-ray photons have lower energy with respect to a specific binding energy, no absorption occurs. When the energy is larger, photoionization occurs, since X-rays have enough energy to promote an electron from an inner level to the *continuum*; this leads in turn to an abrupt increase of the absorption coefficient. The absorption edges of different elements are located at different energies, depending on the different nuclear charges of the elements and on the orbitals involved; this renders XAS an element and orbital selective technique. Depending on the initial level occupied by the electron, the absorption edges take different names (K, L, M, *etc.*) according to the Sommerfeld notation. If the electrons are extracted from the 1*s* level to the *continuum*, the absorption edge is called the K edge. If the electrons are extracted from levels with the principal quantic number *n* equal to 2, the absorption edges are called L edges. In this case, the electrons can be photoionized from the level 2*s*, $2p_{1/2}$ or $2p_{3/2}$; consequently, the edge takes the name of L_1, L_2 and L_3, respectively. The selection rules associated with photoionization process are $\Delta s = 0$, $\Delta l = \pm1$ and $\Delta j = 0, \pm1$, where s, l and j are the spin, azimuthal and total angular momentum quantum number, respectively. The relation between the core electronic levels and the high energy edges is summarized in table 1.1.

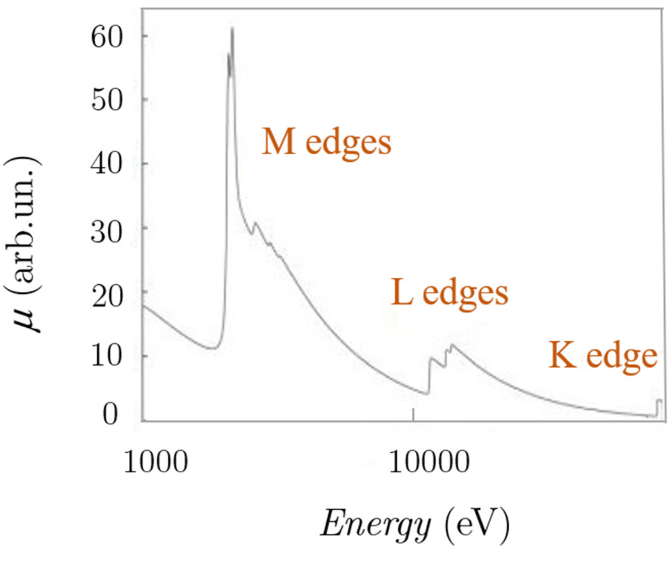

***Figure 1.2**:* Example of different absorption edges in the X-ray range for metallic Ir. The y axis is in logarithmic scale for better understanding. This figure is adapted from Minguzzi A., Ghigna, P., "X-ray absorption spectroscopy in electrochemistry from fundamentals to fixed energy X-ray absorption voltammetry" in *Electroanalytical Chemistry; A series of advances*, 2017[13].

Table 1.1: Relation between the core electronic levels and the high energy edges.

Edge:	M_5	M_4	M_3	M_2	M_1	L_3	L_2	L_1	K
Core level	$3d_{5/2}$	$3d_{3/2}$	$3p_{3/2}$	$3p_{1/2}$	3s	$2p_{3/2}$	$2p_{1/2}$	2s	1s

Looking closely into the absorption edges, the presence of some features and structures can be noted. The X-ray absorption spectrum is obtained by plotting the absorption coefficient μ against the energy, expressed in eV, around a specific absorption edge. An example of XAS spectrum is shown in Fig. 1.3. A XAS spectrum is usually divided into two regions: the X-ray Absorption Near Edge Structure (XANES) and the Extended X-ray Absorption Fine Structure (EXAFS). The XANES is the region immediately close to the edge (from *ca.* -20 eV to + 50 eV with respect to the edge); it can provide information about the oxidation state, the coordination geometry and the density of empty states of the element under consideration. The intense peak in the XANES region, in correspondence of the rising edge is generally referred to as "white line". The EXAFS is the region at higher energies (from 50 eV to *ca.* 1000 eV above the edge); it provides information on the local structure of the investigated element.

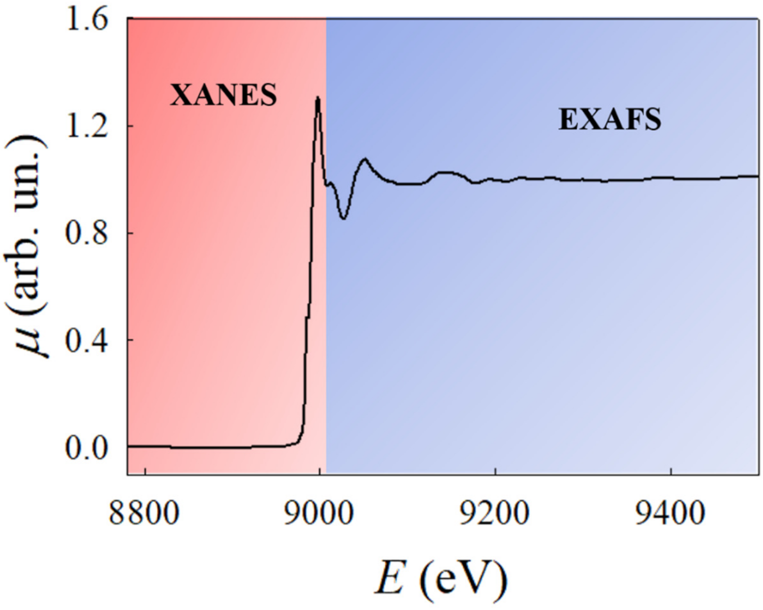

***Figure 1.3**:* Normalized XAS spectrum for CuO at the Cu K-edge. The XANES region, close to the absorption edge, is marked in red, while the EXAFS region, at higher energies, is marked in blue.

1.3 The EXAFS region

The electron generated after the absorption process (the photoelectron) presents a kinetic energy given by the following relation:

$$E_{kin} = h\upsilon - E_i \tag{1.4}$$

Where $h\upsilon$ is the energy of the incident photons and E_i is the binding energy of the core level from which the electron is extracted. In the EXAFS region, the energy of the incident X-rays is well beyond the edge energy, so the resulting photoelectrons will have a high kinetic energy; from wave-particle duality, a photoelectron with high kinetic energy can also be visualized as a wave characterized by a low wavelength λ. In case of isolated atoms, the photoelectrons emitted from the absorbing atom (the photoabsorber) cannot interact with any other surrounding atom; as a result, the spectrum in the EXAFS region will show only a slight decrease of μ at increasing energy according to equation (1.3). In solids and molecules, however, the photoabsorber is never isolated, but is surrounded by other atoms, either of the same or different nature, and disposed around it in a specific geometry. The emitted photoelectron strongly interacts with the surrounding atoms, which in turn act as back-scattering centres.

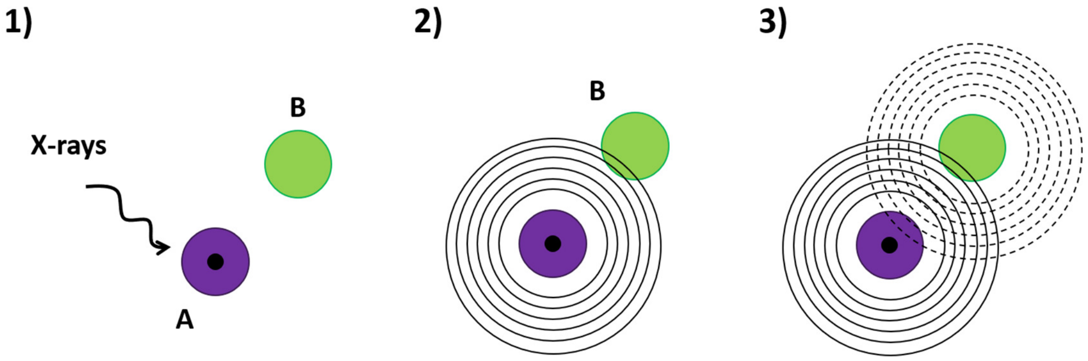

Figure 1.4: Scheme of the EXAFS phenomenon. 1) the X-rays impinge on the photoabsorbing atom A 2) the outgoing photoelectron wave function reaches the neighbouring atom B 3) the back-scattering occurs, leading to a superposition of the outgoing photoelectron wave and the back-scattered wave in correspondence of the photoabsorber.

Considering the wave-particle dualism, the photoelectron emitted from the photoabsorber can be visualized as an outgoing wave which is then backscattered by the surrounding atoms (see Fig. 1.4). The outgoing photoelectron wave and the back-scattered wave superimpose in correspondence of the photoabsorber, and may interfere in either constructive or destructive ways. This physical phenomenon causes a modulation of the absorption coefficient in the EXAFS region which, in contrast to the case of isolated atoms, shows not only a slight decrease with energy, but also additional oscillations (the so-called fine structure). The frequency of these EXAFS oscillations strictly depends on the distance between the photoabsorber and the surrounding atoms, while the amplitude is proportional to the nature and number of the back-scattering atoms.

The EXAFS signal as a function of energy, $\chi(E)$, can be extracted from the XAS spectrum in the EXAFS region by subtracting the contribution of the isolated atom $\mu_0(E)$ to $\mu(E)$ and then normalizing by the number of photoabsorbers.

$$\chi(E) = \frac{\mu(E) - \mu_0(E)}{\Delta\mu_0} \tag{1.5}$$

The EXAFS signal, however, is usually expressed as $\chi(k)$, where k is the wave vector. $\chi(k)$ can be obtained from $\chi(E)$ using the following expression:

$$k = \sqrt{\frac{2m \cdot (E - E_0)}{\hbar^2}} \tag{1.6}$$

Where m is the electron mass, E_0 is the absorption edge energy of the given element and $\hbar$ is the reduced Planck constant. As pointed out before, in the EXAFS region the photoelectron wavelength is small, so to a first approximation it can be assumed that the photoelectron interacts with the immediate neighbouring atoms only with two-body interactions. The two-body interaction can be treated quite easily from a mathematical point of view, thus allowing an approximated analytical expression for the EXAFS function to be derived.

The absorption coefficient is related to the probability of the transition, according to the Fermi's golden rule. In case of an isolated atom, μ_0 is expressed as:

$$\mu_0(\omega) \propto \left| \langle \psi_f^0 \left| \boldsymbol{H_{int}} \right| \psi_i \rangle \right|^2 \tag{1.7}$$

Where ψ_f^0 is the wave function of the final state in case of an isolated atom, ψ_i is the wave function of the initial state and H_{int} is the interaction Hamiltonian.

When the atom is not isolated but surrounded by other atoms, the photoelectron undergoes back-scattering; in the EXAFS region, the energy of the photoelectron is much larger than the electron-atom interaction, so that the interaction causes a weak perturbation of the final state expressed as $|\psi_f\rangle = |\psi_f^0 + \delta\psi_f\rangle$. Expression (1.7) can therefore be rewritten as:

$$\mu(\omega) \propto \left| \langle \psi_f^0 + \delta\psi_f \left| \boldsymbol{H_{int}} \right| \psi_i \rangle \right|^2 \tag{1.8}$$

The EXAFS signal $\chi(k)$ can be obtained inserting the absorption coefficients (1.7) and (1.8) into equation (1.5), and then converting the energy into wave vector. As shown in equation 1.7 and 1.8, in case of isolated atoms, the absorption coefficient is proportional to the superposition integral of the localized core wavefunction and the outgoing wavefunction. In case of non-isolated atoms, the total photoelectron wavefunction is given by the superposition of the outgoing wavefunction and the back-scattered waves. As anticipated before, an approximated equation for EXAFS can be obtained considering only two-body interactions (Single Scattering approach, SS) and treating the photoelectrons and the corresponding back-scattered as spherical waves. Considering, therefore, an interaction between the photoabsorber atom A and the near atom B (as shown in Fig. 1.4), separated by a distance R, it can be demonstrated[12] that the EXAFS equation can be written as:

$$\chi(k) = \frac{e^{ikR}}{kR}\left[2k\, f(k)\, e^{i\delta(k)}\right]\frac{e^{ikR}}{kR} + C.C. \tag{1.9}$$

The term C.C. is the complex conjugate and is added to deal with real numbers. f is the back-scattering factor, that strictly depends on the atomic number Z of the neighbouring atom; $e^{i\delta(k)}$ is the phase-shift, where $\delta(k)$ is also dependent on the nature of the neighbouring atom. Equation (1.9) can be re-elaborated and written as:

$$\chi(k) = \frac{f(k)}{kR^2} sin\,[2kR + \delta(k)] \tag{1.10}$$

The previous equation takes into consideration only the photoabsorber atom and one neighbouring atom. However, all the N atoms in the proximity of the photoabsorber can give back scattering. Moreover, a term accounting for thermal and structural disorders of atoms (the Debye-Waller factor $e^{-2k^2\sigma_j^2}$) should be added. If the sum is extended to each shell j around the photoabsorber (each shell contains N_j atoms of the same type at the same distance R_j from the central atom), the following expression is obtained:

$$\chi(k) = \sum_j \frac{N_j\, e^{-2k^2\sigma_j^2}\, f_j(k)}{kR_j^2} sin\big[2kR_j + \delta_j(k)\big] \tag{1.11}$$

As previously stated, the outgoing photoelectron can be seen as a spherical wave that is back-scattered by the surrounding atoms. In this process, the photoelectron can also be scattered inelastically from other sources; in order to contribute to the EXAFS, however, it is mandatory that the photoelectron is scattered *elastically* by the neighbouring atom and that it returns to the absorbing atom. To take this into account, the inelastic mean free path $\lambda(k)$ of the photoelectrons must be included into the equation.

The plot of the inelastic mean free path as a function of k is shown in Fig. 1.5; this plot is generally considered as universal, since $\lambda(k)$ has only a slight dependence on the material under investigation[14]. It can be observed from Fig. 1.5 that, at least in the range of the EXAFS acquisition (*i.e.* k from 0 to *ca.* 15 Å^{-1}), photoelectrons scatter elastically only within *ca.* 25 Å from the photoabsorber. Above this value, inelastic collisions heavily damp further contribution to the EXAFS signal.

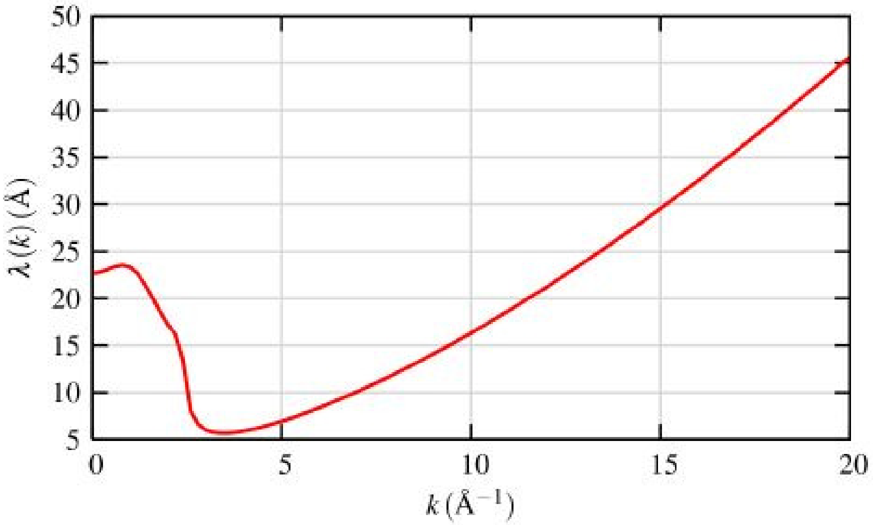

***Figure 1.5**:* Inelastic mean free path λ of photoelectrons as a function of k. This term includes both the inelastic scattering and the finite core-hole lifetime of the photoelectron. Reprinted from "Fundamentals of XAFS" by M. Newville. [12]

Moreover, the photoelectron must be scattered back to the photoabsorber before the excited state decays. These two conditions (the elastic scattering and the core-hole lifetime) are satisfied using a damped spherical wave, so that the EXAFS equation takes the following form:

$$\chi(k) = \sum_j \frac{N_j\, e^{-2k^2\sigma_j^2}\, e^{-\frac{2R_j}{\lambda(k)}}\, f_j(k)}{kR_j^2} sin\left[2kR_j + \delta_j(k)\right] \tag{1.12}$$

Equation (1.12) represents the final equation for the EXAFS signal. Since the sum is extended to a maximum of 25 Å, and due to the term R_j^{-2}, EXAFS is indeed a probe for the local structure around the photoabsorber. The analysis of the EXAFS signal is based on a fitting procedure, where equation (1.12) is employed to calculate a theoretical signal, which is then compared to the experimental one. After the fitting procedure, the refined values of the interatomic distances R_j, the coordination number N_j and the Debye-Waller factors, all referred to the short-range structure, can be obtained. The details on the extraction and the fitting procedure will be given in Chapter 3, Section 3.1.5.

1.4 The XANES region

The XANES region is the portion of the spectrum immediately close to the absorption edge (from *ca.* -20 eV to + 50 eV with respect to the edge). Differently from the EXAFS region, the energy of the incoming X-rays is slightly lower than that necessary to cause photoionization. As a result, the emitted photoelectrons have a low kinetic energy and can be visualized as waves characterized by a high wavelength. These photoelectrons are still back-scattered by the surrounding atoms, but in this case their interaction is not limited to two-body interactions but mainly to multi-body interactions, as schematically shown in Fig. 1.6. As a consequence, the single scattering (SS) formalism cannot be employed for the XANES region, and the inclusion of multiple scattering (MS) is mandatorily required. This aspect complicates the theory to the point that a simple analytical expression for the XANES region cannot be derived. Fitting the XANES region is, therefore, difficult, even if various approaches can be used for this purpose[15,16]. Fortunately, the XANES region is extremely informative even without performing a fitting procedure, thanks to its *fingerprinting* properties. As a matter of fact, even considering a single element, the XANES spectrum that originates can be extremely different depending on its oxidation state, on the chemical surrounding and the coordination geometry. A very clear example of this is given in Fig. 1.7 a, where Fe K-edge XANES spectra derived from Fe, FeO, Fe_3O_4 and Fe_2O_3 are shown. One of the information that can be immediately obtained from the XANES region is the oxidation state of the element under investigation. In fact, it can be noted from Fig. 1.7 a that moving from Fe(0) to Fe(III) the spectrum is shifted to the higher energies, an effect that can be rapidly understood: at higher oxidation state the nuclear positive charge is higher, so the electron cloud around the nucleus is more compressed. Consequently, the energy necessary for the photoionization is higher; the result is that the absorption spectrum shifts to the right (higher binding energies) as the oxidation state of the element is increased.

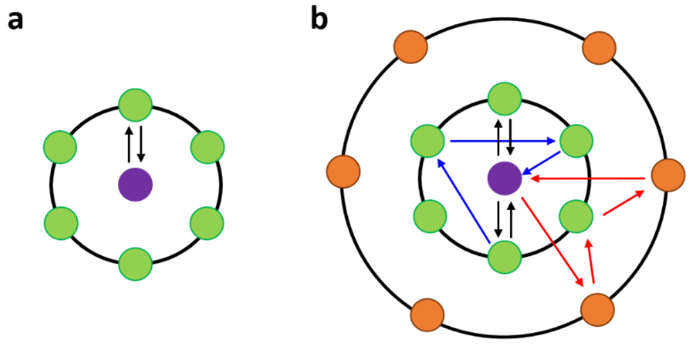

Figure 1.6: (a) Scheme of the two-body interaction, occurring in the EXAFS region and b) scheme of the multi-body interaction occurring in the XANES region. The violet atom corresponds to the photoabsorber.

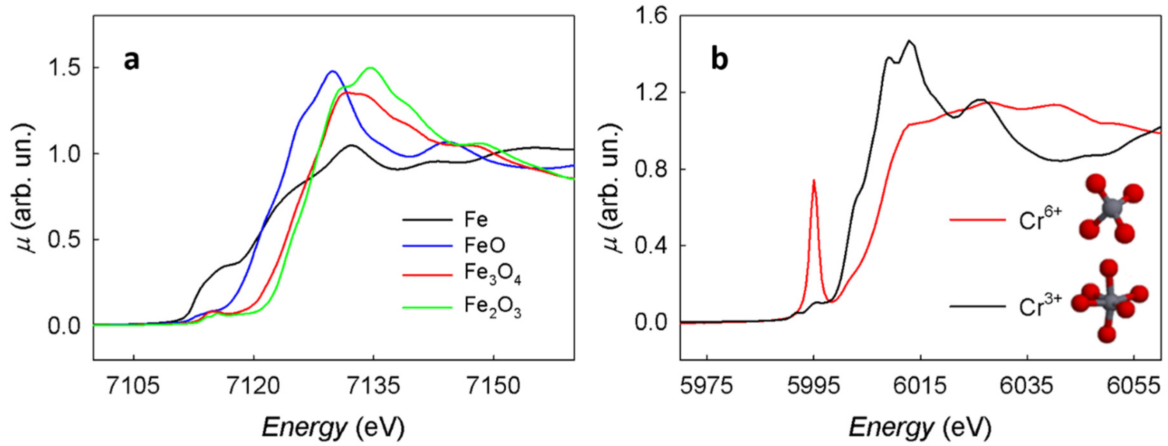

Figure 1.7: (a) XANES spectra at the Fe K-edge for various iron-based compounds b) XANES spectra at the Cr K-edge for CrO_3 (red line) and Cr_2O_3 (black line).

In contrast to the EXAFS, in the XANES region the energy of the incoming X-rays is just above the absorption edge and therefore nearly enough to cause photoionization. As a result, the electrons are not promoted to the *continuum*, but to specific empty orbitals (in case of molecules) or to empty electronic states above the Fermi level (in case of solids). The probability of the electronic transition to occur is regulated by the Fermi's golden rule, according to which the transition occurs if there is a parallel variation of the electric dipole momentum of the transition. This translates into the well-known selection rules, that in the simplest case of centrosymmetric groups are $\Delta s = 0$, $\Delta l = \pm 1$ and $\Delta j = 0, \pm 1$.

Considering, therefore, the K-edge, the allowed electronic transition will be from the filled *s* orbital to empty *p* orbitals; in case of the L_2 or L_3-edges the electron coming from a *p* orbital can have access only to *d* or *s* empty orbitals. Since the transition occurs towards non-occupied final states, XANES is a valuable tool to probe empty electronic states. The result is that, in the XANES region, all the features and the peaks of the spectrum can be ascribed to specific electronic transitions, which are obviously different depending on the oxidation state of the element, the coordination geometry and the type of the surrounding atoms. From Fig. 1.7 a it can be noted how all the spectra, apart from being shifted in energy, also have very different shapes, thus allowing for an immediate discrimination between different species.

An iconic case that shows how different a XANES spectrum can be even for the same element is presented in Fig. 1.7 b, where the spectra of CrO_3 and Cr_2O_3 at the Cr K-edge are displayed. The peak at 5995 eV is due to the transition 1*s* → 3*d*. In principle, this transition is forbidden by the selection rule Δl = ±1 (the Laporte rule); however, this rule is strictly valid only for dipolar transitions, and not for transitions of higher order. In Cr_2O_3, Cr(III) has a centrosymmetric octahedral coordination, so the selection rule is valid and the transition 1*s* → 3*d* has substantially only a quadrupolar nature; this results into a peak of low intensity (black curve in Fig. 1.7 b). On the contrary, Cr(VI) has a tetrahedral coordination, were the inversion centre is not present; the transition is thus allowed and this results into a strong peak at 5995 eV (red curve in the figure). It is therefore clear that, only by a brief look in the XANES region, and without any data treatment, immediate and qualitative information regarding the valence state, the coordination geometry and the nature of the empty states of a given element can be easily obtained.

2. In situ and operando X-ray absorption spectroscopy in electrochemistry

The fundamentals of XAS and the information that can provide have been described in the previous Chapter. Some features of XAS make the technique particularly suitable to be applied in *operando* in the field of electrochemistry; in this thesis, *operando* XAS has been extensively employed as a powerful tool to study the mechanism of electrochemical reactions. In this Chapter, a brief introduction to the electrochemical reactions investigated will be first given. Afterwards, the potentialities of XAS in electrochemistry will be explained and the state of the art on the application of XAS in this field described.

2.1 Electrochemical reactions for sustainable energy production

In the recent years, increasing energetic demands and the necessity of replacing energy sources based on fossil fuel, as a result of enhanced awareness of the effects that these sources have upon environment and human health, have led to much research in the field of sustainable energy production. Electrochemical reactions represent a simple method to provide and store electrical energy through the formation of chemical bonds. One of the most studied reaction involved in clean and sustainable energy storage and conversion is the following:

$$H_2O \leftrightarrows H_2 + \frac{1}{2}O_2 \tag{2.1}$$

This reaction is called water electrolysis, or more commonly water splitting, and leads to the formation of hydrogen and oxygen gas from water. The Gibbs free energy associated with this reaction is 237.2 KJ/mol, corresponding to 1.23 V vs a reversible hydrogen electrode (RHE), so the process is highly endergonic; one of the current aims is to perform this reaction using solar energy, in so-called photocatalytic water splitting[17]. This process leads to energy storage via the formation of chemical bonds, in this case in form of H_2, which is an important vector of clean energy that is expected to have a major importance on the economy of the future. The opposite reaction, the recombination of gaseous H_2 and O_2, can also provide clean electrical energy where water is the only by-product; this reaction is at the basis of the fuel cell technology[7].

The two reactions involved in the storage of energy by water electrolysis are the Hydrogen Evolution Reaction (HER) and the Oxygen Evolution Reaction (OER). The two opposite reactions involved in the conversion of energy by recombination of H_2 and O_2 are the Hydrogen Oxidation Reaction (HOR) and the Oxygen Reduction Reaction (ORR). A scheme of the reactions involved and of the associated overpotentials is shown in Fig. 2.1. While the HER/HOR occur almost without overpotential, the kinetics of the OER/ORR reactions are much more sluggish and strongly limit the efficiency of both the technologies described above. To overcome these problems, catalysts are often employed to improve the performances of the cathodic and anodic materials.

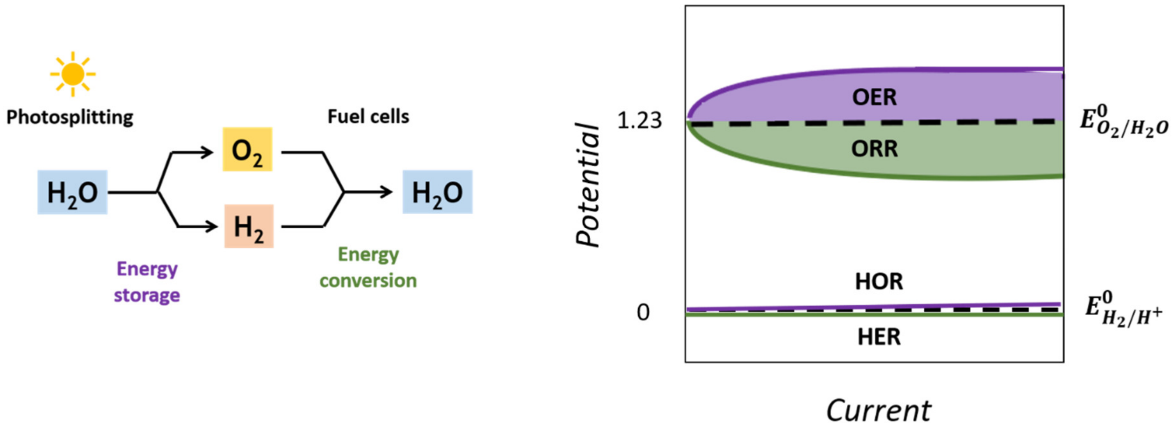

***Figure 2.1**:* (Left) Scheme of the hydrogen and oxygen cycle for energy storage and conversion. (Right) Scheme of the reactions and the overpotentials involved in HER/HOR and OER/ORR.

2.1.1 The hydrogen evolution reaction

The hydrogen evolution reaction is undoubtedly one of the most studied electrochemical reactions, even if nowadays an absolute certainty about the effective mechanism has not been reached[18]. In fact, since the reaction is very fast (especially on transition metals like Pt and Ir), it is not straightforward to follow the reaction over a large range of potentials. In addition, this process, and therefore the reaction mechanism, are largely dependent on the type of the electrode and on the state of its surface. In acidic media, the hydrogen evolution reaction can be written as follows:

$$2H^+ + 2e^- \leftrightarrows H_2 \tag{2.2}$$

This reaction (HER), as well as the opposite one (HOR), requires an electrocatalyst, which is generally a transition metal. The reaction on the metal occurs via two subsequent steps: i) the adsorption of H^+ at the surface of the metal and ii) the H_2 formation. The first step occurs through the following reaction, which takes the name of Volmer reaction:

$$M + H^+ + e^- \rightarrow M\text{-}H_{ad} \quad \textit{(Volmer reaction)} \tag{2.3}$$

During this step, the hydronium ion is discharged on the surface of the electrode leading to the adsorption of atomic H_{ad} on the metal. The second step can occur via two alternative pathways:

$$2M\text{-}H_{ad} \rightarrow 2M + H_2 \uparrow \quad \textit{(Tafel reaction)} \tag{2.4}$$

or

$$M\text{-}H_{ad} + H^+ + e^- \rightarrow M + H_2 \uparrow \quad \textit{(Heyrovsky reaction)} \tag{2.5}$$

The first path (2.4) is known as Tafel reaction; according to this reaction, two H_{ad} chemically recombine to give gaseous H_2[19]. The second pathway (2.5) is known as Heyrovsky reaction; in this case, one H_{ad} reacts with a H^+ species from the solution, generating H_2 through an electron transfer reaction[20]. Depending on the preferred pathway, the overall hydrogen evolution reaction can therefore proceed through a Volmer-Tafel mechanism or through a Volmer-Heyrovsky mechanism. On *sp* metals like Hg or Cd, the reaction seems to proceed via the Volmer-Tafel mechanism; on the contrary, on the *d* metals Ag and Cu, the reaction proceeds via the Volmer-Heyrovsky mechanism. In the other *d* metals, both mechanisms can occur[21].

One of the most common ways to determine the performances of metal electrocatalysts towards the hydrogen evolution reaction is the Volcano plot. In this plot, the standard exchange current density is plotted versus the energy of adsorption of a hydrogen atom on the electrode. The Volcano plot, in the most famous version by Trasatti[22], is shown in Fig. 2.2. In this version, the x-axis is not exactly the adsorption energy of hydrogen on the metal, but the energy of formation of the metal hydride M-H_{ads}, since the adsorption energies were still not fully reliable at that time. In this plot, the highest is the value of M-H_{ads}, the strongest is the bond formed. A high value of M-H_{ads} strongly favours the Volmer step, due to the favourable energy gain related to the process of adsorption. This is reflected in the Volcano plot, where in the first part (the ascending part) the exchange current increases at higher M-H_{ad} energies. However, if the bonding is too strong, the successive step, being it the Tafel of the Heyrovsky, is hindered; in fact, the bond needs to be broken before H_2 can evolve. As a result, the Volcano plot, after reaching a maximum, has a descending part where the exchange current density decreases again.

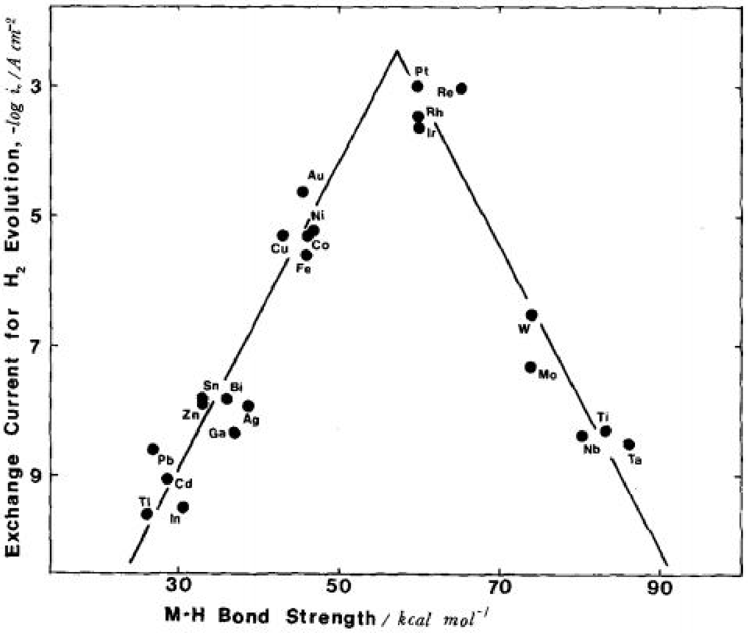

Figure 2.2: Exchange currents for electrolytic hydrogen evolution vs strength of intermediate metal-hydrogen bond formed during the electrochemical reaction itself. Reprinted from[22] with permission of Elsevier.

The metals at the top of the Volcano plot are therefore the best electrocatalyst towards HER. In actual fact, it has been shown that the descending part of this plot is rather inconsistent, considering that, under conditions of operation, the metals form an oxide layer which prevents hydrogen evolution[23]. In addition, various versions of the Volcano plot have been proposed with the purpose of reaching a higher accuracy, *e.g.* by plotting on the x-axis the adsorption energies, calculated through density functional theory (DFT)[24]. What remains unquestionable, however, is that Pt and Pt-based materials are among the best electrocatalysts towards the hydrogen evolution reaction.

2.1.2 The oxygen evolution reaction

Contrary to the hydrogen evolution reaction, oxygen evolution presents a poor kinetics that strongly limits the technologies based on this reaction. In acidic media, the oxygen evolution reaction can be written as follows:

$$2H_2O \leftrightarrows O_2 + 4H^+ + 4e^- \qquad (2.6)$$

The standard Nernstian potential for this reaction is 1.23 V vs RHE. This reaction implies the transfer of four electrons simultaneously, thus leading to the sluggish kinetics mentioned above; as a result, the effective potential necessary to carry out the OER is much higher (in other words, a high overpotential is associated to this reaction). This limit can be partially overcome by using an appropriate electrocatalyst for this reaction; however, the overpotentials often remain high and the quest for the perfect electrocatalyst is ongoing[25].

Metal oxides have rapidly emerged as electrocatalysts towards OER, due to their exceptional stability under reaction conditions. Moreover, it has been noticed that, even in case of solid metals electrodes, the anodic OER always occurs at an oxidized surface[26]. The best electrocatalysts for this reaction have turned out to be iridium and ruthenium oxides, but these compounds are expensive and of low abundancy on earth[27]. For this reason, much attention has been devoted in the recent years to finding low cost, non-toxic, and abundant transition metal oxides, especially including transition metals of the first row. These oxides are typically unstable in acidic conditions, but they have a long-term stability in basic environment, making them attractive for technological application.

Unfortunately, unlike the hydrogen evolution reaction, where a general mechanism can be outlined, a unified theory of the working mechanism of the electrocatalysts towards OER is still lacking. A generalized mechanism on oxides suggests that water coordinates to a surface-active site, with a concomitant proton transfer to the solvent and an electron transfer to form a M-OH species at the surface[28].

$$M + H_2O \rightarrow MOH + H^+ + e^- \qquad (2.7)$$

At this point, a M-O species is believed to form either through a proton-coupled oxidation of the active site (2.8) or through the disproportionation of two M-OH species (2.9).

$$MOH \rightarrow MO + H^+ + e^- \qquad (2.8)$$

or

$$2\ MOH \rightarrow MO + M + H_2O \qquad (2.9)$$

The M-O species can then decompose bimolecularly (2.10) or they can be attacked by water to generate O_2 (2.11).

$$2\ MO \rightarrow 2M + O_2 \qquad (2.10)$$

or

$$MO + H_2O \rightarrow M + O_2 + 2H^+ + 2e^- \qquad (2.11)$$

Numerous alternative pathways have been proposed that also include different intermediates, such as MOOH[25].

In 1980, Trasatti also reported a Volcano plot (Fig. 2.3) for the OER reaction, analogous to that proposed for HER; in this case, the graph correlates the overpotential with the standard enthalpy change for a lower to higher valent oxide transformation $MO_x \rightarrow MO_{x+1}$[29].

This plot is able to predict the high activity towards OER displayed by RuO_2 and IrO_2. The correlation shown in the plot can be rationalized considering that in the mechanism of the reaction, at a certain point, species like MO, MOH or MOOH are formed. The interaction of these species with the surface of the metal oxide MO_x could lead to an increase of the coordination sphere of the metal, thus explaining why the overpotential can be correlated to the enthalpy of formation of the oxide at the M^{+1} valence state[29,30]. In this sense, as stated by Dau *et al.*[31], the OER reaction can be visualized as the formation and the subsequent decomposition of high-valent metal surface oxides.

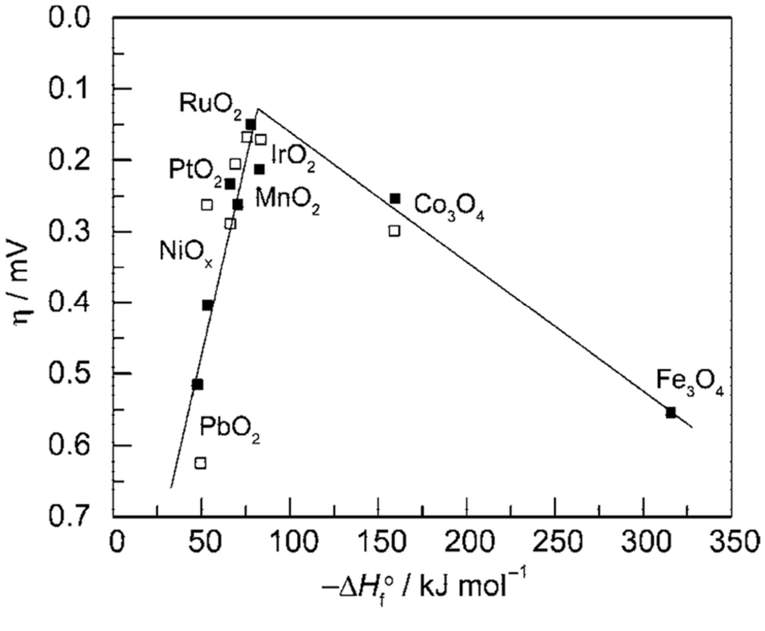

Figure 2.3: Volcano plot showing activity for O_2 production on metal oxide surfaces vs the enthalpy of transition of the oxide in acidic (black squares) and basic (white squares) media. The overpotential is measured relative to 0.1 mA·cm^{-2} current density. Reprinted from [32] with permission of The Royal Society of Chemistry.

As pointed out before, despite all the effort, the mechanism of the OER reaction remains confusing and controversial, and even now the majority of catalysts are intuitively developed using a trial-and-error approach.

2.1.3 Photocatalytic water splitting

The water splitting reaction driven by solar radiation has gained a lot of attention in recent years. It represents a promising and sustainable way to produce clean hydrogen and to store energy in form of chemical bonds, analogous to what happens in photosynthesis[6,33].

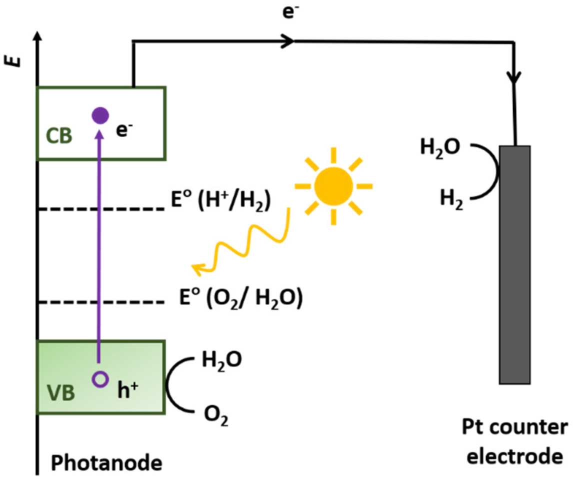

Figure 2.4: Schematic representation of the photocatalytic water splitting process in PEC cells.

A common way to carry out this process is using photoelectrochemical cells (PEC cells), where the anode or the cathode are photoactive materials, typically semiconductors. When illuminated, the semiconductor promotes an electron to the conduction band, while a hole is formed in the valence band. In an insulated semiconductor the holes and the electrons formed by absorption of visible light immediately recombine. In an electrochemical device, though, the photogenerated carriers are separated thanks to the electrical field that arises at the interface between the electrode and the electrolyte (Semiconductor Liquid Junction, SLJ), and can act as powerful chemical reagents: photogenerated electrons are responsible for the reduction of water to hydrogen, while the holes drive the oxidation of water to oxygen. For *p*-type semiconductors the cathodic reaction occurs at the semiconductor surface, while the anodic reaction is driven at the counter-electrode; in this case the semiconductor acts as photocathode, promoting the hydrogen evolution reaction. Analogously, *n*-type semiconductors can be used as photoanodes, promoting the oxygen evolution reaction; in this case, the hydrogen evolution occurs at the counter-electrode. A schematic representation of the photocatalytic water splitting process carried out in PEC cells is shown in Fig. 2.4.

As stated above, the potential associated to the water splitting reaction is 1.23 V, so in order to drive the reaction exclusively with the solar energy, the ideal semiconductor should have a band gap higher than 1.23 eV. It should be considered, however, that the oxygen evolution reaction is the bottleneck of the process; therefore, due to the overpotential, the effective value of band gap should be higher than 1.23 eV (at least between 1.6 and 2.4 eV)[34]. In addition, in order to drive the reaction spontaneously, the bottom of the valence band should be more negative than the redox potential of H^+/H_2, while the top of the valence band should be more positive than the redox potential of O_2/H_2O. Usually, the semiconductors which satisfy all these requirements are wide-band gap semiconductors, *e.g.* TiO_2; nevertheless, employing these materials would lead to an extremely low efficiency considering that, due to the high band gap, they absorb only a small portion of the solar radiation (TiO_2, for instance, absorbs only the 5% of solar radiation). For this reason, it is preferred to employ semiconductors with a lower band gap even if they don't have an optimal position of the valence and the conduction band, and then apply an external potential to drive the water splitting reaction. Moreover, in the ideal semiconductor for photocatalytic water splitting, the radiative or non-radiative recombination of the photogenerated carriers should be slow, so that the carriers have a sufficiently long lifetime to be involved in the reactions of interest. As a last, but not less important requirement, the material should be stable under the operative conditions, and should be non-toxic and abundant, considering that photocatalytic water splitting should be employed in the field of sustainable energy.

The requirements that should be fulfilled are, therefore, many and can be hardly satisfied by a single material. In order to improve the performances of the photoanode or the photocathode employed in the PEC cells, catalysts are often deposed on the semiconductor as thin layers or nanoparticles to improve the kinetics of the reactions (especially of the OER) or to enhance the stability of the electrode. The role of the overlayer is, however, still controversial: it can act just as a barrier for the electron-hole recombination in the semiconductor, or it can have an active role in the entire process[35]. Moreover, the photogenerated carriers can have a different fate: they can recombine, in a radiative or non-radiative way, they can be involved in the reactions of interest or be transferred to the overlayer. Studying the working mechanism of each photosystem is therefore necessary to improve water-to-hydrogen efficiency, towards a rational design of materials adequate for this purpose.

2.2 *In situ* and *operando* XAS in electrochemistry

As evident by the previous Sections, many electrochemical reactions involved in processes for energy storage and production lack of a basic and fundamental understanding of their underlying mechanism. As already pointed out before, the electrocatalysts for HER and OER, as well as the photoelectrocatalysts involved in the photocatalytic water splitting, are generally searched with a trial-and-error procedure based on intuition rather than following a rational design. It has therefore emerged the need to rationalize the reaction mechanisms and develop new tools to determine the nature of the intermediates formed during the reaction or, in the specific case of electrocatalysts, to determine the nature of the active sites. For this purpose, a consistent number of *in situ* and *operando* techniques have flourished, with the aim of studying electrochemical or catalytic reactions in *operando*, *i.e.* in conditions closely approaching the realistic ones[36].

In this sense, XAS possesses some characteristics that make this technique particularly suitable to interrogate the mechanism of electrochemical reactions. Broadly speaking, electrochemistry consists in the application of an external potential that leads in turn to a change in the electron chemical potential, thus causing modifications in the valence and in the electronic density of states of a given element. XAS, in turn, is an ideal probe to monitor the effects of an electrochemical reaction, easily allowing the determination of all the structural and electronic changes occurring in a material during a given process. This is particularly advantageous in catalysis, where the working mechanism is based on changes in the oxidation state of the metallic centre, and in photoelectrocatalysis, to monitor the fate of the photogenerated carriers.

XAS is also particularly suitable for *operando* investigations of electrochemical reactions. Firstly, hard X-rays (X-rays with an energy higher than 5000 eV) have a high penetration depth, also in the order of millimetres. This means that i) the incoming X-rays are not absorbed by air, thus allowing to carry out experiments at ambient pressure ii) they are not strongly attenuated by the electrolytic solution, as long as its thickness is not too large (*e.g.* not superior to *ca.* 1 mm and iii) they can penetrate through some thin supports as long as they are composed by light elements (*e.g.* through carbon-based supports). Moreover, XAS is element-selective, thus allowing to acquire information only and specifically on one element; this is extremely important, since the measurement is not disturbed for instance by the electrolytic solution or by the support. In this sense, the possibility of acquiring the XAS spectra in fluorescence rather than in transmission mode further facilitates the *operando* experiment. Finally, this technique can be applied to any sample in any state of matter (solid, liquid and gaseous) as well as to nanomaterials and amorphous samples.

All the characteristics marked above allow to effectively work with real samples and re-create realistic *operando* conditions of a given electrochemical process. XAS can be therefore considered a powerful tool for studying the mechanism of electrochemical reactions.

Nevertheless, as any other technique, it is not exempt from some drawbacks. The major disadvantage is that the XAS experiments must be carried out in synchrotron radiation facilities. Nowadays, however, the number of facilities is increasing (an outlook of the existing facilities can be found at https://lightsources.org/lightsources-of-the-world/); in parallel, innovative benchtop laboratory X-ray spectrometers are currently available and hopefully they could be employed in the future for *in situ* and *operando* experiments at the laboratory level.

The second drawback concerns the high penetration depth of X-rays; as outlined before, this represents a great advantage that actually makes *operando* experiments possible. At the same time, however, this property makes the technique sensitive to the bulk and not to the surface of the electrode material, while electrochemical reactions involve the interface between the electrode and the electrolyte. However, this disadvantage can be overcome by a sapient design of the experiment and a proper choice of the sample, as it will be shown later in this work.

Many examples are present in literature on the application of *in situ* and *operando* XAS for the study of the mechanism of electrochemical reactions, especially concerning electrocatalysis and the field of lithium-ion batteries[13]. Here, some examples will be shown only regarding (photo)electrocatalysis, being strictly connected with the topic of this thesis.

2.2.1 *In situ* and *operando* XAS for the investigation of Pt-based electrodes

The large majority of the papers regarding the application of *in situ* and *operando* XAS in electrocatalysis deals with Pt or Pt alloys-based electrodes employed as cathode catalysts in fuel cells for the oxygen reduction reaction[37]. For instance, XAS was particularly useful to determine how the particle size can influence the chemical properties of Pt nanoparticles. In this sense, not only the EXAFS analysis but also the same XANES region was helpful to determine the dimensions of the nanoparticles; in fact, the intensity of the white line is notably different in case of nanoparticles with respect to the bulk material[38].

XAS also proved to be particularly useful to identify the adsorbed species and the intermediates (*e.g.* Pt-H, Pt-O or Pt-OH) that are formed at the surface of the electrode during the catalysis. It was noticed that when the dimension of the Pt nanoparticles is low the adsorption processes are stronger, so that the smallest nanoparticles (with dimensions lower than 5 nm) showed a decreased activity towards ORR due to strong adsorption of OH[39].

In order to understand the nature of the adsorbate species, the $\Delta\mu$ method proved to be very effective[40]. In the case of adsorption, for instance, the $\Delta\mu$ signal can be obtained by subtracting to the spectrum of interest, where adsorption is expected, the spectrum of clean Pt.

$$\Delta\mu = \mu_{\mathrm{A}} - \mu_{\mathrm{clean}} \tag{2.12}$$

This method was first used by Teliska *et al.* to isolate the effects of H after adsorption on the Pt surface[41]. It was possible to distinguish between delocalized H adsorption, occurring at low H coverages, from a localized adsorption (atop or threefold) occurring at specific sites. This technique allowed understanding the adsorption processes occurring at different applied potentials in great detail; the same research group studied the adsorption of O and OH on Pt, which are important intermediates or inhibitors in the catalytic activity[42]. The authors calculated theoretical $\Delta\mu$ spectra for different possible adsorption sites and they compared them with experimental ones. They found evidence of atop OH adsorption at low potentials, followed by the formation of O on bridged sites, while at still higher coverages O adsorbs into a higher coordinated sub-surface site, which is the result of Pt-O site exchange and oxide formation. More recently, the nature of the adsorbed species on Pt was studied in *operando*, *i.e.* using a real operating PEM (Polymer Electrolyte Membrane) fuel cell, since the catalyst was directly deposed on the ion exchange membrane[43].

Another strategy that was widely adopted to study Pt-based catalysts is the acquisition of the XAS spectra both at the L_2 and L_3-edges, which allows estimating the occupancy of the Pt *5d* band[44]. Furthermore, many works can be found in literature regarding the adsorption of CO on Pt[45,46], a process which is particularly important for direct alcohol fuel cells and for the steam reforming, or dealing with innovative Pt-based catalysts[47,48].

2.2.2 *In situ* and *operando* XAS for the investigation of catalysts for the oxygen evolution reaction

For many years, XAS has been employed to study the behaviour and the mechanism of metal oxides electrodes for energy conversion devices. This research is nowadays mainly focused on metal oxides that are active for the OER reaction which, as shown before, is the bottleneck in water electrolysis. Despite the high cost, IrO_2 is one of the most studied electrodes for this purpose. Several methods now allow the production of hydrous non-stoichiometric IrO_x as thin films; these materials are highly hydrated and amorphous, so almost all Ir sites can be considered electrochemically active towards the OER. The most famous examples of these films are the EIROF (Electrodeposited Iridium Oxide Film), the SIROF (Sputtered Iridium Oxide Film) and the AIROF (Anodic Iridium Oxide Film). Since these films are amorphous, they cannot be structurally characterized using X-ray diffraction, so XAS proved to be the best choice for this purpose. In 1993, the valence of iridium in the AIROF was studied *in situ* in a specifically designed cell with a Kapton film holding a thin layer of electrolytic solution due to capillarity[49]. XAS spectra were acquired at different potentials, showing that at increasing potential, the Ir oxidation state increases to a value higher than IV, suggesting that Ir(V) is formed at the highest potentials. Similarly, SIROF electrodes were studied at different potentials, even if the cell configuration did not allow to reach the OER conditions[50]. Contrary to the previous case, the authors did not observe the formation of Ir(V) at the highest potentials.

Among all, however, the EIROF is the Ir-based film more suitable for fundamental studies, since all Ir sites can be considered active towards OER. Similarly to what was found for AIROF, the oxidation state of Ir was found to be higher than IV at the highest potentials in EIROF films[51]. XAS measurements were performed on EIROF in OER conditions; it was noticed that at these potentials there is a coexistence of Ir(III) and Ir(V), proving that both species participate in the catalytic cycle. This study allowed an elucidation of the working mechanism of this catalyst[52]. Furthermore, IrO_x was studied as an overlayer on hematite (Fe_2O_3) for photocatalytic water splitting; it was shown that under illumination a charge transfer occurs from the hematite to the iridium oxide[53].

Analogously, RuO_2 has been studied with XAS, being the best catalyst towards OER in acidic media together with IrO_2. Also, for this catalyst, the structure of hydrous RuO_2 was investigated and compared with that of anhydrous RuO_2[54]. In this case, the determination of the oxidation state was not straightforward; differently from IrO_2, in fact, the valence of Ru cannot be easily derived from the chemical shift of the Ru K-edge XANES region. An *operando* study on a RuO_x|Nafion|IrO_x supercapacitor was attempted[55], using a strategy similar to FEXRAV[56] (Fixed Energy X-ray Voltammetry), a method widely adopted in this thesis that will be shown in the next Chapter. In this work, the authors demonstrated, through this technique, that it was possible to follow the valence state changes of Ru in real time.

In recent years, a need to replace expensive catalysts based on noble metals has clearly emerged; as a result, some recent XAS experiments were dedicated to oxides of metals belonging to the first transition row. Cobalt-based oxides have been widely studied, especially since the discovery of the so-called Co-Pi, an electrodeposited Co-based catalyst obtained in neutral water containing phosphate and Co^{2+}, which proved to be a good candidate for artificial photosynthesis[57]. This catalyst was studied by the same group through *in situ* XAS using a cell with two compartments and an X-ray transparent window. They studied different thicknesses of this film and they were able to determine its structure through EXAFS, concluding that it is similar to CoOOH[58]. In addition, they determined the presence of Co with oxidation state higher than Co(III) in oxygen evolution conditions.

Recently, an interesting XAS experiment was carried out on an electrodeposited Co catalyst, named "CoCat", which can be fabricated in absence of phosphates[59]. In this work, both XAS and UV/Vis spectra were acquired to monitor the Co oxidation state at different potentials. The experiment was carried out with a freeze-quench XAS approach: the working electrode was polarized at a certain potential for two minutes and, while keeping constant the potential between the working electrode and the counter electrode, it was quenched inside liquid nitrogen. After freezing, the potential was disconnected, and the measurements were acquired at 20 K. Thanks to this approach, the formation of Co(IV) during the oxygen evolution reaction was determined.

2.2.3 New perspectives

In the previous Section, a brief review on some *in situ* and *operando* XAS experiments in electrocatalysis has been given. In particular, only the most famous electrocatalysts, *i.e.* Pt for HER and Ir, Ru and Co oxides for OER have been considered. Clearly, many other examples are present in literature regarding new catalysts based on metal oxides, but also metal complexes, which have been developed for the water splitting and for artificial photosynthesis. In addition, only conventional XAS experiments were considered; however, many different acquisition techniques are now available at synchrotrons and have been successfully employed in the field of electrocatalysis. Examples of other techniques are the HERFD-XAS (High Energy Resolution Fluorescence Detected XAS) and RIXS (Resonant Inelastic X-ray Scattering), that allow a partial elimination of core-hole broadening effects, and thus permit the selection and study of specific electronic transitions in detail.

Furthermore, many XAS resources now allow the acquisition of entire XAS spectra very rapidly, thus opening the possibility to perform dynamic and time-resolved experiments[60]. Examples of these approaches are energy-dispersive XAS and quick-XAS. The time resolutions that can be reached range between hundreds of nanoseconds to femtoseconds. In this sense, the advent of X-ray free electron lasers (FEL) is pushing time-resolved XAS to a new level[61].

In this thesis, *in situ* and *operando* XAS has been employed to study the mechanism of electrochemical reactions relevant to the field of (photo)electrocatalysis. Particular attention was devoted to creating *operando* conditions as close as possible to the real working ones, selecting efficient materials, and employing a specifically-designed electrochemical cell. For this purpose, techniques like FEXRAV and differential light and dark acquisition were adopted. In addition, part of this work was devoted to developing new strategies for *operando* studies of electrochemical reactions; from, on the one hand, a pioneering XAS experiment with soft X-rays (X-rays with energy lower than 5 keV) at ambient pressure, to, on the other hand, the use of DMFA (Dynamic Multi-frequency Analysis) as a new method to monitor and extract kinetic parameters in the hydrogen evolution reaction catalysed by platinum. All these methods and strategies will be explained in detail in the following Chapter.

3. Investigating reaction mechanisms in electrochemistry: methods and strategies

In this Chapter, the methods and strategies adopted in this thesis to study the mechanism of electrochemical reactions with *operando* spectroscopy are shown. This Chapter is divided into three Sections, according to the three different approaches used in this thesis. The first Section regards the use of *operando* XAS to assess the mechanism of (photo)electrocatalytic reactions. In this first Section the details regarding the selection of the sample, the characteristics of the spectroelectrochemical cell, and the experimental methods employed in this work will be explained. The second and the third Sections are devoted to the two innovative strategies presented in this thesis, namely soft-XAS at ambient pressure and dynamic multi-frequency analysis (DMFA). To facilitate the comprehension of this last technique, a brief outlook on classical and dynamic impedance will be given.

3.1 *In situ* and *operando* XAS in (photo)electrocatalysis

Operando XAS experiments were carried out to study the mechanism of electrochemical reactions relevant for electrocatalysis or photoelectrocatalysis. An *operando* XAS experiment consists of four steps: i) selection of the sample ii) design of the spectroelectrochemical cell iii) data acquisition iv) data analysis. All these aspects will be considered in the following subsections.

3.1.1 Selection of the sample

In order to re-create realistic *operando* conditions, the samples must be electrodes showing good efficiency and performance, rather than samples created *ad hoc* for the experiments. For this purpose, prior to the experiments, all the electrodes were tested and characterized in conventional cells in the laboratory. All the samples were synthesized by (photo)electrodeposition or spin-coating deposition on FTO (Fluorine-doped Tin Oxide), a support that is particularly suitable for photoelectrochemical experiments, being both conductive and transparent to the visible light.

For every investigated material it is necessary to estimate an optimal loading of the electrode, in order to have an appreciable absorption and therefore a good signal-to-noise ratio. The loading, however, should not be too high, in order to avoid ohmic drops or diffusion limitations. Usually, the loading suitable for the XAS experiment is a bit higher than the optimal one suitable for technological application. With a higher loading, it is possible that not all the material is active towards the selected reaction. This can be an issue, considering that XAS (at least with hard X-rays) is bulk sensitive and not surface sensitive; it is necessary, therefore, that all the layer, and not only the surface, participates to the reaction. This problem is generally overcome since the materials employed in catalysis are usually nanomaterials or highly hydrated/amorphous electrodes; in these cases, the exposed surface is high and almost all the material can be considered active, despite the larger thickness.

The materials investigated in this thesis are α and γ-FeOOH, with the aim of understanding the phase formed under hydrogen evolution conditions, and the photoanode WO_3, the photocathodes Cu_2O and CuO, and the photosystem α-Fe_2O_3/NiO_x to understand their working mechanism during the photocatalytic water splitting reaction. The details of the synthesis and the motivation for each experiment will be given in each of the following dedicated Chapters.

3.1.2 Design of the electrochemical cell

The spectroelectrochemical cell employed in the *operando* XAS experiments must be carefully designed in order to satisfy two important prerequisites. The first is that the thickness of the electrolytic solution in front of the electrode must be large enough to have a good electrochemical response, but not too large to attenuate the incoming X-rays. Usually, the thickness of the electrolytic solution should not exceed 1 mm. The second prerequisite is that, in order to mimic real *operando* conditions, the electrochemical response in the spectroelectrochemical cell configuration should not differ too much from the response obtained using a conventional cell.

Different versions of the spectroelectrochemical cell were designed and employed in the experiments; an example of 3D-printed cell is shown in Fig. 3.1. The cell is entirely composed of photopolymer resin and has a three-electrode configuration, presenting therefore three allocations for the working electrode (WE), the reference electrode (RE) and the counter electrode (CE).

The main body of the cell is held together with a rectangular cover and nuts and bolts; this configuration is meant to create a small location for the working electrode which ensures the presence of a low thickness (~ 1 mm) of electrolytic solution in front of it, as shown in the schemes in Fig. 3.1 (left panel). Both the front of the cell and the rear part present a circular window that allows the illumination with both X-rays and UV/visible light; an O-ring is inserted to avoid leakage of the electrolyte. The rectangular-shaped electrolyte chamber presents an upper slot where the counter electrode can be inserted, so that it is in electrical contact with the working electrode. The lodging for the reference electrode is achieved by a hole in the upper part of the cell. Finally, it can be seen that the main body of the cell contains an electrolyte reservoir, which is open in the upper side and therefore electrochemically connected with the working electrode. The electrolyte reservoir helps to cope with possible radiation damage (*e.g.* local heating or formation of radicals) induced by the X-ray beam, which can lead to a fast evaporation of the electrolyte. More details on the design and realization of these 3D-printed spectroelectrochemical devices can be found in Achilli *et al.*[62].

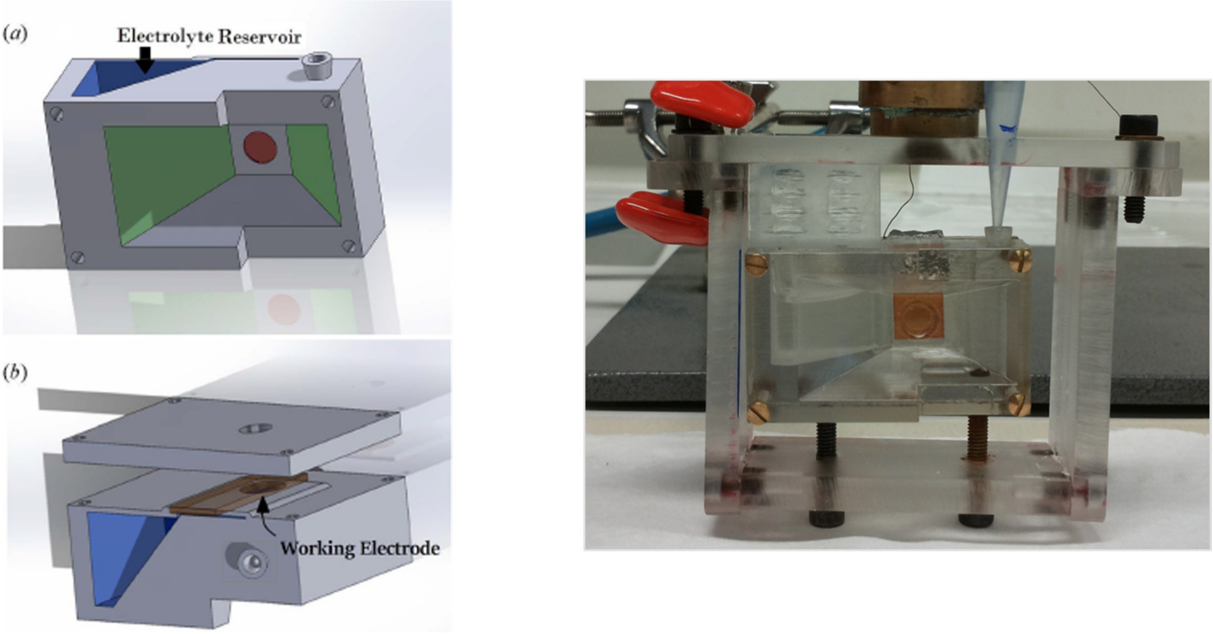

Figure 3.1: (Left panel) Scheme of the 3D-printed version of the spectroelectrochemical cell showing the electrolyte reservoir and the rectangular covered with the circular hole, where the working electrode is allocated. (Right panel) Photograph of the 3D-printed cell.

In many cases, a simplified hand-made version of this 3D-printed cell was employed, where the backbone of the cell is made of silicon rubber and the walls are composed of a polyethylene terephthalate layer with a Mylar® window in correspondence of the working electrode position. The working electrode was placed with the deposited layer faced towards the X-rays source. The thickness of the cell is slightly higher than the thickness of FTO, so that the layer of electrolyte in front of the electrode was in the order of hundreds of micrometres. A scheme of this simplified cell is shown in Fig. 3.2 (left panel).

In all the experiments here presented, a platinum wire was used as counter electrode while the Ag/AgCl electrode was used as reference in a double bridge obtained from a pipette filled with the electrolyte. To avoid contamination of the main cell chamber with Cl^- ions, the tip of the pipette was filled with pressed cotton.

Clearly, with respect to a standard cell, the usage of these two spectroelectrochemical setups can lead to a lower conductivity of the solution layer and to higher ohmic drops, due to the higher inter-electrode distance. However, dramatic changes in the electrochemical response were never observed.

3.1.3 Data acquisition: the *operando* experiment

The experiments were carried out at the European Synchrotron Radiation Facility (ESRF) in Grenoble (France) at the beamline BM08-LISA[63]. At this beamline, the radiation comes from a bending magnet, so it is characterized by a high intensity over a broad range of energies (photon flux above 10^{10} photons/s with a resolution $\Delta E/E = 10^{-4}$) and by a naturally high collimation. The range of energies covered by this beamline are from 5 to 90 keV, thus allowing investigation of the K-edges of elements from Ca to Au and the L-edges of the elements successive to Sb. The monochromator is a Si double-crystal (311), while the harmonic rejection is obtained with Pd mirrors with a cut-off energy of 20 keV. The detector is a 13-element Ge fluorescence detector, which is suitable for fluorescence measurements and for highly diluted samples. The measurements were acquired in fluorescence mode, with the detector located at 90° with respect to the X-ray source. The absorption coefficient in this case is defined as follows:

$$\mu = \frac{I_f}{I_0} \tag{3.1}$$

The use of fluorescence acquisition is mandatory for these *operando* measurements, since the transmitted signal is completely attenuated by the presence of either the FTO or the backbone of the cell. In addition, fluorescence can be advantageous in case of diluted samples. It should be noted, however, that one of the major drawbacks for the fluorescence acquisition is the possible presence of self-absorption. This phenomenon is due to the absorption of the X-rays emitted by fluorescence by the material itself and can cause severe distortion in the spectrum profile. However, self-absorption phenomena occur in case of highly concentrated samples, and they were never observed in all the systems investigated in this thesis. In fact, in all cases, the sample loading was accurately selected as to have a good signal-to-noise ratio and negligible self-absorption at the same time.

A schematic of the experimental apparatus is shown in Fig. 3.2. During the *operando* experiment, the electrode was irradiated with X-rays impinging on the front of cell while an external potential was applied with a potentiostat. All the spectroscopic measurements were therefore combined with standard electrochemical measurements, like chronoamperometry (CA) or cyclic voltammetry (CV).

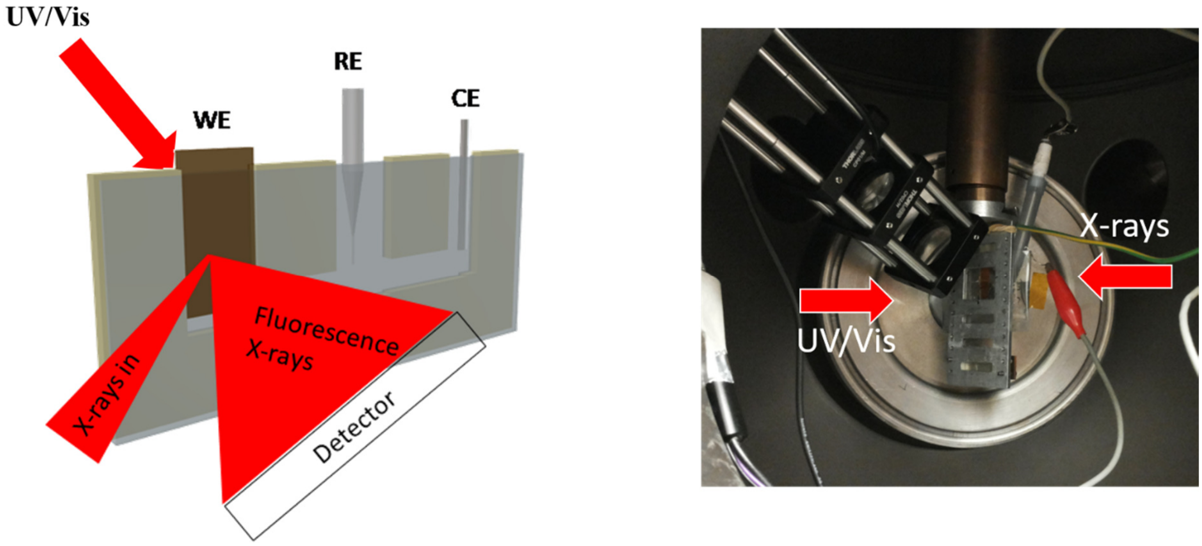

Figure 3.2: (Left) Schematic representation of the experimental setup. The X-rays impinged on the front of the cell, and the fluorescence XAS signal was acquired at 90°. The UV/Vis radiation was sent to the rear part of the cell. (Right) Photograph of the experimental setup inside the hutch at the BM08-LISA beamline.

In case of experiments with photoelectrocatalysts, the electrode was also illuminated by UV/visible radiation, coming from a LED (light-emitting diode) set at λ = 400 nm. When the photocatalyst was a bare semiconductor (not coupled to a catalyst or overlayer) the UV/Vis radiation could be sent either on the front or on the rear part of the cell. In presence of the overlayer, the UV/Vis radiation had to impinge on the rear part of the cell, in order to reach the semiconductor.

3.1.4 Data acquisition: $\Delta\mu$ (Light – Dark) method and Fixed Energy X-ray Absorption Voltammetry (FEXRAV)

In case of photoelectrocatalysts, it is expected that in appropriate conditions illumination with UV/Vis light induces changes in their electronic structure, that will in turn lead to changes in the profile of the XAS spectrum in light with respect to dark conditions. In any case, these differences between dark and light are expected to be small and therefore difficult to detect. To overcome this problem, the LED illumination at 400 nm is preferred to other possible sources (*e.g.* solar simulator) in order to have a considerable absorption from the photoactive material. Secondly, a specific technique was used to acquire the spectra in dark and light condition in parallel, in order to be able to perceive also small yet meaningful differences. Usually, a XAS spectrum is acquired measuring the fluorescence intensity while the monochromator shifts in energy. In this case, a parallel acquisition was performed; for each energy value the fluorescence signal was measured both in dark and in light conditions. Typically, the acquisition time was 30 s for every point, while other 30 s of wait time were introduced before shifting from light to dark, to let the system relax. In this way, the spectrum in dark and the spectrum under UV/Vis illumination could be acquired simultaneously. The main advantage of this parallel acquisition is that the two spectra are acquired under the same conditions, thus minimizing the systematic errors. In this way, it is possible to assume that the differences between the spectrum in light and the spectrum in dark (if present) are only due to the electronic changes occurring in the material under illumination.

In order to better perceive these differences, the $\Delta\mu$ signal can be calculated by subtracting the spectrum in dark to the spectrum in light:

$$\Delta\mu = \mu_{\text{light}} - \mu_{\text{dark}} \tag{3.2}$$

Another technique which has been extensively used in this thesis is the Fixed Energy X-ray Absorption Voltammetry (FEXRAV)[56]. It consists in measuring the absorption coefficient at a fixed selected energy while scanning the applied potential, usually according to a cyclic voltammetry. The energy is kept constant at a value which ensures the maximum contrast of absorption coefficient between two oxidation states of the element under investigation.

An example is shown in Fig. 3.3. Here, the FEXRAV was acquired on a $Ni(OH)_2$ electrode at a fixed energy of 8350 eV while acquiring a CV between 1.35 V and 1.73 V vs RHE. In the left panel, the standard spectra at the Ni K-edge of $Ni(OH)_2$ and of β-NiOOH, where Ni is present as Ni(III), are shown as a cyan line and an orange line, respectively.

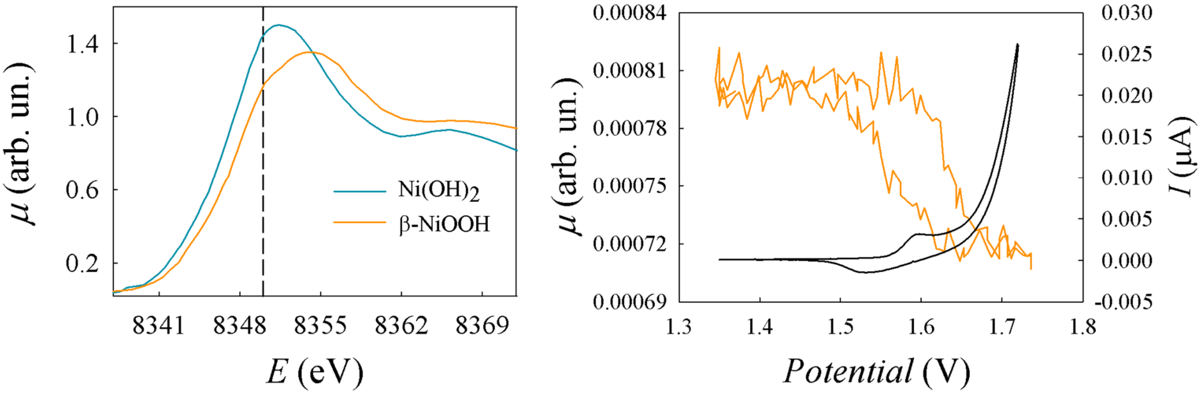

Figure 3.3: (Left) Standard spectra at the Ni K-edge of $Ni(OH)_2$ (cyan line) and β-NiOOH (orange line). The FEXRAV was recorded in correspondence of 8350 eV (indicated by the black dashed line). (Right) FEXRAV scan (orange line) and cyclic voltammetry (black line).

At 8350 eV the two spectra show the largest difference; in particular, it can be noted that the absorption coefficient is higher in $Ni(OH)_2$, where the oxidation state of Ni is Ni(II). In the right panel, the FEXRAV is shown by the orange curve, together with the cyclic voltammetry (black curve). Between 1.3 V and 1.5 V the absorption coefficient is stable; after 1.5 V, the absorption coefficient starts to decrease. As evident by the standard spectra, a decrease of the absorption coefficient indicates an oxidation of Ni from Ni(II) to Ni(III).

FEXRAV is therefore a fast and powerful tool for monitoring the variations of the absorption coefficient in real time, thus allowing a precise isolation of the changes resulting from an applied external stimulus. However, an energy-fixed (single point) acquisition cannot specify the absolute nature of the speciation nor which intermediate structures are exactly involved. For this reason, FEXRAV should be considered useful as a preliminary investigation, and it can be efficiently coupled with electrochemical measurements with the aim to select the potentials in correspondence of which whole XAS spectra can then be acquired with good resolution.

A variation of FEXRAV which can be useful for photoelectrochemical investigations consists in recording the absorption coefficient at a fixed energy and at a fixed potential while alternatively switching on and off the UV/Vis radiation; this allows to catch in real time the response of the photosystem to illumination at various potentials.

3.1.5 Data analysis: fit of the EXAFS and of the XANES region

The analysis of XAS spectra starts with the normalization of the spectrum through subtraction of a pre-edge and a post-edge background. An example of data normalization and extraction is here shown taking as an example the spectrum of CuI acquired at the Cu K-edge. The pre-edge is usually simulated with a straight line (green line in Fig. 3.4), while the post-edge can be fitted with polynomial of nth order or splines. This procedure is illustrated in Fig. 3.4 A.

This first data treatment allows definition of the edge jump, $\Delta\mu_0$, which depends on the number of photoabsorbers, *i.e.* on the quantity of sample. At this point, the spectrum can be normalized to unit absorption by dividing by the edge jump; this is a key step to compare spectra from different samples. The normalized spectrum, obtained after this procedure, is shown by the blue line in Fig. 3.4 B. In order to extract the EXAFS signal, the normalized spectrum must be fitted in the post-edge region with a cubic spline, shown by the red line in Fig. 3.4 B. This spline simulates what in the first Chapter has been defined as μ_0, *i.e.* the absorption of an isolated atom. The spline should be smooth in order to keep the natural oscillations of the EXAFS region, which are due to the presence of neighbouring atoms. The EXAFS signal is obtained by subtracting this cubic spline to the experimental data, according to (1.5).

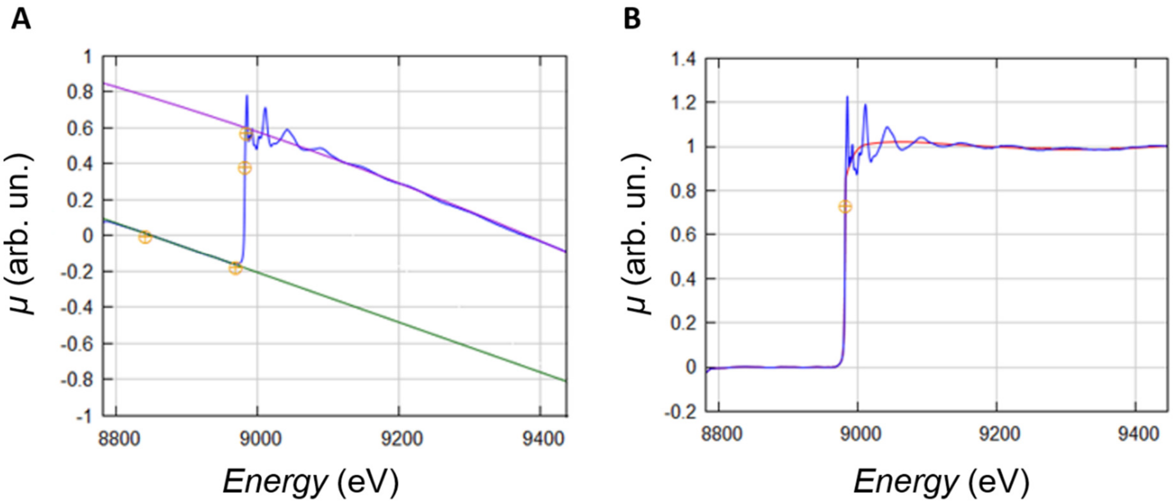

Figure 3.4: (A) Pre edge and post edge fitting of a XAS spectrum. The example is referred to the spectrum of CuI acquired at the Cu K-edge. (B) Post edge background fitting of the normalized spectrum by means of a cubic spline.

As anticipated previously, the EXAFS is then most conveniently expressed as a function of k. Moreover, this signal is generally multiplied by a weighing factor to account for the damping of the EXAFS function at higher k. The resulting EXAFS signal $\chi(k)\cdot k^2$ is shown in Fig. 3.5 A. The modulus of the Fourier Transform (FT) of the EXAFS signal is shown in Fig. 3.5 B. This signal can be considered to some extent as a radial distribution function (RDF) centred on the photoabsorber. The position of the peaks is in fact related to the interatomic distance R_j, while the peak amplitude and the broadening is related to number of atoms in a shell N_j and to the Debye-Waller factors. Nevertheless, this function is not exactly a RDF, since the position of the peaks is not equal to R_j but must be corrected by the phase shift. Moreover, the intensity of the peaks strongly depends also on the scattering function $f_j(k)$, which being non-monotonically dependent with k can also lead to additional peaks in the FT function.

The EXAFS data fitting is done starting from the EXAFS equation (1.12), derived in Chapter 1. In order to fit the data, a structural model must be first generated, where the atoms are grouped into shells composed of Nj atoms of the same kind at the same distance from the photoabsorber. In this thesis, the fit was performed for the EXAFS and the FT signal using the EXCURVE code that allows, starting from the structural model, the generation of a function that simulates the experimental one.

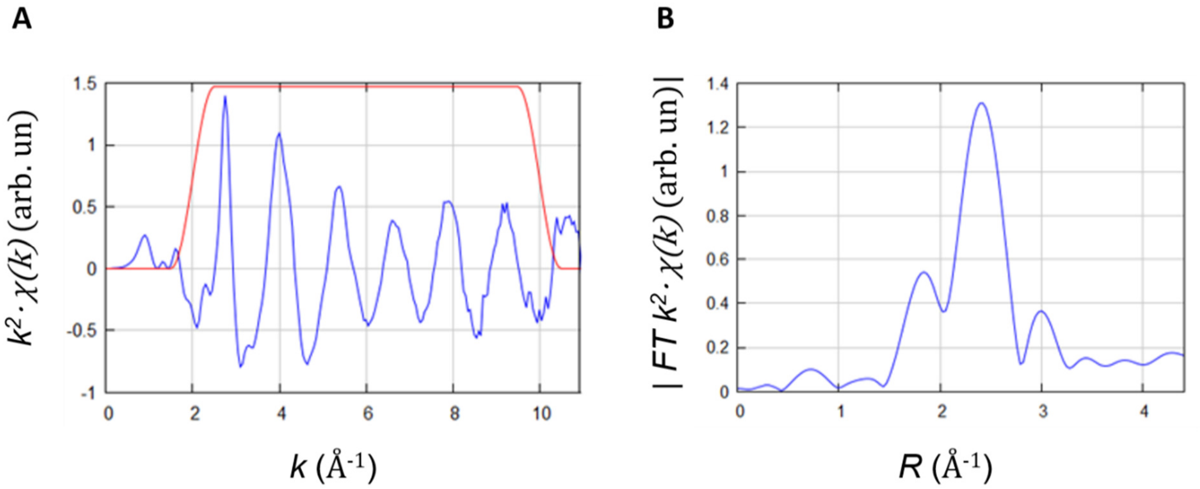

Figure 3.5: (A) EXAFS function $\chi(k)$ multiplied by k^2 for CuI. The red line is a window function, which selects the range of application of the Fourier transform. (B) Corresponding Fourier transform signal.

The number of shells, as well as the number and the type of the parameters that are included in the fit or kept fixed, must be chosen on a case-by-case basis. The fitting proceeds through several iterations, while the difference between the theoretical and the experimental curve is minimized through the Newton-Raphson algorithm. The goodness of fit is evaluated by means of the F factor:

$$F = 100 \cdot \sum_{i}^{N} \frac{(\chi_{i,exp} - \chi_{i,calc})^2}{\sigma_i} \qquad (3.3)$$

From the F factor it is possible to understand if the starting structural model is valid. At the end of the fitting procedure, the optimal values of the parameters included in the fit (typically the interatomic distances and the Debye-Waller factors) are given.

In this thesis, fits of the XANES region were also performed using a dedicated implementation of the EXCURVE code. As already anticipated in the first Chapter, the fit of a XANES spectrum is much more complicated than the fit of the EXAFS region. Generally, two approaches can be used for this purpose; the first approach aims at reproducing the XANES region on the basis of the electronic structure of the element in the compound under examination. In fact, the XANES signal can be seen as the result of transitions to localized empty electronic states, with a broadening due to the core-hole lifetime (clearly, the theory is much more complicated, and many problems arise when dealing with a XANES fitting). Initial information on the electronic states can be obtained with density functional theory (DFT) calculations[64,65] or molecular dynamics (MD) simulations[66,67]. The second approach, and the one employed in this thesis, consists in starting from a geometrical model (analogously to the EXAFS) and then fit the data according to Full Multiple Scattering (FMS) theory, taking into account a sufficient number of possible multiple scattering paths[68,69]. For a sufficiently high number of paths considered, the two abovementioned approaches are supposed to bring to the same result.

3.2 Towards new strategies: quasi-*operando* soft-XAS

In the previous Sections, *operando* XAS has been presented as an effective and versatile way to unravel the mechanism of electrochemical reactions. This is generally valid for XAS experiments carried out with hard X-rays, *i.e.* X-rays with an energy superior to *ca.* 5 keV. These experiments are in fact consolidated, and almost any experimental condition can be reached to simulate a realistic process. The same cannot be said for *operando* XAS experiments with soft X-rays, *i.e.* X-rays with an energy inferior to 5 eV. In fact, their low penetration depth has strongly hindered a parallel development of the technique in this energy regime. Having a low energy, the soft X-rays are absorbed by light elements and are therefore strongly absorbed by air. Clearly, vacuum limitations are not easily compatible with an *operando* experiment, and conventionally soft-XAS experiments, *i.e.* XAS with soft X-rays, are *ex-situ* measurements carried out in high vacuum.

In principle, *operando* soft-XAS experiments, especially in the field of electrochemistry, could be highly informative. From the one hand, soft X-rays would give access to the investigation in *operando* of the absorption edges of light elements, like the O K-edge, the C K-edge, or the Li K-edge. This, of course, would be of invaluable importance in the field of catalysis and batteries. In addition, the L-edges of transition metals of the first row could be probed, thus providing direct access to the empty *d* states. From the other hand, unlike hard X-rays, the low penetration depth of soft X-rays can in principle render them sensitive to the surface and not to the bulk; this would pave the way to the investigation of electrochemical reactions at the interface. Some examples are present in literature, where liquid flow-cells were employed to acquire soft-XAS spectra on electrochemical systems[70,71]. In these cells, the membrane served both as support for the deposition of the working electrode and to separate the liquid from the surrounding vacuum conditions. Since the seminal work of Roper *et al.*[72], several investigations have been made to obtain reliable XAS spectra at ambient pressure. However, these cells for ambient pressure soft-XAS were only limited to energies higher than 1 keV. It is only in the recent years that specific cells have been developed to acquire soft XAS measurements at ambient pressure and at energies lower than 1 keV[73,74]. Moreover, some examples of *in situ*/*operando* experiments in the field of electrochemistry have started to appear[75,76].

In this thesis, a cell for ambient pressure XAS has been employed to carry out an *operando* experiment at ambient pressure at the O K-edge and at the Sn $M_{4,5}$-edges. The aim of the experiment was to investigate the interaction of some reducing gaseous targets with SnO_2 nanoparticles. In this cell, a silicon nitride membrane (Si_3N_4) separates the ambient pressure chamber (where the sample is located) with the rest of beamline in high vacuum. The use of soft X-rays, together with the Total Electron Yield (TEY) acquisition mode, permits a high degree of surface sensitivity (only the first few nanometres of the sample were probed) to be achieved. This can be considered a pioneering experiment, which showed the potentiality of *operando* soft-XAS at ambient pressure. The future aim is to adapt this cell and this configuration also for *operando* experiments in the field of (photo)electrocatalysis. The details of the cell and of the experiment will be given in Chapter 8.

3.3 Towards new strategies: dynamic multi-frequency analysis

In heterogeneous electrocatalysis, the activity towards a specific reaction (for example the OER) is often accompanied by a consequent change in the oxidation state of the active metal. This change, which is often not possible to determine with electrochemical techniques, is evidenced by the *operando* XAS spectroscopy in a relatively straightforward manner. This can be considered an advantage of XAS: being somehow decoupled and independent from the electrochemical measurement. After an *operando* XAS experiment, a picture of the mechanism of the reaction is derived by coupling the spectroscopic and the electrochemical information obtained during the experiment, where the latter is usually extracted by simple techniques, such as chronoamperometry and cyclic voltammetry. Clearly, if *operando* XAS could be combined with more sophisticated electrochemical techniques, this would in turn lead to a deeper understanding of the reaction, from both a spectroscopic and an electrochemical point of view. In this sense, dynamic impedance spectroscopy could be a good candidate to be coupled to XAS for *operando* experiments. The possibility of acquiring dynamic impedance spectra using Dynamic Multi-frequency Analysis (DMFA) has been introduced in 2016 by Battistel *et al.*[77]; the DMFA technique allows dynamic impedance spectra to be obtained while cycling the electrode according to a cyclic voltammetry. This can, therefore, be considered as an *operando* spectroscopy, from which information on the evolution of electrochemical parameters with time and/or with the potential can be derived. In this thesis, DMFA has been employed for the first time to study the mechanism of reactions in electrocatalysis. As a test case, the most well-known electrocatalytic reaction was chosen: the hydrogen evolution on Pt electrodes. In this Section, a brief overview of classical impedance and an introduction to the basics of DMFA are presented; the results obtained with this spectroscopy will be shown in Chapter 9.

3.3.1 Classical electrochemical impedance spectroscopy

Electrochemical Impedance Spectroscopy (EIS) represents one of the most commonly employed electrochemical techniques. An impedance spectrum is usually obtained by perturbing an electrochemical system with an AC (Alternating Current) potential of small amplitude over a wide range of frequencies and measuring the current response at each frequency[78]. The AC potential V at a certain time t has the form:

$$V(t) = V_a \sin(\omega t) \tag{3.4}$$

where V_a is the amplitude of the signal and ω the radial frequency, related to the applied AC frequency by the relationship $\omega = 2\pi f$. In a linear system, the corresponding current response I has an analogue form, but it is different in amplitude and shifted in phase (ϕ):

$$I(t) = I_a \sin(\omega t + \phi) \tag{3.5}$$

Considering that the impedance Z could be simplistically defined as the ratio of the potential over the current, Z can therefore be written as:

$$Z = \frac{V(t)}{I(t)} = \frac{V_a \sin(\omega t)}{I_a \sin(\omega t + \phi)} \tag{3.6}$$

It is common to express *Z* as a complex number, exploiting Euler's formula:

$$e^{i\vartheta} = cos\theta + isin\theta \tag{3.7}$$

The potential *V*(*t*) can therefore be written as:

$$V(t) = V_a e^{i\omega t} \tag{3.8}$$

and the current as:

$$I(t) = I_a e^{i\omega t - i\phi} \tag{3.9}$$

The impedance takes then the form:

$$Z = \frac{V(t)}{I(t)} = Z_a e^{i\phi} = Z_a(cos\phi + isin\phi) = Z_{Re} + iZ_{Im} \tag{3.10}$$

As showed by (3.10), the impedance is now expressed as a complex number, composed of a real part (Z_{Re}) and an imaginary part (Z_{Im}). This representation is particularly advantageous to study the effect of various circuit elements on the impedance. An ideal resistor follows the Ohm's law, so by applying an AC voltage perturbation through a resistor, the resulting current response will not be shifted in phase. The impedance of a resistor has therefore only the real component and is independent of frequency:

$$Z_{resistor} = R \tag{3.11}$$

Where *R* represents the ability of a circuit element to resist to the flow of the electric current. When an AC voltage is applied through a capacitor or an inductor, the resulting current is shifted in phase with respect to the voltage. As a result, in both cases *Z* will be frequency dependent and it will have only the imaginary component. In the case of a capacitor, its impedance decreases as the frequency is raised and the current passing through a capacitor is shifted of -90° with respect to the voltage. The impedance of a capacitor is expressed as:

$$Z_{capacitor} = \frac{1}{i\omega C} \tag{3.12}$$

Where *C* is the capacitance. The behaviour of an inductor is opposite to that of a capacitor, with the impedance increasing at higher frequencies and the current shifted of +90° with respect to the voltage. The expression of the impedance for an inductor is:

$$Z_{inductor} = i\omega L \tag{3.13}$$

where *L* is the inductance.

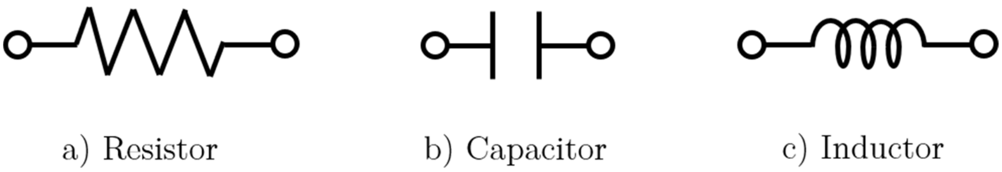

Figure 3.6: Passive elements in an electric circuit.

3.3.2 Describing electrochemical phenomena with equivalent circuits

Most of the electrochemical phenomena, *e.g.* electrochemical reactions, adsorption or double-layer formation, can be efficiently described using the circuit elements illustrated in the previous Sections (resistors, capacitors and inductors), on the base of their contribution to the impedance. As a result, an electrochemical system can be described by combining in series or in parallel the circuit elements, giving origin to an equivalent circuit (EC). The equivalent circuit is then used as a model to fit the impedance spectra. One of the most common equivalent circuits is the Randles circuit, here shown in Fig. 3.7 a, which simulates the impedance response of a faradaic reaction coupled to a mass transfer. In this model, the resistance of the electrolytic solution and the faradaic charge transfer are described as resistors (R_s and R_{ct} respectively), while the electric double-layer originating at the interface electrode/electrolyte is described through a capacitor (C_{dl}). The diffusion of the reactant towards the electrode (or of the product from the electrode to the bulk solution) is described through the Warburg element (W), which gives the following contribution to the impedance, where σ_W is called Warburg coefficient.

$$Z_{Warburg} = \frac{\sigma_W}{\sqrt{i\omega}} \tag{3.14}$$

The impedance spectrum of a Randles circuit is shown in Fig. 3.7 b as a Nyquist plot, which is obtained by plotting the real part of the impedance on the x-axis and the negative of the imaginary part of the impedance on the y-axis.

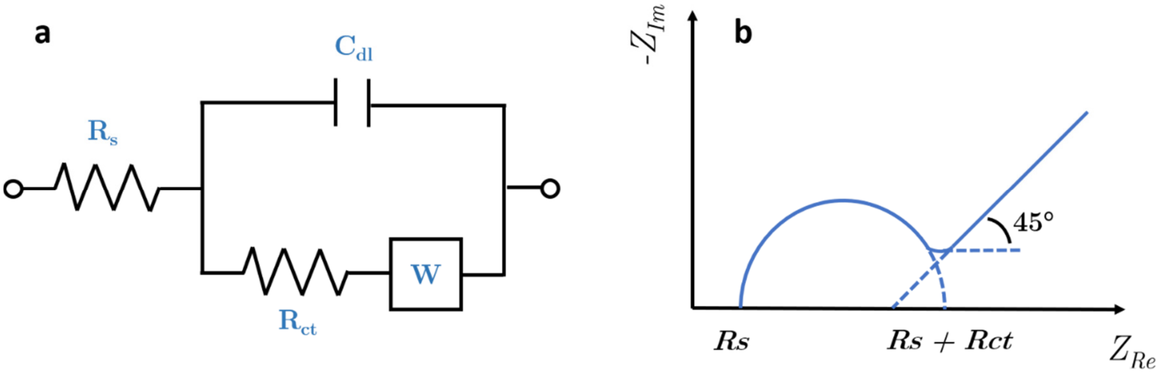

Figure 3.7: (a) Randles circuit and (b) corresponding impedance spectrum using the Nyquist representation. R_s is the resistance of the electrolytic solution, C_{dl} the double-layer capacitance, R_{ct} the charge transfer resistance and W is the Warburg element.

Other representations of the impedance spectra that make the frequency explicit are possible (*e.g.* the Bode plot); in this thesis, however, only Nyquist plots will be employed. The solution resistance can be found reading the real axis value at the high frequency intercept (left part of the x-axis). In the low frequency region (right part of the x-axis) the Warburg impedance appears as a straight line with a slope of 45°.

The Randles circuit represents a simplified model, and in most cases it is too naive to represent the reactions occurring in a real electrochemical system. Nevertheless, it is useful to consider it as a starting point to derive more complicated and realistic models.

3.3.3 Dynamic multi-frequency analysis

As mentioned before, a standard EIS spectrum is acquired by imposing an AC voltage perturbation and measuring the impedance response at a single frequency at the time. Before every measurement it is necessary that the system is in a steady-state condition, since the theory of classic impedance spectroscopy is strictly valid only under the assumption of stationarity. The requirement of steady state represents a huge limit to the study of the dynamics and the mechanisms of reactions. A strategy which has been adopted to study the mechanism of reactions is to acquire standard EIS at different potentials relevant to the reaction, recording a complete EIS spectrum at each potential step and always waiting between one potential and the other for the system to be stationary[79]. While this allows obtaining information regarding the electrochemical parameters at each potential step, the exact evolution of these parameters in time and/or with the potential is not directly observable. In addition, many electrochemical systems are intrinsically out of equilibrium or can undergo irreversible modifications during the acquisition.

The concept of dynamic impedance, or non-stationary impedance, deals with the possibility of acquiring EIS spectra in non-stationary conditions and continuously in time. Many approaches have been used in the last years to determine the temporal evolution of impedance, such as dynamic electrochemical impedance spectroscopy (dEIS)[80] or short-time Fourier transform (STFT)[81]. In this work, dynamic impedance spectra were obtained using Dynamic Multi-frequency Analysis (DMFA), an alternative to STFT developed in 2016 by Battistel *et al.*[77]. With this approach, instead of applying a single frequency at a time and then measuring the impedance response, all the frequencies are sent simultaneously through a multisine wave, with the result that it is possible to acquire a whole impedance spectrum in few seconds. In a typical experiment, the electrochemical system under consideration is simultaneously perturbed with a multisine signal and a quasi-triangular wave. In this way, the potential is swept according to a quasi-cyclic voltammetry, and a huge amount of impedance spectra are simultaneously recorded in the whole range of the quasi-CV. A pictorial scheme of the concept of DMFA is shown in Fig. 3.8.

It can be noted that the quasi-triangular wave, here shown in the upper left panel, is substantially similar to the standard triangular wave applied for DC (Direct Current) voltammetry, with a small difference only near the maximum (or minimum) of the intensity. The preference of the quasi-triangular wave is justified by a greater simplicity in data treatment, as shown by Koster[82]. The multisine waveform is created by the sum of single sine waves, each of them with a frequency which is multiple of a base frequency. In addition, the shape of the multisine has to be specifically designed so that the frequencies do not interfere with each other, neither their sum nor difference should interfere with the fundamental harmonics. The multisine allows simultaneous injection of all the frequencies, which are usually in high number (45-50) and covering five or six decades. The details regarding the design of the multisine signal can be found in Battistel *et al.*[77].

The result of the superposition of the quasi-triangular wave and the multisine signal is shown in the lower part of the figure.

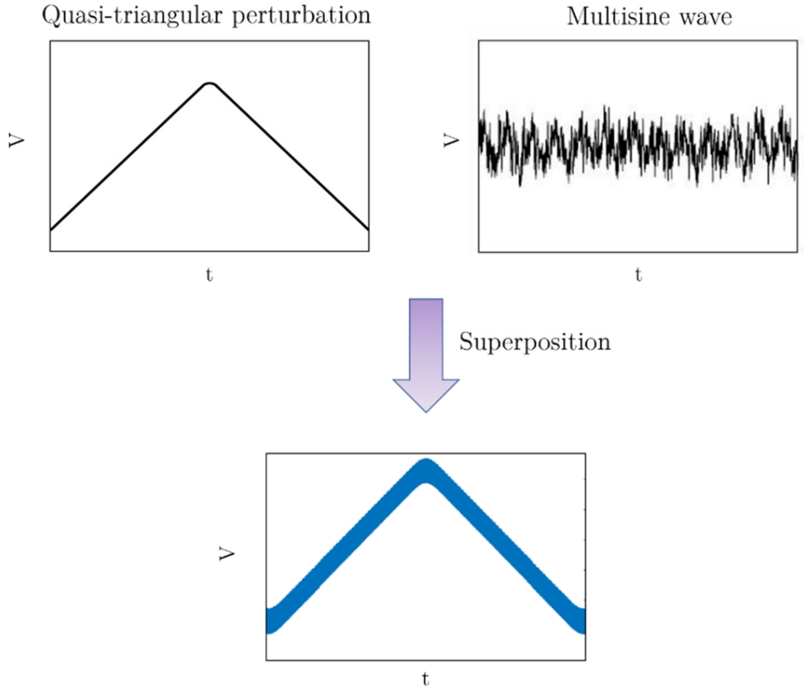

Figure 3.8: Examples of a quasi-triangular perturbation (upper left panel), of the multisine signal (upper right panel) and of the result of their superposition (lower panel).

In Fig. 3.8, all these signals are represented in the time domain. The mathematical operation that allows converting the signal from the time domain to the frequency domain is the Fourier Transform (FT). A more rigorous way to define the impedance is through the following expression, which is valid for linear systems, where the principle of superposition can be applied:

$$Z(\omega) = \frac{FT[V(t)](\omega)}{FT[I(t)](\omega)} \tag{3.15}$$

Where $V(t)$ and $I(t)$ have the form shown in equation (3.8) and (3.9). This expression defines the impedance in the frequency domain. Through the inverse Fourier Transform (iFT) the impedance is reconstructed in the time domain and can be defined as shown in equation (3.10).

In these operations, however, all the time dependence is deleted, so that in classical impedance Z is not a time-dependent function. Equation 3.12 can be rewritten with an apparent time dependence[83,84], leading to the following expression:

$$Z'(\omega, t) = \frac{iFT[V(\omega') \cdot g(\omega' - \omega, bw)]}{iFT[I(\omega') \cdot g(\omega' - \omega, bw)]} \tag{3.16}$$

Where g is a quadrature filter function applied in a suitable bandwidth bw, which can be chosen case by case in order to capture the time variation of the electrochemical system. This is the core of DMFA: the application of a filter function of finite bandwidth in the inverse Fourier Transform which allows that maintenance and extraction of the temporal variation of the impedance signal. Therefore, by using an appropriate filter in an appropriate bandwidth, it is possible to calculate for each frequency a value of $V(t)$ and $I(t)$, leading to a value of $Z(t)$.

Clearly, in order to apply equation (3.16) it is strictly necessary that the timescales of the cyclic voltammetry and of the impedance spectrum are distinct and do not overlap. A visual example is given in Fig. 3.9, where the Fourier transform of the current response signal after a typical DMFA experiment is shown in the frequency domain.

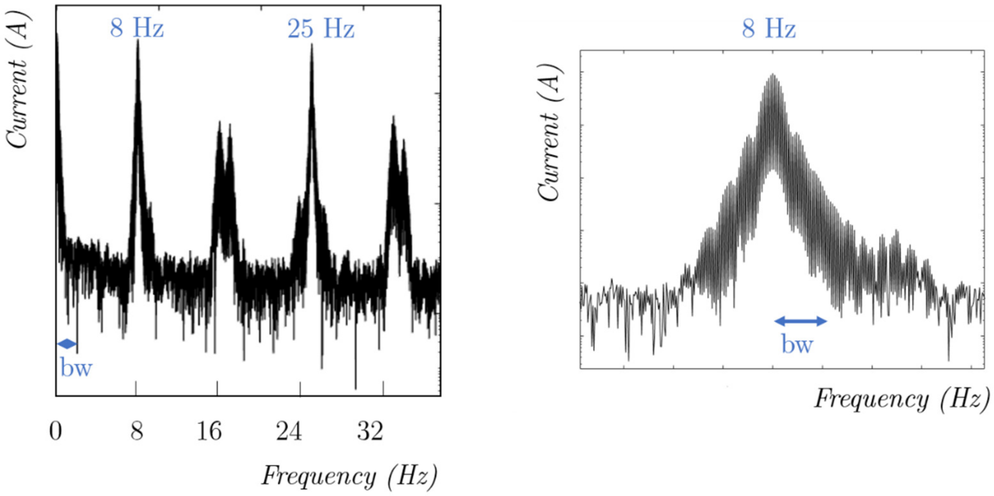

Figure 3.9: (Left panel) FT of the current response signal in the low-frequency range. The fundamental harmonics of the multisine signal lie at 8 and 25 Hz. (Right Panel) Magnification around 8 Hz and indication of a proper bandwidth.

The signal of the quasi CV appears at 0 V and extends, in this case, for about 0.5 Hz. The first two fundamental harmonics of the multisine signal can be found as peaks at frequencies of 8 Hz and 25 Hz, while the peaks at 16 and 17 Hz are due to their interference. The skirts around these peaks are due to the intermodulation between the fundamental frequencies of the multisine signal and the harmonics of the quasi-CV and can be related to the time variation of the system. As shown in the right panel of figure 3.9, where the peak around 8 Hz is magnified, the skirts around this signal extend for 0.5 Hz, as expected from the previous considerations. Therefore, in the present case a good choice of bandwidth to be used in equation (3.16) would be 0.5 Hz.

As already stated before, DMFA has been here applied as a novel electrochemical technique to study the mechanism of the hydrogen evolution reaction catalysed by platinum. The results of this experiment will be presented in Chapter 9. For further details on the principles behind DMFA, the Reader is referred to [77,82–84].

4. Operando XAS in electrocatalysis: a study of α and γ-FeOOH in HER condition

In this Chapter, X-ray absorption spectroscopy was employed to investigate α-FeOOH (goethite) and γ-FeOOH (lepidocrocite) electrodes during hydrogen evolution conditions. These materials are usually found as corrosion products of steel electrodes in a technologically-relevant route: the sodium chlorate process. Identifying the nature of the active species during the hydrogen evolution reaction, as well as the overall behaviour of these materials during the reduction and the re-oxidation, is crucial to clarify their role in the process. X-ray absorption spectroscopy proved to be particularly useful for this purpose, since a combined fit of the EXAFS and the XANES region allowed the identification of the phase formed under reducing potentials. In addition, the FEXRAV technique was employed to acquire a preliminary understanding of the behaviour of the electrodes in the desired potential range.

The contents of this Chapter have been partially published in Fracchia M. *et al.*, "α- and γ-FeOOH: stability, reversibility, and nature of the active phase under hydrogen evolution", *ACS Appl. Energy Mater.* 2018, 1, 1716-1725 [85]. Some parts are here reprinted or adapted with permission (Copyright 2019 American Chemical Society).

4.1 Theoretical background and motivation for the experiment

The chemistry of iron is particularly interesting and complex, since iron shows a great versatility and can form an incredible number of different compounds and crystal structures[86]. The existing Fe-O-H phases, counting oxides, hydroxides and oxyhydroxides are numerous and sometimes difficult to distinguish; the emblematic case, in this sense, is represented by the maghemite and magnetite[87]. Fe-O-H compounds are widely used for various applications, *e.g.* as catalysts, magnetic materials and pigments. Moreover, they are found as corrosion products of steel cathodes. Steel is employed as cathode in countless technological applications, including for $NaClO_3$ production as a precursor of ClO_2, a famous bleaching agent which is employed in chlorine-free bleaching of wood pulp. For safety, the storage of ClO_2 should be limited, since this compound can explosively decompose into Cl_2 and O_2; consequently, it is preferred to produce ClO_2 *in situ* by reduction of $NaClO_3$ with H_2O_2 or methanol in acidic conditions. The production of $NaClO_3$ is generally known as the sodium chlorate process:

$$NaCl + 3H_2O \rightarrow NaClO_3 + 3H_2 \tag{4.1}$$

In this process, which occurs in basic or neutral environments, the chloride is oxidized at the anode to form chlorine, which is immediately dissolved in the electrolytic solution leading, after few steps, to the formation of chlorate ions. At the steel cathode, the hydrogen evolution reaction occurs. This process is high energy-intensive, mainly due to the non-optimal performance of the steel electrodes. In fact, the steel electrodes commonly employed in this process (mild steel, *i.e.* steel with a low amount of carbon) show a high corrosion rate that leads to a loss of activity. The main corrosion products of the cathode were found to be α-FeOOH (goethite) and γ-FeOOH (lepidocrocite)[88,89]. Since the reaction of interest is the hydrogen evolution reaction, there is a strong interest in understanding which phase is formed under these strong cathodic conditions in alkaline and neutral media and to understand the mechanism of the reduction reaction.

Some attempts have been made in this sense, but the conclusions are rather controversial and the nature of the Fe(II) species formed under reducing conditions is still not fully understood. In a work by Stratmann *et al.*, the reduction of goethite at pH 6 was studied through *in situ* Mössbauer spectroscopy[90]. The Fe(II) species formed at cathodic potentials showed a Mössbauer signal similar to that given by $Fe(OH)_2$, but not exactly coincident. Therefore, the Authors called this new phase "$Fe(OH)_2$", describing it as a conductive gel, deposited on γ-FeOOH, with a structure similar but not equal to iron (II) hydroxide. They proposed a solid-state mechanism for this reaction, probably induced by proton hopping. This reaction was investigated also by Monnier *et al.* through XAS and XRD; they studied electrodes composed of either γ-FeOOH or ferrihydrite at pH 7.5 and 9[91]. In this case, the Authors proposed the formation of a mixture of $Fe(OH)_2$ and magnetite, in different proportions depending on the pH. Contrary to Stratmann, they hypothesized a mechanism that proceeds via dissolution and reprecipitation. Recently, *in situ* Raman spectroscopy was employed to study the reduction of both α- and γ-FeOOH; the Raman signal of the starting material disappeared at cathodic potentials, but no other signal appeared. These results indirectly show that the reduced form is probably related to iron (II) hydroxide[92].

While the overall reaction of reduction and re-oxidation is still under debate, there is a general consensus that *in situ* techniques are mandatory to investigate this reaction; it was observed that the electrode undergoes irreversible changes as soon as the material is not biased, thus preventing any reliable *ex-situ* characterization[93].

In this work, electrodes of α-FeOOH and γ-FeOOH were investigated at pH 11 by *in situ* and *operando* XAS, with the aim of identifying the structure of the phase formed in HER conditions and of clarifying the subsequent process of re-oxidation. In addition, fixed energy X-ray absorption voltammetry (FEXRAV) was employed for a rapid screening of the behaviour of the electrodes in the potentials of interest.

4.2 Experimental

4.2.1 Preparation of the sample

FeOOH electrodes were prepared on FTO (Fluorine-doped Tin Oxide, Sigma-Aldrich, 8Ω, 1x1.6 cm) by potentiostatic deposition in 0.01 M $Fe(NH_4)_2(SO_4)_2 \cdot 6H_2O$ (Sigma Aldrich 99 %) + 0.04 M CH_3COOK (Baker analyzed Reagent 99.0 %) at 90 °C in N_2-saturated solution under stirring. The FTO was previously washed in an ultrasound bath for 30 minutes in acetone, 30 minutes in ethanol and 30 minutes with water to remove any trace of grease and dust that could affect the deposition. The electrodes were then dried under N_2 flux before being used. All electrochemical techniques were carried out using a CHI 633D potentiostat/galvanostat. The Linear Sweep Voltammetry (LSV) of the deposition bath is reported in Figure 4.1 in comparison with the same material deposited on Ti foil (Alfa Aesar 99 % metal basis), previously etched in oxalic acid 10% at 80°C for 1 h. A platinum foil (2x1 cm) was used as counter electrode while the reference was a Saturated Calomel Electrode (SCE) in a double bridge filled with KNO_3 0.5 M to avoid Cl^- interferences. All potentials are here referred to the Reversible Hydrogen Electrode (RHE). The electrode area, 1 cm^2, was controlled using a Teflon tape.

The LSV, recorded at a low scan rate (1 mVs^{-1}), allows the identification of the different potential regions for the deposition of the two oxy-hydroxides of interest. Indeed, it is possible to notice a shoulder on the LSV and two distinct peaks.

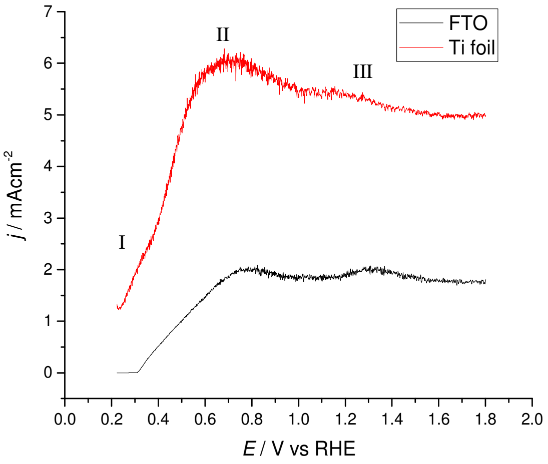

***Figure 4.1**:* Linear sweep voltammetry (LSV) of the two different substrates: titanium foil (in red) or FTO (in black). Bump "I" refers to Fe_3O_4, while "II" and "III" refer to α-and γ-FeOOH, respectively.

The shoulder (I), at about 0.3 V, is related to the formation of Fe_3O_4, while, at higher potentials, the two peaks are related to the formation of α- (II, centred at 0.7-0.8 V) and γ-FeOOH (III, for E>1.0 V), in agreement with Martinez *et al*[94]. The deposition was therefore performed at +0.45 V vs RHE for α-FeOOH and +1.60 V vs RHE for γ-FeOOH. The selected values should ensure high purity of the two materials. Using a Ti substrate the characteristic peaks are more evident (red curve in Fig. 4.1), but even on FTO (black curve) it is clearly possible to identify each specific region. The deposition was stopped after 0.11 C of charge had passed to ensure a 0.1 $mg\cdot cm^{-2}$ loading on the electrode. This value guarantees an adequate X-ray absorption, but it is low enough to reduce the possibility of self-absorption effects in the XAS experiments.

The materials were initially characterized by cyclic voltammetry (CV) in 0.200 M Na_2SO_4 (aq.) with pH 11 set with NaOH. This basic pH was selected in order to simulate the basic condition present during strong hydrogen evolution on industrial plant electrodes.

4.2.2 Description of the experiment

The XAS experiments were performed in the spectroelectrochemical cell described in Section 3.1.2, using a Pt wire as counter electrode and Ag/AgCl (1 M KCl) as reference electrode. All the potentials will be here expressed towards reversible hydrogen electrode (RHE). XAS measurements were performed at the Fe K-edge (7112 eV) in the fluorescence mode at the LISA beamline at the ESRF. A Si(311) double crystal monochromator was used; harmonic rejection was realized by Pd mirrors with a cut-off energy of 20 keV, and a High Purity Germanium fluorescence detector array (13 elements) was used. Energy calibration was performed by measuring the absorption spectrum of metallic iron foil at the Fe K-edge. The energy stability of the monochromator was checked by measuring the absorption spectrum of the Fe foil several times during the experiment. All data were obtained at room temperature. Spectra of Fe_2O_3, Fe_3O_4 and FeO were acquired in the transmission mode and used as standards. For those measurements, a proper amount of sample (as to give a unit jump in the absorption coefficient) was mixed with cellulose and pressed into a pellet.

The signal extraction was performed by means of the ATHENA code, belonging to the set of interactive programs IFEFFIT[95,96]. The EXAFS data analysis was performed with the EXCURVE code, using a k^2 weighing scheme and full multiple scattering calculations. For the XANES analysis, the raw spectra were first background subtracted using a straight line to fit the pre-edge, and then normalized to unit absorption at 800 eV above the edge energy, where the EXAFS oscillations are not visible anymore. XANES calculations were also performed by means of the EXCURVE code; the theoretical signals were generated through a Full Multiple Scattering (FMS) approach. For the fitting of the pre-edge peaks[97] the background due to the rising edge was simulated through a second-order polynomial function, and then subtracted to the experimental signal. The resulting curve was modelled by Gaussian functions.

4.3 Results and discussion

Preliminary characterizations of both α- and γ-FeOOH were performed in 0.2 M Na_2SO_4. The pH was then adjusted to 11 by adding a proper amount of 0.1 M NaOH, in order to mimic the operating conditions of the industrial plants of chlorate production under hydrogen evolution. Slow cyclic voltammetries were acquired with a scan rate of 5 mV/s from 0.9 to 0.1 V vs RHE and are here shown in Fig. 4.2 a. The CV shapes for the gamma and alpha phases nicely agree with those reported in literature in the selected potential window[89]. The XANES spectra of the dry alpha and gamma FeOOH electrodes (deposed on FTO) are shown in Fig. 4.2 b by the black and red line, respectively. Even if the spectra look quite similar, the two phases can be easily distinguished, since the alpha phase gives rise to a more intense and broad white line. These subtle differences reflect the different crystal structure of the two phases, which is shown in Fig. 4.3.

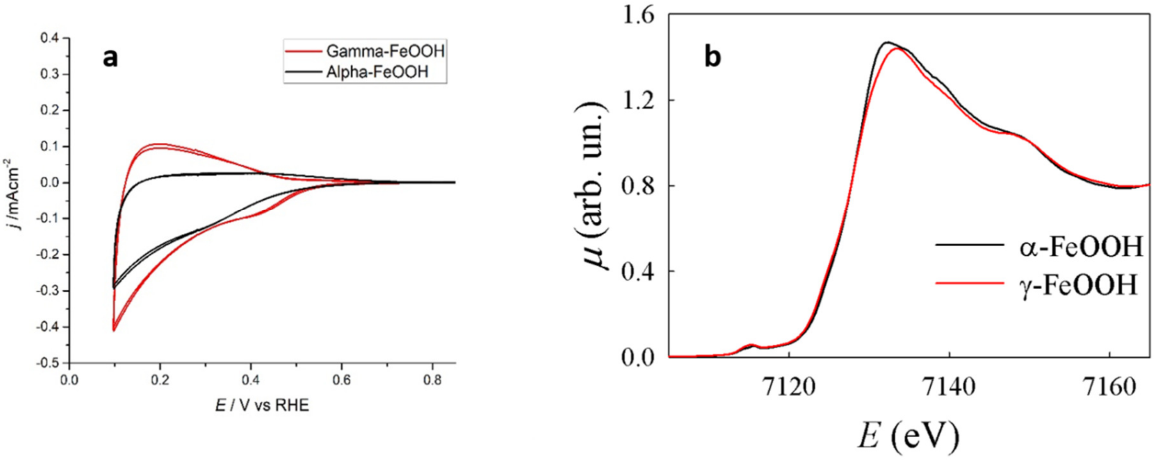

Figure 4.2: (a) Cyclic voltammetries of α-FeOOH electrode (black curve) and γ-FeOOH electrode (red curve) recorded in Na_2SO_4 0.2 M + NaOH, pH 11. (b) XANES spectra recorded at the Fe K-edge of α-FeOOH electrode (black curve) and γ-FeOOH (red curve).

In both goethite and lepidocrocite iron has an octahedral coordination, but the connection between the octahedra is different in the two structures; the lepidocrocite shows a layered-structure, while in the goethite the layers of octahedra are connected, as evident from figure 4.3. As it will be shown later, the best way to distinguish between the two phases is through the EXAFS analysis.

In Fig. 4.4, the spectrum of α-FeOOH deposed on FTO (black line) is compared to the spectrum of α-FeOOH deposed on the titanium foil (pink line). It can be seen that the two spectra are absolutely identical, thus confirming the good reproducibility of the synthesis on different substrates. However, the electrodes deposed on Ti show a remarkably higher activity towards HER that leads to the detachment of the material under hydrogen evolution. To avoid this, all the results here described were obtained on electrodes deposed on FTO.

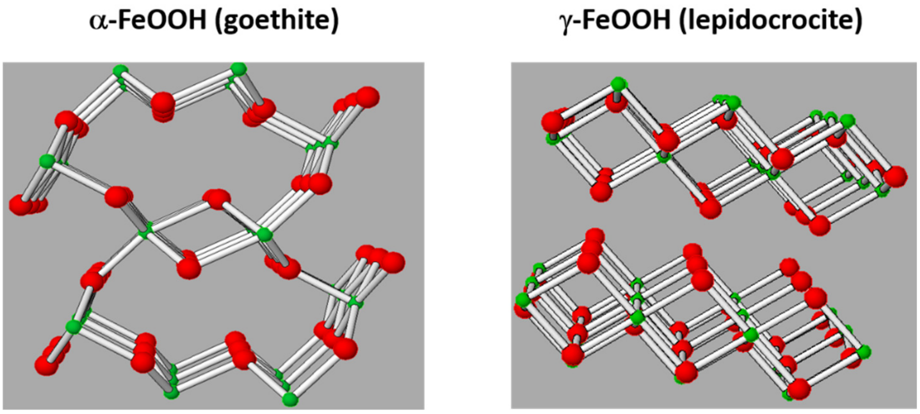

Figure 4.3: Crystal structures of goethite and lepidocrocite. The iron atoms are indicated with the green colour, while the oxygen atoms are indicated in red.

In Fig. 4.4 a, the spectrum of the dried α-FeOOH electrode is compared to the spectrum of the α-FeOOH electrode in the electrolytic solution at OCP (Open Circuit Potential) conditions. Also in this case, the two spectra are identical, so it is possible to conclude that the presence of the electrolytic solution does not affect the structure of the electrode. The value of the open circuit potential is 0.9 V both for α and γ electrodes.

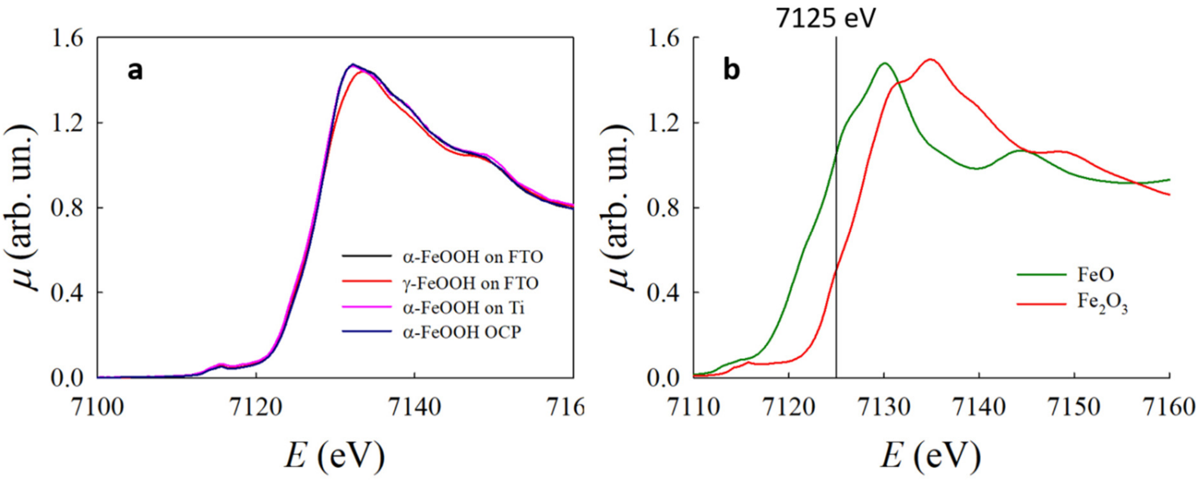

Figure 4.4: (a) XANES spectra recorded at the Fe K-edge for α-FeOOH deposed on FTO (black line), of α-FeOOH deposed on titanium (pink line) and of α-FeOOH deposed on FTO at OCP conditions (blue line). The spectrum of γ-FeOOH is also shown for comparison (red line). (b) Reference spectra of FeO (green line) and Fe_2O_3 (red line). The vertical line is set at 7125 eV, where the absorption coefficients of FeO and Fe_2O_3 show a high contrast.

The FEXRAV analysis (see Section 3.1.4) was performed for a preliminary investigation of the behaviour of the electrodes during the reduction and the subsequent re-oxidation. The absorption coefficient was recorded at the fixed energy of 7125 eV while the potential was scanned from 0.9 V to -0.7 V for two cycles with a scan rate of 1 mVs^{-1}. The energy of 7125 eV was chosen because it gives a good contrast of the absorption coefficient between Fe(II) and Fe(III), as shown in Fig. 4.4 b by comparing the reference spectra of FeO and Fe_2O_3. It can be noted that an increase in the absorption coefficient accounts for the reduction of iron.

Figure 4.5 shows the cyclic voltammetry (a and b) and the corresponding FEXRAV measurement (c and d) for α and γ-FeOOH, respectively. During the first half-cycle (shown by the orange lines in Fig. 4.5 c and d) the two FEXRAV signals are similar and show an increase of the absorption coefficient that indicates a reduction from Fe(III) to Fe(II). In the second half-cycle the absorption coefficient shows in both cases only a slight decrease.

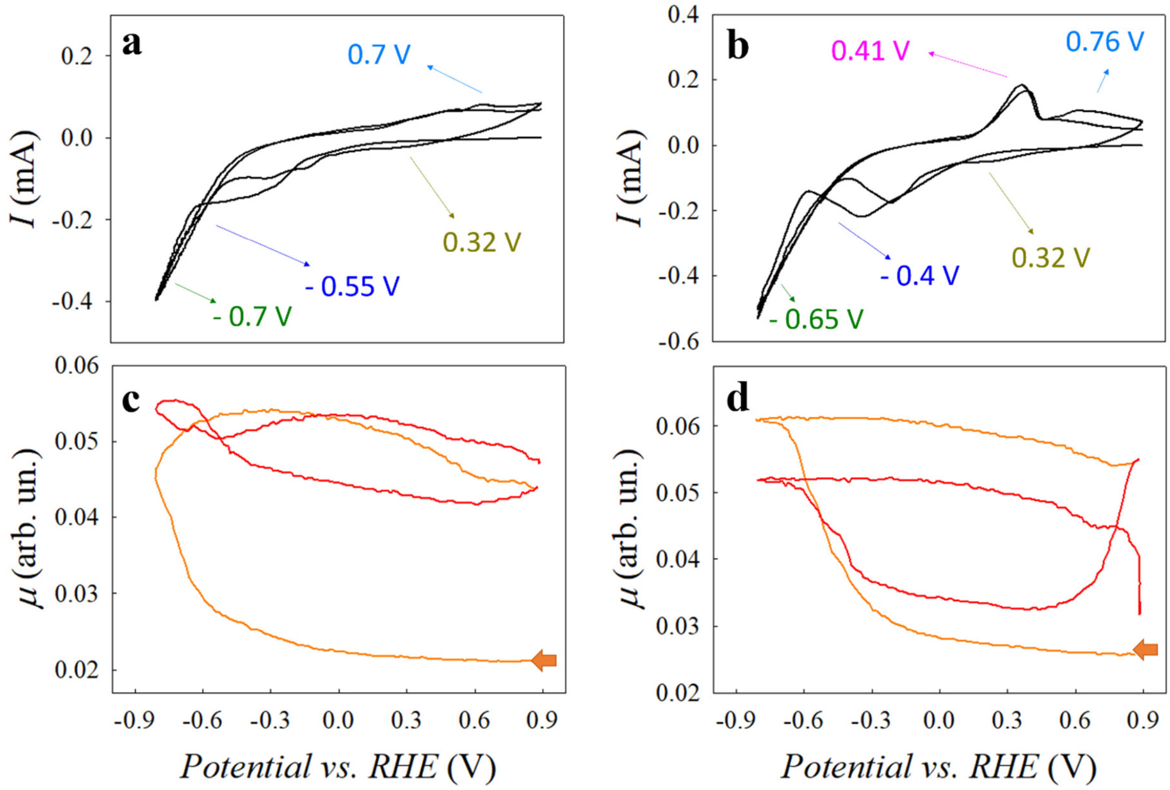

Figure 4.5*:* (a) and (c) show respectively the cyclic voltammetry and the FEXRAV for α-FeOOH, while (b) and (d) show the cyclic voltammetry and the FEXRAV for γ-FeOOH. The potentials investigated by XAS are marked in the two CV curves.

In the second cycle, shown by the red line, the FEXRAV signal becomes markedly different depending on the type of the starting electrode. In the curve corresponding to goethite (α-FeOOH) there is only a slight decrease of the absorption coefficient, thus demonstrating that at the end of the two cycles the electrode is substantially not re-oxidized. The reversibility of α-FeOOH is therefore limited, at least on the timescale considered in this experiment. On the contrary, in the curve corresponding to the lepidocrocite (γ-FeOOH), the initial increase of the absorption coefficient μ is almost fully compensated by a decrease at the beginning of the second cycle; γ-FeOOH shows therefore almost a total reversibility, and the fraction of iron that is reduced is almost completely re-oxidized after the second cycle. The different behaviour during the re-oxidation is also evident from the cyclic voltammetry: in the CV of goethite there is only a small oxidation peak in correspondence of 0.7 V. In the case of lepidocrocite, instead, there is the small peak at 0.7 V and an additional intense peak at 0.41 V, which is not present for goethite.

In order to identify the species formed during the reduction and the re-oxidation process, XAS spectra were acquired for both α and γ-FeOOH at different potentials, chosen on the basis of the cyclic voltammetry and the FEXRAV. The correspondent potentials are indicated by the arrows in the cyclic voltammetries in Fig. 4.5. The XAS spectra were first acquired at 0.32 V, where, as evident from the FEXRAV analysis, the absorption coefficient is constant, meaning that no faradaic process occurs. The spectra at 0.32 V are shown by the dark yellow curve in Fig. 4.6 a and b for goethite and lepidocrocite, respectively, and are compared to the spectrum of the correspondent pristine electrode (indicated in red). It can be seen that, as expected, the spectra at 0.32 V are substantially equal to the spectrum of the pristine material, either acquired in air or in the electrolytic solution.

XANES spectra were then acquired in correspondence of the second reduction peak (-0.55 V for α-FeOOH and -0.4 V for γ-FeOOH); the spectra are shown by the blue curves in Fig. 4.7 a and b. These spectra show a large shift towards lower energies and a drastic change of the spectrum profile. The potential of -0.7 V for α-FeOOH and -0.65 V for γ–FeOOH, in correspondence of the hydrogen evolution reaction, was also tested to identify any possible variation of the oxidation state hidden by the hydrogen evolution signal (dark green lines in figure 4.7 a and 4b). The spectra, however, look almost identical to those obtained at -0.55 V and -0.4 V, indicating that the materials are not further reduced and that the structure is preserved.

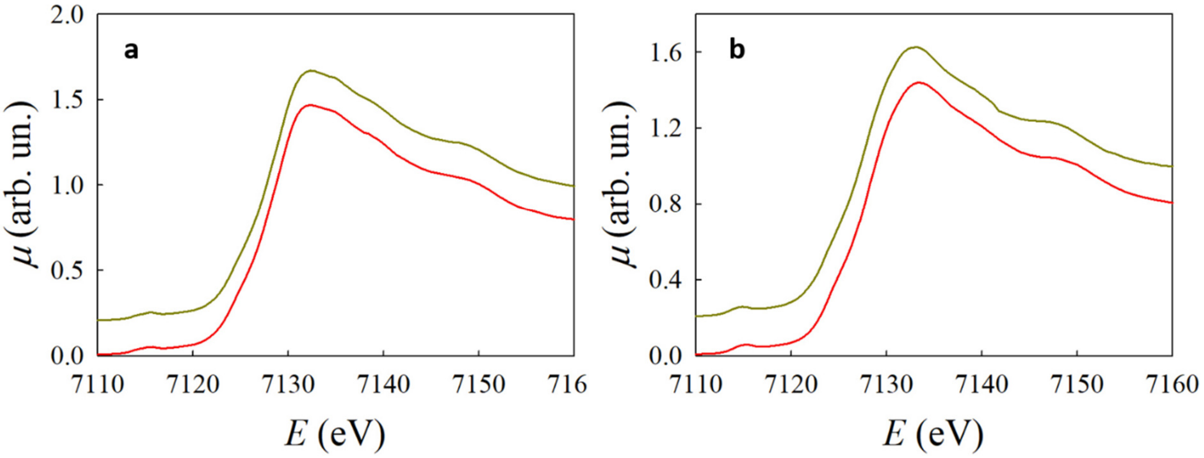

Figure 4.6: (a) XANES spectra of the pristine α-FeOOH electrode at OCP conditions (red curve) and of the electrode at 0.32 V (dark yellow curve) (b) XANES spectra of the pristine γ-FeOOH electrode at OCP conditions (red curve) and of the electrode at 0.32 V (dark yellow curve).

Moreover, neglecting marginal differences, it can be safely stated that all the four spectra obtained at reducing potentials are substantially identical, and independent of the starting phase. This indicates that even if the initial structure is different, at cathodic potentials the same phase is formed. Therefore, a single spectrum (*e.g.* the spectrum at - 0.4 V starting from the γ-FeOOH phase) can be selected as representative of the local structure of Fe at reducing potentials. In the following part, this spectrum will be referred to as spectrum of the reduced phase.

As a first step towards the identification of the reduced phase, the fingerprinting properties of the XANES region were exploited. First of all, it can be noted that the spectrum of the reduced phase is shifted to lower energies with respect to the spectra of the pristine materials, with the edge energy position typical of Fe(II). The spectrum was then compared to the spectra of various iron(II) compounds reported in literature; its overall shape shows some similarities with the spectrum of $Fe(OH)_2$[91,98] and to that of sulphate green rust[99], but the intensity of the white line in the present case is much higher. A possible explanation of this anomalous intensity can be the presence of Fe(II) in a high spin state; in fact, it is known in literature that the amplitude of the white line increases after a Fe(II) low spin → high spin transition[100,101].

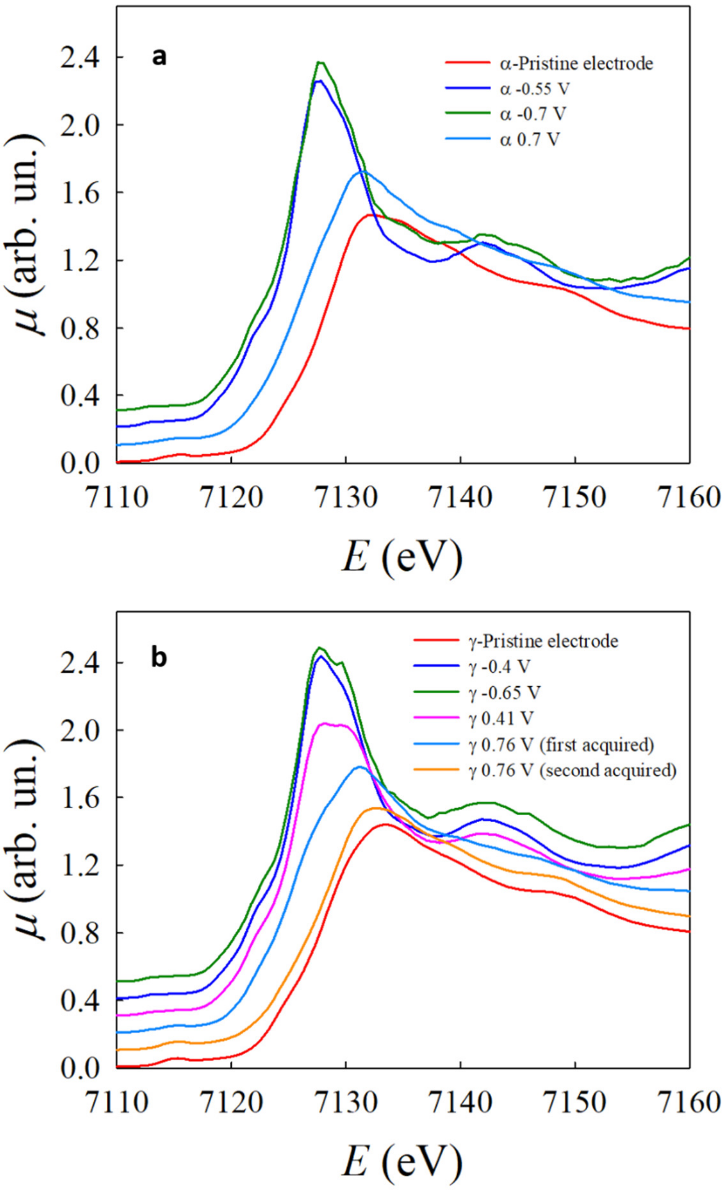

Figure 4.7: (a) XAS spectra at various potentials for α-FeOOH (b) XAS spectra at various potentials for γ-FeOOH. The correspondent potentials are marked in the cyclic voltammetries in Fig. 4.5.

The white line is due to the transition from the 1*s* to the empty 4*p* orbitals. When the transition from low to high spin occurs, the distance between the iron and the atoms in the first coordination shell increases, leading to a lower overlap between the 4*s* and 4*p* orbitals of iron. As a result, the number of accessible empty 4*p* states increases along with the intensity of the white line.

Precise information about the valence, the coordination geometry and the spin state of iron can be obtained by the so-called pre-edge peaks. These peaks result from the formally dipole forbidden 1*s*-3*d* transition and are located just before the white line. These peaks are extremely informative, especially for iron, since their position, their intensity and their shape are sensitive to the structural and electronic properties of iron. The region of the pre-edge peaks was therefore isolated according to the procedure described in the experimental section.

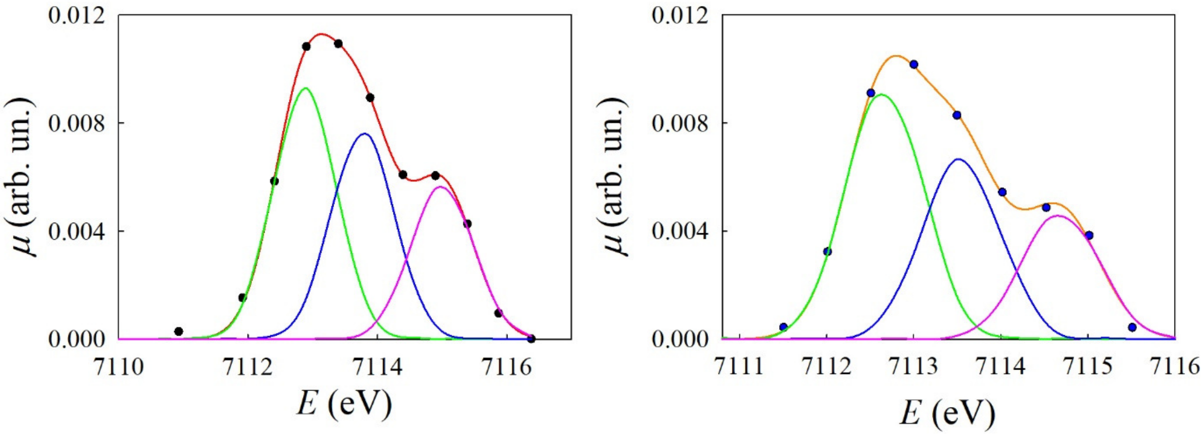

Figure 4.8: Fe K-edge pre-edge peaks for γ-FeOOH at -0.4 V (left) and for α-FeOOH at -0.7 V (right): the black and blue dots represent the experimental signal, while the red and orange curves are the fit. The green, blue and pink curves are the Gaussian functions used for the fitting.

This procedure was repeated for the four spectra at reducing potentials, obtaining the same shape for all of them; in Fig. 4.8 the isolated pre-edge peak for the spectrum of γ-FeOOH at -0.4 V and for α-FeOOH at -0.7 V are shown. The shape of the pre-edge peak shows a characteristic splitting which is consistent with the presence of high spin iron (II) in an octahedral environment[97]. According to Tanabe and Sugano[102], the electronic configuration of octahedrally coordinated Fe(II) in a high spin configuration is expected to give three multiplets in the pre-edge region, each corresponding to an excited state configuration, as shown in Fig. 4.9. Therefore, the pre-edge peak was fitted with three Gaussian functions, corresponding to the three expected transitions. The fit of the signal shows a good agreement with the experimental. The values of the intensity of the pre-edge peak (calculated as total integrated area) and of the centroid (intensity-weighted mean of the energy positions) are listed in Table 4.1 for the four spectra. According to Winkle *et al.*[103], the centroid of the pre-edge peaks is located at 7113.7 eV in minerals where the iron oxidation state is Fe(II). This value is in agreement with that found for reduced γ-FeOOH, while the values resulting from the reduced α-FeOOH are shifted of 0.4 eV towards lower energy. The cause of this shift has not yet been identified; at any rate, it can be safely stated that in all cases the iron is substantially present as Fe(II). The low intensity of the pre-edge peak is consistent with the non-distorted octahedral coordination, where an inversion centre is present; in this case 3*d*-4*p* mixing is strictly forbidden and the 1*s*-3*d* transition has a very weak intensity. The centroid energy position, the low intensity, and the peculiar profile of the pre-edge peak are therefore in accordance with the presence of high spin iron (II) in an almost undistorted octahedral coordination. This is also in agreement with the shape and the intensity of the white line.

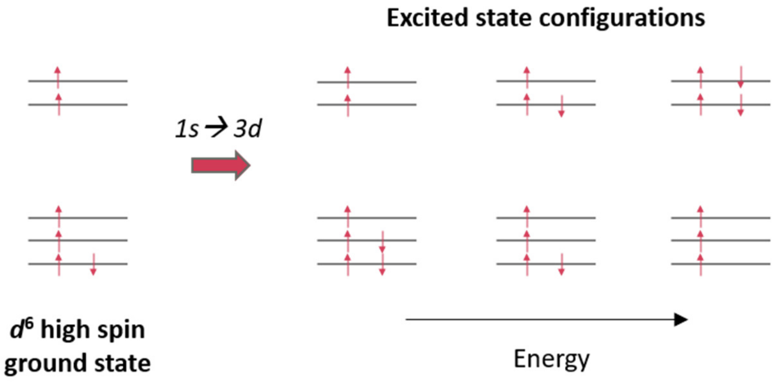

Figure 4.9: Scheme of the ground state and of the excited states for high-spin Fe(II) in an octahedral coordination. The excited states are in ascending order of energy.

Table 4.1: Values of centroids and intensity for the four extracted pre-edge peaks

Spectrum	Centroid	Intensity
α- FeOOH at -0.55 V	7113.34 eV	0.0310
α- FeOOH at -0.7 V	7113.34 eV	0.0258
γ- FeOOH at -0.4 V	7113.71 eV	0.0274
γ- FeOOH at -0.65 V	7113.75 eV	0.0338

With this preliminary knowledge, a combined fit of the XANES and the EXAFS region was performed in the attempt of identifying the structure of the reduced phase. While the EXAFS region gives specific information about the local distances, the XANES calculation is more sensible to the structural details, like bond angles and coordination geometry, and it can help to discriminate between very similar structures. Initially, the model used for the simulation was $Fe(OH)_2$, since it satisfies all the conditions imposed by the pre-edge peak analysis; however, the goodness of fit of the EXAFS and especially of the XANES region was unsatisfactory, as shown in Fig. 4.10 a (green line).

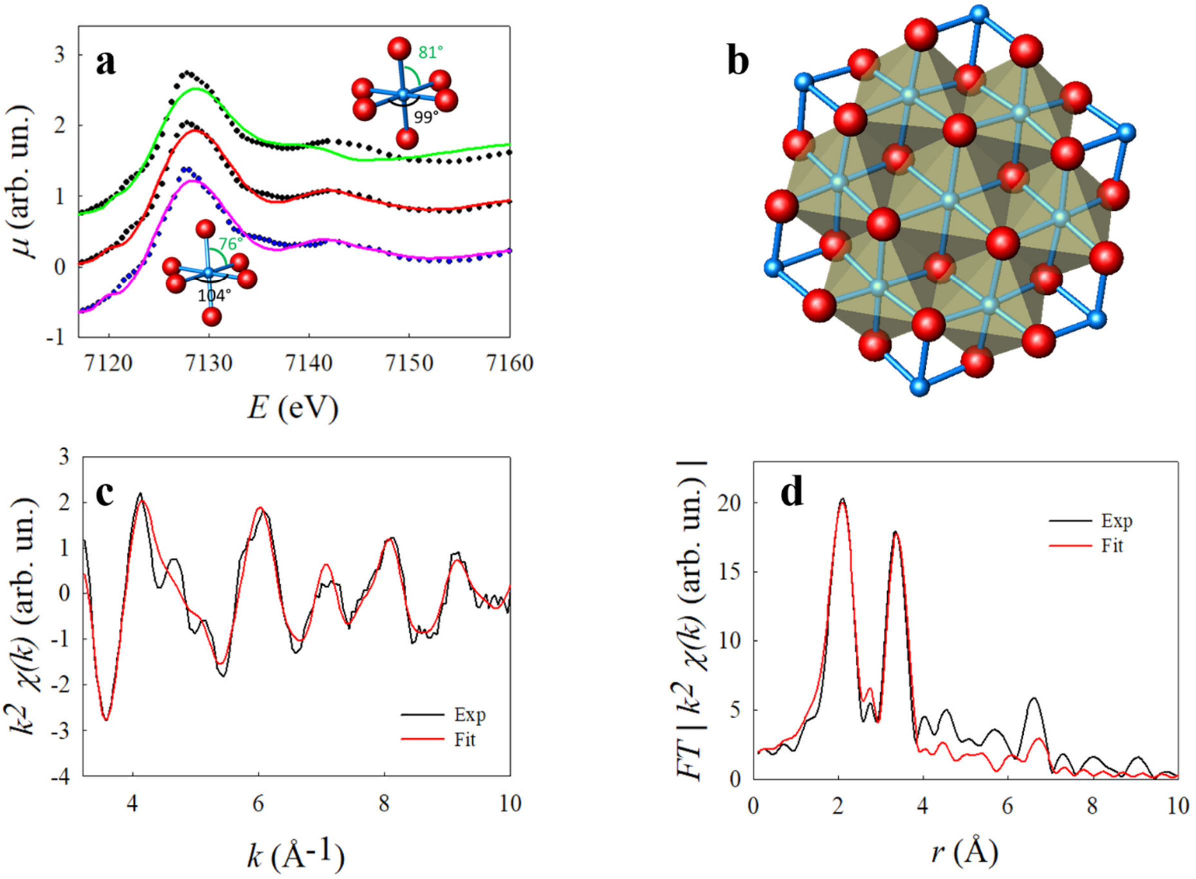

***Figure 4.10**:* (a) XANES simulation of γ-FeOOH at -0.4 V and α-FeOOH at -0.7 V. The black and blue dots represent the experimental signals for γ-FeOOH and α-FeOOH, respectively, while the coloured lines are the simulations with the model of reduced green rust (red and pink lines) and with $Fe(OH)_2$ (green line). The bond angles corresponding to the two structures are also shown. (b) Cluster of reduced green rust obtained after XANES simulation. (c) EXAFS signal and (d) corresponding Fourier Transform of γ-FeOOH at -0.4 V. The black line corresponds to the experimental curve, while the red line is the fit with the reduced green rust model.

The focus was therefore shifted to green rust, which is made by brucite-like layers with alternate Fe(II) and Fe(III), and sulphate anions to compensate the positive charges. Since, in our case, the oxidation state of iron is II, the structure used for the fit represents a reduced green rust, where both Fe(III) and the sulphate anions are not present. As seen from Fig. 4.10, both the XANES and the EXAFS region are well fitted by this model, and their goodness of fit F is respectively 0.54% and 8.97%. In Fig. 4.10 the XANES simulation is shown for γ-FeOOH at -0.4 V and for α-FeOOH at -0.7 V; it can be noted that the fit is essentially identical, as confirmed by the F factor which is equal in both cases. Since also the EXAFS analysis gives the same results for both phases, the fit is shown only for γ-FeOOH to avoid repetition. The parameters obtained after refinement are listed in table 4.2; the fit was also performed including the hydrogen of the hydroxyl group, but this did not affect the goodness of fit. It can be noted that the distance between Fe and the first shell of oxygens is larger with respect to the crystallographic one: this is consistent with the presence of high-spin iron (II). For both the XANES and the EXAFS region the dimension of the cluster was adjusted to a minimum size. For the XANES analysis, 5 shells were enough to simulate the experimental curve. For the EXAFS analysis, more shells were included; in fact, the Fe atoms in shell 2 produce a "lens" effect with the Fe atoms in shell 6 that gives a significant contribution to the EXAFS signal. In order to avoid unnecessary correlations, only few parameters were fitted.

Table 4.2: Parameters obtained after EXAFS and XANES refinement. Only the values marked with * were fitted

Shell	N	Atom	R(Å) XANES	R(Å) EXAFS	σ^2 (Å^2) XANES	σ^2 (Å^2) EXAFS	R (Å) crystallographic
1	6	O	2.20(3)*	2.134(9)*	0.011(8)	0.008(1)	2.031
2	6	Fe	3.3(5)	3.269(9)*	0.011(8)	0.0064(9)	3.189
3	6	O	3.747	3.747	0.011(8)	0.009(6)	3.747
4	12	O	4.894	4.894	0.011(8)	0.04(4)	4.894
5	6	Fe	5.524	5.524	0.011(8)	0.02(1)	5.524
6	6	Fe	-	6.379	-	0.007(4)	6.379
7	12	O	-	6.703	-	0.007(4)	6.703
F XANES = 0.54%; F EXAFS = 7.55 %; Number of EXAFS independent point: 17							

The structural model of reduced green rust used for the fit is very similar to $Fe(OH)_2$, since the connectivity of the atoms is exactly the same, and the distances are not so different in the two cases. What changes between the two structures are the angles formed by the oxygen and the iron atoms. The angle formed by two equatorial oxygens is 104.5° in the reduced green rust and 99° in $Fe(OH)_2$, while the angle formed by an axial and an equatorial oxygen is respectively 75.5° and 81°. This strongly affects the goodness of fit of the XANES simulation, since different bond angles lead to different possible multiple scattering paths of the photoelectron. For this reason, the XANES region is particularly sensitive not only to the coordination geometry but also to subtle variations of the bond angles. The cluster of reduced green rust obtained after the XANES refinement is shown in Fig. 4.10 b, while the coordinates are shown in Table 4.3. These results are in good agreement with the work by Stratmann[90], who performed *in situ* Mossbauer on γ-FeOOH, and with the *in situ* Raman study on α and γ-FeOOH. Contrary to what was reported by Monnier *et al.*[91], the presence of magnetite is excluded in the current case; the presence of this phase would lead to both a higher edge energy and a higher intensity of the pre-edge peak. It should be noted that the thickness of the FeOOH layer can strongly influence the reduction process. In the present work the low thickness of the electrodes (around 2.3 μm), together with the choice of strongly reducing potentials, should ensure the complete reduction of the material. This could therefore be the reason why species of intermediate valence (like magnetite) are not observed. In addition, the pH is also expected to have a strong influence in the reduction process.

Table 4.3: Cluster of $Fe_{13}O_{24}$ (point group: D_{3d}) used for the XANES simulation and coordinates obtained after XANES refinement.

$Fe_{13}O_{24}$ (point group: D_{3d})				
Type	N	x (Å)	y (Å)	z (Å)
Fe	1	0.00	0.00	0.00
O	6	2.007	0.00	0.897
Fe	6	0.00	3.290	0.00
O	6	3.663	0.00	-0.788
O	12	3.621	-3.195	-0.794
Fe	6	-5.524	0.00	0.00

The overall spectral profile at reducing potentials is well fitted with the reduced green rust model both in the XANES and the EXAFS regions. The four spectra obtained at reducing potentials look extremely similar and the subtle differences present in these spectra are well beyond the experimental accuracy that can be reached with the XANES and the EXAFS fit. Moreover, the first half cycle of the FEXRAV is substantially equal for both α and γ-FeOOH, thus pointing towards the fact that the structure formed below -0.4 V may be the same for both phases. Nevertheless, from the pre-edge peak analysis it has emerged that the peak is shifted of 0.4 eV towards lower energies in case of reduced α-FeOOH with respect to reduced γ-FeOOH; this could indicate that the 3*d* band is somehow different in the two cases. This can be the origin of the marked difference in the FEXRAV and in the CV during the re-oxidation process. In fact, as pointed out before, the CV of γ-FeOOH has two oxidation peaks, one at 0.41 V and one at 0.76 V, while the CV of α-FeOOH shows only one oxidation peak at 0.7 V. For what concerns the FEXRAV analysis, it was shown that at the end of the second cycle γ-FeOOH is almost completely re-oxidized. On the contrary, marked irreversibility is found for α-FeOOH, which apparently retains a mixed Fe(II)/Fe(III) oxidation state during the whole second cycle.

In order to better understand the behaviour of the electrodes during the re-oxidation process, XAS spectra were acquired in potentiostatic mode for both materials in the re-oxidation stage in correspondence of the oxidation peaks of the correspondent cyclic voltammetry. The spectra obtained for γ-FeOOH at 0.41 V and at 0.76 V are shown in Fig. 4.7 b by the pink and light blue curves. As regards the spectrum at 0.41 V, its energetic position is slightly higher than, but close to, Fe(II), indicating that at this potential only a small part of iron is re-oxidized. The spectral shape, however, is markedly different, showing a splitting of the white line. The spectrum can be efficiently simulated with a linear combination fit starting from the spectrum recorded at -0.4 V (55 %) and the spectrum recorded at 0.76 V (45%). The linear combination fit is shown in Fig. 4.11.

The spectrum acquired just after having set the potential al 0.76 V (light blue line in Fig. 4.7) presents an edge energy position intermediate between the original spectrum and that of the reduced phase, showing that more Fe(III) is formed. Nevertheless, the reaction is very slow.

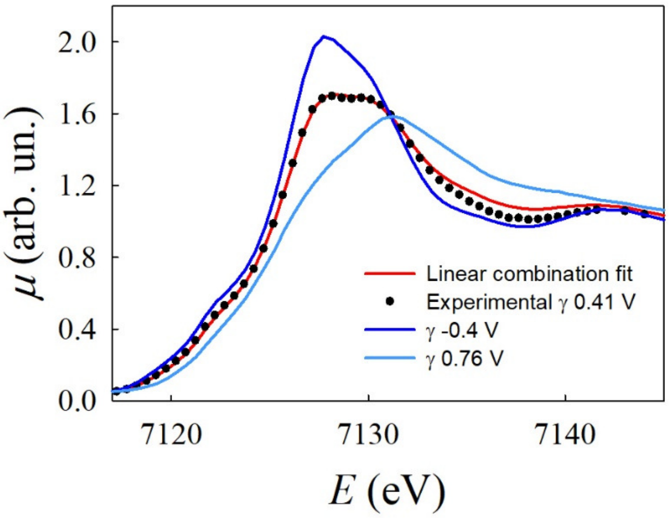

Figure 4.11: Linear combination fit of the spectrum of γ-FeOOH at 0.41 V. The black dots represent the experimental curve, while the red line is the fit obtained with 55% of the spectrum recorded at -0.4 V and 45% of the spectrum recorded at 0.76 V.

A further spectrum, shown by the orange line in Fig. 4.7, was acquired at the same potential just after the end of the previous one (*i.e.* after *ca.* 2 h). It is apparent that, neglecting a residual small shift towards lower energy, the spectrum is now coincident with that of pristine γ-FeOOH.

Concerning the re-oxidation of the α-FeOOH electrode, the spectrum at 0.7 V is shown in Fig. 4.7 as a light blue line. It is evident from the edge energy position that the re-oxidation process is largely incomplete and a mixed Fe(III)/Fe(II) oxidation state is detected. All the findings described above are in agreement with both the FEXRAV and CV results. In particular, the γ-FeOOH is more prone to re-oxidation; on the contrary, the marked irreversibility detected by FEXRAV for α-FeOOH is confirmed by the detailed XANES analysis. A further confirmation can be obtained by integrating the oxidation peaks in the CV: the resulting quantity of charge for γ-FeOOH is nearly the double of that obtained for the α-FeOOH phase. This is rather surprising: even if the product of reduction seems to be the same, and independent of the starting phase, the process of re-oxidation proceeds in a different way in the two cases. An even more surprising information on the re-oxidation process can be obtained by comparing the Fourier transform obtained from the spectrum of γ-FeOOH at 0.76 V (the first acquisition) and the spectrum of α-FeOOH at 0.7 V with the

Fourier transform of the corresponding starting phases. Goethite and lepidocrocite show some structural differences that influence their radial distribution function. Looking at the FT signals, three main peaks can be identified in the region up to 5 Å; the atoms that contribute to every peak are schematized in Figure 4.12, where the atom identified as "central iron" is coloured in black. The intensity of the third peak represents the main difference between the FT of goethite and lepidocrocite, and it can be used as a fingerprint to distinguish the two phases. Lepidocrocite has a layered structure, so all the iron atoms belonging to other layers with respect to the central iron are too distant to give a significant signal. The third peak is therefore due to only two iron atoms (blue in Fig. 4.12 a), which lie in the same plane of the central iron at a distance of 3.87 Å; as a result, this peak in γ-FeOOH is very weak.

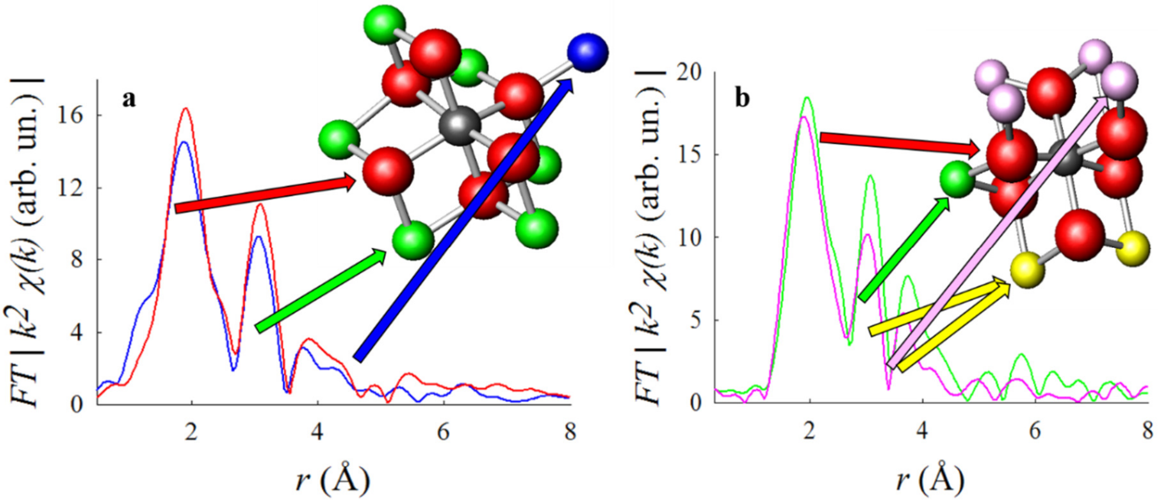

***Figure 4.12**:* Fourier transforms calculated from the corresponding EXAFS signals. (a) Comparison between the FT of pristine γ-FeOOH (red line) and γ-FeOOH at 0.76 V (blue line). (b) Comparison between the FT of pristine α-FeOOH (green line) and α-FeOOH at -0.2 V (pink line). Clusters of γ-FeOOH (a) and α-FeOOH (b) are shown to help identifying the atoms that contribute to the peaks; the central iron is grey, oxygens are red, and all the other atoms are iron atoms at various distances from the central one.

In the goethite, the third peak has two contributions: one from two iron atoms (yellow in Fig. 4.12 b) that lie in the same layer as the central atom (these atoms contribute partially also to the second peak), and one from four iron atoms that serve as a connection between two consecutive layers (pink in the figure). As a result, the third peak is much more intense in goethite than in lepidocrocite. The edge position of the spectra acquired at 0.7 V (α-FeOOH) and 0.76 V (γ-FeOOH) shows that the valence state of iron is intermediate between (II) and

(III); however, their FT signals, shown in Fig. 4.12, are similar to those of FeOOH, indicating that the structure is already substantially coincident with that of the oxidized electrode. In particular, the Fourier transform of the spectrum recorded at 0.7 V shows the intensity of the third peak typical of the alpha phase. On the contrary, the Fourier transform of the spectrum acquired at 0.76 V presents a weak intensity of the third peak, perfectly comparable to that of γ-FeOOH. As a result, it can be stated that even if the reduced phase is substantially the same, and independent of the nature of the starting electrode, a different behaviour arises during the electrochemically driven re-oxidation; the electrode therefore presents a "memory effect", since it is able to preserve a memory of the initial crystal structure. The origin of this memory effect is still unknown and clearly calls for further investigations. Probably, a bond linkage of the starting phase is somehow preserved in the structure of the reduced phase. While the layers of octahedra in the γ-FeOOH are completely independent, the octahedra in the α-FeOOH phase are connected. Maybe, weak correlations are still present between the octahedra in the reduced α-FeOOH phase, while they are absent in the reduced γ-FeOOH phase. If these correlations are weak and randomly distributed, they are expected to give a negligible contribution to the XAS spectra, so that the spectra of the reduced phases look equal. The mere presence of such a reversibility, however, clearly indicates that the reduction process cannot proceed through a dissolution/re-precipitation mechanism.

The spontaneous re-oxidation of the material in air was also investigated. An α-FeOOH electrode was polarized to cathodic potential and then left overnight in air at room temperature. A XANES spectrum was then acquired *ex-situ* on the electrode; the result is that this spectrum can be simulated by a linear combination fit of the spectra of pristine α-FeOOH and γ-FeOOH, demonstrating the formation of 41% of α-FeOOH and 59% of γ-FeOOH. The linear combination fit is shown in Fig. 4.13.

This shows that the oxidation in air destroys the reversibility of the reduced green rust to FeOOH, which probably re-oxidizes following another route that deletes the memory effect.

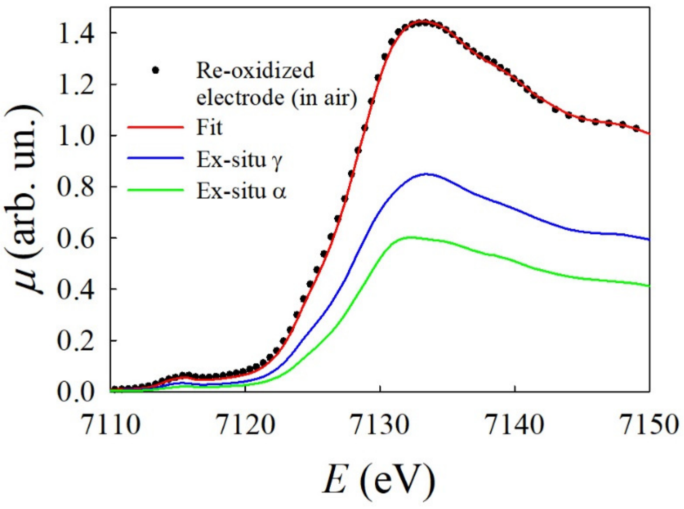

***Figure 4.13**:* XANES fit of the spectrum of the electrode after re-oxidation in air. The experimental signal is represented by the black dotted line, while the fit (red line) is obtained by a linear combination fit of the spectra of dry α-FeOOH (41.4%) and dry γ-FeOOH (58.6%). The spectra of *ex-situ* α-FeOOH (weighted by 41.4 %) and dry γ-FeOOH (weighted for 58.6%) are shown by the green and the blue line, respectively.

4.4 Final Remarks

The aim of this work was to understand, through the application of X-ray absorption spectroscopy, the behaviour of α-FeOOH (goethite) and γ-FeOOH (lepidocrocite) electrodes under condition of hydrogen evolution and during the subsequent process of re-oxidation. Thanks to a preliminary analysis of the pre-edge peaks and to a combined fit of the XANES and the EXAFS region, a structure for the unknown iron(II)-containing phase formed under strong reducing potentials (*i.e.* lower than -0.4 V vs RHE) and under hydrogen evolution was proposed. It was observed in fact that this phase bears a relation with the structure of the green rust (space group P$\overline{3}$1m). The spectra of the reduced electrodes show an impressive similarity, meaning that the structure formed is substantially the same and independent of the starting phase. However, some subtle differences are present that probably affect the re-oxidation process. In fact, the electrodes show a memory effect, since after the electrochemically-driven re-oxidation the original phase (α-FeOOH or γ-FeOOH) is restored. While for the γ phase the entire process of re-oxidation was followed, for the α phase the complete re-oxidation was not achieved in the selected range of potentials. Nevertheless, reversibility was clearly observed in both cases, since the spectra showing an intermediate oxidation state Fe(II)/Fe(III) demonstrate that the structure is already that typical of the correspondent pristine electrodes. This is valid only for the electrochemically-driven re-oxidation: when the oxidation occurs spontaneously in air, the original phase is not restored and the electrode shows a mixture of goethite and lepidocrocite.

Additional studies are needed to clarify the mechanism of the reduction and to understand the origin of the memory effect. However, it has been demonstrated that precise structural information can be obtained through an exhaustive analysis of the XAS spectrum, even in absence of a pre-existing model. These results are expected to be of interest in the field of iron corrosion and especially for the development of cathodes for the sodium chlorate process, in order to reach a higher stability and a better selectivity for the hydrogen evolution reaction.

5. Operando XAS in photoelectrocatalysis: investigating WO_3 photoanodes

In the previous Chapter, XAS has been applied in the field of electrocatalysis to study the behaviour of the electrode during the process of reduction/re-oxidation and during hydrogen evolution condition. In this Chapter, the feasibility of *operando* XAS in the field of photoelectrocatalysis is shown. WO_3 is one of the most studied photoanodes for water splitting and environmental remediation; in the present work, *operando* experiments were conducted at the W L_3-edge on WO_3 photoanodes to directly observe the electronic changes in the 5*d* band during UV/Vis illumination. The differences in the XANES spectra between dark and light conditions are expected to be small; however, the recording of differential spectra in dark/light states, and the use of a technique similar to fixed-energy X-ray absorption voltammetry (FEXRAV) permitted these subtle differences, that otherwise risked to be masked by experimental error or subsequent manipulation during data analysis, to be observed.

The contents of this Chapter have been partially published in Fracchia M. *et al.*, "*Operando* X-ray absorption spectroscopy of WO_3 photoanodes", *Electrochim. Acta* 2019, 320, 134561.[104]

5.1 Theoretical background and motivation for the experiment

As shown in Chapter 2, the photocatalytic water splitting has attracted lot of attention in the recent years, as it allows the production of clean hydrogen in a sustainable way by exploiting solar radiation. In this process, a semiconductor, employed as photocatalytic material, absorbs the visible light creating electron-hole pairs. The electrons are then responsible for the reduction of water to hydrogen, while the holes are responsible for oxidation of water to oxygen. Further details on this process can be found in Section 2.1.3. In the semiconductor, the photogenerated electrons and holes are separated thanks to the electric field which is created within the semiconductor at the semiconductor/liquid junction (SCLJ). Several methods have been employed to obtain a better understanding of the SCLJ, from purely electrochemical techniques (*e.g.* the analysis of transient photocurrent, impedance spectroscopy and scanning electrochemical microscopy) to X-rays-based techniques and transient spectroscopies[105]. XAS could represent a powerful tool in this sense, since it is element selective and allows information on the oxidation state and the chemical surrounding of the absorbing atom to be obtained. However, and as already pointed out in this thesis, XAS is sensitive to the bulk and not to the surface. This can be a drawback in the study of interphases, as XAS gives information that averages over all the absorbing atoms sampled by the X-ray beam. This notwithstanding, *operando* XAS has proved to be effective in determining the nature of active sites in case of inner-sphere reactions[106].

In the field of photoelectrocatalysis, though, *operando* XAS has been scarcely employed and is limited to only a few studies, *e.g.* on hematite photoanodes[107] or on relevant overlayers[53,108]. This is mainly due to two reasons: i) the limited access to synchrotron radiation facilities and ii) the limited number of long-lived photogenerated carriers in a photocatalyst, as photogenerated carriers rapidly undergo recombination or they are accumulated in surfaces states, where they cannot be detected with a bulk technique like XAS. This leads to a high difficulty in detecting with sufficient statistics the subtle differences between dark and light conditions. In principle, ultrafast time-resolution XAS could be used to detect these short-lived charges; however, and at least up to now, ultrafast XAS has never been applied in *operando*. In order to overcome this difficulty, two main solutions can be contemplated. The former consists in the *ad hoc*-preparation of samples with high surface-to-bulk ratio; in this way, the charges stored at the surface could be easily detected. However, this would lead to the employment of unrealistic samples with likely diminished performance, thus losing the concept of an "*operando* experiment", where realistic working conditions and performance should be retained. The second solution, that is employed in the present work, is to develop *ad hoc* techniques that may highlight the small differences between dark and light conditions, *i.e.* the small changes in the absorption coefficient μ (in the order of a few percent), making them well evident and above the experimental error. Two complementary techniques were employed for this purpose in this work: i) the acquisition of differential spectra $\Delta\mu$: this technique, already introduced in Section 3.1.4, consists in acquiring in parallel the spectrum in dark and under illumination. This ensures that the absorption coefficients under light and dark are measured under the same instrumental condition and can therefore be directly subtracted. ii) the absorption coefficient is measured alternatively in dark and light at a fixed energy and at a fixed potential. Similarly to the FEXRAV, the energy is chosen as to give the maximum contrast between two oxidation states of two different standard phases. This technique allows an immediate comparison of the absorption coefficient in dark and light situations, and the simultaneous recording of spectroscopic and electrochemical information without the need for any data treatment.

In this experiment, WO_3 was chosen as a model photoelectrocatalyst, as it is one of the most studied and promising *n*-type semiconductor for water splitting in PEC cells and wastewater remediation[109,110]. The spectra were acquired at the L_3-edge, which results from the $2p \rightarrow 5d$ transition, and therefore allows the empty $5d$ band of tungsten to be monitored directly.

The aim of this work is to demonstrate the feasibility of *operando* XAS for the study of a semiconductor/liquid junction, with the possibility of directly observing the conduction band of a photoelectrocatalyst under working conditions.

5.2 Experimental

5.2.1 Preparation of the sample

H_2WO_4 was generated from 2.5 g of Na_2WO_4 (AlfaAesar) by addition of 20 ml of concentrated HCl (Aldrich), followed by several washings in order to eliminate NaCl. The colloidal suspension of H_2WO_4 was obtained by addition of 2 g of oxalic acid (Sigma-Aldrich) at 60 °C. The electrodes were prepared by sequential spin coating deposition of the H_2WO_4 precursor on well-cleaned FTO (Fluorine Tin-doped Oxide). The H_2WO_4 precursor was prepared by adding 20% w/w Carbowax (Sigma-Aldrich, 15000–20000 u) and triton X-100 (Fluka) (1 drop/2 g of colloidal precursor) to the H_2WO_4/oxalic acid colloid. After each deposition the electrode was heated at 550°C for 30 min in air. Up to six spin coated layers led to nanocrystalline electrodes having a thickness of *ca.* 1.5 µm. As shown by Atomic Force Microscopy (AFM) and Scanning Electron Microscopy (SEM), these films are characterised by a network of roughly spherical nanoparticles of *ca.* 50 nm diameter[111]. All electrodes have a geometrical active area of 1 cm^2.

5.2.2 Description of the experiment

X-ray Absorption spectra at the W L_3-edge (10207 eV) were acquired in the fluorescence mode at the LISA beamline at ESRF (European Synchrotron Radiation Facility), using a Si(311) double crystal monochromator, Pd mirrors with a cut-off energy of 20 keV for harmonic rejection, and a 13-elements Ge fluorescence detector. Energy calibration was performed by measuring the absorption spectrum of a metallic W foil at the W L_3-edge. The spectra of reference samples were acquired in the transmission mode; for these measurements, a proper amount of sample, that yielded a unit jump in the absorption coefficient, was mixed with cellulose and pressed into a pellet. All data were obtained at room temperature. To simulate the real operating conditions of the water splitting reaction, the electrode was placed in the electrochemical cell and simultaneously irradiated with X-rays and UV/Vis light, while an external potential was applied. The measurements were acquired in the spectroelectrochemical cell described in Section 3.1.2. The working electrode was a WO_3 nanocrystalline electrode, the counter electrode was a Pt wire and the reference Ag/AgCl (1 M KCl). The electrolytic solution was aqueous Na_2SO_4 0.1 M. The electrode potential was controlled through a CHI633D potentiostat (CH Instrument); all potentials are referred to reversible hydrogen electrode (RHE). The UV/Vis illumination was achieved by means of a 400 nm Light Emitting Diode (LED), focused at the back of the photoelectrode, while the X-rays impinged at the front. Spectra in UV-Vis light and dark conditions were acquired in parallel: for each energy value, the acquisition was performed both in presence and in absence of UV-Vis illumination before moving to higher energy values in order to minimize systematic errors. The acquisition time for each point was set to 10 s. For each potential, three repetitions of the measurement were acquired. Extraction of the X-ray signal and normalization were performed by means of the ATHENA code, belonging to the set of interactive programs IFEFFIT[95,96]. The pre-edge background was fitted by means of a straight line and the post edge background by means of a cubic spline.

5.3 Results and discussion

Prior to the experiment, a cyclic voltammetry was recorded at 20 mVs^{-1} on the WO_3 electrodes from 0.22 V to 1.32 V vs RHE in 0.1 M Na_2SO_4. The curves were recorded in the experimental hutch at ESRF inside the spectroelectrochemical cell, both in dark and under the LED illumination. The two CV curves in dark and light are shown in Fig. 5.1 (black and red line respectively). The CV recorded in light inside the spectroelectrochemical cell before the XAS experiment is compared to the CV recorded on an electrode coming from the same preparative batch in a conventional electrochemical cell (green line in Fig. 5.1). It can be observed that despite some small differences, which are mostly due to the sample preparation and by a different photoelectrode history (*e.g.* previous illumination and polarization cycle), the two curves look similar. In particular, the photoanodic onset potential, which is obviously one of the most important parameters in an *operando* experiment, is totally coincident in both cell configurations. For the spectroelectrochemical cell the slope of the J/E curve is lower with respect to the conventional cell; this is due to a higher IR drop in the spectroelectrochemical cell, where the interelectrode distance is higher and therefore not optimal.

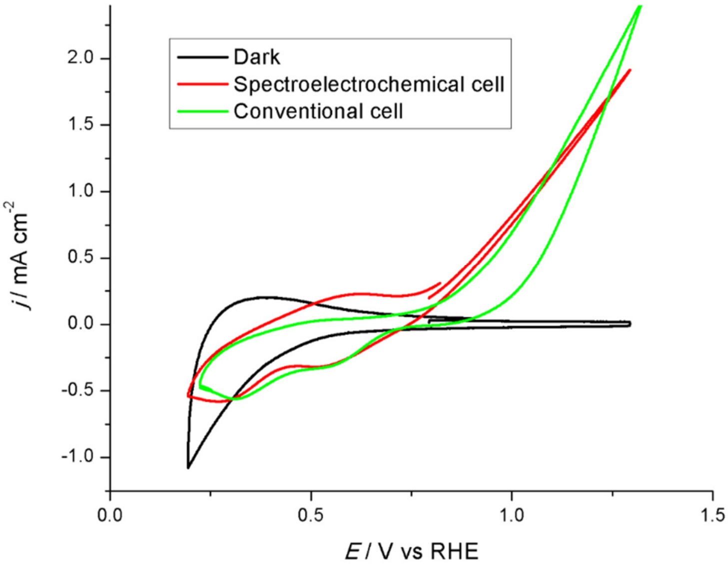

***Figure 5.1**:* CV curves recorded inside the spectroelectrochemical cell in dark and light (black and red line) and CV curve recorded under illumination in a conventional electrochemical cell (green line).

Despite this difference in the slope, the magnitude of the photocurrent around 1.2-1.3 V is totally comparable to that obtained for the conventional cell. During the experiment, the potential was limited to 1.3 V to avoid excessive bubble formation. Therefore, it is possible to conclude that the two situations are comparable, and that the spectroscopic results obtained in the spectroelectrochemical cell can be considered as indicative of “operational conditions”.

The XANES spectra of some reference compounds were acquired at the W L_3-edge and are shown in Fig. 5.2 a. The spectrum of WO_3 in shown by the blue line; the white line presents a typical shape which is due to the transition from the W 2*p* orbitals to the empty 5*d* orbitals. In the WO_3 structure the tungsten atoms have an octahedral coordination with six surrounding oxygen atoms, leading to a splitting of the 5*d* orbitals into t_{2g} and e_g, according to the crystal field theory[112]. As a result, the white line shows two small peaks, separated by *ca.* 2 eV, one related to the transition to the empty t_{2g} orbitals, at lower energies, and one related to transition to the empty e_g orbitals, at higher energies[113]. This is better evidenced in the inset in Fig. 5.2 a.

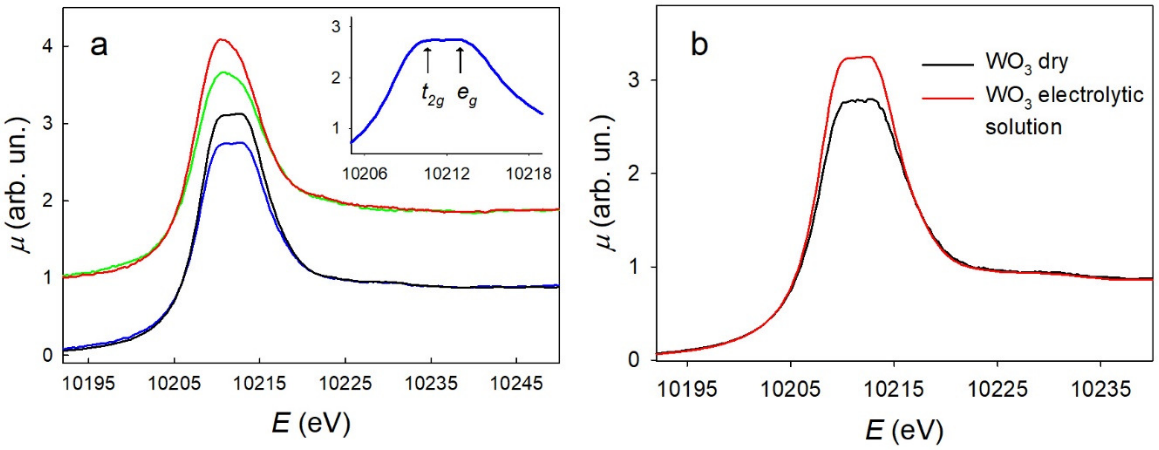

Figure 5.2: a) W L_3-edge XANES spectra of WO_3 (blue line), WO_3 after annealing in air at 900 °C for 1 hour (black line), WO_3 after reduction with gaseous NH_3 flux at 900 °C for 12 hours (green line) and of sodium tungsten bronze (red line). The spectra of the reduced species are shifted on the y-axis for better clarity. Inset: magnification of the white line b) W L_3-edge XANES of the dry WO_3 electrode (black line) and of the WO_3 electrode in the electrolytic solution without any applied potential (red line).

When the WO_3 powder is heated at 900 °C for one hour, the intensity of the white line shows a marked increase, probably due to a local distortion of the WO_6 octahedral units[114].

The reduction of tungsten with gaseous NH_3 flux leads to a small shift of the spectrum to lower energies, and to a change in the profile of the white line, which becomes higher in intensity and loses its characteristic splitting. This is compatible with the formation of some sub-stoichiometric WO_3 phases like $W_{18}O_{49}$ or $WO_{2.90}$, where the increase of the white line intensity is related to higher distortion of the WO_6 octahedra[114,115]. The shift to lower energy in XAS is also indicative of a lower oxidation state.

The red line in Fig. 5.2 a is the spectrum of sodium tungsten bronze (Na_xWO_3, where x is 1 or lower than 1). In this structure, W has a valence state slightly lower than VI; the spectrum presents a shape similar to reduced WO_3 (green line), even if the white line is more intense. Also in this case, this is probably due to changes in the WO_6 units related to the presence and intercalation of Na^+ inside the structure.

Fig. 5.2 b shows the XANES spectra of the dry WO_3 electrode (black line) and of the WO_3 electrode inside the electrolytic solution without any applied potential (red line). The spectrum of the electrode inside the solution shows a marked increase of the intensity of the white line with respect to that given by the dry electrode. This can be due to the hydration of the electrode or to a slight intercalation of ions from the electrolytic solution. It is clear both from these spectra and from the reference spectra that even minor changes in the local coordination can lead to considerable changes in the white line intensity.

After this preliminary characterization, the behaviour of the WO_3 electrode was studied at different applied potentials. The resulting spectra are shown in Fig. 5.3.

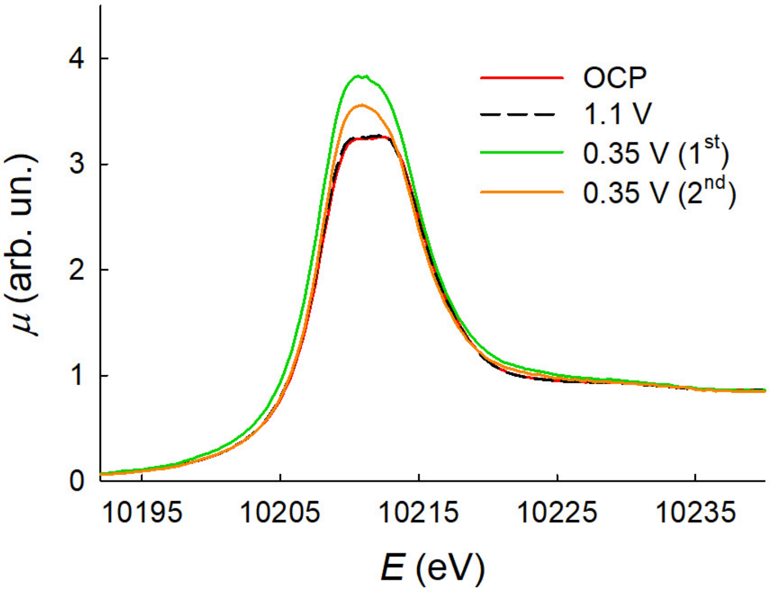

***Figure 5.3**:* W L_3-edge XANES spectra of WO_3 photoanodes at OCP (red line), at 1.1 V vs RHE (black dashed line), at 0.35 V (green line) and at the same potential but after 2 hours (orange line).

At 1.1 V the spectrum is coincident with that obtained at OCP conditions, since WO_3 cannot be oxidized further. At 0.35 V, *i.e.* at potentials more cathodic than the OCP, the spectrum changes its profile, showing the increase of the white line together with the loss of the splitting typical of WO_3. As shown before, this spectrum profile can be indicative of a reduction of WO_3 to form a sub-stoichiometric phase and/or to the intercalation of Na^+ from the electrolytic solution inside the structure, with the formation of a structure close to tungsten bronze. This second hypothesis is somehow confirmed by the fact that the second spectrum acquired at 0.35 V, recorded after leaving the WO_3 electrode polarized at this potential for two hours, shows a decrease in the intensity of the white line. This is indicative of an underlying process occurring with a slow kinetic rate, which is compatible with a slow diffusion of Na^+ inside the structure (or OH^- outside the structure).

The behaviour of WO_3 as photoelectrocatalyst was investigated at the W L_3-edge at OCP conditions, under a potential where no photocurrent is observed (0.35 V) and at 1.1 V, in correspondence of which a consistent photocurrent is observed, but not so high as to cause bubble formation that would disturb the acquisition. As explained in the previous Sections, the spectra in dark and light were acquired simultaneously with a differential technique that helps minimization of systematic errors; the $\Delta\mu$ signal, derived from the subtraction of the spectrum in light minus the spectrum in dark, was calculated for each potential. The resulting difference signals $\Delta\mu$ are shown in Fig. 5.4 (left panel) together with the spectrum of WO_3. The dashed lines in the Figure indicate the energies in correspondence of the empty t_{2g} and e_g orbitals. As expected, the resulting $\Delta\mu$ signals have a very low intensity. An estimation of the number of W centres involved in the photoexcitation process can be given considering that i) at 400 nm the excitation power has a value of 0.1 W/cm^2 ii) the film is formed by spherical particles with an average diameter of 50 nm for a total thickness of 1.5 μm and iii) each nanoparticle is formed by WO_6 octahedra having a spherical footprint with a radius given by the W-O distance. This gives a value of about 1/100 of the excited W atoms in the film, contributing for an electron.

As evident by Fig. 5.4, $\Delta\mu$ is above the experimental noise only at OCP conditions; in addition, the amplitude of this $\Delta\mu$ signal is compatible with the experimental number given above.

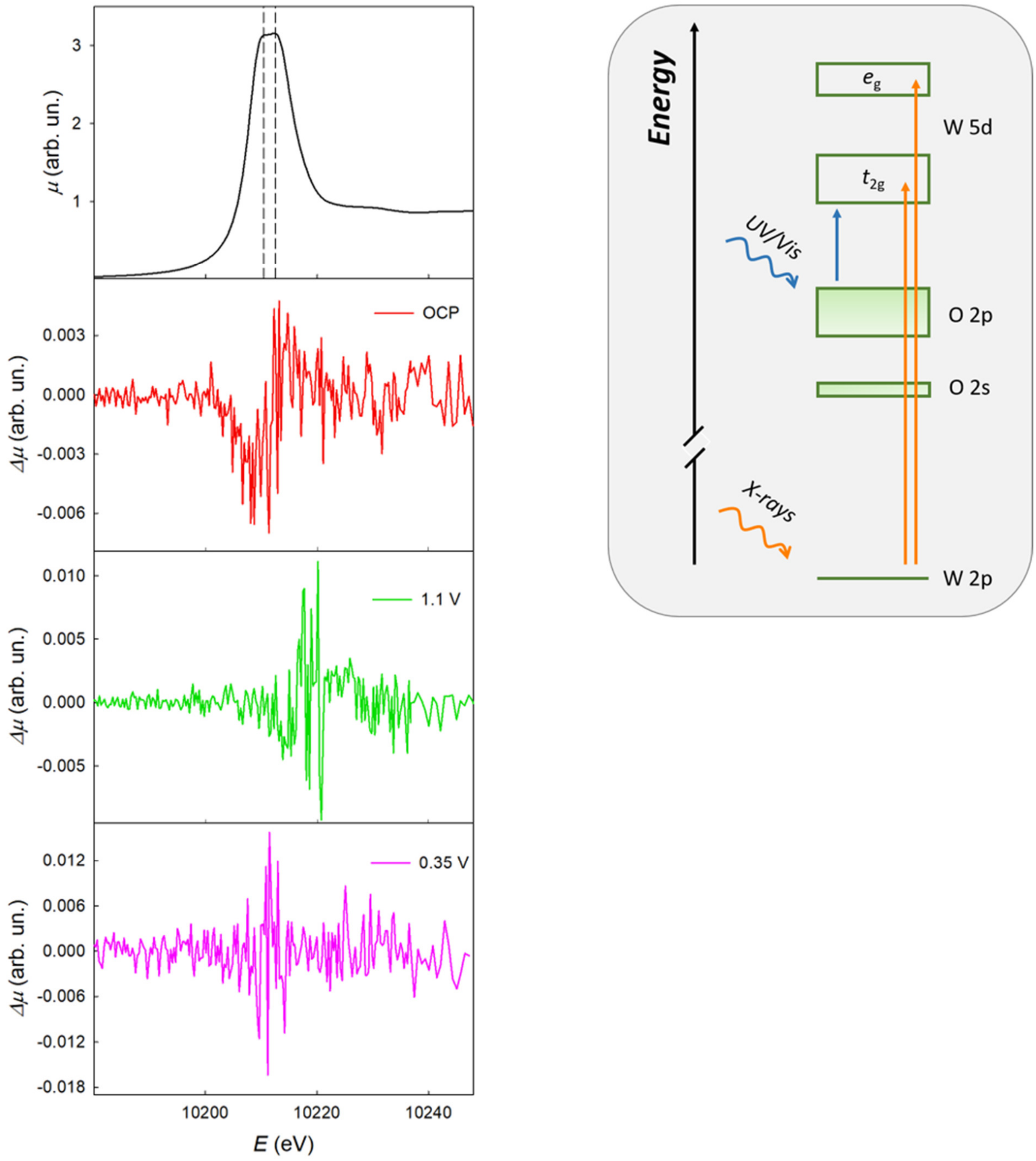

Figure 5.4: (Left panel) Δμ spectra at the W L_3-edge at OCP (red curve), 1.1 V (green curve) and 0.35 V (magenta curve); the black curve in the upper panel shows the XANES W L_3-edge spectrum of WO_3 and the dashed lines are set in correspondence of the energy of the t_{2g} and e_g orbitals. (Right panel) Scheme of the band structure of WO_3 and of the electron excitations described in this Section.

It can be noted that the difference spectrum at OCP is significantly negative in correspondence of the t_{2g} orbitals only, while it is negligible in correspondence of the e_g orbitals. This therefore indicates that the spectrum in light, with respect to the spectrum in dark, has a lower intensity only in correspondence of the t_{2g} orbitals. X-ray absorption spectroscopy is a probe for the empty states above the Fermi level, so a decrease in the intensity of the spectrum at that energy indicates a decrease of empty available orbitals. This can be related to the photoexcitation process, where the electrons are promoted from the valence to the conduction band, thus partially filling the empty t_{2g} orbitals. A scheme of the band structure of WO_3 and of the electronic excitations is shown in Fig. 5.4 (right panel). It should be noted that the LED at 400 nm allows a direct excitation from the valence band to the t_{2g} orbitals, but the energy is not so high to cause an excitation to the e_g orbitals, for which an energy of at least 5-6 eV would be necessary.

At 1.1 V and at 0.35 V no significant difference between dark and light condition can be observed. This is probably due to the fact that, upon the applying of a potential, the electrons are rapidly swept from the electrode and immediately transferred to the counter-electrode through the external circuit.

A pump and probe investigation of dispersed WO_3 nanoparticles was performed by Uemura *et al.* [116,117]; in that case, the authors noticed a decrease of the $\Delta\mu$ signal also in correspondence of the e_g orbitals. However, this was not attributed to a direct photoexcitation to these orbitals but rather to a modification in the WO_3 structure that occurs immediately after the photoabsorption process. It should be noted that the timescale of the experiment of Uemura was in the order of hundreds of picoseconds, so it is quite reasonable that their response is different from the quasi-steady state experiment described in this Section. Undoubtedly, as evidenced by Uemura, the processes underlying the photoexcitation are more complicated, and $\Delta\mu$ shows only a part of these processes.

In order to get a better understanding of this complex behaviour, a technique similar to FEXRAV was applied. The absorption coefficient was measured while switching alternatively on and off the light in OCP conditions at a fixed energy. The experiment was performed both at the energy of the t_{2g} orbitals and at the energy of the e_g orbitals. The results are shown in Figure 5.5.

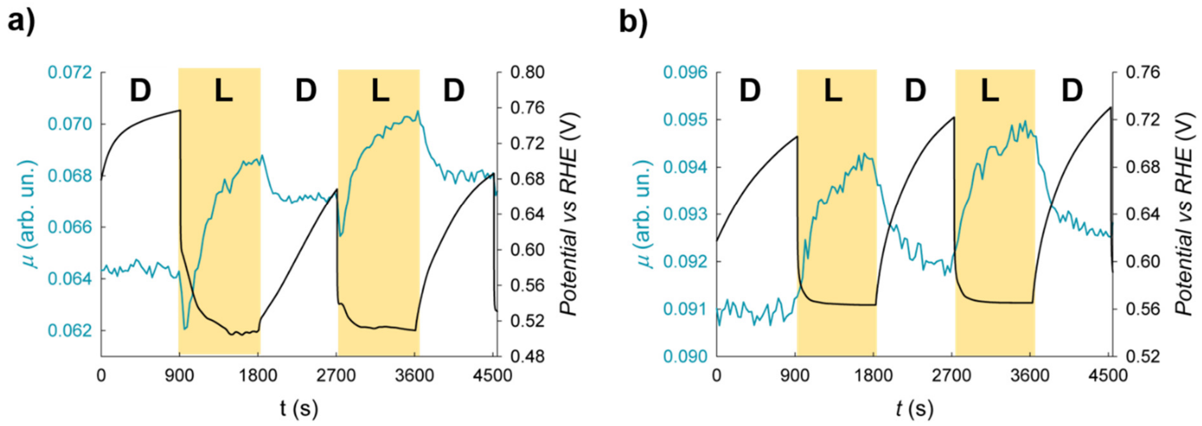

***Figure 5.5**:* Left, blue axes: Fixed energy X-ray absorption coefficient plotted as a function of time (a) at the energy of the W t_{2g} (10211 eV) and (b) at the energy of the W e_g orbitals (10213 eV). Right, black axes: open circuit potential.

In correspondence of the t_{2g} energy (Fig. 5.5 a), when the light is switched on, μ has a sharp decrease due to the injection of the electrons in these states, followed by a slow increase to a steady value. In addition to this trend, the value of μ in stationary conditions increases after each light/dark cycle. On the contrary, the same plot at the e_g energy shows only the increasing trend of μ, thus demonstrating that no direct injection occurs in these orbitals. This is in agreement with the $\Delta\mu$ difference reported in Figure 5.4 at OCP condition, which refers to the initial 10 s that follow every illumination or dark step. Finally, these results demonstrate the presence of some processes, likely related to some structural rearrangements in the electrode, that take place on a very long timescale, which would be out of reach by pump and probe experiments. It is quite reasonable to associate these structural changes with the ionic flux to or from the current collector, that compensates the negative charge due to the accumulation of electrons in the conduction band at OCP conditions.

5.4 Final remarks

In this work, the feasibility of *operando* X-ray absorption spectroscopy for the study of photoelectrodes has been demonstrated. The term "*operando*" was adopted since the experimental conditions were as close as possible to those normally adopted for photoelectrochemical characterization (in terms of presence of the electrolyte, use of a cell with a three-electrode configuration and illumination with visible light).

In order to study the WO_3 photoelectrodes, differential spectra acquisition and constant energy absorption coefficient determination proved to be effective in highlighting small differences between the dark and the light conditions. This can lead to new insights into the semiconductor/liquid junction, together with the possibility to have a direct access to the *d* conduction band of tungsten. In addition, these techniques can have a general application in all the field of photocatalysis.

In the case of WO_3 photoelectrodes in contact with Na_2SO_4 aqueous solution, at OCP and under illumination, two parallel (and most likely correlated) phenomena occur: i) a structural change, which leads to an increase of the white line and ii) the filling of the t_{2g} orbitals as a consequence of the photogeneration of electrons in the conduction band, which leads in turn to a decrease in the white line only in correspondence of the energy of these orbitals.

While the second process prevails on short timescales (within the first tens of seconds), the first process prevails in the longer term (for times longer than 20 s). A possible interpretation of this behaviour is that the photogenerated electrons partially fill the t_{2g} orbitals and progressively drive a solid-state redox transition that leads to a structural rearrangement of the photoanode. This happens only at OCP conditions: when a potential is applied, either lower or higher, no difference is detected between light and dark conditions, meaning that the photogenerated electrons and holes are immediately drained towards the solution/current collector.

6. *Operando XAS in photoelectrocatalysis: a study on Cu_2O and Cu_xO photocathodes*

As already pointed out in the previous Chapter, *operando* XAS studies in the field of photoelectrochemistry are quite scarce and are mostly dedicated to composite systems, rather than to pure semiconductors. However, improving our knowledge of the primary photocatalytic processes occurring in semiconductors, *e.g.* charge generation, trapping and recombination dynamics is crucial to improve the performances of the photoactive materials. In this Chapter, *ex-situ* and *operando* XAS is used to extensively study the behaviour of Cu_2O and CuO electrodes, which are promising photocathodes for hydrogen generation in photocatalytic water splitting. The phase composition of the materials, in both pristine conditions and after photocorrosion, were investigated along with considering the role of the applied potential in the dark and under illumination. The fate of the photogenerated carriers during the water splitting reaction was investigated by means of differential XANES spectra in dark and light.

The contents of this Chapter have been partially published in Baran T. *et al.*, “An efficient Cu_xO photocathode for hydrogen production at neutral pH: new insights from combined spectroscopy and electrochemistry”, *ACS Appl. Mater. Interfaces*, 2016, 8 (33), 21250–21260[118] and in Visibile A. *et al.*, “Electrodeposited Cu thin layers as low cost and effective underlayers for Cu_2O photocathodes in photoelectrochemical water electrolysis”, *J. Solid State Electrochem.*, 2019, under press, DOI: 10.1007/s10008-019-04441-z.[119] Some parts are here reprinted or adapted with permission from [118] (Copyright 2019 American Chemical Society).

6.1 Theoretical background and motivation for the experiment

As shown in Section 2.1.3 of this thesis, photocatalytic water splitting is a promising solution for sustainable H_2 production. In PEC cells, this process is based on the creation of a semiconductor/liquid junction, where the minority carriers (electrons for *p*-type semiconductors and holes for *n*-type semiconductors) photogenerated after the absorption of visible light are driven to the electrolytic solution where they promote the reaction of interest; *p*-type semiconductors are therefore employed as photocathodes to drive the reaction of water reduction to H_2, while the oxidation of water to O_2 occurs at the counter electrode. Several photocathodes, *e.g.* chalcogenides (CdS, CdSe)[120], phosphides (GaP, $GaInP_2$)[121] nitrides (Ta_3N_5)[122], p-Si and SiC[123] have shown good performances and a high efficiency of water conversion. However, most of these materials are of low abundance and/or are highly toxic: these characteristics are clearly contradictory to photocatalytic water splitting technology, which was conceived as a feasible and sustainable alternative for energy production and storage. The ideal photocathode should therefore have low toxicity, high abundance, and should be easily produced with scalable processes, so that the final device has a net low cost of fabrication. In this sense, both Cu_2O and CuO have received a lot of attention as possible photocathodes. Compared to the above-mentioned materials, copper oxides-based photocathodes display lower photocurrent density, but they are attractive due to their activity under visible light, low cost, easy synthetic protocols, low toxicity and high abundance. Compared with CuO, Cu_2O has received more attention as a photocathode, due to its direct band gap, equal to *ca.* 2 eV, which is suitable for water splitting under visible light irradiation, and to an appropriate conduction band potential for hydrogen generation. CuO is also a *p*-type semiconductor with a smaller band gap (1.2 – 1.5 eV) implying that CuO is, in principle, capable of generating a higher cathodic photocurrent density. Moreover, copper(II) oxide has an appropriate conduction band alignment for water reduction to hydrogen. Both Cu_2O and CuO can therefore drive half of the water splitting reaction spontaneously, while an external potential should be applied to drive the other half (the water oxidation). These photocathodes, however, have a major drawback, which lies in the poor stability of Cu_2O and CuO in aqueous solution; in fact, the redox potential for the reduction of Cu_2O to Cu and of CuO to Cu_2O lies within the band gap. A scheme of the energy band positions for Cu_2O and CuO and the redox levels of the reactions involved is shown in Fig. 6.1.

The present work focuses on understanding the behaviour of both copper oxide materials by X-ray absorption spectroscopy under both *ex-situ* and *operando* conditions. *Operando* studies (in an illuminated electrochemical cell under an external bias), are of great utility because many properties of photoelectrodes are intimately coupled to the features of the liquid-phase electrolyte and enable the direct observation of photomaterials under irradiation with light and/or the application of a potential, whereas *ex-situ* investigations provide complementary characterizations of the photoelectrodes. In this work, XANES fingerprinting, together with the fit of the EXAFS region, were employed to yield an exhaustive *ex-situ* characterization of the two photocathodes. Fixed energy X-ray absorption voltammetry (in dark and light conditions), and the acquisition of differential spectra in presence and in absence of illumination, served to provide a deeper understanding of the behaviour of these electrodes in *operando* conditions.

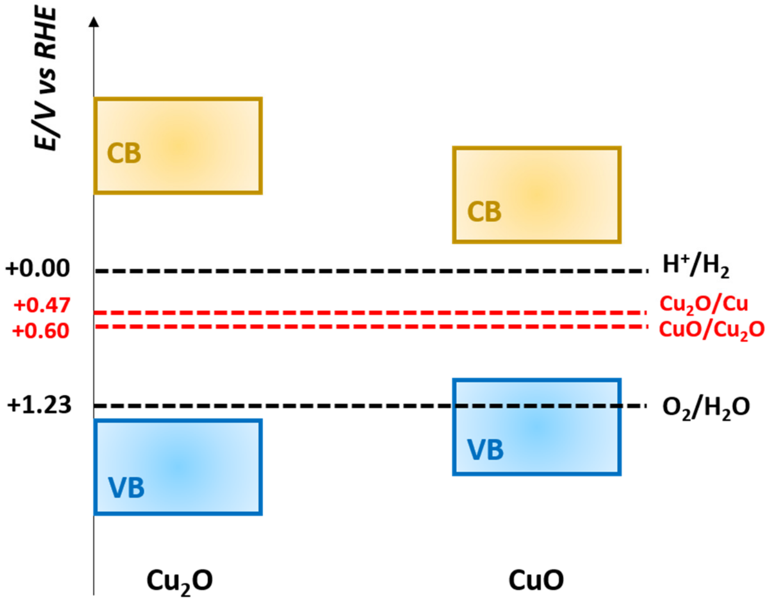

Figure 6.1: Scheme of the energy band positions for Cu_2O and CuO and of the redox levels of the reactions involved.

6.2 Experimental

6.2.1 Preparation of the samples

Cu_2O electrodes were prepared from a lactate-stabilized copper bath containing 0.2 M $CuSO_4$, 0.5 M K_2HPO_4 and 3 M lactic acid (all purchased from Sigma Aldrich), whose pH is adjusted to 12 using 2 M KOH[124]. Electrochemical depositions were carried out by applying -0.4 V vs Saturated Calomel Electrode (SCE) at 60 °C until the total amount of charge (1 C) is reached.

Cu(I) electrodes were studied in combination with two different underlayers: i) Cu_2O/Cu/FTO, that presents a metallic Cu underlayer electrodeposited from the same deposition bath but at 25 °C and at -1.5 V vs SCE. The total charge passed during the deposition of the underlayer is 0.47 C; ii) Cu_2O/Au/FTO, that presents a thin gold underlayer obtained by physical vapor deposition (thickness of about 200 nm).

CuO electrodes were prepared starting from copper iodide. Copper iodide was first synthesized according to the following procedure: 100 ml of aqueous 0.01 M Na_2SO_3 were added to 60 ml of 0.05 M $CuSO_4$ while stirring. 300 ml of aqueous 0.01 M KI were then added dropwise to the resulting green suspension. The obtained white precipitate (CuI nanoparticles) was separated by centrifugation, washed three times with water and ethanol, and dried in air at about 80°C for 8 hours. The CuI suspension was prepared in ethanol (3 mg ml^{-1}) by sonication for five minutes. Subsequently, 100 µl of the suspension were drop-casted on a FTO (fluorine doped tin oxide, Aldrich, surface resistivity ~7 Ω/sq) glass plate, previously washed with H_2SO_4, water and ethanol under ultrasounds. The electrodes were then dried in air at room temperature and subsequently annealed in air at 400°C. The resulting photoelectrodes will be denoted as Cu_xO.

6.2.2 Description of the experiment

XAS measurements were performed in fluorescence mode at the LISA beamline (BM08) at the European Synchrotron Radiation Facility (ESRF) at the Cu K-edge (8979 eV). A Si (311) double crystal monochromator was used; the harmonic rejection was realised by Pd mirrors with a cut-off energy of 20 keV, and a High Purity Germanium fluorescence detector array (13 elements) was used. Energy calibration was performed by measuring the absorption spectrum of metallic copper foil at the Cu K-edge. The stability, in energy, of the monochromator was checked by measuring the absorption spectrum of a Cu foil several times during the experiment and was always found to be better than ±0.05 eV. All data were obtained at room temperature. Spectra of standard samples CuO, Cu_2O and CuI were acquired in transmission mode. For the measurement a proper amount of sample (so as to give a unit jump in the absorption coefficient) was mixed to cellulose and pressed to pellet. The measurements were acquired in the spectroelectrochemical cell described in Section 3.1.2. The working electrodes were Cu_2O or Cu_xO electrodes, the counter electrode was a Pt wire and the reference Ag/AgCl (1 M KCl). The electrode potential was controlled through a CHI633D potentiostat (CH Instrument). All potentials are here referred to the Reversible Hydrogen Electrode (RHE). UV/Vis illumination was achieved by means of a 400 nm Light Emitting Diode (LED).

Spectra in UV-Vis light and dark conditions were acquired in parallel: the spectra (light/dark) were collected at the Cu-K edge by setting the monochromator at the desired energy and then waiting for 30 seconds for stabilization. The point in dark conditions was acquired and the light was subsequently switched on. After 30 seconds, the photocurrent was stable and the X-ray absorption under illumination was recorded. The light was then switched off and the whole sequence was repeated for each energy point.

Signal extraction was performed by means of the ATHENA code.[95,96] For the XANES analysis, background subtraction of the raw spectra was achieved using a straight line and the spectra then normalized to unit absorption at 800 eV above the edge energy, where the EXAFS oscillations are not visible anymore. EXAFS data analysis was performed by using the EXCURVE code, using a k^2 weighing scheme and full multiple scattering calculations.

6.3 Results and discussion – Cu_2O electrodes

Electrodes of Cu_2O directly deposed on FTO (Cu_2O/FTO) and Cu_2O electrodes with a metallic underlayer (Cu_2O/Cu/FTO and Cu_2O/Au/FTO) were considered for this experiment. Au is a common underlayer for this electrode, since it increases the reproducibility of the recorded photocurrents and improves the conductivity of the electrode, thus maximizing the probability of charge separation with respect to electron-hole recombination. Metallic copper represents a far cheaper alternative as underlayer[119], considering that copper and gold have a similar resistivity (1.59 and 2.44×10^{-8} Ωm, respectively)[125]. The performances of these electrodes were tested prior to the experiment with a linear sweep voltammetry alternatively in dark and light, as shown in Fig. 6.2 (right panel). The LSV measurements were acquired at 10 mVs^{-1} in 0.5 M Na_2SO_4 + 0.5 M NaOH under pulsed solar simulator light (1.5 AM) in N_2-purged solution. In case of Cu_2O/Cu/FTO, two different loadings were considered. In the complete absence of underlayers the photocurrents are one order of magnitude lower than in the presence of a metallic support. The presence of a metallic underlayer strongly affects the amount of hydrogen produced by the semiconductor. In particular, Au allows the generation of high cathodic photocurrent at lower (less negative) potential, while Cu presents higher photocurrents at more negative (less positive) potential. No appreciable differences in the photocurrent can be evidenced in case of Cu(0) deposited at different potentials. In order to see if the underlayer can affect the electronic and structural properties of Cu_2O, XAS spectra were acquired *ex-situ* at the Cu K-edge on Cu_2O/FTO, Cu_2O/Au/FTO and Cu_2O/Cu/FTO (-

0.55 V). The resulting XANES spectra are shown in Fig. 6.2 (left panel) and compared with standard Cu_2O (orange line).

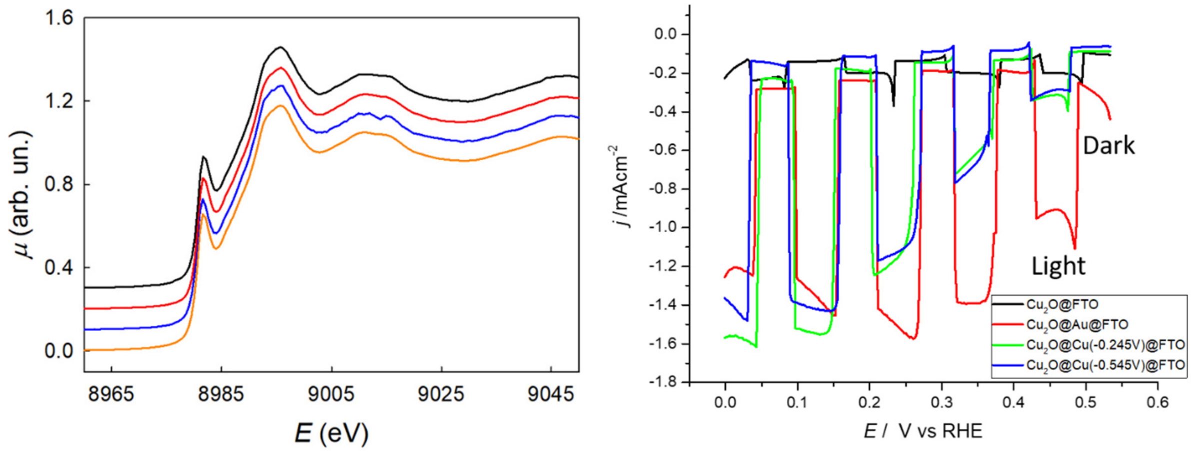

***Figure 6.2**:* (Left) *Ex-situ* XANES spectra at the Cu K-edge of standard Cu_2O (orange line), Cu_2O/Cu(-0.55 V)/FTO (blue line), Cu_2O/Au/FTO (red line) and Cu_2O/FTO (black line). (Right) Linear sweep voltammetry in dark and under illumination of Cu_2O/FTO (black line), Cu_2O/Au/FTO (red line), Cu_2O/Cu(-0.25 V)/FTO (green line) and Cu_2O/Cu(-0.55 V)/FTO (blue line).

To evaluate any possible difference in the chemical environment, the fit of the EXAFS region was also performed for the three electrodes starting from the crystal structure of Cu_2O. The results are shown in Fig. 6.3, 6.4 and 6.5 while the fitting parameters are displayed in Table 6.1, 6.2 and 6.3 for Cu_2O/FTO, Cu_2O/Au/FTO and Cu_2O/Cu/FTO, respectively.

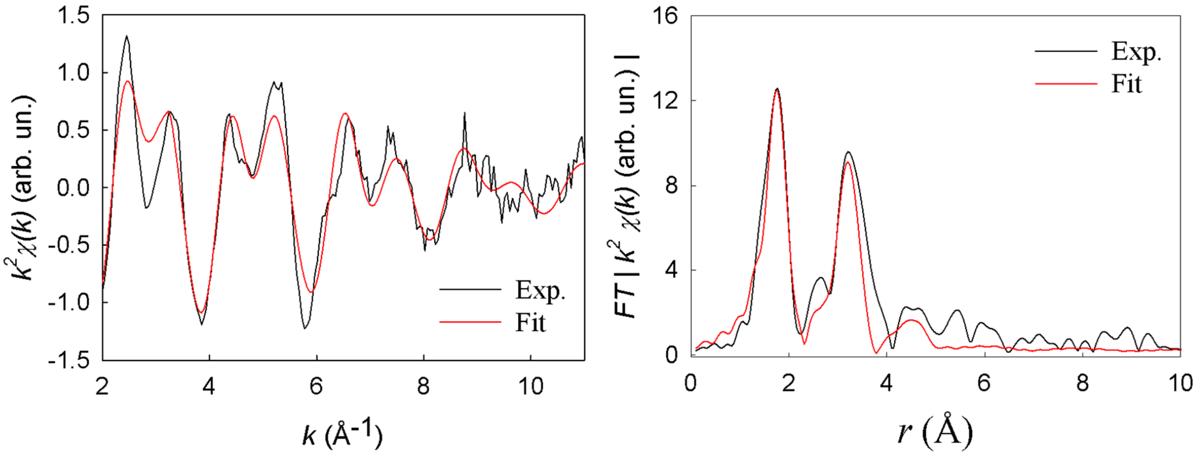

***Figure 6.3**:* EXAFS spectra (on the left) and FT (on the right) for the Cu_2O/FTO electrode. The black line is the experimental data while the red one is the theoretical one after the fit.

Table 6.1: Fitting parameters for the local surrounding of Cu in the Cu_2O/FTO electrode.

Shell	N	Atom	R(Å)	σ^2 (Å^2)	R (Å) crystallographic
1	2	O	1.89 (2)	0.010(2)	1.849
2	6	Cu	2.90 (4)	0.021(8)	3.019
3	6	Cu	3.04 (2)	0.014(3)	3.019
F=11.2%					

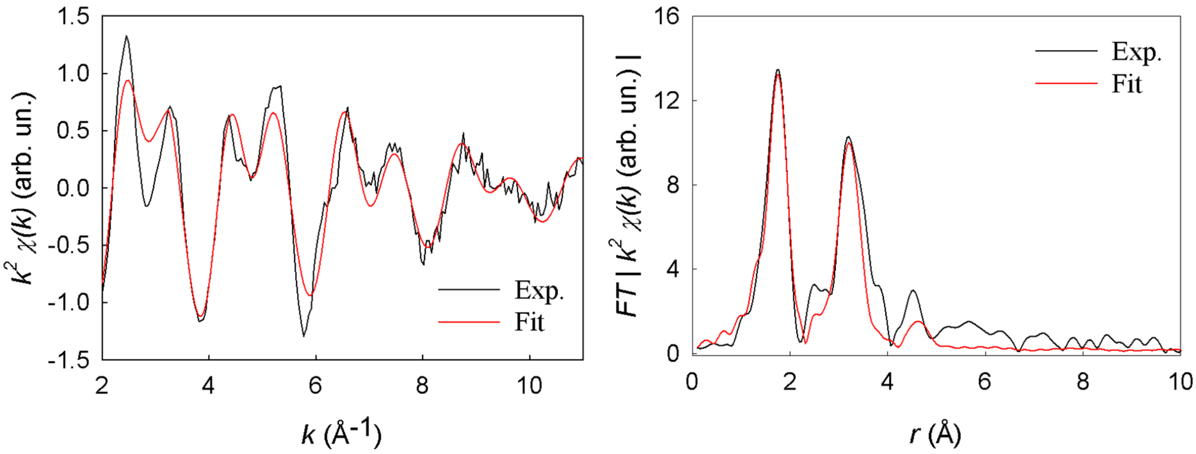

Figure 6.4: EXAFS spectra (on the left) and FT (on the right) for the Cu_2O/Au/FTO electrode. The black line is the experimental data while the red one is the theoretical one after the fit.

Table 6.2: Fitting parameters for the local surrounding of Cu in the Cu_2O/Au/FTO electrode.

Shell	N	Atom	R(Å)	σ^2 (Å^2)	R (Å) crystallographic
1	2	O	1.89 (2)	0.009(2)	1.849
2	6	Cu	2.89 (3)	0.020(6)	3.019
3	6	Cu	3.04 (2)	0.012(2)	3.019
F=9.8%					

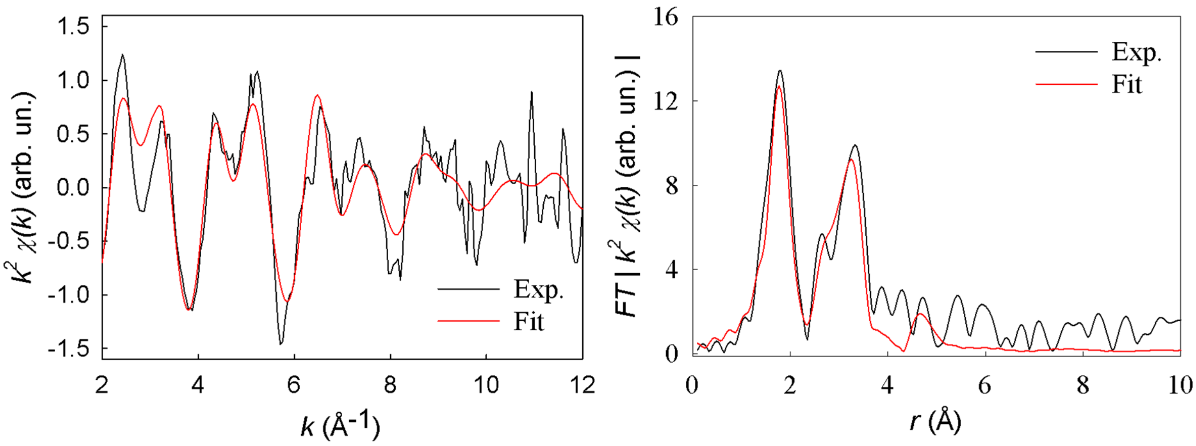

Figure 6.5: EXAFS spectra (on the left) and FT (on the right) for the Cu_2O/Cu/FTO electrode. The black line is the experimental data while the red one is the theoretical one after the fit.

Table 6.3: Fitting parameters for the local surrounding of Cu in the Cu_2O/Cu/FTO electrode.

Shell	**N**	**Atom**	**R(Å)**	σ^2 (Å^2)	R (Å) crystallographic
1	2	O	1.90 (2)	0.007(3)	1.849
2	6	Cu	2.94 (2)	0.010(2)	3.019
3	6	Cu	3.10 (2)	0.010(2)	3.019
F=16.3%					

The structural parameters obtained for the different samples after the EXAFS fitting show no differences, at least within the experimental error, thus leading to the conclusion that the presence of different underlayers does not change the local chemical surrounding of Cu_2O. However, when compared to the parameters derived from the crystal structure of Cu_2O (marked in the Tables as R (Å) crystallographic) significant distortions can be observed for all the samples. The second coordination shell of Cu in Cu_2O is made up by 12 copper atoms divided in two subsets of 6 atoms each. A marked contraction in the coordination distance is observed for the first subset, while a slight expansion is observed for the second set. If the crystal structure is projected along the <111> direction, then the first subset makes a hexagon of copper atoms surrounding the central Cu, while the second subset is composed by three copper atoms above the plane of the hexagon and three copper atoms below the hexagon plane. Therefore, both the contraction and the expansion of the coordination distances of the two second neighbouring shells can be attributed to the film nature of the samples.

Considering the Cu_2O photocathode in a photoelectrochemical water splitting system, three reactions are expected to occur in parallel:

1) The photoelectrochemical reduction of water to hydrogen:

$$2H_2O + 2e^- \rightarrow H_2 + 2OH^- \qquad E° = 0.00\ V \qquad (6.1)$$

2) the same as 1) but driven exclusively by the applied potential (in this case the reaction can be observed in the dark as well as under illumination)

$$2H_2O + 2e^- \rightarrow H_2 + 2OH^- \qquad E° = 0.00\ V \qquad (6.2)$$

3) the reduction of the photocathode material:

$$Cu_2O + 2e^- + H_2O \rightarrow 2Cu + 2OH^- \qquad E° = 0.471\ V \qquad (6.3)$$

The changes in the oxidation state of copper during the photoelectrochemical reaction were monitored in real time using FEXRAV, which allows decoupling of the overall photocurrent from parasitic processes occurring at the photoelectrode.
The energy of the incoming X-rays was fixed at a value where the difference between the absorption coefficient of two or more phases is at its maximum. The choice was made after recording spectra of standard materials. In the present case, the energy of the incoming X-rays was fixed or at 8979 eV, giving the maximum contrast between Cu_2O and Cu, as shown in Fig. 6.6. The FEXRAV measurement was carried out on the Cu_2O/Au/FTO electrode while sweeping the electrode potential from 0.53 V to -0.3 V at 1 mVs^{-1} in 0.5 M Na_2HPO_4 and 0.5 M NaOH (pH 11.1).

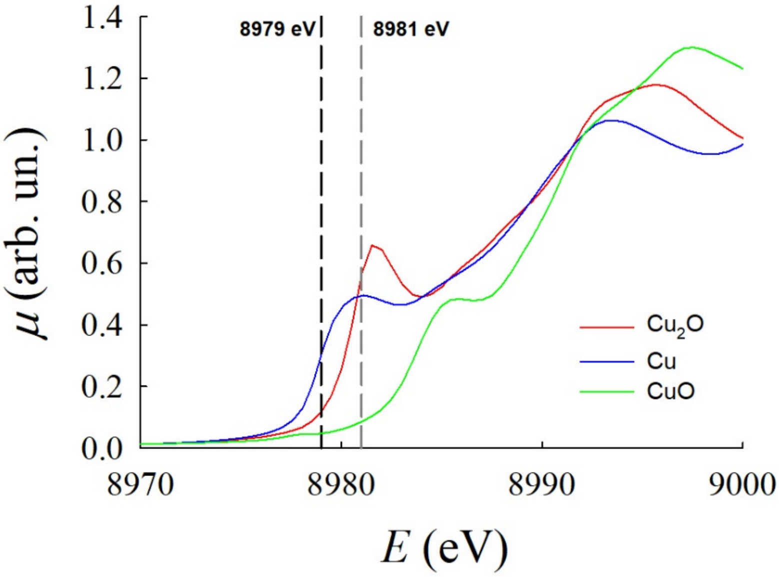

***Figure 6.6**:* XANES spectra at the Cu K-edge of standard Cu (blue line), Cu_2O (red line) and CuO (green line). The black dashed line indicates the energy chosen for the FEXRAV analysis on the Cu_2O electrodes. The grey dashed line indicates the energy chosen for the FEXRAV analysis of the Cu_xO electrodes.

During this FEXRAV experiment, the electrode potential was swept in the dark in the first cycle and under illumination in the second cycle. The two FEXRAV cycles are shown in Fig. 6.7. In the first half-cycle in dark, the absorption coefficient is constant, indicating that no change in the oxidation state occurs. In the second half cycle, however, the absorption coefficient shows an increase. As evident from Fig. 6.6, at 8979 eV an increase in the absorption coefficient indicates a reduction from Cu_2O to metallic copper (reaction 6.3). In the second cycle, carried out under illumination, the absorption coefficient starts to increase in correspondence of the first half-cycle, just below 0 V. Moreover, the overall increase of μ is much higher under illumination with respect to dark conditions.

Additional information can be obtained by comparing the FEXRAV analysis and the cyclic voltammetry. In particular, through the FEXRAV analysis it is possible to estimate the fraction of metallic copper formed during the cycles, knowing the value of the absorption coefficient of Cu and Cu_2O at 8979 eV and the relative change of μ during the cycle.

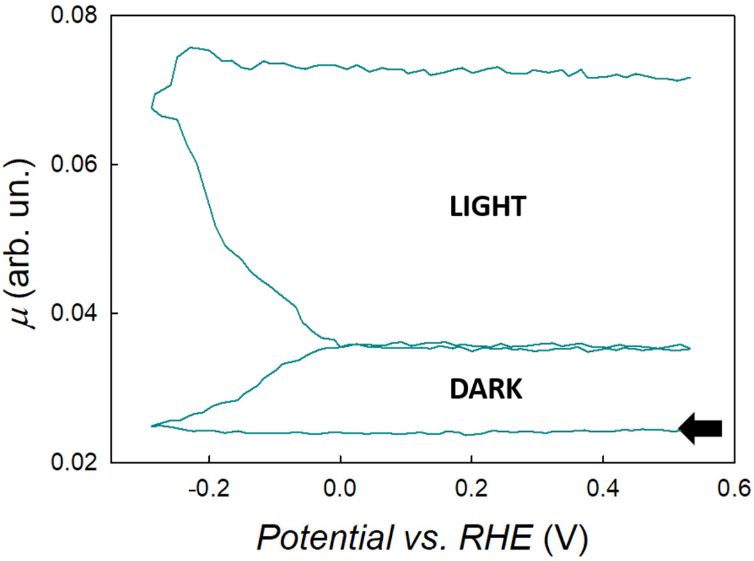

***Figure 6.7**:* FEXRAV measurement on Cu_2O/Au/FTO, carried out in dark and light condition at the fixed energy of 8979 eV.

It is therefore possible to attain a quantitative comparison between:

1) the degree of reduction calculated by FEXRAV, through which it is possible to estimate the composition of the photoelectrodes during the potential scan.

2) the overall integrated quantity of charge that, for the sake of an easier comparison, is here considered fully due to the electrode material reduction.

With this strategy, 1) and 2) are immediately comparable. Obviously, if 2) exceeds 1) the recorded current is not only caused by reactions 6.3, but also to reaction 6.1 or 6.2.
In Fig. 6.8 the cyclic voltammetry, the fraction of transformed Cu_2O calculated by FEXRAV and the fraction calculated by the CV is shown for both dark and light conditions. Figure 6.8 shows that, in dark, the FEXRAV indicates a stable composition of the electrode until *ca.* -0.3 V, in correspondence of the onset of reduction. The increase stops when the applied potential is swept back and up to 0 V. In the second cycle in light, the reduction starts at 0 V and eventually stabilizes.

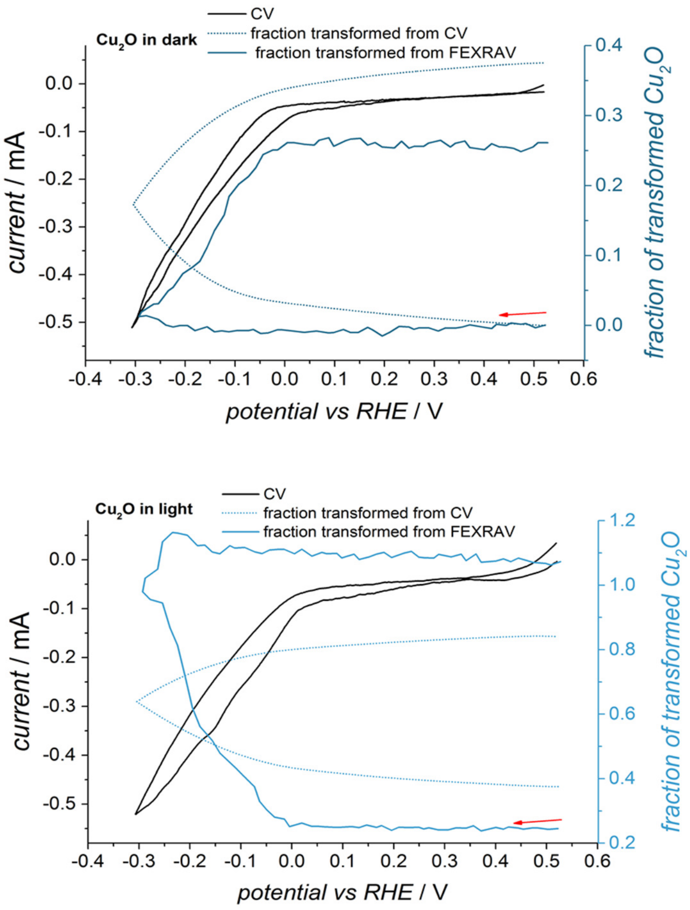

***Figure 6.8**:* Left, black axis: current intensity and right, blue axis, fraction of reduced Cu_2O as a function of the applied potential during the FEXRAV experiment on Cu_2O/Au/FTO electrode in dark (upper panel) and in light (lower panel) conditions. The starting points are indicated by arrows.

This occurs in parallel to a dramatic increase of the current at 0 V. Before that a photocurrent of about -0.05 mA is observed as the only contribution. This is the reason why the integrated current increases from the beginning, indicating the photogeneration of H_2. Overall, the amount of reduced Cu_2O is larger in the second cycle and eventually reaches 100%.

The related trend of the integrated quantity of charge clarifies the stability/activity relation: in the dark, the quantity of charge raises immediately, much faster than FEXRAV, indicating that part of the current is not only due to the reduction of the material (reaction 6.3) but also to H_2 evolution (reaction 6.2). Similarly, under illumination, the integrated quantity of charge rises from the beginning but, from 0 V, and together with FEXRAV, becomes steeper until the complete reduction of Cu_2O to Cu is achieved. It is therefore evident that Cu_2O is indeed active towards the hydrogen evolution, but this occurs in parallel to a severe reduction of the electrode material to metallic copper.

In order to further investigate the stability of the electrode under hydrogen evolution conditions, XANES spectra were acquired at the Cu K-edge. The electrode was placed at E=0.136 V vs RHE and under 400 nm LED illumination until its photocurrent was reduced to 50% and then to 25% of its initial value. At this potential a photocurrent can be observed, meaning that there is hydrogen evolution; moreover, the HER reaction is exclusively due to reaction 6.1 and not to 6.2. The *ex-situ* XANES spectra recorded after these treatments are displayed in Fig. 6.9 and show a shift of the spectrum towards lower energies after use, indicating a partial reduction of Cu_2O to Cu. This shift is particularly evident in correspondence of the pre-edge peak region, which is magnified in the inset for better clarity.

Most of the reduction has already occurred after the decrease to 50% of the initial photocurrent (green line); the spectrum corresponding to the decrease of 75% of the photocurrent, shown by the blue line, is almost overlapped to the green line, except for a slight increase of μ in correspondence of 8979 eV. This likely indicates a slightly higher quantity of metallic copper. An attempt of quantification of the two components is possible by fitting the XANES spectra with a linear combination starting from the standard spectrum of Cu and the spectrum of the pristine material, as shown in Fig. 6.10. The results indicate the formation of 8(1)% and 12(2)% of metallic Cu after 50% and 75% of photocurrent decrease, respectively. It is therefore clear that when this material is used as photocathode for H_2 evolution, significant changes in the composition are detected together with a drastic decrease of the photocurrent.

The Cu_2O-based electrode was also irradiated with UV/Vis irradiation overnight without applying any potential (at OCP conditions), to check its stability towards photodegradation. The material was not damaged by the UV/Vis irradiation, since the resulting spectrum was perfectly coincident with that of the pristine electrode.

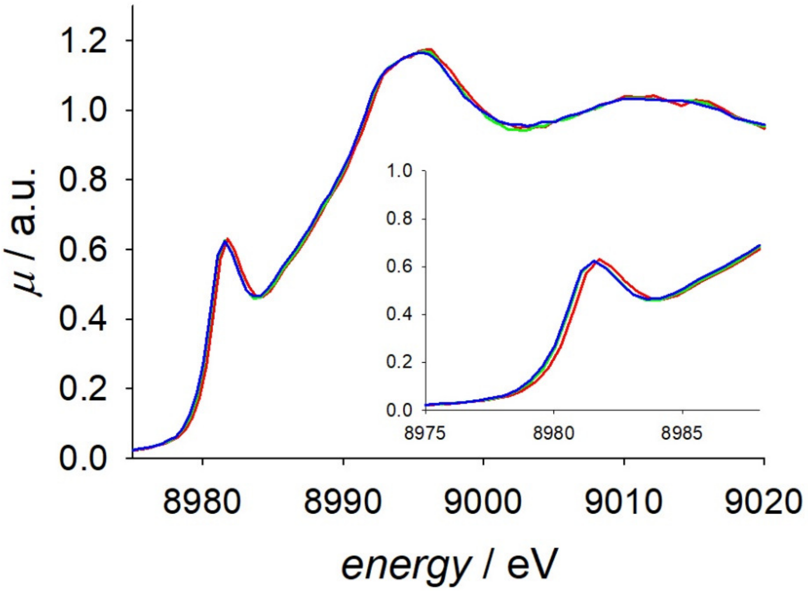

Figure 6.9: XANES spectra of Cu_2O/Cu/FTO as new (red line), after the 50% reduction of his initial photoactivity (green line) and 75% of reduction (blue line). The photoelectrodegradation of the electrode was performed in pH 11.1 electrolyte under 400 nm LED light at 0.136 V vs RHE. Inset: magnification of the pre-edge peak.

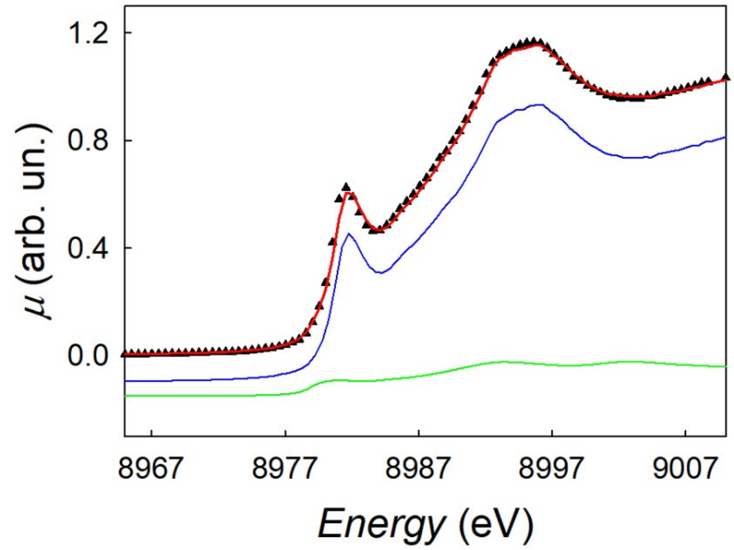

Figure 6.10: Linear combination fit of the spectrum corresponding to decrease to 25% of the initial value of photocurrent. The experimental signal is represented by the black triangles, while the fit (red line) is obtained by a linear combination fit of the spectrum of the pristine electrode (88%) and standard Cu (12%). The spectrum of the pristine electrode (weighted by 88%) and standard Cu (weighted for 12%) are shown by the blue and the green line, respectively.

In order to study in *operando* the behaviour of the Cu_2O-based electrodes during the photosplitting process, differential spectra in dark and light were acquired, according to the procedure shown in the experimental and in Section 3.1.4 of this thesis. The spectra were acquired at 0.49 V, where a cathodic photocurrent is observed (see Fig. 6.2, right panel), but the stability is guaranteed, as shown by the FEXRAV analysis. Differential spectra were acquired for both Cu_2O/Cu/FTO and Cu_2O/Au/FTO, obtaining comparable results. All the $\Delta\mu$ spectra (light – dark) were therefore merged to increase the statistical significance. The resulting spectrum is shown in Fig. 6.11 A and compared to the spectrum of the electrode in dark condition.

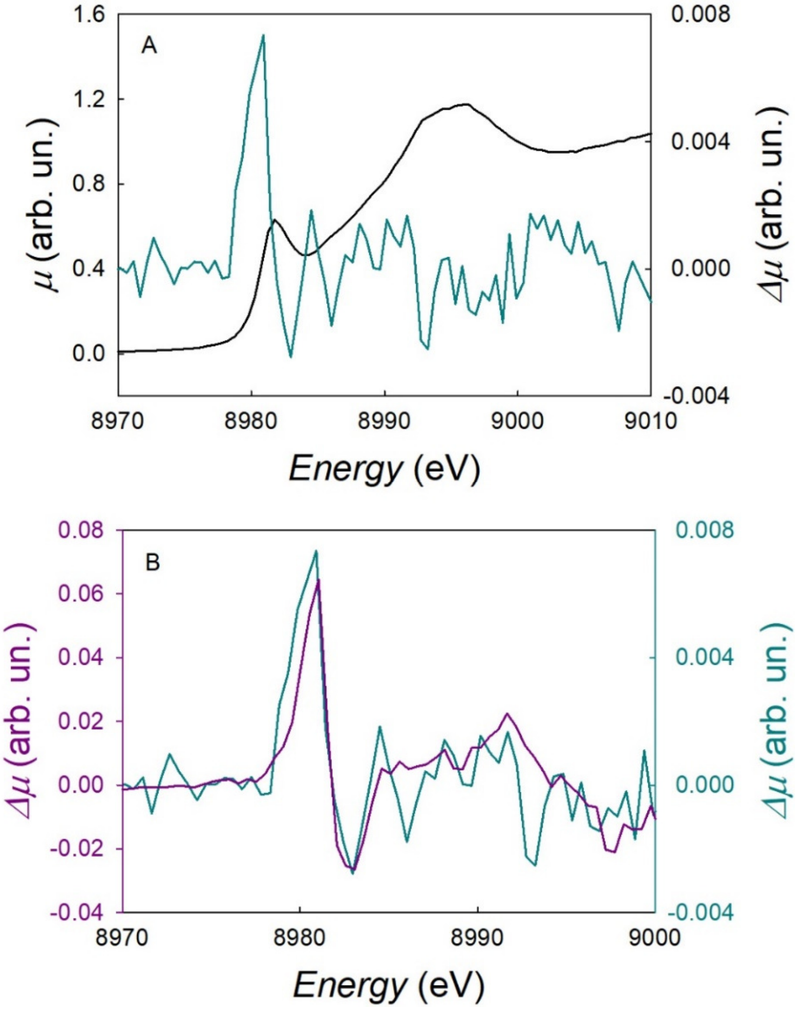

***Figure 6.11**:* (A) the merge of the $\Delta\mu$ spectra (light – dark) is shown by the dark cyan line and is compared to the spectrum of Cu_2O/Au/FTO acquired in dark at 0.49 V (black line). (B) comparison of the merge of the $\Delta\mu$ spectra (light – dark), shown by the dark cyan line, and the difference obtained subtracting the *ex-situ* spectrum of pristine Cu_2O/Au/FTO to the *ex-situ* spectrum of Cu_2O/Au/FTO spoilt until decrease to 75% of the initial photocurrent (dark pink line). The two difference signals are plotted on two different y-axes for better clarity.

As expected, the $\Delta\mu$ signal has a low intensity, indicating that the differences between light and dark conditions are small; the signal presents an evident positive peak around 8980 eV, in the region of the Cu_2O pre-edge peak. As seen before, an increase of the absorption coefficient in this region can be symptomatic of a reduction of Cu_2O to Cu. In fact, this was noticed both from the FEXRAV and from the *ex-situ* analysis showing that the photocatalytic activity leads to the formation of metallic copper on the electrode. It is therefore straightforward to compare the $\Delta\mu$ signal (light minus dark) with the difference of the spectrum of the electrode spoilt until the decrease to 75% of its photoactivity minus the spectrum of the pristine electrode. Their comparison is shown in Fig. 6.11 B, where the two signals are presented on different y-axes for better clarity; it can be seen that the two curves display a striking similarity. This points towards the fact that under UV/Vis illumination, a small quantity of metallic copper is formed. The natural explanation of this is to suppose that after the absorption of the visible light, the electrons are partially trapped in the semiconductor, leading to the formation of localized Cu(0) sites. This happens since the reduction potential of Cu_2O to Cu lies within the band gap, as already mentioned in Section 6.1.

6.4 Results and discussion – Cu_xO electrodes

The study of Cu_2O-based electrodes was propaedeutic to the investigation of the Cu_xO photocathodes. These electrodes were synthetized as explained in the experimental section, starting from copper iodide. The *ex-situ* spectrum at the Cu K-edge of the pristine electrode was therefore compared to the standard spectra in order to check its composition. As displayed in Fig. 6.12, in the Cu_xO/FTO electrode all copper is oxidized to Cu(II) after the annealing procedure, leaving no trace of CuI. The spectrum of the electrode, indeed, is similar to that of CuO, with some differences in correspondence of the pre-edge peak (at *ca.* 8985 eV) and in the white line (at *ca.* 9000 eV), which are likely related to some structural difference in the electrode with respect to the crystalline structure of CuO. In copper oxide, Cu has a highly distorted octahedral coordination, with four equatorial oxygens at the distance of *ca.* 1.9 Å and two apical oxygens at the distance of *ca.* 2.8 Å. A rough analysis carried out with multiple scattering calculations starting from the crystal structure of CuO showed that decreasing the distance between the Cu central atom and the two apical oxygens leads to the increase of the intensity of the white line.

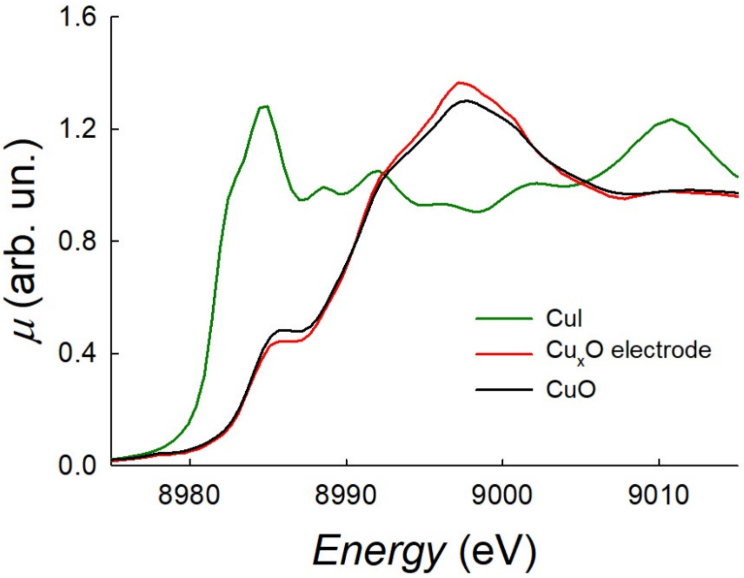

***Figure 6.12**:* XANES spectra at the Cu K-edge of standard CuO (black line), CuI (green line) and Cu_xO/FTO *ex-situ* (red line).

According to this, it could be supposed that, in the electrode, the structure is slightly more symmetric with respect to the crystalline structure of CuO. Unfortunately, this hypothesis could not be confirmed using either EXAFS or XANES fitting, which led to equal structural parameters (within the error) in both the electrode and the standard CuO; any differences in the parameters are probably below the detection limits of these techniques. It should be noted, however, that this hypothesis would also explain the lower intensity of the spectrum of the electrode around 8985 eV. According to literature[126], in fact, this peak is attributed to the transition from 1*s* orbitals to the 4*pπ* orbitals of copper. The attribution of the XANES features to the correspondent electronic transitions for Cu_2O and CuO is schematized in Fig. 6.13. If the octahedral geometry is less distorted, the two apical oxygens are closer to the central atom, thus leading to a larger overlap of the orbitals and consequently to a larger π-type interaction. This, in turn, leads to a larger number of available empty final states, and therefore to a lower spectral intensity at 8985 eV. The decrease of the CuO_6 distortion can be due to a modification of the material's surface, that is enriched in adsorbed -OH when immersed in the electrolyte. A similar change in the geometry of the octahedral units in presence of the electrolyte was also observed for $Ni(OH)_2$ at the Ni-K edge[127].

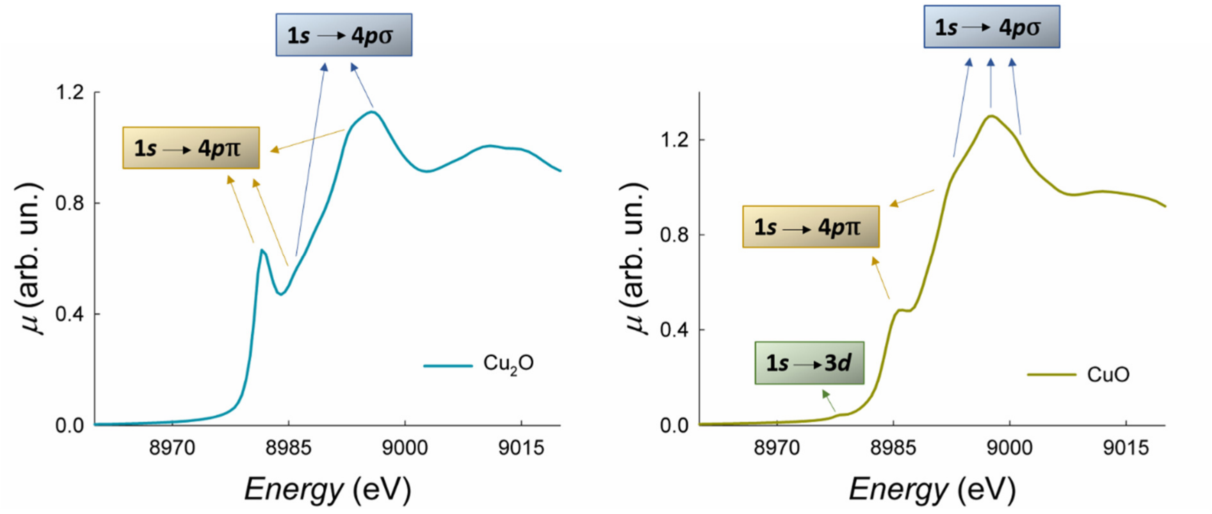

***Figure 6.13**:* Attribution of the features of the XANES spectrum to the correspondent electronic transitions for Cu_2O and CuO. Further details can be found in K. Akeyama *et al.*[126].

Analogously to Cu_2O-based electrodes, the Cu_xO electrodes were also investigated through the FEXRAV analysis. Also, in this case, and considering the photocathode in a photoelectrochemical water splitting system, three reactions occur in parallel: the photoelectrochemical reduction of water (reaction 6.1), the same but driven exclusively by the applied potential (reaction 6.2), and the reduction of the photocathode material, which can be written as follows:

$$2CuO + 2e^- + H_2O \rightarrow Cu_2O + 2OH^- \qquad E° = 0.60\ V \qquad (6.4)$$

The situation is further complicated because, in principle, the Cu_2O formed after the electrode degradation could also be reduced to metallic copper, according to reaction (6.3). Nevertheless, from previous XPS analysis, no traces of metallic copper were ever observed on these electrodes[118].

The FEXRAV measurement was carried out on the Cu_xO/FTO electrode while sweeping the electrode potential from 0.64 V to -0.08 V at 1 mVs^{-1} in 0.1 M K_2HPO_4 + KH_2PO_4 (pH 7). The energy was set at 8981 eV, which shows the highest contrast of absorption coefficient between CuO and Cu_2O (see Fig. 6.6); an increase of the absorption coefficient indicates the reduction of CuO to Cu_2O. Assuming that only Cu_2O is formed during the photoelectrochemical activity, the fraction of Cu$_2$O formed during the scan can be estimated through FEXRAV and the cyclic voltammetry (this assumption is confirmed by the detailed XANES analysis, as it will be shown afterwards). The CV, the fraction of the formed Cu$_2$O estimated by FEXRAV and the fraction of Cu$_2$O estimated by the CV are shown for dark and light conditions in Fig. 6.14.

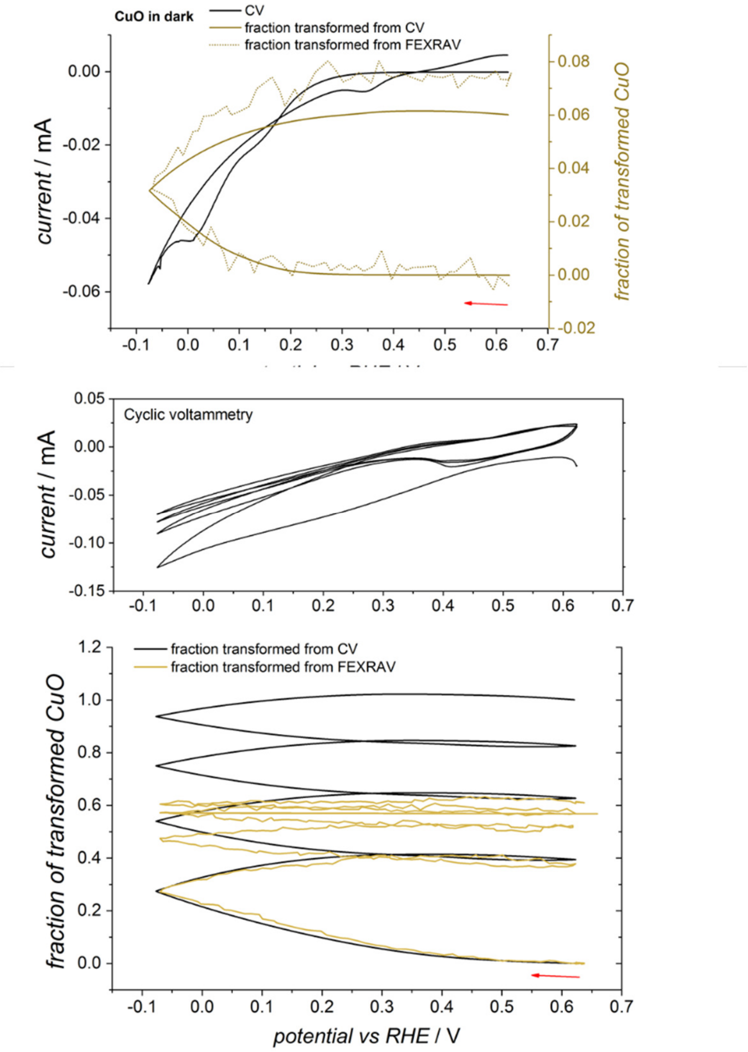

Figure 6.14: Fraction of reduced CuO and current intensity as a function of the applied potential during a FEXRAV experiment of a Cu$_x$O electrode at 8981 eV in the dark (upper panel) and under LED 400 nm illumination (middle and lower panel). 0.1 M K$_2$HPO$_4$ + KH$_2$PO$_4$, pH = 7, was used as an electrolyte. The starting points are indicated by arrows.

In dark conditions, the absorption coefficient rises starting from 0.2 V and then stabilizes at the end of the second cycle, indicating an irreversible reduction of the electrode. Quite interestingly, no activity towards H_2 evolution is observed in the dark: here in fact the two traces (FEXRAV and quantity of charge) overlap to a high degree. On the contrary, through the observation of four consecutive cycles recorded under illumination, an interesting trend is easily recognizable: while the quantity of charge constantly increases, the FEXRAV signal tends to stabilize up to a constant value of about 60% of reduced CuO. An increasing quantity of charge that occurs in parallel to an invariable FEXRAV indicates that the photocurrent efficiency for H_2 evolution is close or equal to 100%. In turn, this indicates that a partial reduction of CuO to Cu_2O is at the heart (and is thus needed) to obtain an active material towards H_2 production. The final reduced fraction indicates the formation of a Cu_2O shell (*ca.* 60%), a value that can be considered an optimal final composition of Cu_xO particles to have both activity and stability. It can be noted the higher intrinsic stability of Cu_xO with respect to Cu_2O: while the latter is easily reduced to Cu, the second is less prone to be further reduced after a stable composition is reached.

In order to further investigate the stability of the electrode under hydrogen evolution conditions, XANES spectra were acquired at the Cu K-edge in 0.1 M K_2HPO_4 + KH_2PO_4 (pH 7). The electrode was placed at E=0.3 V vs RHE and under 400 nm LED illumination for eight hours. At this potential, as shown by the FEXRAV, the material is not reduced in dark conditions, while a photocurrent is observed under illumination. The resulting spectrum, acquired *ex-situ*, is shown in Fig. 6.15 by the black curve. As expected, after the photoactivity, the composition of the photocathode is drastically changed; the resulting spectrum, in fact, is more similar to the spectrum of standard Cu_2O, despite a small shift towards higher energy and a different intensity of the pre-edge peak. Linear combination fitting was performed, starting from the spectrum of the pristine electrode and the spectrum of standard Cu_2O, and resulted in the conclusion that 80(1)% of Cu_2O is formed. The fitting of the EXAFS region was also performed, starting from a two-cluster model composed of CuO and Cu_2O, where the quantity of the two phases was included as a parameter of the fit. The best fit (F=7.1%) was obtained with 70(1)% of Cu_2O and 30(1)% of CuO. The EXAFS and the corresponding Fourier transform are shown together with the fit in Fig. 6.16 by the black and red line respectively, while the parameters obtained after the fitting procedure are shown in table 6.4 for both phases.

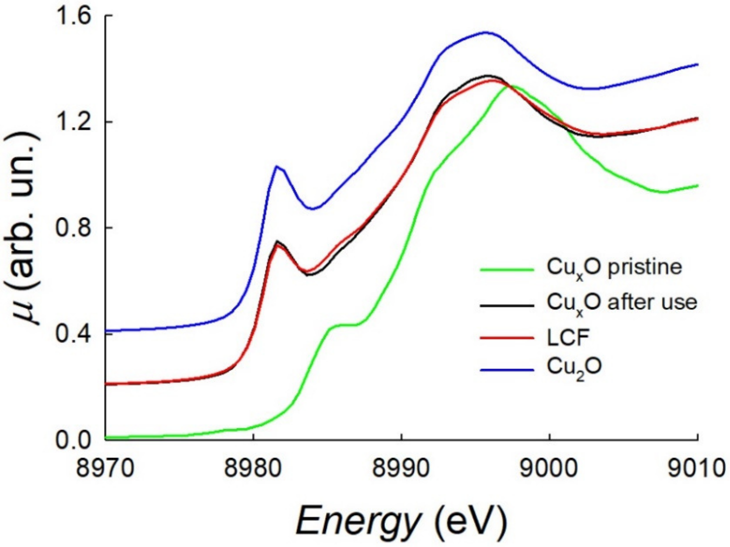

***Figure 6.15**:* XANES spectra acquired at the Cu K-edge of standard Cu_2O (blue line), pristine Cu_xO (green line) and Cu_xO kept at 0.3 V under 400 nm LED irradiation for 8 hours (black line). The linear combination fit (LCF) obtained with 80% of Cu_2O and 20% of pristine Cu_xO is shown by the red line.

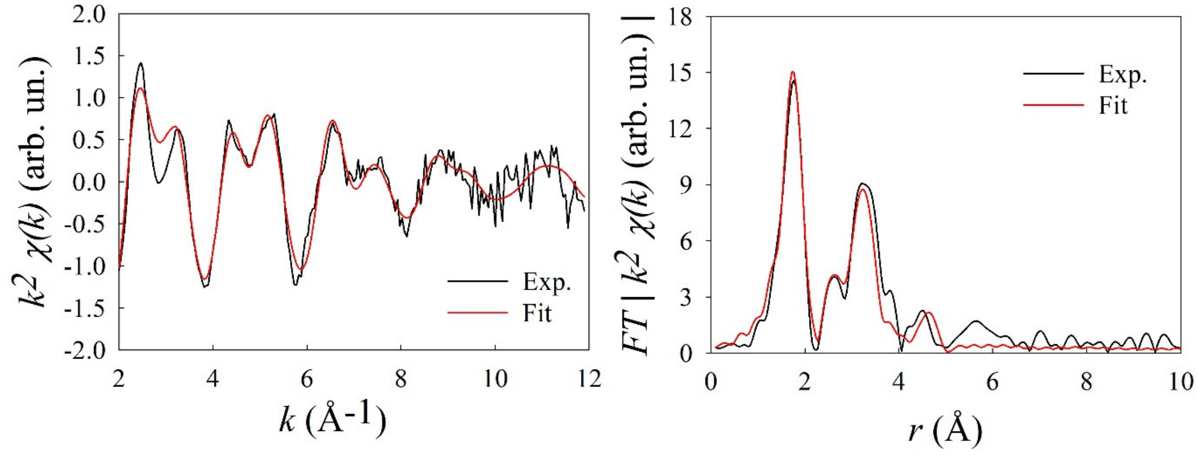

***Figure 6.16**:* EXAFS spectra (on the left) and FT (on the right) for the Cu_xO electrode kept at 0.3 V under 400 nm LED irradiation for 8 hours. The black line is the experimental data while the red one is the theoretical one after the fit.

Table 6.4: Fitting parameters for both the CuO and the Cu_2O clusters obtained after EXAFS refinement.

Cluster of CuO – 30%

Shell	N	Atom	R(Å)	σ^2 (Å^2)	R (Å) crystallographic
1	2	O	1.99(2)	0.006(4)	1.950
2	2	O	1.99 (2)	0.006(4)	1.961
3	2	O	2.35 (6)	0.01(1)	2.792
4	2	Cu	2.900	0.01(1)	2.900
5	2	Cu	2.900	0.01(1)	2.900
6	2	Cu	3.086	0.01(1)	3.086
7	2	Cu	3.086	0.01(1)	3.086
8	2	Cu	3.179	0.01(1)	3.179

Cluster of Cu_2O – 70%

Shell	N	Atom	R(Å)	σ^2 (Å^2)	R (Å) crystallographic
1	2	O	1.849	0.0001(1)	1.849
2	6	Cu	2.95 (4)	0.013(7)	3.019
3	6	Cu	3.09 (3)	0.013(7)	3.019

The linear combination fit of the XANES region and the EXAFS fitting show an acceptable agreement, neglecting a difference of 10% in the quantification of the two phases. What can be stated with absolute certainty is that the presence of metallic Cu is excluded, indicating that even if Cu_2O is formed as predominant phase during the photoactivity, a further reduction to metallic copper does not occur.

The Cu_xO electrode was also irradiated with UV/Vis irradiation for 10 hours without applying any potential (at OCP conditions), to check its stability towards photodegradation. In this case, impressive differences are detected: the XANES spectrum presents in fact a marked shift of the pre-edge peak towards higher energies with respect to the pristine material, as shown in Fig. 6.17 by the light blue line.

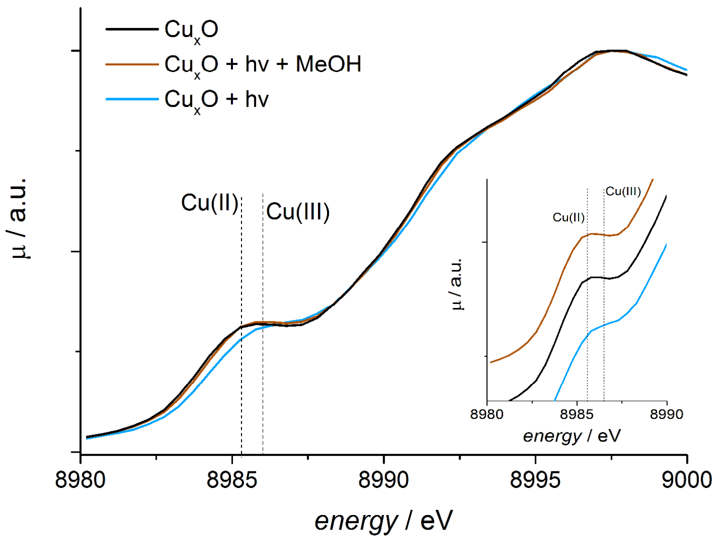

Figure 6.17: XANES spectra of Cu$_x$O electrode freshly prepared (black line), irradiated in the electrolyte for 10 h (light blue line) and irradiated in the electrolyte with addition of methanol (brown line). The inset shows the spectra on an enlarged energy scale. For better reference, the energies of the first maximum in the absorption coefficient of CuO and of a Cu(III) compound ($KCuO_2$, as taken from the literature) are shown as vertical lines.

In the XANES region, a shift to higher energies is usually indicative of a higher oxidation state. For better clarity, the pre-edge peak region is magnified in the inset of Fig. 6.17 and the energies of the first maximum in the absorption coefficient for CuO and $KCuO_2$ (a Cu(III)-containing compound, whose spectrum is available in literature)[128,129] are made evident by the vertical lines. The same measurement was acquired after adding methanol (30 % vol.) in the electrolyte; the resulting spectrum is shown by the brown line in Fig. 6.17. Very interestingly, in this case the shift to larger shift is not observed. It is therefore reasonable to suppose that at OCP conditions and in presence of illumination, some photogenerated holes are trapped inside CuO leading to the formation of copper(III); this process can be blocked by the addition of methanol, a well-known sacrificial hole scavenger. These findings indicate that photogenerated holes are long-lived and that, with no applied bias, the oxidation of water to oxygen is not favoured with respect to the oxidation of the material itself. It is worth noting that Cu(III) can be strongly stabilized when complexed by suitable ligands (*e.g.* oxamate, hydroxyiminoamide or polyanionic chelating ligands)[130,131]. Moreover, no changes in the XANES with formation of Cu(III) were observed when the sample was irradiated in air. This confirms that the presence of an electrolyte is essential for the observed phenomenon to occur.

After these results, it can be safely suggested the formation of Cu(III) centres according to the following reaction:

$$\mathrm{Cu(II)O} + h^+ + \mathrm{OH}^- \rightarrow \mathrm{Cu(III)O(OH)} \qquad (6.5)$$

Where h^+ here indicates the photogenerated holes. This behaviour recalls what occurs on TiO_2 illuminated in the presence of a hole scavenger, when a self-reduction of Ti centers occurs[132].

In order to study the behaviour of the Cu_xO electrodes during the photosplitting process, differential spectra in dark and light were acquired, according to the procedure shown in the experimental and in Section 3.1.4 of this thesis. The spectra were acquired at 0.7 V; at this potential a cathodic photocurrent is observed in light conditions, while in dark the current approaches zero, indicating that copper is not electrochemically reduced. Three spectra were acquired successively in time; during the measurements, the electrode undergoes a modification, and the difference spectrum $\Delta\mu$ (light – dark) changes its shape from the first to the third measurement. The three spectra and the corresponding $\Delta\mu$ signals are shown in Fig. 6.18. The first spectrum shows that the material is almost fully made of CuO, with a small presence of Cu_2O, indicated by the feature at *ca.* 8981.5 eV. The spectra in dark and light show a clear difference which is evident even before calculating the difference $\Delta\mu$, especially in the intensity of the white line. In particular, the spectrum obtained under illumination is positive in the whole range of energy from *ca.* 8980 to 9000 eV.

As shown before, an increase in the intensity of the white line likely indicates an increased symmetry of the CuO_6 octahedral units. In this case, however, the difference is not only positive in correspondence of the white line but also in correspondence of the edge; this can indicate the presence of a partial reduction to Cu_2O under illumination, considering that the spectrum of Cu_2O has a larger absorption coefficient with respect to the spectrum of CuO in this energy range (see Fig. 6.6). It is therefore possible that, under illumination, the material undergoes a reversible structural change and a partial reduction.

The second and the third spectra in dark show that during the measurements the electrode material is progressively reduced to Cu_2O, as indicated by the larger intensity of the feature at 8981.5 eV.

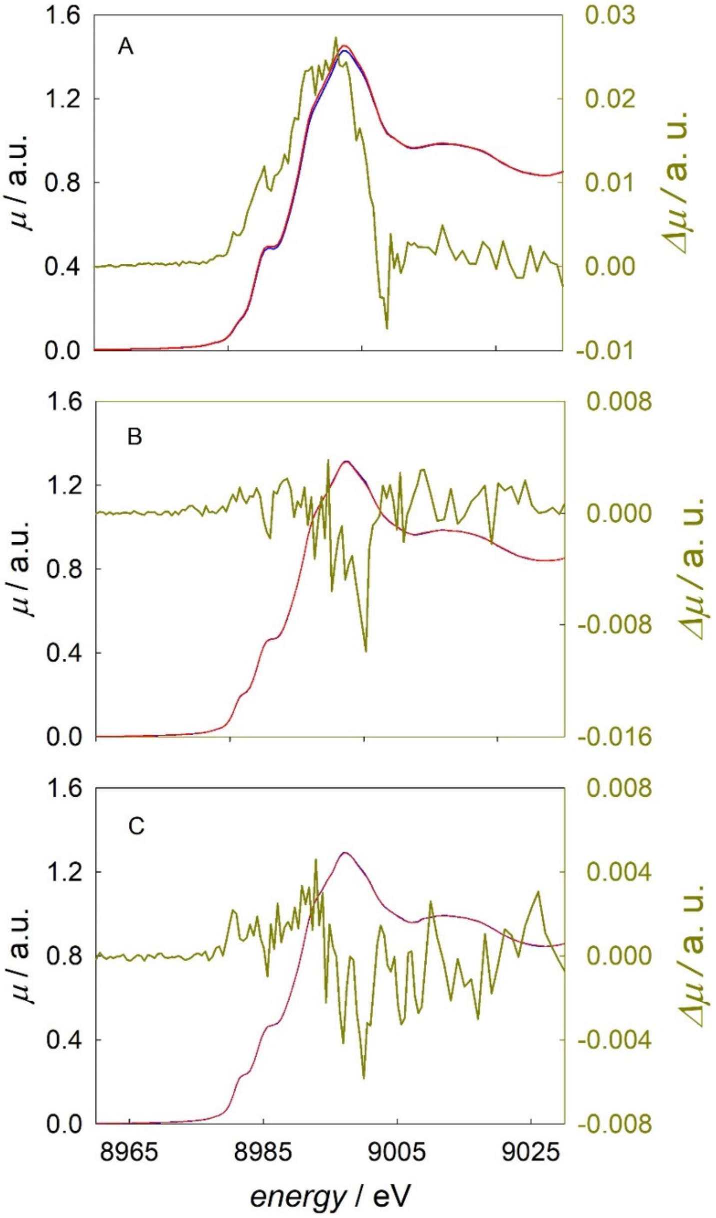

***Figure 6.18**:* Differential XANES spectra at the Cu K-edge recorded in dark (blue line) and light (red line) and corresponding Δ*μ* difference (light – dark), indicated by the yellow line, for Cu_xO/FTO electrode at 0.7 V in 0.1 M K_2HPO_4 + KH_2PO_4, pH = 7. The A, B and C panels indicate the three measurements acquired subsequently in time.

A quantification of the Cu_2O is possible through a linear combination fit starting from the spectrum of the pristine material and the spectrum of standard Cu_2O, and indicates the formation of 18% and 25% of Cu_2O, respectively. The second and the third Δ*μ* spectra show a similar trend, different from the first one. The intensity of the difference is much lower (especially for the last measurement), while the profile shows two distinct positive peaks centered at *ca.* 8982 eV and 8990 eV, and a negative peak at *ca.* 9000 eV. In Fig. 6.19, the $\Delta\mu$ signal obtained for the second measurement (yellow curve) is compared with the difference spectrum of Cu_2O minus CuO, obtained using the reference spectra (black curve).

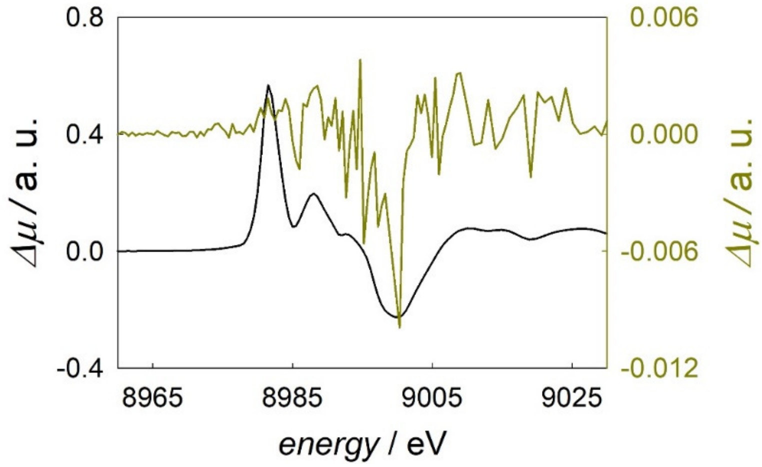

Figure 6.19: Comparison of the second difference spectrum (yellow curve) and the difference of Cu_2O minus CuO, obtained from the standard spectra (black curve). The two signals are plotted on different y-axes for better clarity.

It can be observed how the position of the features and the shape is coincident in the two cases, indicating that Cu_2O is formed under illumination. However, two things should be noted: i) as evidenced before, the broad peak at 9000 eV is not observed in the second and the third measurement. The symmetrisation probably occurs as a consequence of the interaction with the electrolyte and seems to be further enhanced by illumination. After the first measurement, however, a considerable layer of Cu_2O is already formed on the electrode, thus preventing contact with the electrolyte. This can explain why this effect is not present in the last two $\Delta\mu$ difference spectra. ii) the relative intensity of the first two peaks is different in the second and the third measurement with respect to the difference of the Cu_2O and CuO standards. It is probable that, along with a partial reversible reduction to Cu_2O, other underlying processes occur as a result of illumination.

This study, conducted under conditions of operation, helps to clarify the working mechanism of Cu_xO electrodes. From the FEXRAV analysis, it is evident that, in contrast to Cu_2O, CuO is not active towards the hydrogen evolution reaction. Under working conditions, Cu_2O is formed until a stationary and optimal composition is reached: in this state, the desired process reaches the 100% efficiency and the photocathode shows a stable photocurrent. An active Cu_xO photoelectrode is thus created. Interestingly, pure Cu_2O photocathodes show a rapid degradation forming metallic Cu, whilst in the case of Cu_xO electrode metallic copper is never observed. These data therefore give important clues about the reasons behind the behaviour of the CuO core - Cu_2O shell combination, where photogenerated electrons preferentially reduce water to hydrogen and CuO to Cu_2O, rather than Cu_2O to Cu. In CuO, the photogenerated holes are not stored in the core but can either move towards the current collector or re-oxidize Cu_2O to CuO. The latter option is, at the end, equivalent to a recombination of photogenerated electrons.

The proposed mechanism, based on the *operando* XAS observations, is schematically reported in Figure 6.20 (Left panel).

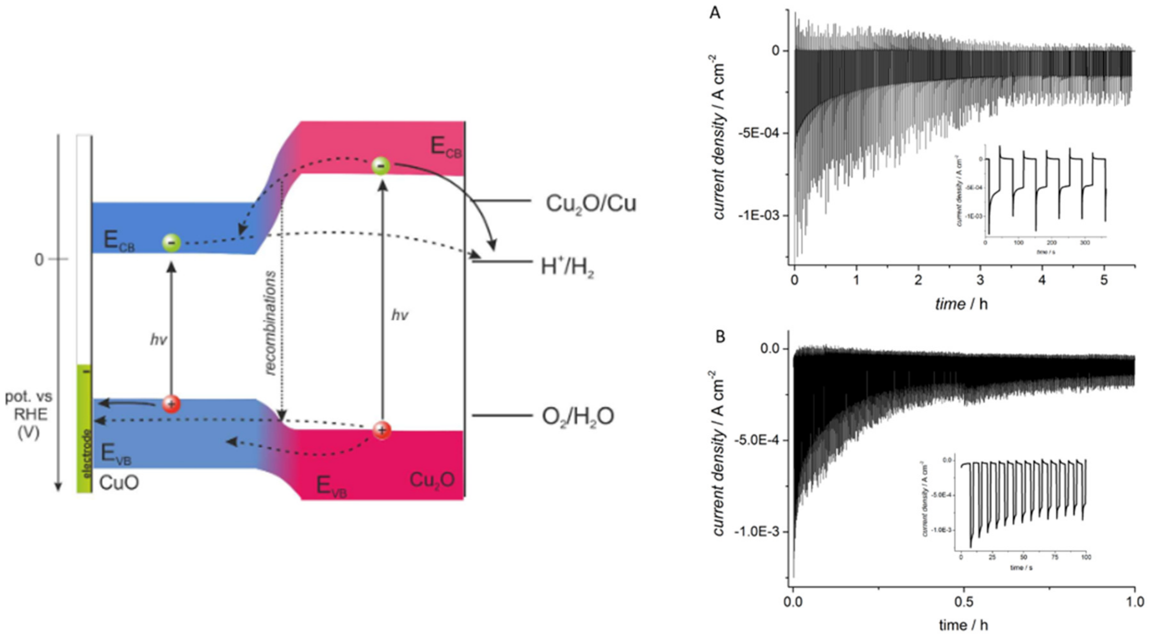

Figure 6.20: (Left) Scheme of the band structure of Cu_2O and CuO and possible fate of the photogenerated carriers. (Right) Stability test (A) at 0.35 V vs RHE in 0.1 M K_2HPO_4 + KH_2PO_4 (pH 7) under chopped illumination with LED λ = 400 nm and (B) at 0.44 V vs RHE in 0.1 M $KClO_4$ + NaOH (pH 11). Inset: magnification of the initial time scale.

In the right panel, the long-term stability tests for the Cu_xO electrodes are also shown. The experiment was carried out in the laboratory with a conventional three-electrode cell under chopped light (frequency = 0.03 Hz) at 0.35 V vs RHE. It can be seen that the efficiency of the light conversion decreases after the first hour; beyond this point the current density reaches a plateau and the electrode retains its activity for more than five hours.

6.5 Final remarks

This work aimed at demonstrating that *operando* XAS is effective in clarifying the behaviour of Cu-oxide based photocathodes for water splitting. This system is of particular complexity because of the different states that can co-exist and cause the rapid corrosion of the material. Prior to the study of Cu_xO photocathodes, Cu_2O electrodes with different underlayers were investigated. Even if the electronic properties (*i.e.* the electrical conductivity) change depending on the nature of the underlayer, the spectroscopic properties were found to be the same in all cases. FEXRAV analysis of Cu_2O in dark and light confirmed that a rapid degradation of the material, to form metallic copper, occurs during its activity, while the photocurrent drastically decreases. This is due to the fact that the reduction potential of Cu_2O lies within the band gap. However, Cu_2O was shown to be active towards the hydrogen evolution reaction. Differential spectra acquired in dark and light, and under conditions of operation, showed that upon illumination Cu_2O is reversibly reduced to metallic copper. Apparently, a fraction of the electrons is not involved in the photogeneration of H_2, but localizes inside the material to form Cu.

The behaviour of CuO was markedly different. In contrast to the Cu_2O-based photocathodes, this electrode showed an exceptional stability with time, and retained its activity for many hours. The reasons behind this stability were investigated with FEXRAV under dark and light conditions; differently from Cu_2O, pure CuO is indeed inactive towards the hydrogen evolution reaction. However, the composition of the electrode rapidly changes to form Cu_2O and the electrode starts to be active. Once the electrode reaches an optimal CuO/Cu_2O composition, the HER occurs with 100% efficiency. The XANES and EXAFS spectra acquired in potentiostatic conditions showed that only Cu_2O is formed, while metallic copper is never observed. Differential spectra acquired in dark and light under operative conditions showed that upon illumination Cu_xO is reversibly reduced to Cu_2O; also in this case, no traces of metallic copper are detected. These results explain the high retention of photoactivity for this electrode: the electrons generated after the absorption of visible light, in fact, reduce water or CuO preferentially, rather than the layer of Cu_2O. Metallic copper, which is responsible for the spoilage of the Cu_2O photocathodes, is never formed. The photogenerated holes are, in turn, not stored inside the material but they can either be transferred to the current collector or they can oxidize Cu_2O to CuO.

7. Operando XAS in photoelectrocatalysis: a study of α-Fe_2O_3/NiO_x photoanodes

In the previous two Chapters, the photoactive materials employed for the water splitting process were composed of pure semiconductors (WO_3 as photoanode and Cu_2O/CuO as photocathodes). However, it is common to couple the semiconductors with overlayers that have either a protective function or/and a catalytic activity towards the oxygen or the hydrogen evolution reaction. The effective role of the overlayer is often controversial, and the mechanisms underlying the observed photocurrent and the onset potential improvements are barely understood. In this sense, XAS can provide a valuable tool to monitor the charge transfers occurring between the semiconductor and the overlayers, and the possible changes in the oxidation state involved in the water splitting reaction. In this Chapter, a photosystem composed by α-Fe_2O_3 and NiO_x, which are respectively one of the most employed photoanodes and one of the most famous catalysts towards OER, is investigated.

7.1 Theoretical background and motivation for the experiment

As already stated in the previous Chapter, photocatalytic water splitting is usually carried out in photoelectrochemical cells (PEC cells), whose efficiency strongly depends on the performance of the photoabsorber. In order to compensate for the shortcomings of pure semiconductors, composite materials should be employed with the final aim to make PEC a competitive technology in terms of efficiency and cost. The most considered design strategy consists in covering the semiconductor with an electrocatalyst to improve both the photogenerated charge separation and the interfacial charge transfer (surface catalysis)[133]. While the performance of a composite electrode were shown to be improved, the effective role of the overlayer is not exactly understood[35]; in fact it is still not clear if the catalyst has an active role, being directly involved in the reaction of water oxidation/reduction, or a passive role, preventing electron/hole recombination. More precisely, several models have been proposed to explain the effects of the overlayer, ranging from charge transfer between the semiconductor and the overlayer, through passivation of the defects responsible for the electron/hole recombination and/or Fermi level pinning, that results in improved band bending at the semiconductor/overlayer with respect to the semiconductor/electrolyte interface.

In the present work, photoanodes composed by hematite (α-Fe_2O_3) and NiO_x were investigated at the Ni K-edge together with pure NiO_x electrodes for comparison. Hematite is one of the most employed photoanodes for photocatalytic water splitting, showing an optimal band gap (1.9 - 2.2 eV) and being earth-abundant, highly stable and non-toxic. However, this material suffers from low electron mobility (10^{-2} $cm^2V^{-1}s^{-1}$) and short hole diffusion length (5 nm), which decrease the charge separation efficiency[134]. In addition, the non-optimal position of band edges requires the application of an external bias. In order to overcome these limitations, the hematite is often coupled with electrocatalysts or passivation layers. Several spectroscopic techniques have been used to shed light into the role of the overlayer in the performance of the overall photosystem. Transient absorption spectroscopy (TAS) has been employed to study hematite coupled to CoO_x and Ga_2O_3, suggesting that the electrocatalyst layer does not, of itself, drive water oxidation, but rather serves to passivate surface states[135]. Intensity modulated photocurrent spectroscopy (IMPS) was also used to investigate hematite under working conditions and different surface treatments[136]. A recent approach consists in the application of an electrical contact to the overlayer in order to directly measure its operating potential *in situ* during the experiment in the PEC cell[137]. The results suggest that, in all cases, the overlayer acts as a hole collector, resulting in an increased electrocatalyst potential due to the accumulation of photogenerated holes[138–140]. These findings point toward the fact that PEC water oxidation is driven and accelerated in correspondence of the catalyst surface. However, this type of technique lacks elemental sensitivity and does not allow a direct observation of the oxidation state of the electrocatalyst.

In this work, X-ray Absorption Spectroscopy has been employed to unravel the changes in oxidation state occurring in Ni during the reaction at different potential values. For this purpose, both differential acquisition of spectra in dark and light and Fixed-Energy X-ray Absorption Voltammetry (FEXRAV) analysis (see Section 3.1.4) were used at the Ni K-edge.

7.2 Experimental

7.2.1 Preparation of the sample

Thin films of hematite were deposited on fluorine-doped tin oxide (FTO)-coated glass substrates (Solaronix, 10 Ω/sq.) by thermal-solution deposition at 70°C for 3 h using aqueous solutions of $FeCl_3 \cdot 6H_2O$ (0.15M) and $NaNO_3$ (1M), at pH 1.5 optimized with HCl solution. The samples were calcined at 550°C for 1h, followed by 20 min at 800°C.

NiO_x electrocatalyst films were deposited onto the hematite electrodes both by electro- and photo-deposition. α-Fe_2O_3 electrodes were immersed in a solution containing 0.1 M $Ni(NO_3)_2 \cdot 6H_2O$, whose pH was corrected with NaOH until pH 6.6 was reached. Before use the solution was degassed in nitrogen for 1 hour. Electrodeposition of NiO_x was carried out in galvanostatic condition: -16 mA/cm^2 for 60s. Photodeposition was carried out at open circuit voltage (V_{oc}) for 30 min. After the electrocatalyst was deposited, the electrodes were rinsed with deionized water to remove any excess Ni ions.

The different deposition procedures enabled deposition of different amounts of NiO_x on hematite electrodes, and consequently different thicknesses of NiO_x: about 1-2 nm for the photodeposition, and about 80 nm thick for the electrodeposition. Ni is deposited as $Ni(OH)_2$; however, at potentials relevant to oxygen evolution reaction, the active species is expected to be NiOOH; for this reason, the loading will be indicated as NiO_x.

7.2.2 Description of the experiment

XAS measurements were performed in the fluorescence mode at the LISA beamline (BM08) at the European Synchrotron Radiation Facility (ESRF) at the Ni K-edge (8333 eV). A Si (311) double crystal monochromator was used; harmonic rejection was realised by Pd mirrors with a cut-off energy of 20 keV, and a High Purity Germanium fluorescence detector array (13 elements) was used. Energy calibration was performed by measuring the absorption spectrum of metallic nickel foil at the Ni K-edge. The energy stability of the monochromator was checked by measuring the absorption spectrum of a Ni foil several times during the experiment and was always found to be better than ±0.05 eV. All data were obtained at room temperature. Spectra of standard samples were acquired in transmission mode. For the measurement a proper amount of sample (as to give a unit jump in the absorption coefficient) was mixed to cellulose and pressed to pellet.

The measurements were made in the spectroelectrochemical cell described in Section 3.1.2. The working electrodes were NiO_x or α-Fe_2O_3/NiO_x electrodes, the counter electrode was a Pt wire, and the reference Ag/AgCl (1 M KCl). The electrode potential was controlled through a CHI633D potentiostat (CH Instrument). All potentials are here referred to the Reversible Hydrogen Electrode (RHE). UV/Vis illumination was achieved by means of a 400 nm Light Emitting Diode (LED).

Spectra in UV-Vis light and dark conditions were acquired in parallel: the spectra (light-dark) were collected at the Ni K-edge by setting the monochromator at the desired energy and then waiting for 30 seconds for stabilization. The point in dark conditions was acquired and the light was subsequently switched on. After 30 seconds, the photocurrent was stable and the X-ray absorption under illumination was recorded. The light was then switched off and the whole sequence was repeated for each energy point. Signal extraction was performed by means of the ATHENA code.[95,96] For analysis of the XANES, the raw spectra were first background subtracted using a straight line, and then normalized to unit absorption at 800 eV above the edge energy, where the EXAFS oscillations are not visible anymore.

7.3 Results and discussion

Cyclic voltammetry scans were first acquired in a conventional three-electrode cell in NaOH 1 M. Three electrodes were considered: an electrode made by bare α-Fe_2O_3 and two composite electrodes, α-Fe_2O_3/NiO_x -L and α-Fe_2O_3/NiO_x -H, which have respectively a low amount of Ni (~ 2 nm) and a higher amount of Ni (~ 80 nm). The scans were acquired both in dark and under AM 1.5G illumination for all samples (Fig. 7.1, dashed and solid lines respectively). Bare hematite shows a photocurrent onset potential at 0.8 V under illumination (black solid line), followed by a steep increase in the photocurrent density up to *ca.* 1.3 V. α-Fe_2O_3/NiO_x -L and α-Fe_2O_3/NiO_x -H show significantly different behaviours, with the α-Fe_2O_3/NiO_x -L presenting the best performances, having an anticipated onset potential at about 0.6 V (red solid line). The higher Ni-loaded overlayer, on the contrary, clearly reduces the photoelectrode performance. Interestingly, and in contrast with α-Fe_2O_3/NiO_x -L, α-Fe_2O_3/NiO_x -H distinctly shows two sets of redox peaks. The first, around 1.3 V (reduction) and 1.45 V (oxidation), corresponds to the typical transformation of $Ni(OH)_2$ to NiOOH. The second set of peaks is located at 0.55 V and 0.8 V and is less evident in α-Fe_2O_3/NiO_x -L, where the abovementioned peaks are much smaller.

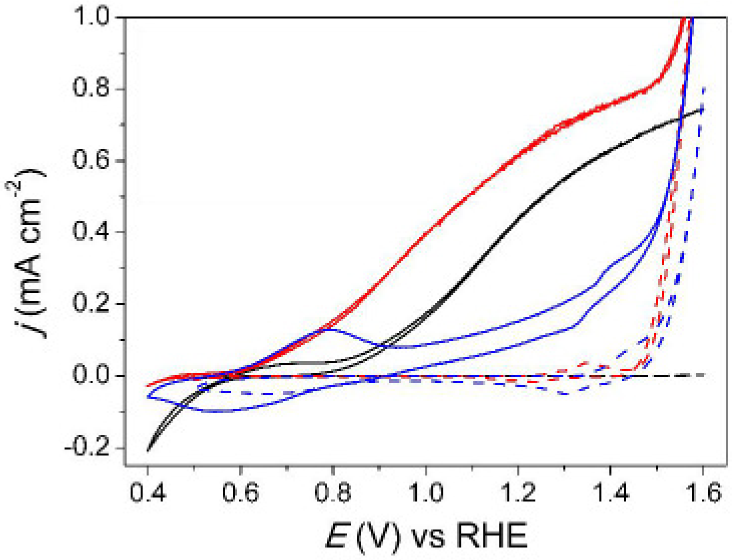

Figure 7.1: Cyclic voltammetry scans of α-Fe_2O_3 (black lines), α-Fe_2O_3/NiO_x-L (red lines) and α-Fe_2O_3/NiO_x-H (blue lines) measured in 1 M NaOH both under 1 Sun irradiation and in dark conditions. Solid lines correspond to light conditions, while dashed lines correspond to dark conditions.

In a simple hematite electrode, these peaks were attributed by Zandi *et al.* to transient redox processes involving the formation of Fe in high oxidation states[141]. The authors managed to observe the cathodic charge of the Fe redox peak only by applying a very high potential (2 V for 60 s under 1 Sun illumination) and using a high scanning rate in dark conditions. In the present work, this phenomenon is visible during the cyclic voltammetry carried out at 10 mV/s and under illumination, *i.e.* in presence of photogenerated holes. It seems likely that the presence of a thick layer of NiO_x results in a high level of charge storage and a high resistance at the hematite/electrolyte interface, as detectable from the area under the CV curve: the capacitance of this electrode is in fact much higher than the capacitance of the other two. Moreover, the oxidized iron may extract electrons from NiO_x inducing an anticipated oxidation of the nickel. Therefore, these peaks at 0.55 V and 0.8 V may be considered as the sum of Fe and Ni redox processes. The Ni oxidation process is likely to occur also in α-Fe_2O_3/NiO_x -L, but the pertinent redox peaks are not observable because of the low amount of Ni that does not result in significant charge storage. Very interestingly, the redox peaks at 1.3 – 1.4 V almost disappear under illumination in the case of α -Fe_2O_3/NiO_x -L, implying that most of the Ni redox processes occur at lower potential (0.55 – 0.8 V), corresponding to the photocurrent onset potential. In contrast, for α -Fe_2O_3/NiO_x -H the redox peaks at 1.3 – 1.4 V are still visible under illumination, although their area decreases by two thirds with respect to that detected in dark conditions. These observations strongly suggest that the presence of the photogenerated holes anticipates the Ni oxidation processes.

After this preliminary characterization in the laboratory, XAS experiments were acquired on both NiO_x and α-Fe_2O_3/NiO_x -H electrodes at the Ni K-edge in NaOH 0.1 M. The experiments could not be carried out on α-Fe_2O_3/NiO_x -L, where the loading of Ni is too low to yield an adequate signal-to-noise ratio.

The reference XANES spectra at the Ni K-edge of $Ni(OH)_2$, β-NiOOH and γ-NiOOH are shown in Fig. 7.2 a. With respect to $Ni(OH)_2$, the edge position of β-NiOOH is shifted towards higher energies by *ca.* 1 eV, while the edge position of γ-NiOOH is shifted by *ca.* 2.5 eV. These figures are in agreement with previous literature[142] and confirm that the oxidation state of Ni in β-NiOOH is close to Ni(III), while γ-NiOOH contains Ni in a higher mean oxidation state (up to *ca.* 3.6 according to the literature[143]).

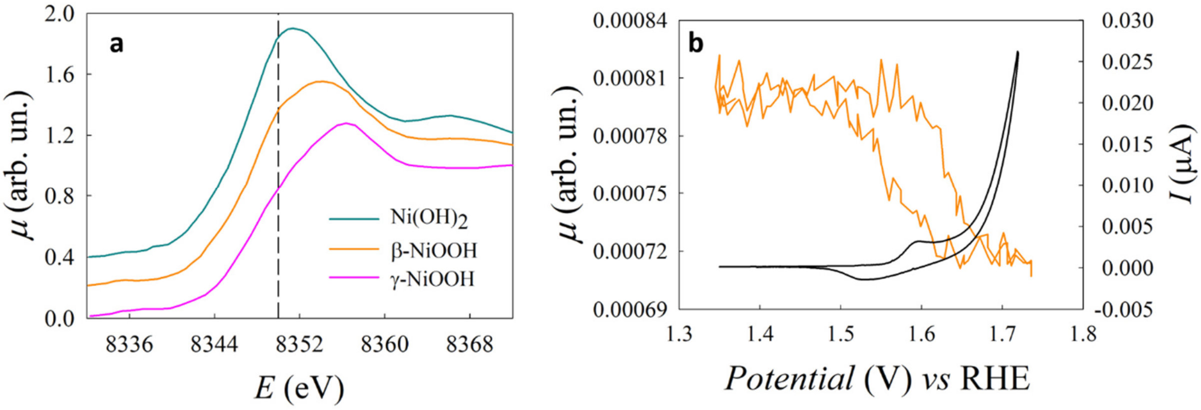

Figure 7.2: (a) XANES reference spectra at the Ni K-edge of $Ni(OH)_2$ (green line), β-NiOOH (orange line) and γ-NiOOH (magenta line). The spectra are shifted along the y-axis for better clarity. The dashed black line is in correspondence of 8350 eV, the fixed energy chosen for the FEXRAV analysis (b) FEXRAV curve (orange line) and CV curve (black line) carried out on NiO_x electrodes.

As a preliminary investigation, electrodes of bare NiO_x were considered in order to study the electrochemical behaviour of the electrocatalytic material in absence of the hematite underlayer. After the electrochemical deposition, Ni is present on FTO as $Ni(OH)_2$. At anodic potentials, however, Ni is expected to oxidize to NiOOH. In order to monitor the change in the oxidation state occurring at anodic potentials, FEXRAV analysis was first employed; the energy of the incoming X-rays was fixed at 8350 eV (indicated in Fig. 7.2 a by the dashed line), a value where there is a good contrast between the absorption coefficient of $Ni(OH)_2$ and that of either β or γ-NiOOH. In this case, a decrease of the absorption coefficient is indicative of the oxidation of Ni. The FEXRAV curve was acquired while recording a cyclic voltammetry from 1.35 V to 1.72 V at 1 mV/s and is shown by the orange line in Fig. 7.2 b, together with the cyclic voltammetry indicated by the black line. The oxidation peak of the cyclic voltammetry is at *ca.* 1.6 V vs RHE; as expected, at this potential value the FEXRAV curve shows a decrease of the absorption coefficient, indicating Ni oxidation. At the end of the cycle, all Ni is completely restored to its initial oxidation state.

For a detailed analysis, XANES spectra were acquired at fixed potential values of 1.3 V, before the oxidation peak in the CV curve, 1.6 V, in correspondence of the oxidation peak, and 1.7 V, where the oxygen evolution reaction occurs. The resulting spectra are shown in Fig. 7.3 a. At 1.3 V the spectrum profile and the edge energy are consistent with that of $Ni(OH)_2$; the white line, in the case of the Ni-based electrode, is more intense with respect to standard $Ni(OH)_2$, probably due to local distortion or/and to the presence of the electrolytic solution.

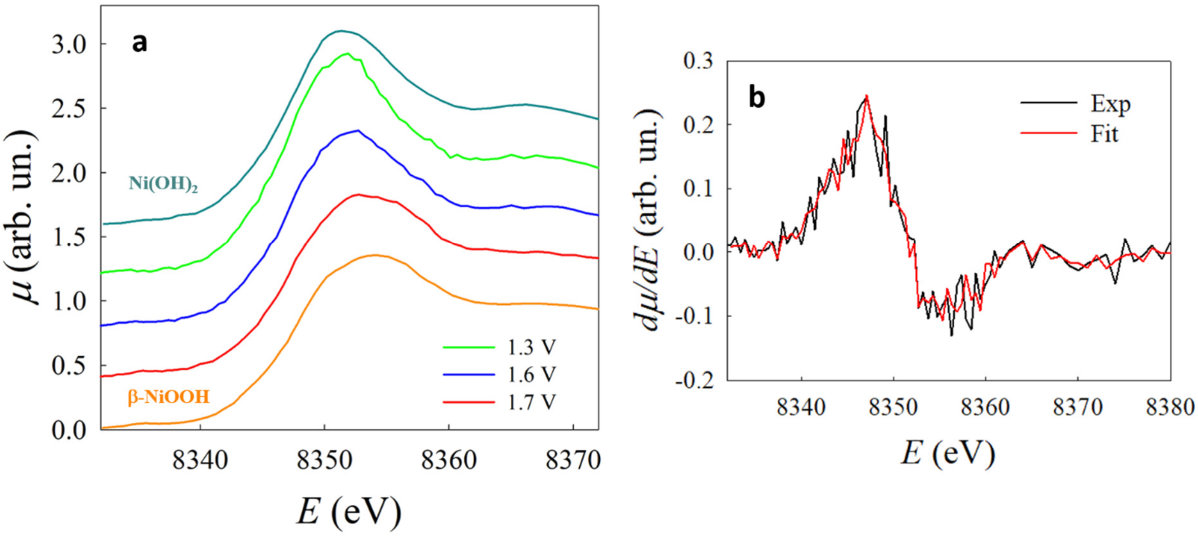

Figure 7.3: (a) XANES spectra at the Ni K-edge obtained on NiO_x electrodes in NaOH (0.1 M) at 1.3 V (green line), 1.6 V (blue line) and 1.7 V (red line). These spectra are compared with standard spectra of $Ni(OH)_2$ and β-NiOOH (orange line). The spectra are shifted along the y-axis for better clarity. (b) Linear combination fit of the derivative spectrum obtained at 1.6 V starting from 50.3 % of $Ni(OH)_2$ and 49.7% of β-NiOOH.

At 1.6 and 1.7 V the XANES spectrum is shifted towards higher energy, indicating a progressive oxidation of Ni; at 1.7 V the spectrum profile and the edge energy is coincident with that of β-NiOOH, indicating that at this potential the mean oxidation state of Ni in the sample is Ni(III). In order to assess the mean oxidation state at 1.6 V, the derivative spectrum obtained at this potential was fitted with a linear combination fit starting from the derivative spectra of $Ni(OH)_2$ and β-NiOOH (Fig. 7.3 b). The best fit shows the presence of 50.3% of $Ni(OH)_2$ and 49.7% of β-NiOOH; assuming that the oxidation state of Ni in β-NiOOH is (III), it can be estimated that at 1.6 V the mean oxidation state of Ni is ~ 2.5.

With this preliminary information on the electrochemical behaviour of bare NiO_x electrodes, composite α-Fe_2O_3/NiO_x were investigated. Also in this case, FEXRAV measurements were first acquired at 8350 eV to monitor in real time the changes in oxidation state occurring at Ni at anodic potentials. This time, the measurements were acquired both in dark and under illumination. The two correspondent FEXRAV curves are shown in Fig. 7.4 together with the cyclic voltammetry acquired between 0.4 V and 1.3 V.

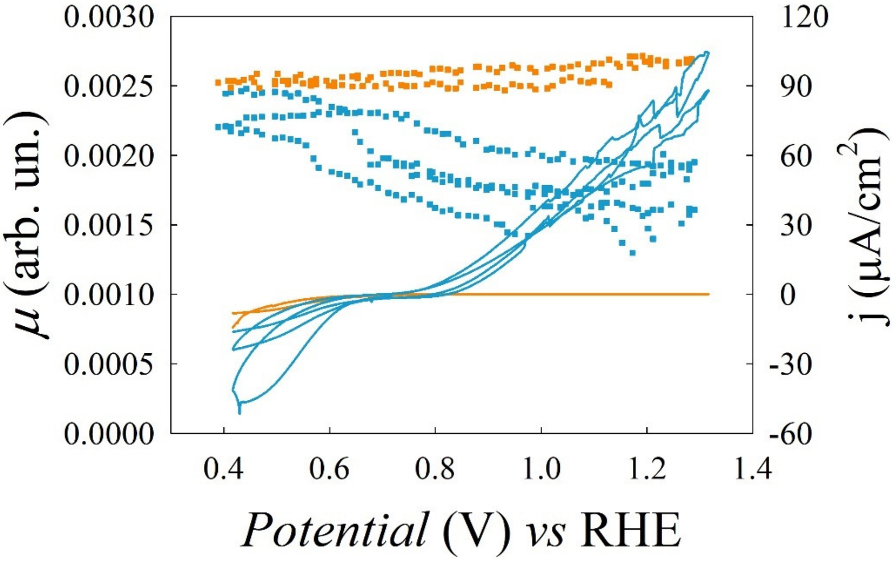

Figure 7.4: Cyclic voltammetry and FEXRAV curve of α-Fe_2O_3/NiO_x electrodes in dark (orange solid line and orange dotted line, respectively) and upon illumination (cyan solid line and cyan dotted line, respectively).

In dark conditions the FEXRAV curve is completely flat indicating that, as expected by the previous analyses, no change in the Ni oxidation state occurs in this range of potentials. A markedly different behaviour is observed upon illumination; the absorption coefficient is stable from 0.4 V to 0.7 V, while it dramatically decreases afterwards, accounting for an increase in the Ni oxidation state. The μ value then stabilizes around 1.1 V.

In order to get additional and more detailed information on the behaviour of α-Fe_2O_3/NiO_x under photocatalytic conditions, differential spectra in dark and light were acquired, according to the procedure shown in the experimental and in Section 3.1.4 of this thesis. The spectra were acquired at i) 0.5 V, at flat band potential ii) at 0.7 V, in correspondence of the photocurrent onset and iii) at 1.3 V, where a consistent photocurrent is detected. The results are shown in Fig. 7.5. It is apparent that without illumination, the Ni-K edge manifold remains unchanged in the 0.5-1.3 V potential window (Fig. 7.5, panel B). When the light is switched on at 0.5 V, the spectra with and without illumination are still coincident, indicating that illumination does not change the Ni(II) oxidation state at this potential (panel C). However, when a potential of 0.7 V is applied, both a shift of the absorption edge towards higher energies and a modification of the spectral shape are observed. A linear combination fit of the XANES derivative starting from the derivative spectra of $Ni(OH)_2$ and γ-NiOOH suggests the formation of Ni in an average oxidation state of 2.45. The same result is obtained fitting with β-NiOOH instead of γ-NiOOH. Notably, the shift in energy of the XANES edge induced by illumination becomes even larger at 1.3 V, pointing towards the presence of Ni in a mean oxidation state larger than Ni(III). The fitting procedure this time indicates indeed the presence of Ni in oxidation state 3.4.

The formation of Ni in higher oxidation state is further evidenced by calculating the $\Delta\mu$ light-dark difference spectrum for each potential (panel D) and comparing it with the difference between the standard spectra γ-NiOOH – $Ni(OH)_2$. At 0.5 V, the difference spectrum is completely flat. At 0.7 V, a larger difference is detected, while at 1.3 V the curve becomes nearly coincident with the difference between the standard spectra.

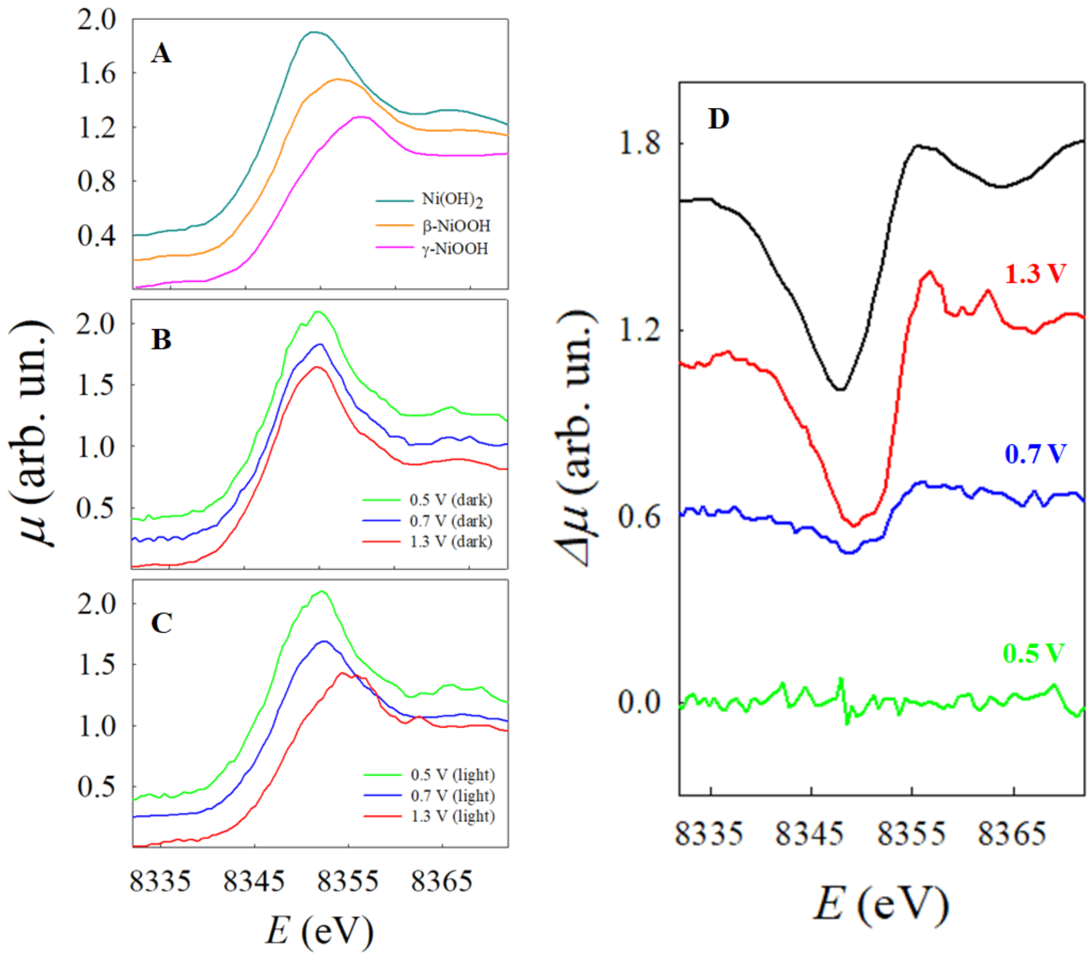

Figure 7.5: Ni K-edge XANES spectra of the α-Fe_2O_3/NiO_x photoelectrode. (Panel A) spectra of the reference materials (Panel B) spectra at different potentials without illumination (panel C) same as B, but with illumination at 400nm. (Panel D) difference spectra (light-dark) at different potentials; the difference spectrum between γ-NiOOH and $Ni(OH)_2$ is also shown as a black line for better reference. All the spectra are shifted along the y-axis for better clarity.

The above results point towards a strong electronic coupling between hematite and the NiO_x layer. In particular, it is first observed that the illumination of the α-Fe_2O_3 layer shifts the oxidation processes of Ni towards much lower potential. Secondly, the fact that this takes place only upon illumination implies that photogenerated holes are responsible for this phenomenon. In addition, it should be noted that during the oxygen evolution reaction Ni has a mean oxidation state of 3.4 upon illumination, indicating that Ni is present both as Ni(IIII) and Ni(IV). The observation of Ni(IV) strongly suggests that this species is directly involved in the catalytic cycle leading to the oxygen evolution.

Additional evidence is given by measuring the absorption coefficient at a fixed energy (8350 eV) and potential (1.3 V) while switching alternatively on and off the light. As shown in Fig. 7.6, the absorption coefficient shows a drastic decrease upon illumination. The comparison with the plot of the chopped photocurrent shows that μ reaches a constant value only when the current is stationary, suggesting that a constant Ni oxidation state is necessary to have a stationary signal. Moreover, after the light is turned off, the regeneration of the pristine NiO_x layer requires dozens of seconds, much more than its oxidation after illumination, which is almost instantaneous. This may be explained considering that the oxidation and regeneration of electrocatalyst proceeds through two different redox processes that are different in nature. Oxidation of NiO_x is photoinduced by holes generated inside α-Fe_2O_3 and is therefore very rapid, in contrast to the recovery of NiO_x oxidation state, which is driven by the reaction with water, a kinetically sluggish process. This evidence strongly suggests that the overlayer not only acts as a hole collector, but it also directly participates in water oxidation.

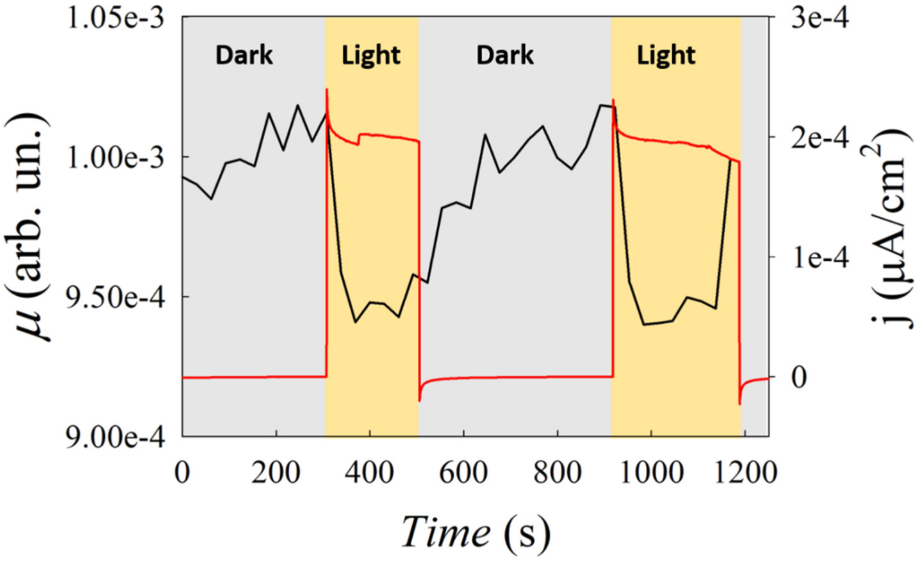

Figure 7.6: Fixed energy X-ray absorption coefficient (black curve) plotted as a function of time at the energy of 8350 eV at 1.3 V at alternatively dark (grey rectangles) and light (yellow rectangles) conditions. The current density is also plotted as a red line.

All these findings jointly imply that in the α-Fe_2O_3/NiO_x photoanode, the hematite acts as an antenna for capturing visible photons. The photogenerated holes are then readily transferred to the NiO_x layer producing an oxidation to Ni(III). When the OER occurs, Ni(IV) is concomitantly observed, thus suggesting that the Ni(IV) could be the active specie in the catalytic cycle. A scheme of the hypothesized mechanism of α-Fe_2O_3/NiO_x photoanode during OER conditions is pictured in Fig. 7.7. Higher oxidation states around 3.5-3.7 have already been observed in Ni-based electrodes, *e.g.* in both overcharged hydrous NiO_x[144], in Ni-borate electrocatalysts for water oxidation[142] and in NiCoFeP under OER conditions[76]. In the present electrodes, the holes are very likely to accumulate before reaching the surface and oxidise water: this is probably the reason why XAS detects a large oxidation state. The presence of Ni(IV) has not been observed in the pure NiO_x electrocatalyst, where the Ni oxidation state under OER conditions is Ni(III). This may be due to the fact that the Ni(IV), if formed, does not accumulate and is therefore difficult to be directly observed.

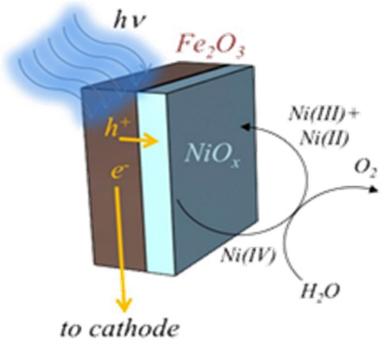

Figure 7.7: Schematic representation of the hypothesized mechanism for α-Fe_2O_3/NiO_x during OER conditions.

7.4 Final remarks

In the present work, the possibility of using operando XAS to follow in real time the catalytic turnover of NiO_x electrocatalyst deposited on hematite has been demonstrated. In particular, this allowed to directly observe the presence of a charge transfer between the hematite and the Ni-based overlayer. Fixed energy X-ray absorption voltammetry and amperometry revealed that the electrocatalyst acts as a hole collector and probably also as catalytic centre for the water splitting reaction. The photogenerated holes drive Ni oxidation, that involves a turnover between Ni(III) and Ni(IV), starting at more cathodic potentials values than those typical of NiOOH. The presence of Ni(IV) can be due to the combined effect of the high energy of the photogenerated holes, and the tendency for them to accumulate at the semiconductor/electrocatalyst junction.

To conclude, *operando* XAS and in particular FEXRAV were effective in investigating the role of the electrocatalyst in composite electrodes for water splitting and could also be employed to other multilayer systems for the investigation of charge transfer processes at the complex hetero-interfaces utilized in sustainable chemical transformations.

8. Operando soft-XAS: investigating solid-gas reaction mechanism on SnO_2

Operando XAS with highly energetic X-rays (hard X-rays) is well-established, and almost every experimental condition can be reached to simulate a realistic process. The same cannot be said for soft X-rays (X-rays with low energy) since severe vacuum limitations and the low penetration depth of soft X-rays have prevented a parallel development. An *operando* XAS experiment with soft X-rays was carried out to study the interaction of SnO_2 nanoparticles with different gaseous species. Thanks to a specific cell configuration, the experiment was conducted at ambient pressure, thus recreating realistic working conditions. In addition, the low penetration depth of soft X-rays together with the TEY (Total Electron Yield) acquisition mode made the technique surface sensitive. This represents a pioneering experiment than can hopefully lead the way to the investigation of electrochemical reactions with *operando* soft-XAS.

8.1 Theoretical background and motivation for the experiment

As shown in the previous Chapters, *operando* XAS with hard X-rays has been successfully carried out to investigate the mechanism of electrochemical reactions. The main advantage of hard X-rays is that, having a high energy and consequent high penetration depth, they are not absorbed by light elements. This renders them particularly suitable to study electrochemical reactions, since the X-rays are not strongly attenuated by either air or by the electrolytic solution. Nevertheless, this same characteristic leads to a major drawback: *operando* XAS with hard X-rays is sensitive to the bulk and not to the surface.

On the contrary, *operando* XAS with soft X-rays would be surface sensitive, and this could, in principle, pave the way to the investigation of electrochemical reactions at the interface. The difficulty lies in recreating the realistic conditions necessary for an *operando* experiment, since soft X-rays are not only absorbed by the electrolytic solution, but also by air, and this is the reason why in the vast majority of cases soft XAS experiments are *ex-situ* and are carried out in high vacuum.

Here an *operando* XAS experiment with soft X-rays at ambient pressure is presented. The aim of the experiment was to study the gas sensing mechanism of SnO_2 nanoparticles towards three different reducing gases (H_2, CH_4 and CH_3CHCH_2). SnO_2 is a wide-band gap semiconductor which has been widely employed for its gas sensing properties towards many gaseous species[145,146]. These species interact with SnO_2 causing, depending on their nature, a decrease or an increase of the electrical resistance: monitoring the change in this electric property is at the basis of gas sensing. The modification of the electrical resistance occurs as a consequence of the interaction between the gas and the surface of semiconductor. In fact, SnO_2 is oxygen sub-stoichiometric and this leads to the formation of defects:

$$O_O^x \leftrightarrow V_O^{\cdot\cdot} + \frac{1}{2} O_2 + 2e' \tag{8.1}$$

This process is reversible, and atmospheric oxygen can be re-adsorbed, giving rise to species like O_2^- on the surface.

$$O_2 + e' \leftrightarrow O_2^- \tag{8.2}$$

The surface of SnO_2 is highly defective and presents both hydroxyl groups and reactive oxygen species. When a reducing gas like CH_4 approaches the surface, at sufficiently high temperature, it reacts with these species and it oxidizes (in this case to form methanol or CO_2): as a result, electrons are released into the conduction band and the resistance decreases. Vice versa, if the gas has oxidizing properties an increase in the electrical resistance is observed. Many efforts have been devoted to understand which species are responsible for the gas sensing, and many have been proposed (superoxide ions, charged atomic oxygen, peroxide ions, *etc.*)[147,148,149,150]. Nevertheless, a general consensus has not been reached and a unified theory regarding the gas sensing mechanism is still lacking. In actual fact, water species are ubiquitous on oxide surfaces, and these species are expected to play a role in the sensing properties. For example, it has been demonstrated that CO_2 cannot be adsorbed on heat treated SnO_2 in dry air [151]. As the relative humidity increases, CO_2 is adsorbed forming carbonate on the surface. When the surface is fully hydroxylated, carbonate is adsorbed by replacing surface -OH groups. However, the presence of hydroxyl groups is often scarcely taken into account when dealing with the mechanisms of adsorption on SnO_2.

The water that can be formed through reactions involving surface hydroxyl groups can easily be detected at the O K-edge. Furthermore, the $M_{4,5}$ edges of tin at *ca.* 485-495 eV can be probed, thus permitting to access all valence states of the materials, searching for variations in the oxidation state of Sn [152,153].

In this experiment, SnO_2 was investigated both at the O K-edge and at the $M_{4,5}$-edges while fluxing three different reducing gaseous species. The experiment was carried out at the ELETTRA synchrotron facility in Trieste in the APE-HE beamline[154]. This experiment represents one of the few examples of *operando* soft-XAS at ambient pressure[155–157].

The ambient pressure conditions were obtained using a cell specifically designed by the APE-HE staff. Moreover, the intrinsic sensitivity of the soft X-rays to the surface was exploited using a Total Electron Yield (TEY) detection method.

8.2 Experimental

8.2.1 Preparation of the sample

Nanocrystalline SnO_2 was prepared by precipitation from an aqueous solution of $SnCl_4$, prepared by dissolving 0.01 mol of $SnCl_4 \cdot 5H_2O$ in 90 mL of milliQ water. Then, 210 mL of a 0.33 M urea aqueous solution was added. All the reagents were purchased at analytical grade from Sigma-Aldrich and were used without further purification. The reaction mixture was stirred for 8 h at 90°C and then overnight at room temperature. The resulting precipitate was washed by centrifugation-resuspension cycles with water/ethanol. It was then suspended in water and treated in a Teflon-lined autoclave for 4 h at 130°C. The powder was then dried in oven at 80°C and calcined for 6 h at 400°C under O_2 flux.

8.2.2 Sample characterization and DFT calculations

Fourier transform infrared (FTIR) spectra were recorded on a Perkin Elmer Spectrum 100 spectrophotometer working in Attenuated Total Reflectance (ATR) mode. Spectra were acquired using a resolution of 4.0 cm^{-1} and a total of 12 scans between 4000 and 400 cm^{-1}. Thermogravimetric analysis (TGA) curves were acquired on a Mettler-Toledo TGA/DSC 3+ STAR System in the 30-900 °C range with a 5 °C min^{-1} heating rate under N_2 flux.

DFT calculations were performed for water loaded $SnO_2(110)$ interfaces with the Vienna Ab Initio Simulation Package (VASP 5.4.1)[158] using the GGA approach. The PBE exchange-correlation was applied[159,160]. To include van der Waals interactions, the dDsC dispersion correction method is employed (PBE-dDsC). The projector augmented wave approximation (PAW) is used to describe the interaction between the valence electrons and the atom cores. Sn and O were treated with 4 and 6 electrons in the valence, respectively. Bulk SnO_2 was optimized using a plane wave kinetic energy cut-off of 1000 eV and a Γ-centered k-point grid of at least 12x12x12. For SnO_2, the optimized cell parameters are (a=b), 4.82 Å in the a- and b-direction and 3.24 Å in the c-direction respectively. Subsequently, a 4-layered (4x4) slab is constructed with SnO_2(110) termination at the top and bottom of the z-direction. On such slabs, water chemisorption and the fate of methane are studied. All bulk SnO_2(110) slabs were structurally relaxed using a plane wave cut-off energy of 450 eV and Brillouin zone sampling was restricted to the Γ-point. A Gaussian smearing[161] of 0.05 eV was applied to improve convergence. Additionally, the convergence criterion for the electronic self-consistent field (SCF) problem is set to 10^{-5} eV for cell optimizations and structures are relaxed until all forces are below 0.03 eV/Å. A vacuum of at least 18 Å in the z-direction is present for all optimized models.

8.2.3 Description of the XAS experiment

The experiment was carried out at the beamline APE-HE at the ELETTRA synchrotron in Trieste. The cell is installed in the beamline and can operate from room temperature to 360 °C [74,154]. A schematic representation of this cell is shown in Fig. 8.1. This cell is designed for ambient pressure soft-XAS experiments. The main body of the cell consists on an aluminium cylinder containing the sample holder, four holes for the gas flow, and an electrical contact for measuring the sample drain current. The top of the cell presents a membrane made of silicon nitride (Si_3N_4), a material substantially transparent to soft X-rays. The membrane is 500 μm x 500 μm sized with a thickness of 100 nm). The sample, in form of powder, is pressed with the aid of silver paste on an aluminium support, which is allocated just below the membrane (in the figure, the sample allocation is turned by 90° for better clarity). The distance between the sample and the membrane is 300 μm. The membrane separates this thin region in front of the sample, at ambient pressure, with the remaining part of the beamline, which is under high vacuum. The X-rays impinge on the membrane, thus reaching the sample generating secondary electron emission.

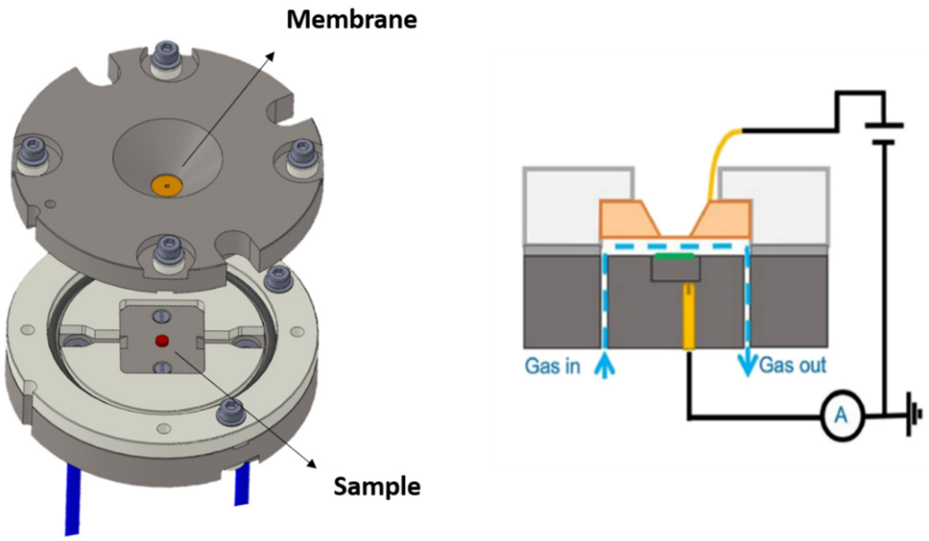

Figure 8.1: (Left) schematic representation of the cell for ambient pressure soft XAS experiments. (Right) scheme of the electrical circuit for the TEY acquisition, where the drain current is measured from the sample. This figure is adapted from Castán-Guerrero, C. *et al,*. *Rev. Sci. Instrum*. 89, (2018)[74].

The resulting signal coming from the sample (photoelectrons, Auger electrons, secondary electrons) is detected in the Total Electron Yield (TEY) mode, measuring the drain current from the sample with a picoammeter, and applying a positive bias voltage (20 V) to the membrane. Since the escape depth of such electrons at moderate kinetic energies is very small (of the order of few nanometres), only very few atomic layers below the surface are probed. In order to collect the photoelectrons coming from the sample, helium gas is used as a carrier, thus helping to enhance the signal and the quality of the resulting spectrum. As shown in Fig. 8.1 (right), the gas is injected in a small tube and is channelled in front of the sample. The monochromator of the APE beamline allows for a continuous scanning of the X-ray energies; this, combined with the high signal-to-noise ratio of TEY, allows recording XAS spectra in very short times, in the order of few seconds. This is fundamental to perform this *operando* experiment, where a process must be followed in real time. Moreover, the undulator of APE-HE covers the whole range of energies of interest for this experiment, allowing rapid switching from the O K-edge to the Sn-$M_{4,5}$ edges (the range of energy covered by the undulator goes from 200 eV to 1400 eV).

Before the experiments, reference spectra of SnO and SnO_2 (both purchased from Sigma-Aldrich) at the O K-edge (between 530 and 550 eV) and at the Sn-$M_{4,5}$ edges (between 480 and 510 eV) were acquired. The *operando* measurements were then acquired fluxing together the gas carrier (helium) and the reducing gas of interest (H_2, CH_4 or CH_3CHCH_2) in various proportions (the gas flow rate is here expressed in Standard Cubic Centimetres per Minute, SCCM). All the spectra have been background subtracted by fitting the pre-edge with a straight line. The spectra at the Sn-$M_{4,5}$ edges were normalised at unit absorption at 508 eV. The spectra at the O K edge are shown without further manipulation, except in cases where it is explicitly stated differently.

Due to oxygen contamination of beamline optics (and also of the Si_3N_4 membrane), the photon flux in the O K-edge energy region (like in the C and N region) is not flat and structureless but presents some oscillations due the absorption of the contaminants. To correct the line shape of the measured O K-edge, different normalization procedures are possible[162], however it is not always possible to subtract completely the contribution of the contamination from the spectra and the dip before the white line is a typical residual of the contaminant contribution to the spectrum. The presence of this dip, however, does not affect the validity of the results; here the interest was not focused on obtaining the exact line shape, but rather on searching for modifications of the spectrum during the reactions.

8.3 Results and discussion

The prepared SnO_2 sample was nanometric, with an average grain dimension of 3.5 nm, calculated from its X-ray diffraction pattern with the Scherrer equation, and showed a surface area of 117 m^2g^{-1}; considering the average grain size, the surface area value is indicative of a high degree of aggregation. Prior to the XAS experiment, the nanocrystalline SnO_2 sample was characterized by FTIR (Fourier Transform Infrared Spectroscopy) and with thermogravimetric analysis. The FTIR spectrum (Fig. 8.2 a) shows as main feature a broad band in the 700-400 cm^{-1} region, which is attributed to Sn-O and Sn-O-Sn stretching vibrations[163]. The broad band in the 3700-3000 cm^{-1} range is attributed to stretching vibrations of hydroxyl groups and physisorbed water, mutually interacting by hydrogen bonding. The corresponding bending counterpart can be appreciated at 1640 cm^{-1}. No peaks characteristic of organic contaminants (*e.g.* CH_x or C=O stretching vibrations) can be observed.

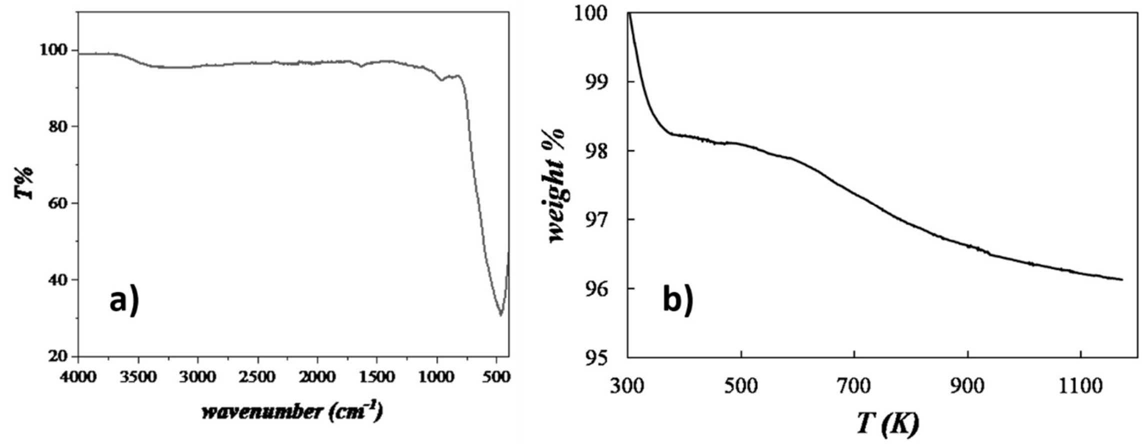

Figure 8.2: a) FTIR spectrum and b) thermogravimetric analysis for the nanocrystalline SnO_2 sample.

Thermogravimetric analysis (TGA) (Fig. 8.2 b) shows a loss of physisorbed water at $T < 100$ °C and a broader feature starting at *ca.* 400 °C accounting for a weight loss of about 4%; the latter can be related, in agreement with FTIR results and previous literature[164], to the loss of chemisorbed water.

In order to clean the surface of the sample from physisorbed water, the sample was mounted in the gas cell and heated from room temperature to 300 °C under He flux (20 SCCM). During the heating process, XAS spectra were acquired at the O K-edge to monitor the change in the spectrum profile. Spectra obtained at different temperatures are shown in Fig. 8.3, while the spectrum of SnO_2 acquired in high vacuum is shown below as a reference, together with the spectrum of water in the gas phase. At room temperature, the spectrum shows some extra peaks with respect to the reference. The intense peak at 532.7 eV is due to molecular oxygen, which probably comes from desorption from within the gas pipeline. By increasing the temperature, this peak gradually disappears, while a dip at the same energy arises. This dip is due to small oxygen impurities in the beamline, as anticipated in the previous Section. Between 538 and 544 eV the spectra at low temperature show broad features that can be attributed to SnO_2, water and molecular oxygen. As a reference, the spectra obtained at the O K-edge for water (magenta line), air (orange line), CO_2 (green line) and $CO+O_2$ (yellow line) are shown in Fig. 8.4. At 300 °C, after the thermal treatment, the spectrum nicely agrees with that obtained in vacuum, demonstrating that SnO_2 is now free of physisorbed water, in agreement with the TGA measurements.

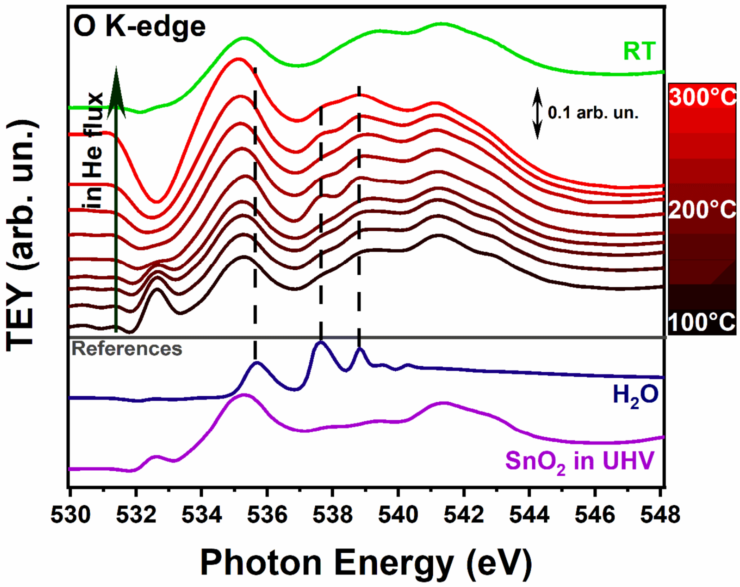

Figure 8.3: (Upper panel) O K-edge spectra of the SnO_2 nanoparticles in flowing He and at different temperatures between 100 °C and 300 °C. (Lower panel) spectrum of the nanoparticles in rough vacuum before the thermal treatment and spectrum of water in the gas phase.

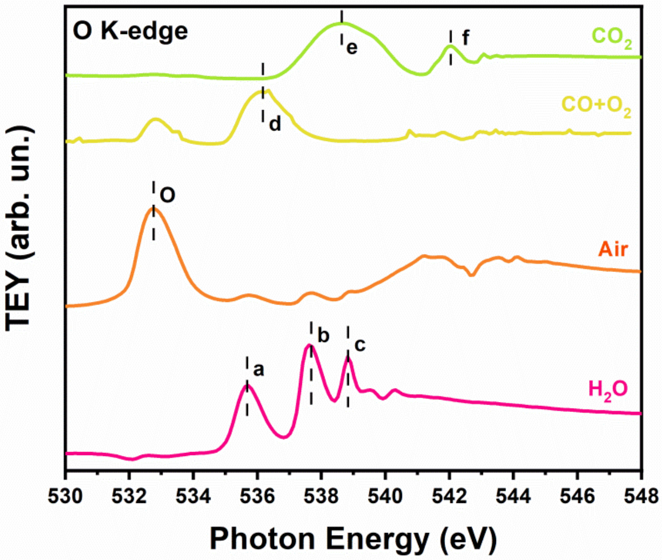

Figure 8.4: O K-edge spectra of reference gases. The spectra are normalised at unit absorption at 548 eV and shifted along the y axis for the sake of better clarity.

It should also be noted that in vacuum the spectrum shows some traces of oxygen, which are not present after the thermal treatment. In addition, the quality of the signal is high and comparable to that obtained in vacuum. From now on, this situation, where SnO_2 is free of physisorbed water and clean, will be referred to as "clean SnO_2 surface". The same spectrum was also obtained after the sample was cooled down again to room temperature under the He flux (green line in Fig. 8.3, upper panel).

After this treatment, the sample was heated while flowing a mixture of He (20 SCCM) and H_2 (5 SCCM). The spectra were acquired both at the O K-edge and at the Sn $M_{4,5}$-edges, and are shown in Fig. 8.5 a and 8.5 b, respectively. At room temperature, the spectrum at the O K-edge corresponds to that of clean SnO_2. Above 150 °C, some additional features start appearing at 535.5 eV, 537.7 eV and 538.8 eV, and become more intense as the temperature is increased. As evident from Fig. 8.4, these peaks correspond both in energy and shape to the spectrum of water in the gas phase. The previous thermal treatment in He led to the complete removal of the physisorbed water, and in this range of temperature no further loss of water is expected by the TGA curve. Therefore, it can be concluded that the formation of water occurs as a consequence of the reduction of SnO_2 by H_2, which in turn oxidizes to form water. The spectra acquired at the Sn $M_{4,5}$-edges confirm this hypothesis; in fact, at 120 °C the spectrum is that typical of SnO_2, showing five peaks which can be attributed to the transition from the filled 3*d* states to the empty Sn 5*p* and Sn 5*f* orbitals[165] (violet curve in Fig. 8.5 b). At higher temperatures, an additional peak at *ca.* 489 eV starts to appear, while the feature at *ca.* 497.5 eV becomes more intense. These features clearly indicate the reduction of SnO_2 to SnO, as demonstrated by the comparison with the spectrum of the SnO powder taken as reference (orange line in Fig. 8.5 b). The formation of water shows a drastic boost at 190 °C, and then shows a decrease after 250 °C. The spectrum at the Sn $M_{4,5}$ -edges shows that at 240 °C the reduction of SnO_2 is consistent and not just limited to the immediate surface. In addition, the formation of SnO is even higher at higher temperature. A quantification of the thickness of the SnO layer can be obtained by measuring the area of the peak at 489 eV, which is only due to Sn(II), normalised by the area of the peaks at 492.5 eV and 494.5 eV, that are due almost exclusively to Sn(IV).

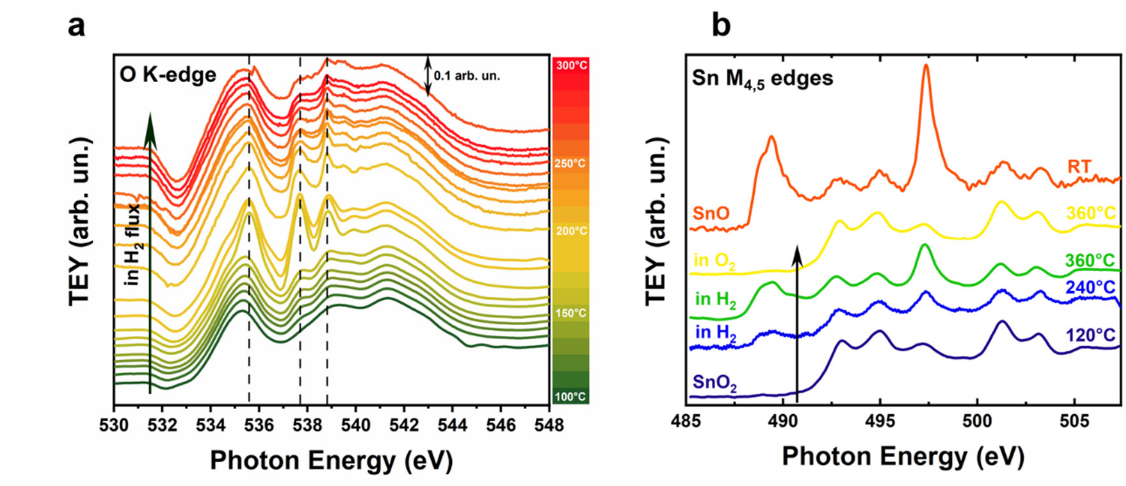

Figure 8.5: Evolution of the O K-edge spectra of the SnO_2 nanoparticles in flowing H_2 as a function of temperature: the spectra are shifted along the y-axis for the sake of better clarity. The vertical dotted lines mark the position of the main peaks of water in the gas phase. b) Sn $M_{4,5}$-edges of the SnO_2 nanoparticles at different temperatures and in different conditions. The spectrum of standard SnO is also shown for reference, and the spectra are shifted along the y-axis.

Taking into account that the mean probing depth of electrons in the TEY mode at 500 eV amounts to *ca.* 3.5 nm[166], the thickness of the reduced layer at 360 °C is *ca.* 1.5(5) nm, which corresponds to a width of at least 3-4 unit cells. The reduction can be fully reversed by flowing O_2 in the cell at temperatures higher than 250 °C. In fact, the spectrum obtained at the Sn $M_{4,5}$-edges after this treatment shows the complete absence of the peak at 489 eV and has the typical shape of SnO_2 (yellow line in Fig. 8.5 b).

The test with the H_2 flux demonstrates that soft-XAS can be used to simulate real working conditions, and that information can be obtained regarding both the product of the reactions (as long as the products contain oxygen) and the changes in the oxidation state of tin. The method was therefore used to monitor the effects of hydrocarbons like CH_4 and CH_3CHCH_2.

Experiments with methane (20 SCCM He and 5 SCCM CH_4) were conducted in a range of temperature between 100 °C and 360 °C. Before running the experiments, the sample was fully oxidised as described above. The results at the O K-edge and at the Sn $M_{4,5}$-edges are shown in Fig. 8.6. At 100 °C, the O K-edge spectrum corresponds to the clean SnO_2 surface, free of physisorbed water. At higher temperatures (T>120°C), it can be seen that the peaks correspondent to water in the gas phase start to appear, they become more intense from 250 °C to 310 °C and then decrease again at temperatures higher than 310 °C.

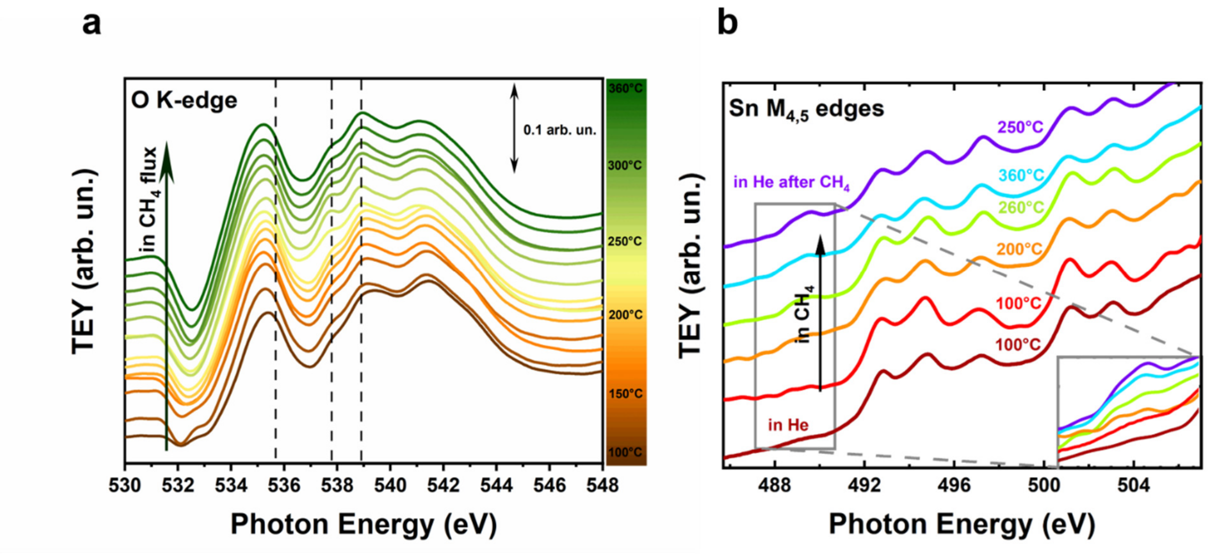

Figure 8.6: a) Evolution of the O K-edge spectra of the SnO_2 nanoparticles in flowing CH_4 as a function of temperature; the spectra are shifted along the y-axis for the sake of clarity, and the vertical dotted lines mark the position of the main peaks of water in the gas phase. b) Sn $M_{4,5}$-edges of the SnO_2 nanoparticles at different temperatures in flowing CH_4. The spectra are shifted along the y-axis as in a). The inset shows the increase of the Sn(II) signature at 489 eV.

Correspondingly, at the Sn$M_{4,5}$-edges (Fig. 8.6 b) the signatures of SnO start to appear at 120 °C and become more intense increasing the temperature. In the inset of Fig. 8.6 b, a magnification of the peak at 489 eV is shown for better clarity.

An analogous behaviour is observed fluxing propylene (20 SCCM He and 5 SCCM CH_3CHCH_2). Before fluxing, the sample was completely re-oxidized fluxing O_2. The spectra were acquired at the O K-edge and at the Sn-$M_{4,5}$ edges in a range of temperature between 100 °C and 260 °C (Fig. 8.7). Also, in this case, the peaks corresponding to water start to appear at temperatures higher than 120 °C, reach their maximum intensity at 200 °C, and then start to decrease at higher temperatures. In this case, the peaks are more intense with respect to the methane, in agreement with the higher reactivity expected for unsaturated hydrocarbons. The propylene flux, analogously to methane, leads to the partial reduction of SnO_2 to SnO, as evident by Fig. 8.7 b. Also in this case, the entity of the reduction is higher for propylene with respect to methane.

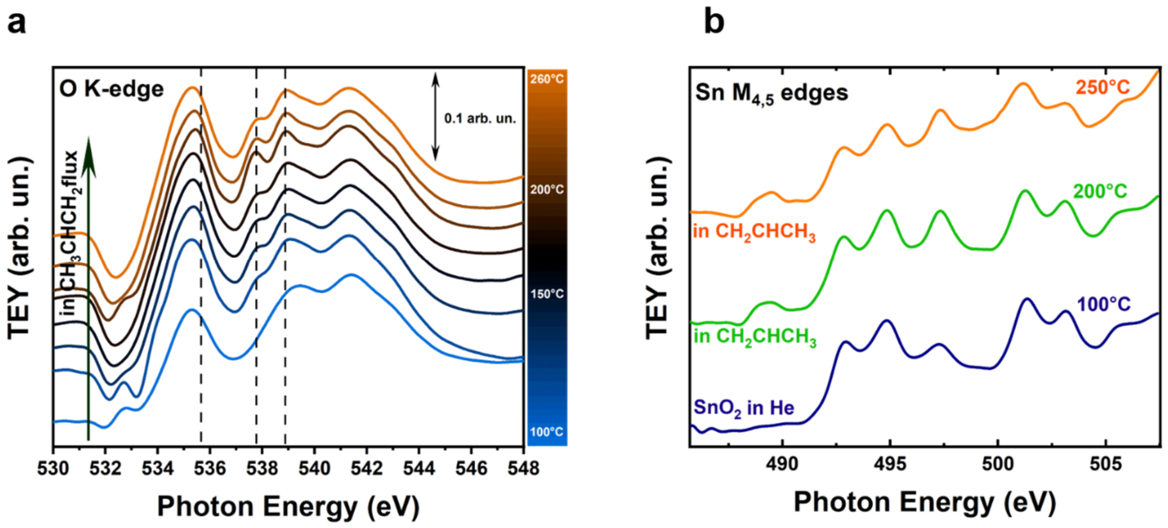

Figure 8.7: Evolution of the O K-edge spectra of the SnO_2 nanoparticles in flowing CH_3CHCH_2 as a function of temperature; the spectra are shifted along the y-axis for the sake of better clarity, and the vertical dotted lines mark the position of the main peaks of water in the gas phase. b) Sn $M_{4,5}$-edges of the SnO_2 nanoparticles at different temperatures in flowing CH_3CHCH_2. The spectra are shifted along the y-axis as in a).

The thickness of the SnO layer at the end of the treatment can be quantified with the same method described above for the reduction with H_2. The resulting values are 0.6(2) nm for CH_4 and 0.5(2) nm for CH_2CHCH_3 (see Fig. 8.8), which correspond to a width of 1-2 SnO_2 unit cells in both cases. Even if the extent of reduction is greater for CH_3CHCH_2, the thicknesses are comparable: this is due to the fact that the SnO_2 nanoparticles have been exposed to methane at high temperature for a longer time. It should be noted that both during the methane and the propylene flux, no traces of CO or CO_2 are detected. These products would be visible at the O K-edge even at low concentrations, considering that they give broad peaks at *ca.* 536.5 eV and *ca.* 539 eV respectively, as shown in Fig. 8.4, and considering that their cross section is experimentally found at least five times larger than for water [167]. The absence of carbon oxide during the experiment, at least at these relatively low temperatures, suggests that the hydrocarbons react with clean SnO_2 surface by directly providing electrons, rather than by extracting surface oxygenated species. SnO_2 behaves therefore like an "electron sponge", easily accepting and returning electrons depending on the nature of the gas species that approach the surface. This is also confirmed by the easiness with which the reduced surface is then fully re-oxidized under O_2 flux.

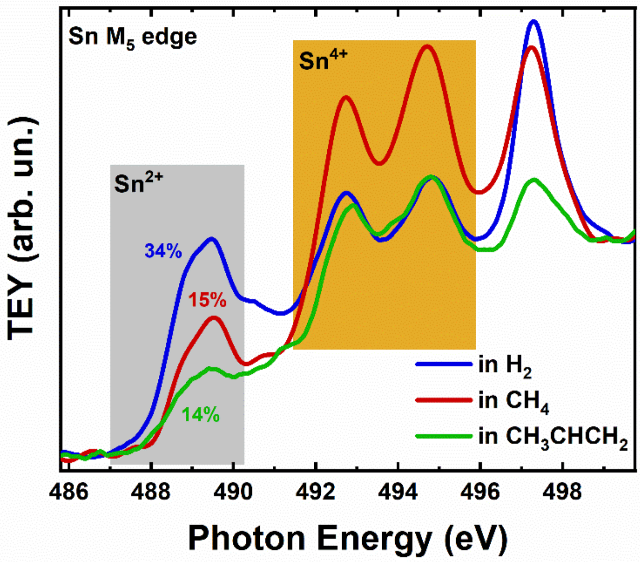

Figure 8.8: Quantification of the thickness of the reduced SnO layer for H_2, CH_4 and CH_3CHCH_2. The figure shows the spectra at the Sn $M_{4,5}$-edge for the SnO_2 nanoparticles at the end of the treatment in the three cases. The percentages shown in the figure are calculated by dividing the area of the peak at *ca.* 489 eV (highlighted in grey), due to Sn(II) only, by the area of the peaks at *ca.* 492.5 and 494.5 eV, both due almost exclusively to Sn(IV) (highlighted in orange).

The electrons provided by the reducing gas remain localised on tin, which is consequently partially reduced from Sn(IV) to Sn(II), forming a layer of SnO on the surface. As expected, the reactivity is larger for H_2 than for hydrocarbons and it is larger for unsaturated hydrocarbons than for alkanes.

These experimental XAS results were coupled to Density Functional Theory (DFT) calculations, in order to gain more information on the expected gas sensing mechanism. The calculations were performed for the interaction between SnO_2 and CH_4 for reasons of simplicity; in all probability, the calculation can be extended also for the case of CH_3CHCH_2. DFT calculations were made for a fully hydroxylated SnO_2(110) surfaces (θ_{H_2O}=1), mimicking the predominantly exposed clean surface of the experiments. These 110 surfaces consist of Sn^{4+} and have both dangling Sn-OH and bridged Sn-OH-Sn groups (Figure 8.9). Furthermore, they are fully H-saturated and therefore the reaction with CH_4 takes place via physisorption of CH_4 (-19.2 kJ/mol), followed by C-H cleavage forming adsorbed CH_3OH. Here, two different reaction possibilities are tested, forming the adsorbed CH_3OH either via CH_3 addition to a dangling Sn-OH bond or to a bridged Sn-OH-Sn bond, represented in

Figures 8.9 and 8.10 respectively. The most stable reorganized structures after O-CH_3 bond formation are at -114.7 and -102.3 kJ/mol (see Figure 8.9 and 8.10). From these states, desorption of CH_3OH and H_2O was considered. As a first approximation of the desorption temperature, the adsorption energy ΔE_{ads} can be divided by the standard (1 bar, 298 K) gas phase entropy contribution of the respective compounds, *i.e.* 0.1272 (CH_3OH) and 0.1888 kJ/(mol·K) (H_2O).

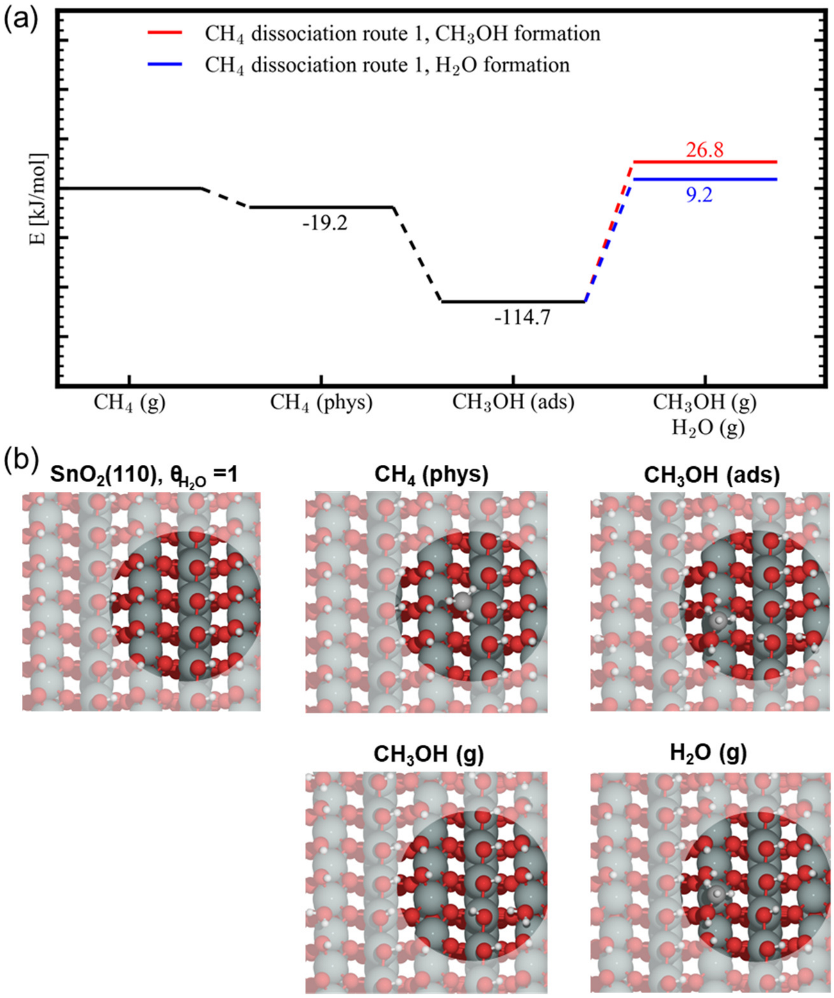

Figure 8.9: (a) Energy diagram for the production of CH_3OH and H_2O from CH_4 on a fully hydroxylated $SnO_2(110)$ surface via CH_3 deposition on dangling Sn-OH bond forming adsorbed (ads) CH_3OH, and (b) the schematic representation of the different states of $SnO_2(110)$ in the above energy diagram (a). Colour code; Sn (green), O (red), C (grey), H (white).

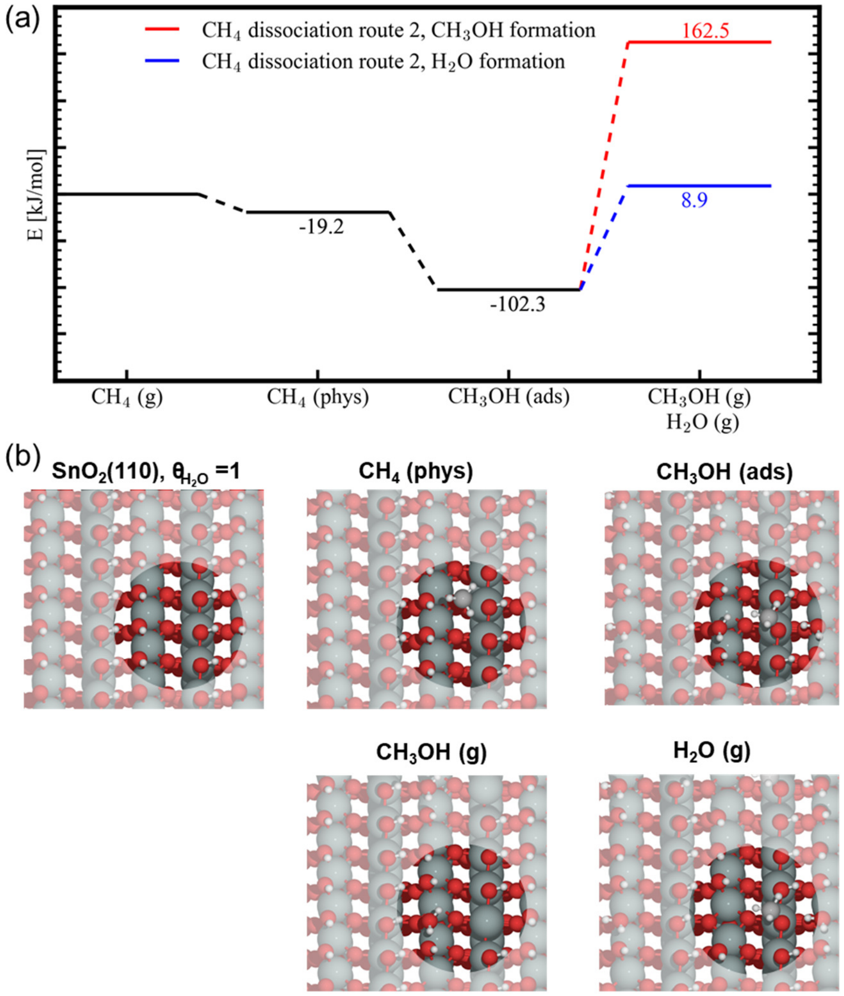

Figure 8.10: (a) Energy diagram for the production of CH_3OH and H_2O from CH_4 on a fully hydroxylated $SnO_2(110)$ surface via CH_3 deposition on Sn-O-Sn bridge forming adsorbed (ads) CH_3OH, and (b) the schematic representation of the different states of $SnO_2(110)$ in the above energy diagram (a). Colour code; Sn (green), O (red), C (grey), H (white).

Assuming that both components have negligible entropy at the surface, then:

$$T_{des} = \frac{\Delta E_{ads}}{S^{\circ}{}_{gas,1\ bar}} \tag{8.3}$$

(in Kelvin).

In terms of desorption temperature, this means that when the adsorption energy is similar, it is much more difficult for CH_3OH compared to H_2O to leave the $SnO_2(110)$ surface. Indeed, the desorption energies of CH_3OH are even higher. In case of water, desorption energies of 124 kJ/mol and 111 kJ/mol are found, corresponding roughly with realistic desorption temperatures of about 383 °C and 316 °C, respectively. However, as the water partial pressures in the experiments are severely lower than 1 bar, the entropy difference is underestimated, thus leading to an overestimation of the desorption temperature. Furthermore, there are also other SnO_2 facets exposed in experiment. Within experiment, it is clear that H_2O evaporation happens from 100 ºC after exposure of the SnO_2 nanoparticles to CH_4, and this agrees with the computational result that reaction between CH_4 lowers the H_2O adsorption energies.

In another investigated scenario, the $SnO_2(110)$ surface is not fully hydroxylated, and therefore one water molecule was removed (θ_{H_2O}=7/8), creating a free Sn site and an O site without hydrogen (Fig. 8.11). In this case, methane is slightly exothermically physiosorbed at the free Sn-site. The nearby oxygen extracts a hydrogen and the remaining $-CH_3$ group gets chemisorbed forming a $Sn-CH_3$ bond. This step is exothermic with about 59 kJ/mol compared with methane in the gas phase. In the next step, a methoxy group is formed and water leaves the surface reforming a free Sn site. This reaction is exothermic with -157 kJ/mol and shows that the CH_3OH group is strongly physisorbed onto the surface. It should be noted that here the term “physisorbtion” is used even if the adsorption energy is quite high, as it is referred to the adsorption of CH_3OH without the cleavage of any molecular bond. Since the active site is reformed, the reaction is autocatalytic and will stop once all available sites are blocked by the methoxy groups. To remove the methanol from the surface requires a desorption energy of about 140 kJ/mol, which corresponds to a desorption temperature higher than 800 °C. The removal of water from the surface is also endothermic by 144 kJ/mol, corresponding to a desorption temperature higher than 400 °C.

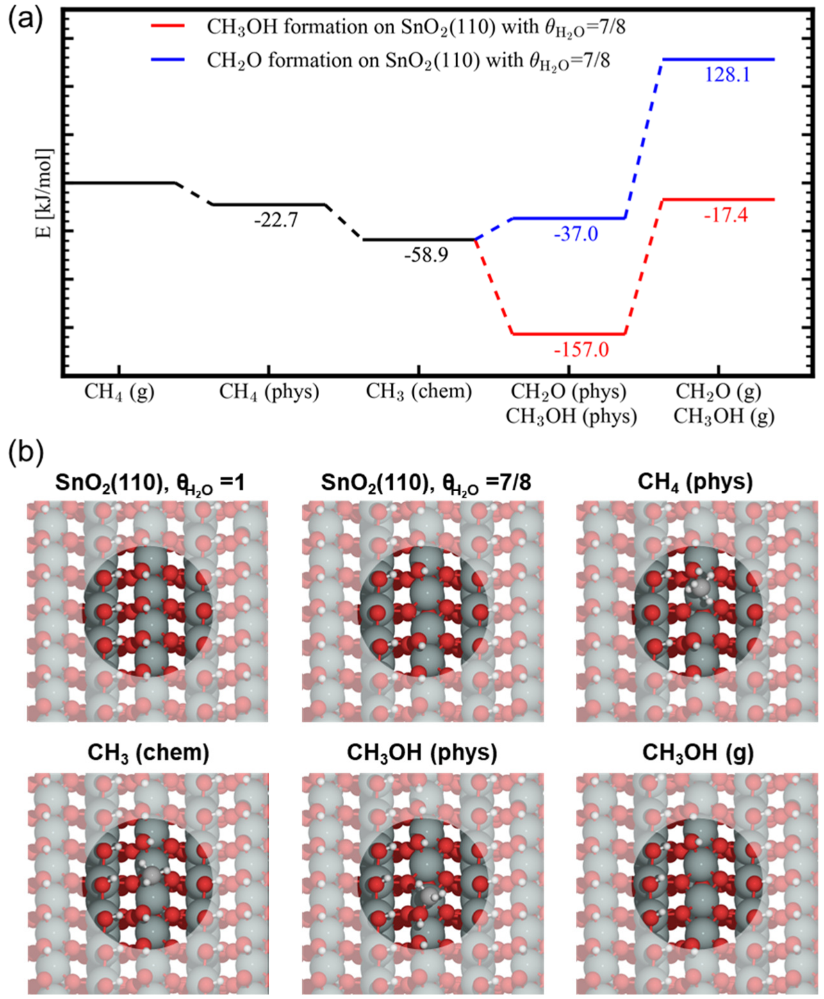

***Figure 8.11**:* (a) Energy diagram for the production of CH_3OH or CH_2O from CH_4 on a hydroxylated $SnO_2(110)$ surface (H_2O coverage $\theta = 7/8$) via CH_3 chemisorption (chem) on the bare Sn-site followed by the formation of physisorbed (phys) CH_3OH or CH_2O and (b) the schematic representation of the different states of $SnO_2(110)$ in the above energy diagram (a). In this case, the formation of H_2O from the physisorbed CH_3OH state is more endothermic than the formation of gas phase CH_3OH (energy level -13.1 kJ/mol). Colour code: Sn (green), O (red), C (grey), H (white).

These results clearly show that both water and methanol cannot be formed unless the desorption energies are further lowered, for example via extra surface reactions with CH_4. It should be noted that, as soon as there are vacant Sn-sites, species in the Sn-CH_3 state can be formed. Through such electron-rich covalent bonds, the surface Sn^{4+} gets eventually reduced. The fact that a Sn^{2+} signature is observed, and that only 1 to 2 layers of SnO were found, experimentally further support the latter mentioned reaction sequence.

On the basis of both experimental and theoretical considerations, a mechanism of the interaction of SnO_2 with hydrocarbons can be hypothesized as schematically shown in Fig. 8.12. According to this mechanism, the reducing gas (methane in the figure) binds at the surface of the semiconductor, covered or partially covered by hydroxyl groups, removing water; through this process it releases electrons that localize at Sn sites, leading to a partial reduction of Sn(IV) to Sn(II).

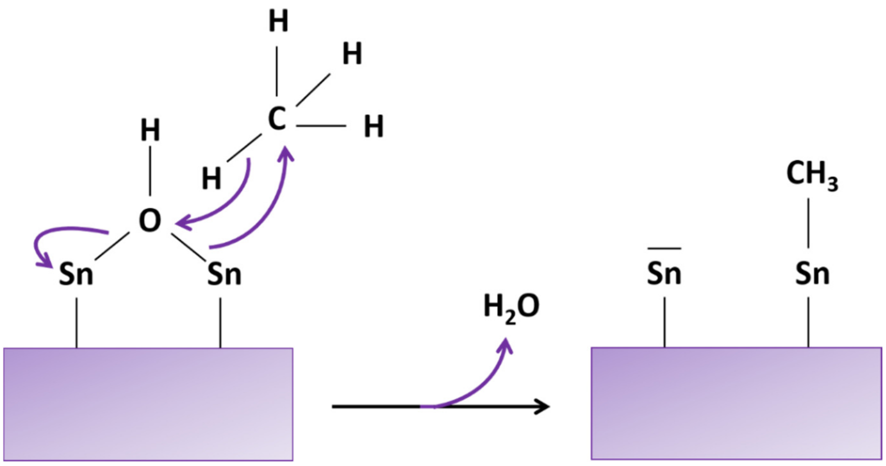

Figure 8.12: Scheme of the reactive adsorption of hydrocarbons (methane in the figure) on SnO_2.

This mechanism seems to be reasonable and to be able to describe, in a simple way, the experimental data. However, as pointed out by the DFT calculations, a mechanism involving the formation of methoxy-like species on the surface cannot be excluded.

8.4 Final remarks

In the present work, ambient pressure *operando* soft X-ray absorption spectroscopy (soft-XAS) was applied to study the reactivity of hydroxylated SnO_2 nanoparticles towards reducing gases. H_2 was first used as a test case, showing that gas phase and surface states can be probed in the same experiment: soft-XAS at the O K-edge gains sensitivity towards the gas phase, while at the Sn $M_{4,5}$-edges tin surface states are explicitly probed. It was then demonstrated that reducing hydrocarbon gases (methane and propylene) react with the hydroxylated SnO_2 surface, removing water and reducing Sn(IV). The reduction is larger for

H_2 than for hydrocarbons and is larger for unsaturated hydrocarbons than for alkanes. The reaction mechanism for the reduction with CH_4 involves the cleavage of the C-H bond of the incoming gas and a subsequent reaction with -OH groups on the surface to form H_2O. Because of this reduction reaction, more loosely bound or physisorbed H_2O is formed, that eventually leaves the SnO_2 surface as experimentally demonstrated. In parallel, the Sn sites in the immediate surface are reduced to form Sn(II). The evidence presented in this Chapter reveals that the hydroxyl groups that are present at the SnO_2 surface play an important role in the adsorption properties of this material and, therefore, on the sensing mechanism.

Finally, all the data here presented demonstrate the feasibility of soft-XAS at ambient pressure and the ability to provide fundamental evidences for the assessment of mechanisms of surface reactions.

9. Dynamic Multi-frequency Analysis: investigation of the hydrogen evolution reaction on Pt

In this Chapter, dynamic multi-frequency analysis is presented as a new strategy for the study of the mechanism of electrochemical reactions. Through this technique, it is possible to directly extract information on the evolution of electrochemical parameters over all the considered potential range. The reaction selected for this purpose is the hydrogen evolution reaction catalysed by Pt microelectrodes. This reaction has been widely studied during the years with countless techniques and generally under stationary, steady state conditions[168–170]; however, new insights could be achieved through investigations made under non-steady state conditions. In addition, this reaction was chosen as a test case to demonstrate that DMFA can be successfully employed in the field of electrocatalysis.

9.1 Theoretical background and motivation for the experiment

As already mentioned in Section 2.1.1 of this thesis, Pt is located at the top of the Volcano plot[22] for the hydrogen evolution reaction (HER) and is the best-known catalyst for this reaction, showing a particularly low overpotential even at high reaction rate in acidic media. It is generally accepted that the hydrogen evolution reaction catalysed by platinum in acidic media occurs via two successive steps [171]: 1) the adsorption of H^+ at the surface of the metal and then 2) H_2 formation. The first step takes the name of the Volmer reaction, while the second step can occur via two alternative pathways: the Tafel reaction, during which two H_{ad} recombine to give gaseous H_2 or the Heyrovsky reaction, during which one H_{ad} reacts with a H^+ from the solution, generating H_2 through an electron transfer reaction. Depending on the preferred pathway, the overall hydrogen evolution reaction can therefore proceed through a Volmer-Tafel mechanism or through a Volmer-Heyrovsky mechanism.

Even if Pt has been extensively studied and employed as a catalyst for HER, the mechanism of the reaction is still not yet well-defined[172]. While the Volmer-Tafel reaction seems to be the preferred mechanism at low potentials, the Heyrovsky mechanism can start giving a major contribution at more cathodic potentials. In addition, it is not excluded that the reaction goes through Volmer-Heyrovsky also at less cathodic potentials, or through a mix of both mechanisms[173,174]. Investigating the reaction mechanism is in fact not so obvious, considering that the kinetic parameters of the overall reaction, the apparent Tafel slope and the reaction order are strongly dependent on numerous parameters *e.g.* the structure of the surface, the pH, the overpotential, and also the presence of adsorbed species or impurities[175,176,177]. The variations of the relevant parameters and of the kinetic values which are found in literature can therefore be related to slightly different experimental conditions.

In the present work, the hydrogen evolution reaction has been investigated through dynamic multi-frequency analysis (DMFA) in acidic media ($HClO_4$ 0.1 M). The principles behind DMFA have already been presented in Section 3.3.3. Through this technique it is possible to acquire a considerable number of impedance spectra while cycling the electrode according to a cyclic voltammetry. Contrary to classic impedance spectroscopy, this permits information regarding the system to be obtained under dynamic conditions and, therefore, extraction of information on the variation of kinetics parameters during the reaction.

DMFA has been only recently introduced[77] and its applications are limited to few experiments [82–84]. The aim of this work was mainly to apply DMFA in the field of electrocatalysis as a powerful and innovative tool to obtain information on the mechanism of an electrocatalytic reaction; this is the reason why the most classic and well-known reaction in the field of electrocatalysis has been selected as a first test case. In addition, new insights into this reaction mechanism could be given, considering the possibility of studying the reaction under non-stationary conditions. Contrary to DMFA, classical EIS can be applied to this system only at potentials more positive than the hydrogen reversible potential, or at very low overpotentials, where steady-state conditions can be easily reached. At high overpotentials, however, the nucleation and then formation of gas bubbles leads to instability and causes a continuous variation of the surface, thus preventing the recording of reliable spectra. All these problems are easily overcome employing DMFA, as it will be shown in the following Sections.

9.2 Experimental

9.2.1 Preparation of the Pt microelectrode

A borosilicate glass capillary with a diameter of 1 mm was sealed at one extremity by means of a torch's flame. A Pt wire with a diameter of 250 µm and a length of 1.5 cm was then carefully inserted from the other extremity, and gently pushed until it reached the sealed part of the capillary. When the Pt wire was in the desired position, it was sealed into the capillary glass by means of a torch flame for a total length of about 1 mm. Before continuing the sealing process, the open side of the capillary was connected to a peristaltic pump through of a flexible polymer tube to create vacuum inside the capillary. The rest of the sealing procedure was then carried out in vacuum, in order to avoid the formation of gas bubbles into the glass mantle. During the sealing, the capillary was manually rotated while moving slowly the flame vertically, until two-thirds of Pt wire was embedded into the glass body. The absence of gas bubbles and the uniformity of the embedding were checked through a microscope. In order to create the back contact, a thin piece of indium was inserted in the capillary together with a Cu wire. The copper wire, the indium and the Pt wire were then sealed together by heating them by means of a heat gun. The tip of the microelectrode was then polished with an abrasive paper of grade 12.6 µm and thoroughly rinsed with ultrapure water.

9.2.2 Description of the experiment

The three-configuration cell employed in the experiment is schematically shown in Fig. 9.1. The cell is designed to have an external jacket which can be connected to a thermostat. The top of the cell is closed by a Teflon cover, which has three holes for the allocation of the working electrode, the counter electrode and the reference electrode, and a smaller hole allowing for the injection of argon inside the cell. The working electrode is a Pt microelectrode (Ø 250 µm), the counter electrode a cylindrical Pt mesh, and the reference Ag/AgCl (3 M KCl). For better clarity, all the potentials will be indicated against reversible hydrogen electrode.

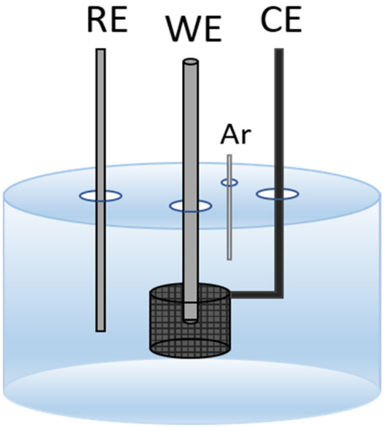

Figure 9.1: Schematic representation of the three-electrode cell configuration employed in the DMFA experiment.

In this configuration, the working electrode is surrounded by the Pt mesh: this ensures that the electric field remains confined inside the counter electrode (CE), so that the electrolytic solution surrounding the mesh can still be considered an equipotential region. Under these conditions, the reference electrode can be placed far from the CE without causing changes in the electrolyte resistance[178]. In addition, this cell's geometry allows the avoidance of any misalignment of the working electrode (WE) during measurements, thus enhancing the quality and the reproducibility of the data. Even if, in principle, in a three-electrode configuration no current should flow between the RE and the WE, in real systems the RE is polarizable to a certain extent, which can induce artefacts in the high-frequencies region in the Nyquist plot. A useful strategy to avoid this consists of tightly coiling a Pt wire (diameter 100 μm) around the tip of the reference electrode and to connect it with a capacitor[179].

Before every set of measurements, the Pt electrode was manually polished with abrasive papers of progressively lower grades (3, 2 and 1 μm, Matador). The electrode was then thoroughly rinsed with ultrapure water. Prior to the DMFA measurements the electrode was activated with 100 voltammetric cycles in 100 mM $HClO_4$ (Sigma-Aldrich) in a potential range between 0 V and 1.45 V vs RHE in argon saturated solution. The DMFA measurements were then acquired in 100 mM $HClO_4$ at different temperatures in Ar saturated solution. In order to perform the DMFA measurements, the WE was polarized at a constant potential of 0.43 V vs RHE and the voltage signal was then perturbed with a quasi-triangular wave superimposed to a multisinusoidal signal. The current range of the potentiostat was set to 1 mA; the voltage input signal and the corresponding current response were detected by a 2-channel oscilloscope 4262 PicoScope (Pico Technology). The quasi-triangular wave had an amplitude of 500 mV and a frequency of 0.02 Hz, corresponding to a scan rate of 20 mV/s. The multisine signal was created by a waveform generator using homemade Matlab scripts (release 2018a from the MathWorks Inc.) and contained 45 frequencies covering 5 decades. Since the base frequency was chosen to be 1 Hz, the range of frequency values ranged from 1 MHz to 8 Hz. The intensity of the multisine signal was 50 mV peak to peak. In each measurement, a full data set was recorded in 200 ns; considering that the total time of a single experiment was 100 s (in order to acquire two full voltammetric cycles), the final number of samples was 5 MSamples, from which 2000 impedance spectra were then extracted. The data were evaluated with Matlab using homemade Matlab scripts. As already demonstrated by Battistel *et al.*[77], dynamic impedance spectra can be fitted using equivalent circuits (EC). All the impedance spectra in a selected potential range (as shown later in this Chapter) were fitted simultaneously, and the goodness of fit was evaluated as in classic impedance, by minimizing the χ_i^2 factor of the i-th impedance spectrum:

$$\chi_i^2 = \sum_{i=1}^{N_f} \frac{[Re(Z_i(\omega_1)) - Re(Z_{i,1})]^2 + [Im(Z_i(\omega_1)) - Im(Z_{i,1})]^2}{[Re(Z_{i,1})]^2 + [Im(Z_{i,1})]^2} \tag{9.1}$$

Where N_f is the number of frequencies. The following function is then minimized:

$$\chi_T^2 = \sum_{i=1}^{N} \chi_i^2 + \sum_{P=1}^{N_P} w_P \cdot S_P \tag{9.2}$$

The second summation is related to the function S_p called "smoothing factor", which can be minimized to preserve the correlation between all the spectra and obtain smooth trends, forcing the parameters not to change too severely. Information on this function can be obtained in Battistel *et al.*[77]. In the present case, however, the smoothing factor was kept to zero to let the parameters change freely and observe their trends with the potential, thereby avoiding additional data manipulation and possible introduction of errors.

9.3 Results and discussion

Before every measurement, the Pt microelectrode was electrochemically activated with 100 CV cycles in 100 mM $HClO_4$ in a potential range between 0 V and 1.45 V vs RHE. $HClO_4$ was chosen for both the activation process and the DMFA measurements, since ClO_4^- anions only weakly adsorb on the Pt surface, compared to other anions like SO_4^{2-} or Cl^-. This pre-treatment of reduction/oxidation of Pt is known to lead to a higher reversibility and reproducibility of the subsequent electrical processes[180]. The activation curve at the end of the 100 cycles is shown in Fig. 9.2; it can be noted that at the end of the cycles, the CV shows well-defined peaks in the potential range between 0 V and 0.5 V. These two cathodic peaks and the little bump around 0.3 V can be attributed to the hydrogen adsorption at the surface of Pt. Analogously, the corresponding anodic peaks are attributed to the hydrogen desorption.

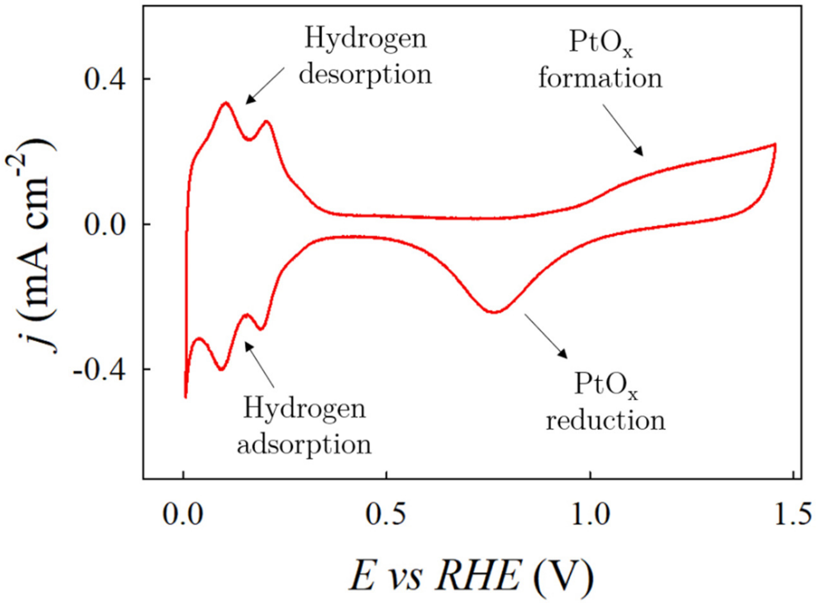

Figure 9.2: Cyclic voltammetry acquired in $HClO_4$ (0.1 M) between 0 V and 1.5 V at 100 mV/s on Pt microelectrode after the activation process.

Around 1 V platinum starts to oxidize, leading to the formation of a PtO_x layer at the surface of the electrode. At this potential, the layer of oxide is still very thin, and is then completely reduced at 0.2 V. This continuous formation and destruction of the layer leads to a progressive reconstruction of the surface, which becomes more active towards the HER[181].

In the range between 0 V and 0.5 V the hydrogen electro-adsorbed at the surface takes the name of H_{UPD}, where UPD stands for Under Potential Deposition, indicating that the species is adsorbed at potentials less cathodic then the standard reduction potential of H^+ (0 V vs RHE). The formation of H_{UPD} is typical of Pt[182], and can be directly observed through the cyclic voltammetry, as shown in Fig. 9.2. At potentials more cathodic than 0 V the adsorbed hydrogen is named H_{OPD}, where OPD stands for Over Potential Deposition. Since the bond strength between the metal and H_{OPD} is lower than between platinum and H_{UPD}, it is possible that H_{OPD} is the species direct responsible for the HER, while H_{UPD} dominates in the adsorption region but does not contribute to the hydrogen evolution[183].

After the surface activation, DMFA measurements were acquired at room temperature superimposing a multisinusoidal signal and a quasi-triangular wave following the experimental procedure outlined in Section 9.2.2. The potential range chosen for the quasi-CV, here shown in Fig. 9.3, is from 0.43 V to -0.07 V vs RHE, while the selected scan rate is 20 mV/s.

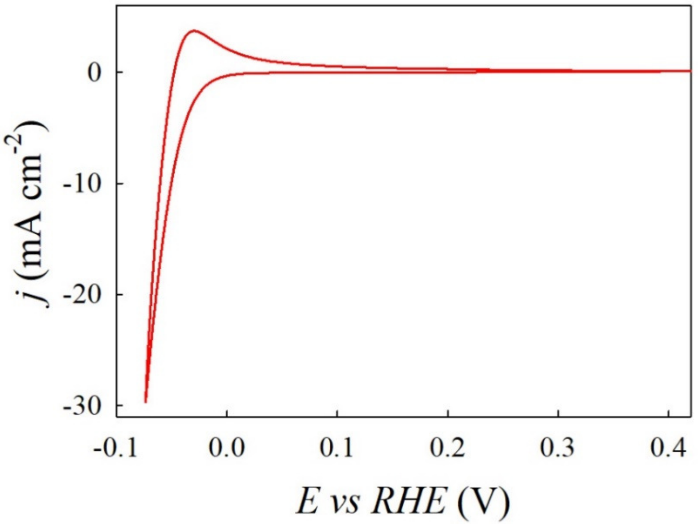

Figure 9.3: Quasi-cyclic voltammetry imposed together with the multisine signal during the DMFA experiment in $HClO_4$ (0.1 M) on Pt electrode. The range of potential is from 0.43 V to -0.07 V vs RHE.

At 0.43 V the current is very low, since this potential value is immediately prior to the beginning of the adsorption region. In this case, the adsorption peaks are impossible to distinguish, since they are completely hidden by the region of hydrogen evolution. The scan was reversed at -0.07 V, where the reaction rate of HER is sufficiently high to be investigated with DMFA, but not so high to cause consistent formation of bubbles at the surface of the electrode. The anodic peak is due to the re-oxidation of the gaseous hydrogen produced during the cathodic scan.

In the whole range of the quasi-CV, 1000 dynamic impedance spectra were simultaneously acquired in a frequency range from 8 Hz to 1 MHz. Figure 9.4 shows a selection of 204 impedance spectra (Nyquist plot representation) in the potential range between 0.16 V and -0.06 V; the region of the high frequencies is magnified in the inset.

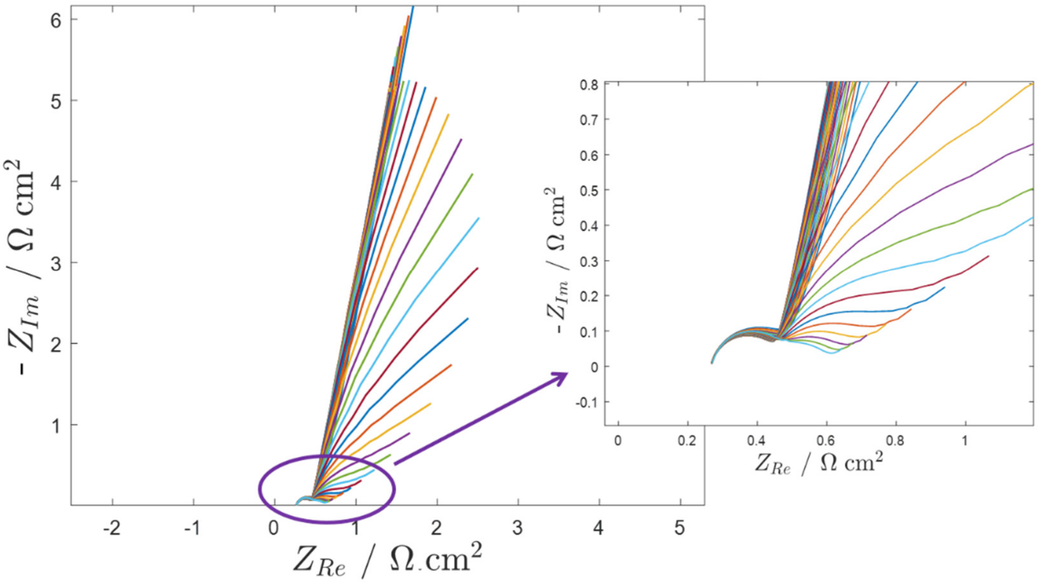

Figure 9.4: Nyquist plot of the dynamic impedance spectra recorded between 0.16 V and -0.06 V vs RHE. In the inset, a magnification of the spectra at high frequencies and at low -Z_{im} is shown.

All the impedance spectra, as well as the parameters that were extracted after the fitting procedure, are normalized by the electrode area. It is evident from figure 9.4 that the impedance spectrum gradually changes in shape as it switches from the hydrogen adsorption to the hydrogen evolution region.

The spectra at 0.154 V and at -0.066 V are shown in Fig. 9.5 for better clarity. In correspondence of 0.154 V, in the middle of the adsorption region, the electrode shows a capacitive behaviour, with a small semicircle at high frequencies related to the discharge of H^+ at the surface. As the HER proceeds, a second semicircle starts slowly to appear, as well as a line with 45° slope, which is indicative of diffusion, as already mentioned in Chapter 3, Section 3.3.2. The second semicircle can be reasonably attributed to the hydrogen evolution reaction. It should be noted that even if at -0.066 V the HER occurs at high rates, the first semicircle is still the dominating feature in the impedance spectrum, with the second semicircle almost hidden by the first one at the proceeding of the HER reaction.

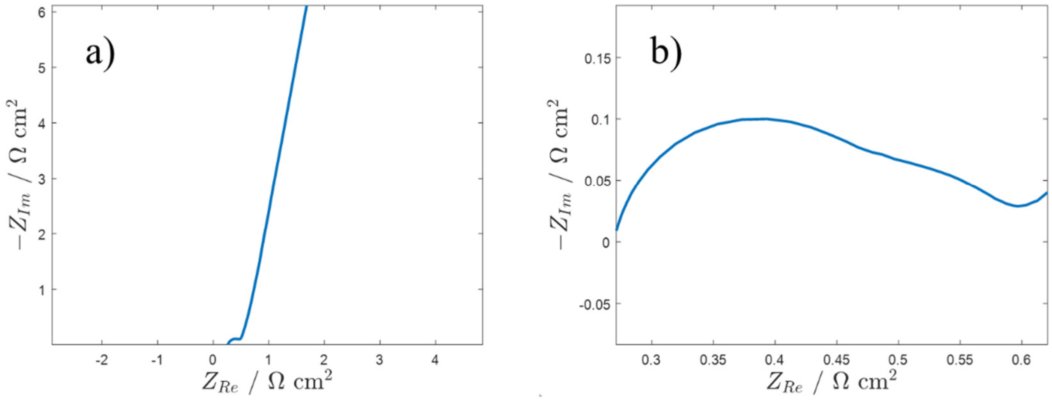

***Figure 9.5**:* (a) Nyquist plot of the dynamic impedance spectrum recorded at 0.154 V, in the middle of the adsorption region, and (b) Nyquist plot of the dynamic impedance spectrum recorded at -0.066 V, where the hydrogen evolution reaction occurs at moderately high rates. In this case, the presence of a second semicircle related to the hydrogen evolution can be observed.

In order to evaluate the mechanism of the reaction and to extract information on the electrochemical parameters involved, a fit of the experimental data was performed. Broadly speaking, there are two general approaches to fit impedance spectra: one consists in starting with some pre-existent equivalent circuits that seem to reasonably describe the electrochemical system under consideration, to eventually modify them and finally evaluating with a trial and error procedure which of them provides the best fit of the data. The equivalent circuit that gives the best fit is then used as a starting point to derive a proper physical model. The second approach is exactly the opposite and consists in modelling the expected reaction mechanism with physical parameters and deriving from the analytical model a circuit that is then used to fit the data, thus understanding if the starting model was adequate. The latter approach is the one used in this thesis. An analytical model, based on the balance laws that describe the processes of adsorption, hydrogen evolution and hydrogen oxidation, was developed assuming either the Volmer-Tafel or the Volmer-Heyrovsky mechanism. A detailed explanation on the derivation of the physical models can be found in Koster *et al.*, Supporting Info[84].

The equivalent circuit derived assuming a pure Volmer-Tafel mechanism is shown in Fig. 9.6. R_s represents the ohmic resistance of the ions in the electrolytic solution. C_{dl} is the double layer capacitance, representing the charging of the double layer as a consequence of the accumulation of ions at the interface. R_{ad} is the resistance related to the process of adsorption of hydrogen at the surface. W_{ad} is a Warburg element, and describes the diffusion of H^+ at the electrode to form adsorbed H_{ad}.

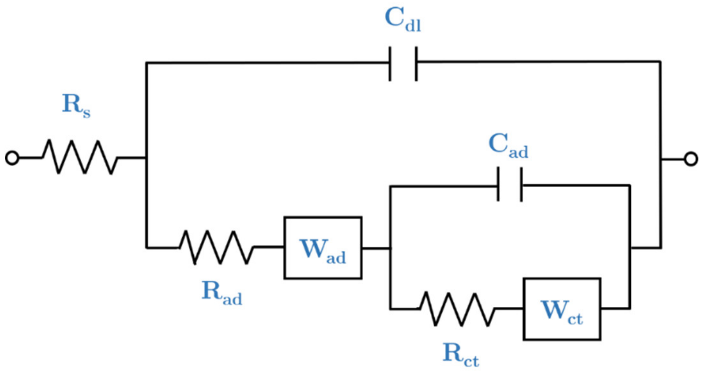

Figure 9.6: Equivalent circuit constructed starting from an analytical model describing the Volmer-Tafel mechanism.

As a consequence of the electro-adsorption of H^+, the accumulation of H_{ad} at the surface gives a contribution in terms of capacity (C_{ad}), in series with R_{ad} and W_{ad}. R_{ct} represents the resistance related to the recombination of two H_{ad} to give H_2. Finally, W_{ct} can either describe the diffusion of H^+ to the electrode or the diffusion of H_2 away from the surface.

The equation derived assuming a Volmer-Heyrovsky mechanism is showed in Fig. 9.7. In this case, the analytical model leads to a mathematical expression of the theoretical impedance, where the electrochemical parameters are made explicit. Unfortunately, deriving the corresponding equivalent circuit from it is not straightforward as for the Volmer-Tafel.

What changes in the Volmer-Heyrovsky model is that the Warburg element related to the diffusion of H^+ to the electrode and H_2 away from the electrode is split into two parameters ($\sigma_{ct,H}$ and σ_{ct,H_2}). Moreover, an additional capacitance is predicted (C_{ct}).

$$\frac{1}{Z}=\frac{2\left(R_{ct}+\frac{\sigma_{ct,H_2}}{\sqrt{i\omega}}+\frac{2}{i\omega C_{ct}}\right)+2\left(R_{ad}+\frac{2}{i\omega C_{ad}}\right)}{\left(R_{ad}+\frac{2\sigma_{ad}}{\sqrt{i\omega}}\right)\cdot\left(R_{ct}+\frac{\sigma_{ct,H_2}}{\sqrt{i\omega}}+\frac{2}{i\omega C_{ct}}\right)+\left(R_{ct}+\frac{2\sigma_{ct,H}+\sigma_{ct,H_2}}{\sqrt{i\omega}}\right)\cdot\left(R_{ad}+\frac{2}{i\omega C_{ad}}\right)}+i\omega C_{dl}$$

Figure 9.7: Expression of the theoretical impedance assuming a pure Volmer-Heyrovsky mechanism.

The fit of the data was performed with both the Volmer-Tafel equivalent circuit and the equation representing the Volmer-Heyrovsky mechanism. In both cases, the double layer capacitance C_{dl} was replaced with Q_{dl}, which is a constant phase element (CPE). The CPE element is commonly used to describe the non-ideal capacitive behaviour of some elements of the circuit, such as the double layer capacitance. The constant phase element is related to the capacitance by the following relation[184]:

$$C=\frac{Q}{\left(R_1^{-1}+R_2^{-1}\right)^{\frac{1-n}{n}}} \tag{9.3}$$

n can have values comprised between 0 and 1, where 1 represents the case of a pure capacitor; the *n* value was also fitted imposing a minimum value of 0.85 as constraint, since a strong deviation from the ideal conditions was not expected for this system. It should be noted that, even without imposing this constraint, the resulting *n* values were in any case always higher than 0.85. All the impedance spectra obtained in a selected potential range were fitted simultaneously, thus extracting for every spectrum the values of the electrochemical parameters and following their evolution with the potential. In order to follow their natural evolution, no constraint was used to force them to change smoothly (in other words, the smoothing factor was kept to zero). The two models presented above describe both the regions of adsorption and hydrogen evolution and were used to fit the impedance spectra in the whole range of potentials, including the region of adsorption (where the HER does not occur). This approach led to satisfying results and allowed catching the evolution of parameters even in the intermediate region, where the H_2 formation is not dominating.

The data were fitted in a potential range between 0.2 V and -0.07 V with both models, with a better goodness of fit being obtained with the Volmer-Tafel model. Anyway, the best fit was obtained using a modified Volmer-Tafel circuit, which is shown in Fig. 9.8.

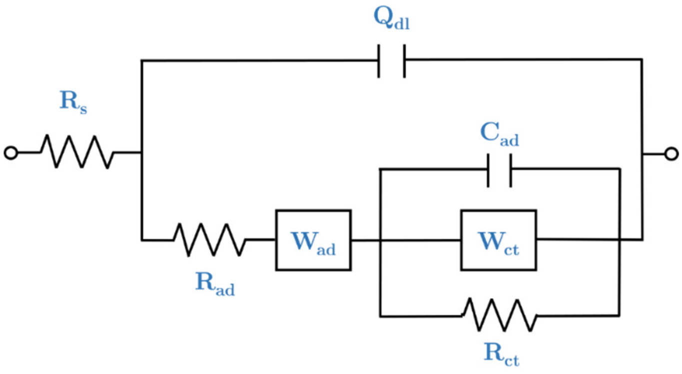

***Figure 9.8**:* Modified Volmer-Tafel circuit used for the fitting of the impedance spectra.

The essential difference between the circuit shown in Figure 9.8 and the unmodified Volmer-Tafel circuit (Figure 9.6) is that C_{ad}, W_{ct} and R_{ct} are all in parallel. The fitting results at 0.154 V and at -0.066 V obtained with the modified Volmer-Tafel circuit are shown in Fig. 9.9 (panel a and c, respectively) and compared to those obtained with the Volmer-Tafel circuit (panel b and d, respectively). It can be observed that while the simulated curves are similar for the two models in the adsorption region, they drastically differ in the hydrogen evolution region. This is also confirmed by the χ^2 value, which in this region is equal to $8 \cdot 10^{-5}$ for the modified Volmer-Tafel versus $1.6 \cdot 10^{-4}$ for the Volmer-Tafel. As evident from panel d in Fig. 9.9, in the hydrogen evolution region the Volmer-Tafel model predicts two distinct semicircles, one for the adsorption and one for the recombination of two H_{ad} to form H_2. The experimental data, anyway, do not show a clear semicircle but only a smooth one, and this is well represented by a parallel disposition of R_{ct} and W_{ct}.

The reasons behind this particular shape of the experimental data and the physical meaning of disposing R_{ct} and W_{ct} in parallel are still unknown. What is evident from the experimental data is that the electro-sorption of hydrogen plays an important role in the whole range of potentials, even at the most cathodic ones. Probably, some underlying process occurs that cannot be fully predicted by the theory of Volmer-Tafel. Considering the highest quality of the fit obtained with the modified Volmer-Tafel equivalent circuit, all the following data were fitted with this modality.

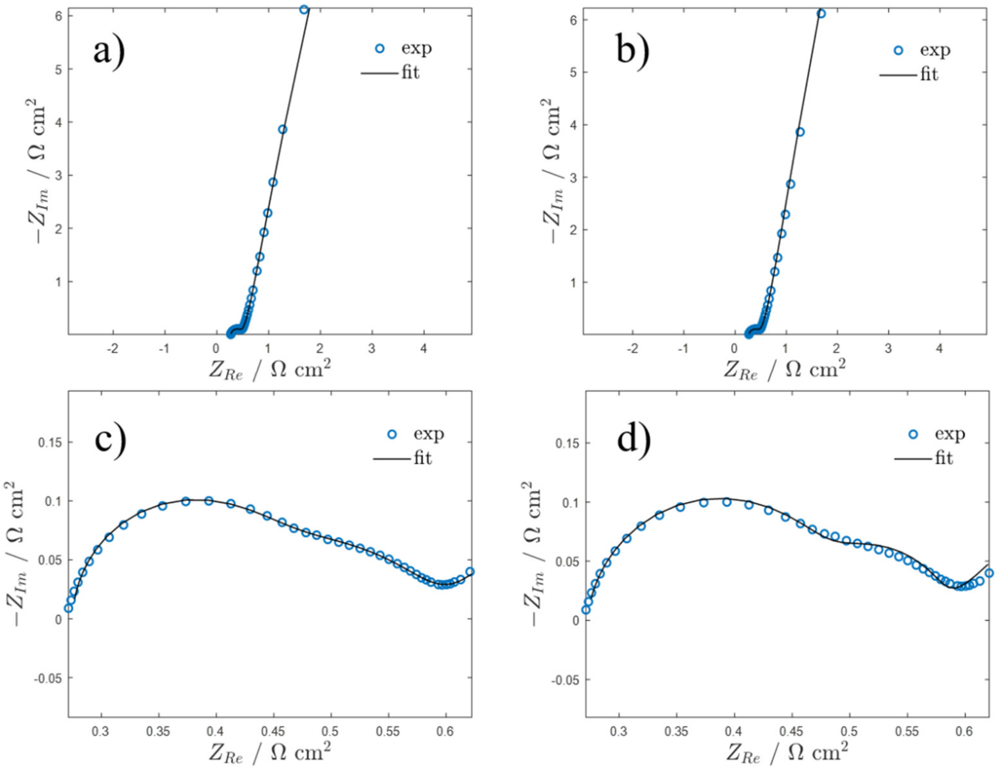

***Figure 9.9**:* Experimental (blue dots) and fitted (black lines) dynamic impedance spectra (a) at 0.154 V using the modified Volmer-Tafel equivalent circuit (b) at 0.154 V using the Volmer-Tafel equivalent circuit (c) at -0.066 V using the modified Volmer-Tafel equivalent circuit (d) at -0.066 V using the Volmer-Tafel equivalent circuit.

It should be noted that the order of magnitude of all the parameters, as well as their trend with the potential, are substantially the same using the two models, with the only difference that the modified Volmer-Tafel circuit leads to a smoother trend in the whole range of potentials, as it will be shown later in this Chapter. In order to ascertain if all the parameters included in the fit are significant in the whole range of potentials or if they could be removed, a t-test was performed. In the modified Volmer-Tafel model, the parameters are eight: R_s, Q_{dl}, n, R_{ad}, σ_{ad} C_{ad}, R_{ct} and σ_{ct}, where σ_{ad} and σ_{ct} are derived by the corresponding W elements. The fitting procedure returns a value of standard deviation for all the parameters at every potential, which can be used to calculate a t value in the whole potential range with this formula:

$$t_i = \frac{\sqrt{N_f} \cdot \hat{x_i}}{\sigma(x_i)} \tag{9.4}$$

Where $\hat{x_i}$ is the estimated value of a parameter i, σ is its standard deviation, and N_f is the number of frequencies of the impedance spectrum. The resulting t values were compared with the Student's t value calculated for the corresponding degrees of freedom (N_f-1) and for a confidence level of 95%. The comparison is shown in Fig. 9.10; the black dotted line indicates the Student's t value, while the other curves are the calculated t values for every parameter at each potential.

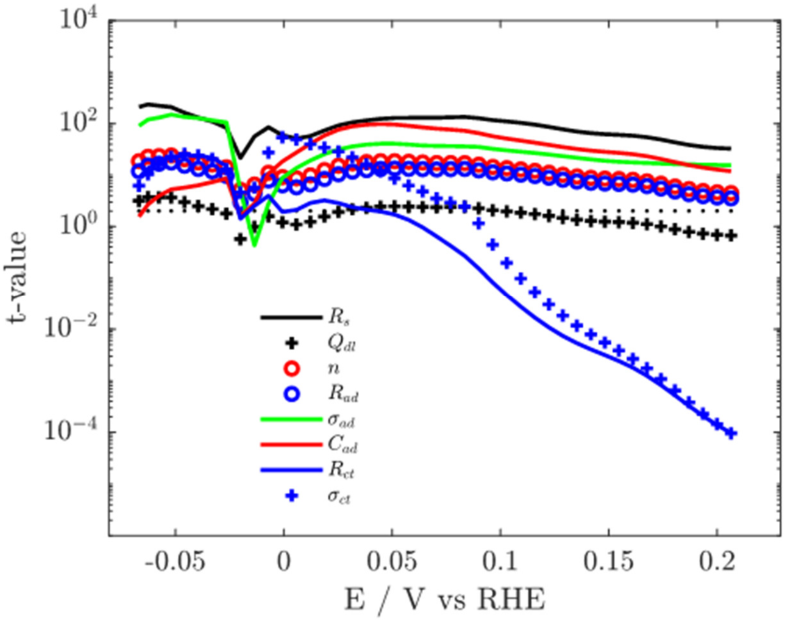

Figure 9.10: t-test for the fitting parameters of the dynamic impedance spectra in the whole range of potentials, obtained using the modified Volmer-Tafel circuit. The black dotted line indicates the Student's t value for N_f-1 degrees of freedom.

According to the t test, the significant t values are those higher than the calculated one. It can be observed that in the hydrogen evolution region all the estimated t values lie above the target, thus confirming that all parameters are significant and cannot be removed. As expected, R_{ct} and σ_{ct} lose their significance above 0.05 V, where the hydrogen evolution does not occur. It should be noted that also Q_{dl} lies slightly below the target value in some regions; however, this is quite frequent for the CPE elements and the fitting procedure with the modified Volmer-Tafel model can be considered valid in the whole potential range, as long as R_{ct} and $\sigma_{ct}$are not considered meaningful in the adsorption region.

Once obtained the best experimental procedure to acquire the data and once assessed the best model to fit the spectra, DMFA measurements were acquired again at different temperatures (5 °C, 10 °C, 15 °C, 20 °C, 25 °C and 30 °C) to study the evolution of the electrochemical parameters with potential and temperature. During these measurements, it was noticed that the impedance value tends to increase in the course of time; in all likelihood, this is due to the rapid modification of the Pt surface which begins immediately after the activation, as already pointed out by James *et al.*[180]. To overcome this problem and have therefore the highest surface reproducibility, the electrode was activated with 20 cycles between one measurement and the other, while changing the temperature in the meantime. The impedance spectra show a nice trend with temperature, as shown in Fig. 9.11, where all the spectra recorded at 0.154 V (in the middle of the adsorption region) are plotted. In fact, going from 5 °C (blue line) to 30 °C (light blue line) the semicircle corresponding to the adsorption process decreases in radius and intensity. The fitting of the dynamic impedance spectra was performed using the modified Volmer-Tafel model in a range from 0.207 V to -0.67 V, covering both the adsorption and the hydrogen evolution. The parameters obtained after the fitting procedure as a function of potential are shown in Fig. 9.12 and 9.13. The resistances and the Warburg elements were normalized through multiplication by the surface area of the electrode, while the capacitances were normalized by division by the surface area. In addition, the effective capacitance of the double layer was calculated from the values of Q_{dl} and n according to equation (9.4). The n values were all found to lie between 0.9 and 0.98, indicating that the behaviour of the CPE approaches that of a pure capacitor. R_{ad}, σ_{ad}, R_{ct} and σ_{ct} are plotted in logarithmic scale to better perceive their variation with the potential.

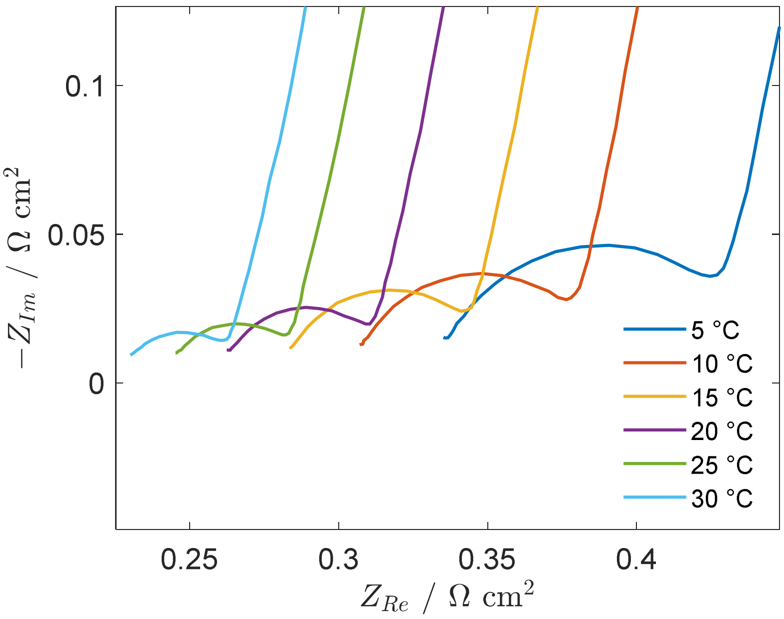

Figure 9.11: Impedance spectra at 0.154 V from 5° to 30° C; between the experiments at different temperatures, the electrode was always activated with 20 cycles.

The value of the electrolyte resistance extracted from the fit at 25 °C is *ca.* 480 kΩ, which is in complete agreement with the theoretical value calculated starting from the ionic conductivity. As expected, both the electrolyte resistance and the double-layer capacitance remain substantially constant in the whole range of potentials (Fig. 9.12 a and b). The electrolyte resistance shows a gradual decrease in passing from 5 °C to 30 °C, due to the higher mobility of the ions of the electrolyte at higher temperature. The double-layer capacitance also shows a slight dependence with temperature, with a lower capacitance at 30 °C with respect to that at 5 °C or 10 °C. This could be understood considering that the higher mobility of ions could slightly hinder the formation of the double layer at the electrode/electrolyte interface. Indeed, a dependence of temperature in this restricted range of temperature is not really expected by the theory, but it should be noted that the variations of C_{dl}, both as a function of potential and temperature, are very low (the highest variation is in the order of 10 μF) and should therefore be discussed with caution. The adsorption resistance (Fig. 9.12 c) shows a rapid decrease in the H^+ adsorption region, reaches a minimum around 0.1 V and then starts to increase again when the hydrogen evolution reaction starts.

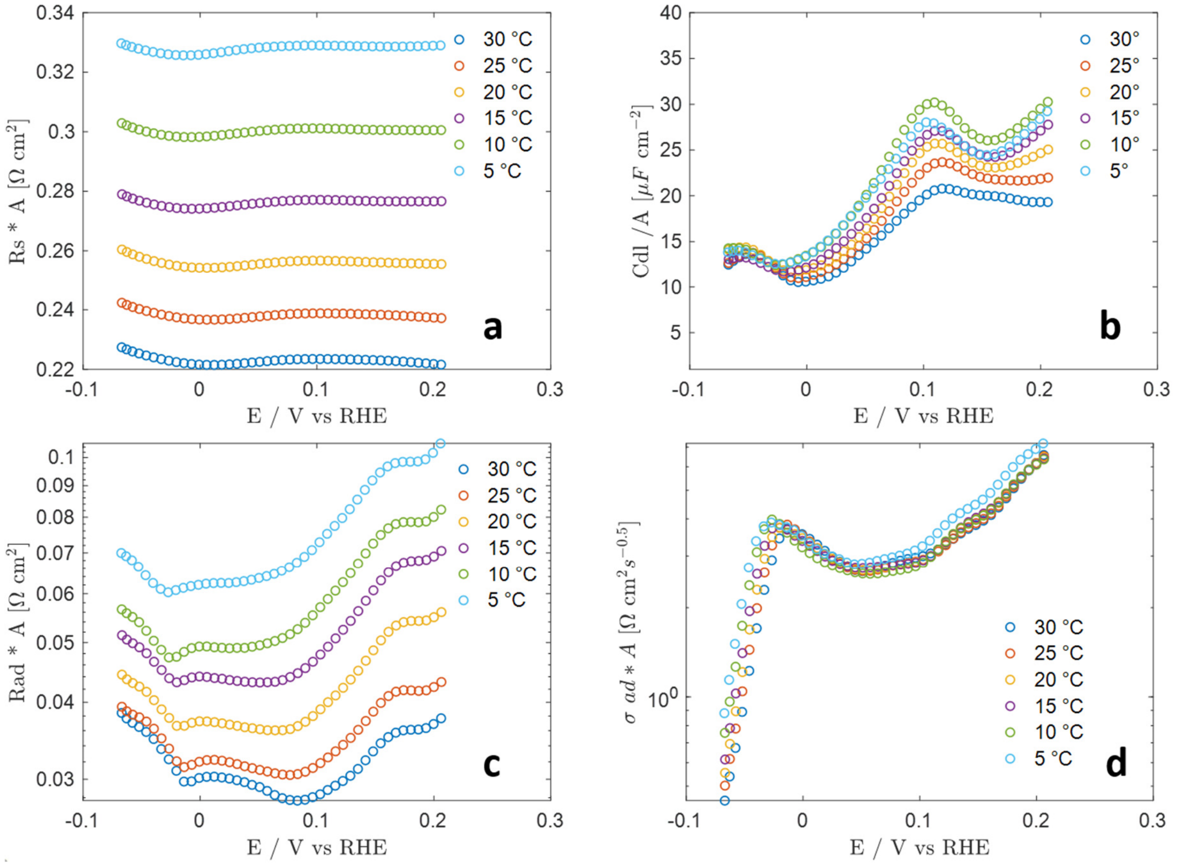

Figure 9.12: Electrochemical parameters obtained after the fitting procedure as a function of potential and temperature. (a) Electrolyte resistance, (b) double-layer capacitance, (c) adsorption resistance and (d) Warburg coefficient related to the adsorption process.

The minimum of the curve shifts to lower potential values at higher temperatures. The adsorption resistance can be defined as:

$$R_{ad} = \left(-F\frac{\partial r_{ad}}{\partial \Delta \Phi}\right)^{-1} \tag{9.5}$$

Where r_{ad} is the rate of the adsorption process, F is the Faraday constant and Φ the electric potential. In the adsorption region, under the assumption that the adsorption step is dominating the kinetics of the reaction, that the adsorption reaction is completely far to the right and that H_2 is formed in negligible quantity, the reaction rate can be expressed by the well-known Butler-Volmer equation.

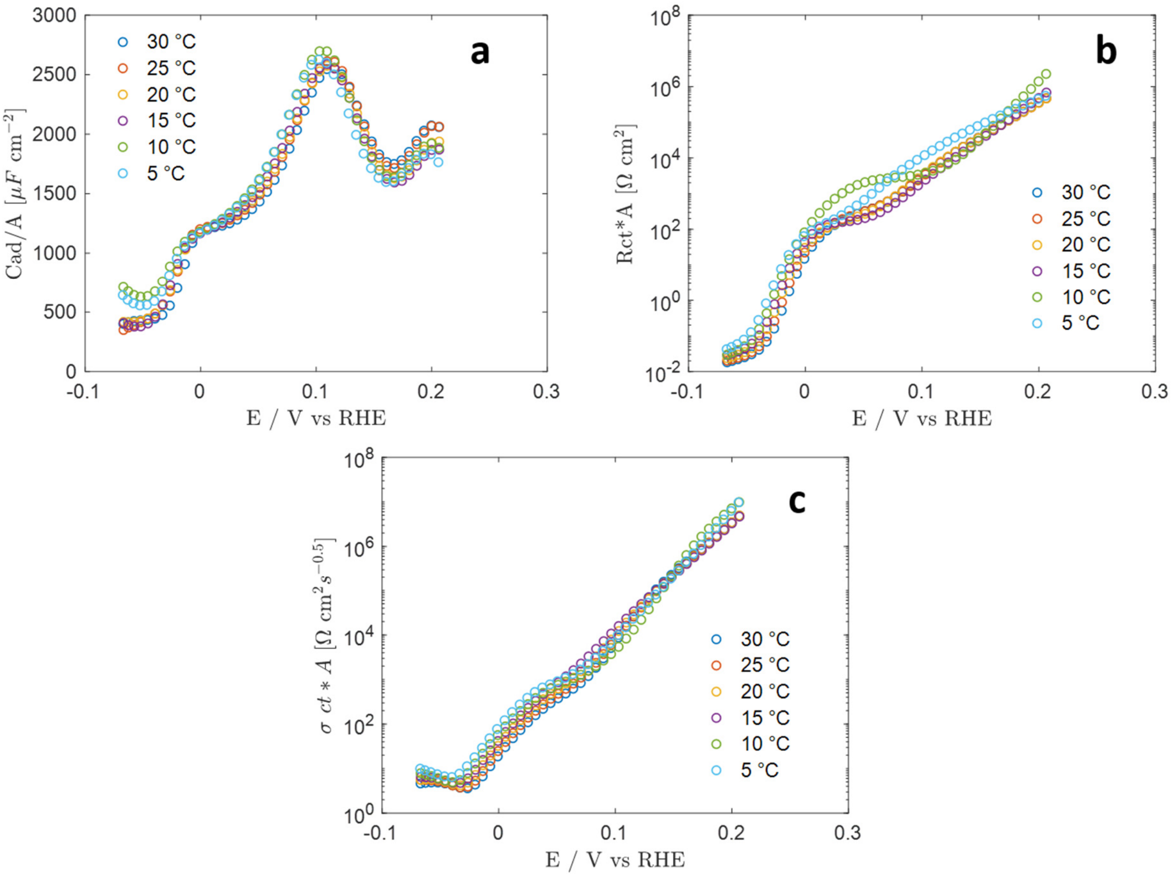

Figure 9.13: Electrochemical parameters obtained after the fitting procedure as a function of potential and temperature. (a) Capacity related to the adsorption process, (b) charge-transfer resistance for the hydrogen evolution and (c) Warburg coefficient related to the hydrogen evolution process.

As a result, the adsorption resistance shows an exponential dependence with the electric potential over the temperature, which explains its trend in the adsorption region: decreasing the potential (*i.e.* more cathodic values), the adsorption resistance decreases exponentially in turn. Moreover, R_{ad} is also dependent on θ_H, the occupancy of the adsorption sites. In fact, the HER reaction on Pt depends on the coverage of H_{ad} on the surface and this value can range between 0 and 1. This term θ_H is responsible for the broadening around the minimum value.

The adsorption resistance has an Arrhenius like-dependence with temperature, from which an activation energy can be extracted. For each temperature, the minimum of R_{ad} at *ca.* 0.1 V was selected, and the logarithm of its inverse was plotted against the inverse of the temperature expressed in Kelvin (see Fig. 9.14).

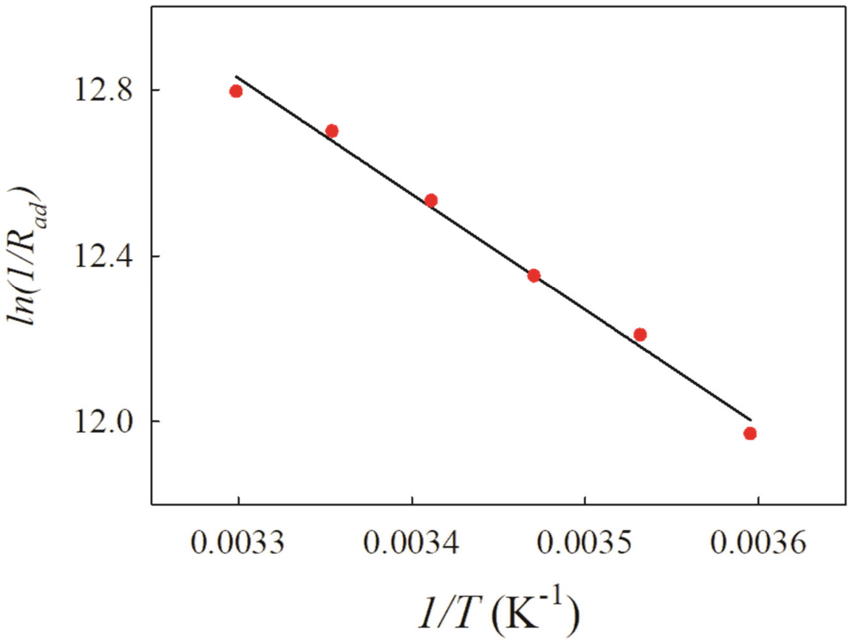

Figure 9.14: Arrhenius plot showing on the y-axis the logarithm of the inverse of adsorption resistance against the inverse of temperature on the x-axis. The experimental values are shown by the red dots while the regression line is in black.

The experimental data were then fitted through a linear regression, obtaining a value of R^2 of 0.996. The slope of the line, multiplied by the gas constant R, gives the activation energy, which resulted to be 0.24 eV.

σ_{ad} remains substantially constant in the entire adsorption region, and then decreases drastically below 0 V, when the hydrogen evolution starts (Fig. 9.12 d). Again, this behaviour can be derived using the Butler-Volmer equation, and considering that σ_{ad} can be written as:

$$\sigma_{ad} = \left(-F \cdot \frac{\partial r_{ad}}{\partial \Delta\Phi}\right)^{-1} \cdot \frac{\partial r_{ad}}{\partial c_H} \frac{1}{\sqrt{D_H}} \tag{9.6}$$

Where c_H is the concentration of H_{ad} at the surface of the electrode, and D is the diffusion constant of the involved species. In the adsorption region, the derivatives $\frac{\partial r_{ad}}{\partial \Delta\Phi}$ and $\frac{\partial r_{ad}}{\partial c_H}$ can be calculated by the Butler-Volmer equation and contain an exponential dependence on the potential. Assuming that the adsorption reaction is completely far to the right (considering therefore only one branch of the Butler-Volmer), the product of $\left(-F \cdot \frac{\partial r_{ad}}{\partial \Delta\Phi}\right)^{-1} \cdot \frac{\partial r_{ad}}{\partial c_H}$ removes the dependence of σ_{ad} on the potential, in agreement with the observed experimental trend.

In the adsorption region, the term σ_{ad} can be explained as a term of electrostatic repulsion of H^+ at the surface of the electrode. When the hydrogen starts evolving, however, the previous simplifications are not valid, and σ_{ad} is therefore expected to show a dependence on potential; in fact, as seen by Fig. 9.12, σ_{ad} has an abrupt decrease just below 0 V.

Regarding the dependence with temperature, it can be noted that its value starts decreasing at less cathodic potentials as the temperature is increased. In the adsorption region, instead, σ_{ad} is almost constant at all temperatures. Strictly speaking, a more complicated model should be developed to better explain this behaviour under HER conditions, since the Butler-Volmer equation cannot be considered valid when a reaction is governed by diffusion.

The adsorption capacitance (Fig. 9.13 a) shows a curious trend with potential. In the adsorption region the trend is rather expected, with C_{ad} showing a maximum around 0.1 V (in correspondence of the minimum of R_{ad}) and then decreasing again; also in this case, the broadening around 0.1 V can be attributed to the term θ_H. Below 0 V, anyway, C_{ad} shows a new sudden decrease, before stabilizing around 500 μF. The reason behind this behaviour is not obvious; in principle, it could be explained by a depletion of adsorbed H_{ad} at the surface of Pt. Nevertheless, this would be expected at more cathodic potentials, where the rate constant related to hydrogen evolution is higher; moreover, if this was the case, the decrease of C_{ad} should be coupled to a parallel increase of R_{ct}, which is not observed. The second hypothesis is that a second group of adsorption hydrogens becomes active towards the hydrogen evolution; it has already been mentioned that while H_{UPD} is the species adsorbed before 0 V, it is has been proposed that H_{OPD} could be the species direct responsible for the HER, due to the weaker bond which this species forms with platinum[183]. Therefore, it is not excluded that this drop may be related to a change of nature of the adsorbed hydrogen from H_{UPD} to H_{OPD}.

Regarding the dependence on temperature, C_{ad} does not show a clear trend with temperature: the values at 5 °C and 10 °C are only slightly higher than those at higher temperatures.

The resistance R_{ct} and the Warburg coefficient σ_{ct} related to H_2 evolution (Fig. 9.13 b and c, respectively) show a similar behaviour. As expected, they start from a high value in the adsorption region, they then exponentially decrease during all the process of adsorption, until they stabilize to constant values at the lowest potentials, where the hydrogen evolution reaction starts. Both parameters show only a slight trend with temperature.

9.4 Final remarks

In the present work, dynamic impedance spectroscopy has been successfully applied in the field of electrocatalysis, demonstrating that this technique can be considered as a new and powerful strategy for the investigation of reaction mechanisms. As a test case, DMFA was here applied to study the hydrogen evolution reaction catalysed by platinum. A quasi-CV, in a potential range covering both adsorption and hydrogen evolution, was superimposed to a multisine signal; as a result, two thousand impedance spectra were acquired in the selected potential range. The spectra in a selected potential range were all fitted simultaneously with an equivalent circuit representing a slightly modified Volmer-Tafel mechanism; after the fitting procedure, the trend of relevant electrochemical parameters with potential and temperature was found. In particular, the values of the electrolyte resistance, the double-layer capacitance, the adsorption resistance and capacitance, the charge-transfer resistance and the Warburg coefficients were plotted as a function of potential at 5, 10, 15, 20, 25 and 30°C. The trend of each parameter was considered, in order to see if it is predictable by the theory and consistent with a Volmer-Tafel model. In the present thesis, the trend of the parameters has been evaluated only qualitatively or starting from the Butler-Volmer equation. However, the future goal is to consider each parameter in order to rationalize and explain in detail its trend with potential and temperature. In particular, it would be interesting to observe if the trends could be explained assuming a pure Volmer-Tafel mechanism, or if the theory fails in giving them a full description, considering that the best fit is not obtained starting from the equivalent circuit derived from the pure Volmer-Tafel reaction. More work is therefore needed for a full understanding of the present data.

Finally, it should be noted that through DMFA it is possible to get a huge number of impedance spectra during a single voltammogram. A future goal consists in combining DMFA and XAS experiments in a single experiment, *e.g.* employing FEXRAV, dispersive XAS or quick-EXAFS, which allow recording the absorption coefficient or even full spectra in few seconds. This would give the unique possibility to combine the complementary information achievable from impedance spectroscopy and X-ray absorption spectroscopy.

Conclusions

In this thesis, it has been demonstrated how *operando* XAS (with hard and soft X-rays) and DMFA can be implemented as fundamental tools for the understanding of the mechanism of electrochemical reactions.

Most of the attention has been devoted to the hydrogen evolution reaction (HER) and the oxygen evolution reaction (OER) which are at the basis of photocatalytic water splitting or, when reversed, of fuel cell technology. These reactions are promoted by (photo) electrocatalysts, which are expected to undergo changes in their electronic and structural properties during the reaction course. *Operando* X-ray Absorption Spectroscopy proved to be an ideal technique to probe these modifications. The electrodes under investigation were studied in a properly-designed electrochemical cell that simulated to a high degree the real operating condition of the reaction; this arrangement, therefore, permitted the coupling of spectroscopic investigation to electrochemical measurements such as chronoamperometry or cyclic voltammetry. In particular, FeOOH, WO_3, Cu_2O/CuO based materials and the α-Fe_2O_3/NiO_x photoarchitecture were studied under *operando* conditions. The experiments were carried out at the European Synchrotron Radiation Facility (ESRF), in Grenoble.

FeOOH-based electrodes were investigated during hydrogen evolution: the structure of the iron(II)-species active during HER was determined and found to be strictly related to the sulphate green rust structure. Attention was then focused on electrodes employed in the photocatalytic water splitting process, in particular on WO_3 photoanodes, copper oxides photocathodes and on α-Fe_2O_3/NiO_x photo-architecture. Differential acquisition of spectra in dark and light was employed as a strategy to catch the subtle differences expected in the material between dark and light conditions. Moreover, Fixed Energy X-ray Absorption Voltammetry (FEXRAV) was largely employed to directly monitor in real time the electronic changes occurring in the material while sweeping the potential or, alternatively, while switching on and off the light. These two strategies allowed, for instance, to see the effect of illumination on WO_3, where the lifetime of the photogenerated carriers is expected to be low, and to directly observe the presence of a hole transfer between α-Fe_2O_3 and NiO_x, thus clarifying the role of the overlayer in this photosystem. Moreover, in the case of copper oxides, it was noticed that while Cu_2O undergoes an irreversible modification leading to complete loss of activity, CuO-Cu_2O composites show an outstanding stability. The approach here employed allowed for a more complete understanding of both behaviours.

Finer details concerning the reaction mechanisms in these photoactive materials could be obtained by *operando* XAS. In particular, the generation and the fate of the photogenerated carriers were directly inspected. In all cases, it was clearly observed that the photogenerated carriers are able to localize in the material, leading to consistent changes in the density of empty states of the metal, and in the majority of cases also to changes in the metal oxidation state, causing the formation of unusual oxidation states like Cu(III) or Ni(IV).

As a further advancement, soft-XAS and DMFA were exploited as new strategies for the study of reaction mechanisms in electrochemistry. Usually, soft-XAS experiments are limited to a surface science approach; in fact, vacuum limitations combined to the low penetration depth of soft X-rays have severely hindered the development of *operando* soft-XAS. In this thesis, a cell configuration available at the Elettra Synchrotron in Trieste was successfully employed for a soft-XAS *operando* experiment at ambient pressure. This allowed studying the reactivity of SnO_2 towards reducing gaseous species, demonstrating the formation of a thin surface layer of SnO. These experiments combined to DFT modelling allowed to establish a mechanism for the reactive adsorption of hydrocarbons.

Finally, dynamic multi-frequency analysis (DMFA) was considered. DMFA allows acquiring impedance spectra in dynamic conditions, while the electrode is cycled according to a cyclic voltammetry. This means that for every point of the cyclic voltammetry, an impedance spectrum can be obtained, thus allowing reconstruction of the exact evolution of relevant electrochemical parameters as a function of the potential. In this thesis, DMFA was successfully employed to study the hydrogen evolution reaction catalysed by platinum, where a modified Volmer-Tafel circuit was used to fit the spectra and extract the kinetic parameters. As a future perspective, DMFA could be coupled to dispersive XAS, quick EXAFS or FEXRAV in a single experiment, thus allowing to simultaneously obtain electrochemical and spectroscopic information for a deep and exhaustive understanding of the mechanism of a reaction.

As a final remark, it should be noted that the precise identification of intermediates and active sites during the course of heterogeneous reactions is a fundamental piece of additional knowledge that can be exploited for a rational synthesis and design of new electrode materials with increased performances. The aim of future work will be therefore to extend the strategies here adopted to other (photo)electrochemical systems or to heterogeneous catalysts with the final goal of developing tailored materials.

Bibliography

1. Internal Energy Agency. Key world energy trends: excerpt from world energy balances. (2017).
2. Badwal, S. P. S., Giddey, S. S., Munnings, C., Bhatt, A. I. & Hollenkamp, A. F. Emerging electrochemical energy conversion and storage technologies. *Front. Chem.* **2**, 1–28 (2014).
3. Kim, S. W., Seo, D. H., Ma, X., Ceder, G. & Kang, K. Electrode materials for rechargeable sodium-ion batteries: Potential alternatives to current lithium-ion batteries. *Adv. Energy Mater.* **2**, 710–721 (2012).
4. Placke, T., Kloepsch, R., Dühnen, S. & Winter, M. Lithium ion, lithium metal, and alternative rechargeable battery technologies: the odyssey for high energy density. *J. Solid State Electrochem.* **21**, 1939–1964 (2017).
5. Zeng, X., Li, J. & Singh, N. Recycling of spent lithium-ion battery: A critical review. *Crit. Rev. Environ. Sci. Technol.* **44**, 1129–1165 (2014).
6. Maeda, K. & Domen, K. Photocatalytic water splitting: Recent progress and future challenges. *J. Phys. Chem. Lett.* **1**, 2655–2661 (2010).
7. O'Hayre, R., Cha, S.-W., Colella, W. & Prinz, F. B. *Fuel Cells Fundamentals*. (John Wiley & Sons, 2016).
8. Copeland, S. On serendipity in science: discovery at the intersection of chance and wisdom. *Synthese* **196**, 2385–2406 (2019).
9. Zhong, L., Chen, D. & Zafeiratos, S. A mini review of in situ near-ambient pressure XPS studies on non-noble, late transition metal catalysts . *Catal. Sci. Technol.* **9**, 3851–3867 (2019).
10. Mobilio, S., Boscherini, F. & Meneghini, C. *Synchrotron radiation*. (Springer-Verlag Berlin Heidelberg, 2015).
11. Thompson, A. J. *X-ray data booklet*. (Lawrence Berkeley National Laboratory, 2009).
12. Newville, M. Fundamentals of XAFS Contents. (2004).
13. Minguzzi, A. & Ghigna, P. *X-Ray Absorption Spectroscopy in Electrochemistry*. (CRC Press-

Taylor and Francis group: Boca Raton, FL, USA, 2017).

14. Seah, M. P. An accurate and simple universal curve for the energy-dependent electron inelastic mean free path † *Surf. Interface Anal.* **44**, 497–503 (2012).

15. Benfatto, M. & Della Longa, S. Geometrical fitting of experimental XANES spectra by a full multiple-scattering procedure. *J. Synchrotron Radiat.* **8**, 1087–1094 (2001).

16. Smolentsev, G. & Soldatov, A. Quantitative local structure refinement from XANES: Multi-dimensional interpolation approach. *J. Synchrotron Radiat.* **13**, 19–29 (2006).

17. Jafari, T. *et al.* Photocatalytic water splitting - The untamed dream: A review of recent advances. *Molecules* **21**, (2016).

18. Strmcnik, D., Lopes, P. P., Genorio, B., Stamenkovic, V. R. & Markovic, N. M. Design principles for hydrogen evolution reaction catalyst materials. *Nano Energy* **29**, 29–36 (2016).

19. Tafel, J. Über die Polarisation bei kathodischer Wasserstoffentwicklung. *Zeitschrift für Phys. Chemie* **50U**, (1905).

20. Heyrovsky, J. A theory of overpotential. *Recl. des Trav. Chim. des Pays-Bas* **46**, 582–585 (1927).

21. Schmickler, W. & Santos, E. *Interfacial Electrochemistry*. (Springer-Verlag Berlin Heidelberg, 2010). doi:10.1007/978364204937-8_14

22. Trasatti, S. Work function, electronegativity, and electrochemical behaviour of metals: III. Electrolytic hydrogen evolution in acid solutions. *J. Electroanal. Chem. Interfacial Electrochem.* **39**, 163–184 (1972).

23. Quaino, P., Juarez, F., Santos, E. & Schmickler, W. Volcano plots in hydrogen electrocatalysis-uses and abuses. *Beilstein J. Nanotechnol.* **5**, 846–854 (2014).

24. Laursen, A. B. *et al.* Electrochemical hydrogen evolution: Sabatiers principle and the volcano plot. *J. Chem. Educ.* **89**, 1595–1599 (2012).

25. Suen, N. T. *et al.* Electrocatalysis for the oxygen evolution reaction: Recent development and future perspectives. *Chem. Soc. Rev.* **46**, 337–365 (2017).

26. Conway, B. E. Electrochemical oxide film formation at noble metals as a surface-chemical process. *Prog. Surf. Sci.* **49**, 331–452 (1995).

27. Hong, W. T. *et al.* Toward the rational design of non-precious transition metal oxides for

oxygen electrocatalysis. *Energy Environ. Sci.* **8**, 1404–1427 (2015).

28. Cook, T. R. *et al.* Solar energy supply and storage for the legacy and nonlegacy worlds. *Chem. Rev.* **110**, 6474–6502 (2010).

29. Trasatti, S. Electrocatalysis by oxides — Attempt at a unifying approach. *J. Electroanal. Chem. Interfacial Electrochem.* **111**, 125–131 (1980).

30. Trasatti, S. Electrocatalysis in the anodic evolution of oxygen and chlorine. *Electrochim. Acta* **29**, 1503–1512 (1984).

31. Dau, H. *et al.* The Mechanism of Water Oxidation: From Electrolysis via Homogeneous to Biological Catalysis. *ChemCatChem* **2**, 724–761 (2010).

32. Yan, Y., Xia, B. Y., Zhao, B. & Wang, X. A review on noble-metal-free bifunctional heterogeneous catalysts for overall electrochemical water splitting. *J. Mater. Chem. A* **4**, 17587–17603 (2016).

33. Liao, C. H., Huang, C. W. & Wu, J. C. S. Hydrogen production from semiconductor-based photocatalysis via water splitting. *Catalysts* **2**, 490–516 (2012).

34. Walter, M. G. *et al.* Solar Water Splitting cells. *Chem. Rev.* 6446–6473 (2010).

35. Steier, L. *et al.* Understanding the role of underlayers and overlayers in thin film hematite photoanodes. *Adv. Funct. Mater.* **24**, 7681–7688 (2014).

36. Shi, H., Lercher, J. A. & Yu, X. Y. Sailing into uncharted waters: Recent advances in the in situ monitoring of catalytic processes in aqueous environments. *Catal. Sci. Technol.* **5**, 3035–3060 (2015).

37. Russell, A. E. & Rose, A. X-ray absorption spectroscopy of low temperature fuel cell catalysts. *Chem. Rev.* **104**, 4613–4635 (2004).

38. Bazin, D., Sayers, D., Rehr, J. J. & Mottet, C. Numerical Simulation of the Platinum L $_{\mathrm{III}}$ Edge White Line Relative to Nanometer Scale Clusters . *J. Phys. Chem. B* **101**, 5332–5336 (2002).

39. Mukerjee, S. & McBreen, J. Effect of particle size on the electrocatalysis by carbon-supported Pt electrocatalysts: An in situ XAS investigation. *J. Electroanal. Chem.* **448**, 163–171 (1998).

40. Ramaker, D. E. & Koningsberger, D. C. The atomic AXAFS and Delta(mu) XANES techniques as applied to heterogeneous catalysis and electrocatalysis. *Phys. Chem. Chem. Phys.* **12**, 5514–5534 (2010).

41. Teliska, M., O'Grady, W. E. & Ramaker, D. E. Determination of H Adsorption Sites on Pt/C Electrodes in $HClO_4$ from Pt L_{23} X-ray Absorption Spectroscopy . *J. Phys. Chem. B* **108**, 2333–2344 (2004).

42. Teliska, M., O'Grady, W. E. & Ramaker, D. E. Determination of O and OH adsorption sites and coverage in situ on Pt electrodes from Pt L_{23} X-ray absorption spectroscopy. *J. Phys. Chem. B* **109**, 8076–8084 (2005).

43. Ramaker, D. E., Korovina, A., Croze, V., Melke, J. & Roth, C. Following ORR intermediates adsorbed on a Pt cathode catalyst during break-in of a PEM fuel cell by in operando X-ray absorption spectroscopy. *Phys. Chem. Chem. Phys.* **16**, 13645–13653 (2014).

44. Mansour, A. N., Cook, J. W. & Sayers, D. E. Quantitative technique for the determination of the number of unoccupied d-electron states in a platinum catalyst using the $L_{2,3}$ X-ray absorption edge spectra. *J. Phys. Chem.* **88**, 2330–2334 (1984).

45. Roth, C. *et al.* Determination of O[H] and CO coverage and adsorption sites on PtRu electrodes in an operating PEM fuel cell. *J. Am. Chem. Soc.* **127**, 14607–14615 (2005).

46. Rose, A. *et al.* In situ Ru K-edge EXAFS of CO adsorption on a Ru modified Pt/C fuel cell catalyst. *Electrochim. Acta* **54**, 5262–5266 (2009).

47. Weir, M. G., Myers, V. S., Frenkel, A. I. & Crooks, R. M. In situ X-ray absorption analysis of ~1.8 nm dendrimer-encapsulated Pt nanoparticles during electrochemical CO oxidation. *ChemPhysChem* **11**, 2942–2950 (2010).

48. Myers, V. S., Frenkel, A. I. & Crooks, R. M. In situ structural characterization of platinum dendrimer-encapsulated oxygen reduction electrocatalysts. *Langmuir* **28**, 1596–1603 (2012).

49. Hüppauff, M. Valency and Structure of Iridium in Anodic Iridium Oxide Films. *J. Electrochem. Soc.* **140**, 598 (1993).

50. Pauporté, T., Aberdam, D., Hazemann, J.-L., Faure, R. & Durand, R. X-ray absorption in relation to valency of iridium in sputtered iridium oxide films. *J. Electroanal. Chem.* **465**, 88–95 (1999).

51. Mo, Y. *et al.* In situ iridium L_{III}-edge X-ray absorption and surface enhanced Raman spectroscopy of electrodeposited iridium oxide films in aqueous electrolytes. *J. Phys. Chem. B* **106**, 3681–3686 (2002).

52. Minguzzi, A. *et al.* Observing the oxidation state turnover in heterogeneous iridium-based water oxidation catalysts. *Chem. Sci.* **5**, 3591–3597 (2014).

53. Minguzzi, A. *et al.* Observation of charge transfer cascades in α-Fe_2O_3/IrO_x photoanodes by operando X-ray absorption spectroscopy. *Phys. Chem. Chem. Phys.* **19**, 5715–5720 (2017).

54. McKeown, D. A. *et al.* Structure of Hydrous Ruthenium Oxides: Implications for Charge Storage. *J. Phys. Chem. B* **103**, 4825–4832 (2002).

55. Mo, Y., Bae, I. T., Sarangapani, S. & Scherson, D. A. In situ Ru K-edge X-ray absorption spectroscopy of a high-area ruthenium dioxide electrode in a Nafion-based supercapacitor environment. *J. Solid State Electrochem.* **7**, 572–575 (2003).

56. Minguzzi, A. *et al.* Fixed energy X-ray absorption voltammetry. *Anal. Chem.* **85**, 7009–7013 (2013).

57. Kanan, M. W. & Nocera, D. G. In situ Formation of an Oxygen-Evolving Catalyst in Neutral Water Containing Phosphate and Co^{2+} *Science* **321**, 1072–1076 (2008).

58. Kanan, M. W. *et al.* Structure and valency of a cobalt-phosphate water oxidation catalyst determined by in situ X-ray spectroscopy. *J. Am. Chem. Soc.* **132**, 13692–13701 (2010).

59. Risch, M. *et al.* Water oxidation by amorphous cobalt-based oxides: in-situ tracking of redox transitions and mode of catalysis. *Energy Environ. Sci.* **8**, 661–674 (2015).

60. Fracchia, M., Ghigna, P., Vertova, A., Rondinini, S. & Minguzzi, A. Time-Resolved X-ray Absorption Spectroscopy in (Photo)Electrochemistry. *Surfaces* **1**, 138–150 (2018).

61. Nilsson, A. *et al.* Catalysis in real time using X-ray lasers. *Chem. Phys. Lett.* **675**, 145–173 (2017).

62. Achilli, E. *et al.* 3D-printed photo-spectroelectrochemical devices for in situ and in operando X-ray absorption spectroscopy investigation. *J. Synchrotron Radiat.* **23**, 622–628 (2016).

63. D'Acapito, F. *et al.* The LISA beamline at ESRF. *J. Synchrotron Radiat.* **26**, 551–558 (2019).

64. Tougerti, A. *et al.* Synergy between XANES Spectroscopy and DFT to Elucidate the Amorphous Structure of Heterogeneous Catalysts: TiO_2-Supported Molybdenum Oxide Catalysts. *Angew. Chemie - Int. Ed.* **52**, 6440–6444 (2013).

65. Pankin, I. A. *et al.* DFT-assisted XANES simulations to discriminate different monomeric Cu^{II} species in CHA catalysts. *Radiat. Phys. Chem.* 108510 (2019). doi:10.1016/j.radphyschem.2019.108510

66. Penfold, T. J. *et al.* Simulations of X-ray absorption spectra: The effect of the solvent. *Phys. Chem. Chem. Phys.* **14**, 9444–9450 (2012).

67. D'Angelo, P., Roscioni, O. M., Chillemi, G., Longa, S. Della & Benfatto, M. Detection of second hydration shells in ionic solutions by XANES: Computed spectra for Ni^{2+} in water based on molecular dynamics. *J. Am. Chem. Soc.* **128**, 1853–1858 (2006).

68. Binsted, N. & Hasnain, S. S. State-of-the-Art Analysis of Whole X-ray Absorption Spectra. *J. Synchrotron Radiat.* **3**, 185–196 (1996).

69. Achilli, E. *et al.* Structure and Stability of a Copper(II) Lactate Complex in Alkaline Solution: A Case Study by Energy-Dispersive X-ray Absorption Spectroscopy. *Inorg. Chem.* **56**, 6982–6989 (2017).

70. Schwanke, C., Golnak, R., Xiao, J. & Lange, K. M. Electrochemical flowcell for in-situ investigations by soft x-ray absorption and emission spectroscopy. *Rev. Sci. Instrum.* **85**, (2014).

71. Bora, D. K. *et al.* An ultra-high vacuum electrochemical flow cell for in situ / operando soft X-ray spectroscopy study . *Rev. Sci. Instrum.* **85**, 043106 (2014).

72. Roper, M. D., van der Laan, G., Flaherty, J. V. & Padmore, H. A. Soft x-ray spectroscopy in atmospheric pressure helium. *Rev. Sci. Instrum.* **63**, (1992).

73. Tamenori, Y. Electron yield soft X-ray photoabsorption spectroscopy under normal ambient-pressure conditions. *J. Synchrotron Radiat.* **20**, 419–425 (2013).

74. Castán-Guerrero, C. *et al.* A reaction cell for ambient pressure soft x-ray absorption spectroscopy. *Rev. Sci. Instrum.* **89**, (2018).

75. Schwanke, C., Xi, L. & Lange, K. M. A soft XAS transmission cell for operando studies. *J. Synchrotron Rad.* **23**, 1390–1394 (2016).

76. Zheng, X. *et al.* Theory-driven design of high-valence metal sites for water oxidation confirmed using in situ soft X-ray absorption. *Nat. Chem.* **10**, 149–154 (2018).

77. Battistel, A., Du, G. & La Mantia, F. On the Analysis of Non-stationary Impedance Spectra. *Electroanalysis* **28**, 2346–2353 (2016).

78. Orazem, M. E. & Tribollet, B. *Electrochemical Impedance Spectroscopy- 2nd Edition*. (2017).

79. Ragoisha, G. A. Potentiodynamic Electrochemical Impedance Spectroscopy for Underpotential Deposition Processes. *Electroanalysis* **27**, 855–863 (2015).

80. Sacci, R. L., Seland, F. & Harrington, D. A. Dynamic electrochemical impedance spectroscopy, for electrocatalytic reactions. *Electrochim. Acta* **131**, 13–19 (2014).

81. Darowicki, K. & Ślepski, P. Dynamic electrochemical impedance spectroscopy of the first order electrode reaction. *J. Electroanal. Chem.* **547**, 1–8 (2003).

82. Koster, D. Nonstationary Impedance Measurements in Forced and Natural Dynamic Conditions using Dynamic Multi-Frequency Analysis. (University of Bremen, 2019).

83. Koster, D., Du, G., Battistel, A. & La Mantia, F. Dynamic impedance spectroscopy using dynamic multi-frequency analysis: A theoretical and experimental investigation. *Electrochim. Acta* **246**, 553–563 (2017).

84. Koster, D., Zeradjanin, A. R., Battistel, A. & La Mantia, F. Extracting the kinetic parameters of the hydrogen evolution reaction at Pt in acidic media by means of dynamic multi-frequency analysis. *Electrochim. Acta* **308**, 328–336 (2019).

85. Fracchia, M. *et al.* α- and γ-FeOOH: Stability, Reversibility, and Nature of the Active Phase under Hydrogen Evolution. *ACS Appl. Energy Mater.* **1**, 1716–1725 (2018).

86. Jolivet, J. *et al.* Iron Oxide Chemistry . From Molecular Clusters to Extended Solid Networks Iron oxide chemistry . From molecular clusters to extended solid networks. *Chem Commun.* 481–487 (2004).

87. Kim, W. *et al.* A new method for the identification and quantification of magnetite-maghemite mixture using conventional X-ray diffraction technique. *Talanta* **94**, 348–352 (2012).

88. Hedenstedt, K., Simic, N., Wildlock, M. & Ahlberg, E. Kinetic study of the hydrogen evolution reaction in slightly alkaline electrolyte on mild steel, goethite and lepidocrocite. *J. Electroanal. Chem.* **783**, 1–7 (2016).

89. Hedenstedt, K., Gomes, A. S. O., Busch, M. & Ahlberg, E. Study of Hypochlorite Reduction Related to the Sodium Chlorate Process. *Electrocatalysis* **7**, 326–335 (2016).

90. Stratmann, M. & Hoffmann, K. In situ Mossbauer spectroscopy study of reactions within rust layers. *Corros. Sci.* **29**, 1329–1252 (1989).

91. Monnier, J. *et al.* XAS and XRD in situ characterisation of reduction and reoxidation processes of iron corrosion products involved in atmospheric corrosion. *Corros. Sci.* **78**, 293–303 (2014).

92. Hedenstedt, K., Bäckström, J. & Ahlberg, E. In-Situ Raman Spectroscopy of α- and γ-FeOOH during Cathodic Load. *J. Electrochem. Soc.* **164**, H621–H627 (2017).

93. Antony, H. *et al.* Study of lepidocrocite γ-FeOOH electrochemical reduction in neutral and slightly alkaline solutions at 25 ° C. *Electrochim. Acta* **51**, 745–753 (2005).

94. Martinez, L. *et al.* Electrochemical Growth of Diverse Iron Oxide (Fe_3O_4, α-FeOOH, and γ-FeOOH) Thin Films by Electrodeposition Potential Tuning. *J. Electrochem. Soc.* **154**, D126 (2007).

95. Newville, M. IFEFFIT: interactive XAFS analysis and FEFF fitting. *J. Synchrotron Radiat.* **8**, 322–324 (2001).

96. Ravel, B. & Newville, M. ATHENA, ARTEMIS, HEPHAESTUS: data analysis for X-ray absorption spectroscopy using IFEFFIT. *J. Synchrotron Radiat.* **12**, 537–541 (2005).

97. Westre, T. E. *et al.* A multiplet analysis of Fe K-edge 1s → 3d pre-Edge features of iron complexes. *J. Am. Chem. Soc.* **119**, 6297–6314 (1997).

98. Réguer, S. *et al.* Iron corrosion in archaeological context: Structural refinement of the ferrous hydroxychloride β-$Fe_2(OH)_3Cl$. *Corros. Sci.* **100**, 589–598 (2015).

99. Suzuki, S. *et al.* Changes in chemical state and local structure of green rust by addition of copper sulphate ions. *Corros. Sci.* **50**, 1761–1765 (2008).

100. Briois, V. *et al.* Full Multiple Scattering and Crystal Field Multiplet Calculations Performed on the Spin Transition $Fe^{II}(phen)_2(NCS)_2$ Complex at the Iron K and $L_{2,3}$ X-ray Absorption Edges. *J. Am. Chem. Soc.* **117**, 1019–1026 (1995).

101. Roux, C., Zarembowitch, J., Itié, J. P., Polian, A. & Verdaguer, M. Pressure-Induced Spin-State Crossovers in Six-Coordinate $Fe^{II}L_nL'_m(NCS)_2$ Complexes with L = L′ and L ≠ L′: A XANES Investigation. *Inorg. Chem.* **35**, 574–580 (1996).

102. Tanabe, Y. & Sugano, S. On the absorption spectra of complex ions II. *J. Phys. Soc. Japan* **9**, (1954).

103. Wilke, M., Farges, F., Petit, P. E., Brown, G. E. & Martin, F. Oxidation state and coordination of Fe in minerals: An Fe K-XANES spectroscopic study. *Am. Mineral.* **86**, 714–730 (2001).

104. Fracchia, M. *et al.* Operando X-ray absorption spectroscopy of WO_3 photoanodes. *Electrochim. Acta* **320**, 134561 (2019).

105. Simpson, B. H. & Rodríguez-López, J. Emerging techniques for the in situ analysis of reaction intermediates on photo-electrochemical interfaces. *Anal. Methods* **7**, 7029–7041 (2015).

106. Fabbri, E., Abbott, D. F., Nachtegaal, M. & Schmidt, T. J. Operando X-ray absorption spectroscopy: A powerful tool toward water splitting catalyst development. *Curr. Opin. Electrochem.* **5**, 20–26 (2017).

107. Braun, A. *et al.* Direct observation of two electron holes in a hematite photoanode during photoelectrochemical water splitting. *J. Phys. Chem. C* **116**, 16870–16875 (2012).

108. Baran, T. *et al.* Operando and Time-Resolved X-Ray Absorption Spectroscopy for the Study of Photoelectrode Architectures. *Electrochim. Acta* **207**, 16–21 (2016).

109. Tacca, A. *et al.* Photoanodes based on nanostructured WO_3 for water splitting. *ChemPhysChem* **13**, 3025–3034 (2012).

110. Bignozzi, C. A. *et al.* Nanostructured photoelectrodes based on WO_3: Applications to photooxidation of aqueous electrolytes. *Chem. Soc. Rev.* **42**, 2228–2246 (2013).

111. Cristino, V. *et al.* Some aspects of the charge transfer dynamics in nanostructured WO_3 films. *J. Mater. Chem. A* **4**, 2995–3006 (2016).

112. Wang, F., DiValentin, C. & Pacchioni, G. Rational Band Gap Engineering of WO_3 Photocatalyst for Visible light Water Splitting. *ChemCatChem* **4**, 476–478 (2012).

113. Yamazoe, S., Hitomi, Y., Shishido, T. & Tanaka, T. XAFS study of tungsten L_1- And L_3-edges: structural analysis of WO_3 species loaded on TiO_2 as a catalyst for photo-oxidation of NH_3. *J. Phys. Chem. C* **112**, 6869–6879 (2008).

114. Oakton, E., Siddiqi, G., Fedorov, A. & Copéret, C. Tungsten oxide by non-hydrolytic sol-gel: Effect of molecular precursor on morphology, phase and photocatalytic performance. *New J. Chem.* **40**, 217–222 (2016).

115. Balerna, A.; Bernieri, E.; Burattini E.; Kuzmin, A.; Lusis, A.; Purans, J.; Cikmach, P. EXAFS studies of MeO_{3-x} (Me = W, Mo, Re, Ir) crystalline and amorphous oxides. *Nucl. Inst. Methods Phys. Res. A* **308**, 234–239 (1991).

116. Uemura, Y. *et al.* In Situ Picosecond XAFS Study of an Excited State of Tungsten Oxide. *Chem. Lett.* **43**, 977–979 (2014).

117. Uemura, Y. *et al.* Dynamics of Photoelectrons and Structural Changes of Tungsten Trioxide Observed by Femtosecond Transient XAFS. *Angew. Chemie - Int. Ed.* **55**, 1364–1367 (2016).

118. Baran, T. *et al.* An Efficient Cu_xO Photocathode for Hydrogen Production at Neutral pH: New Insights from Combined Spectroscopy and Electrochemistry. *ACS Appl. Mater. Interfaces* **8**, 21250–21260 (2016).

119. Visibile, A. *et al.* Electrodeposited Cu thin layers as low cost and effective underlayers for Cu_2O photocathodes in photoelectrochemical water electrolysis. *J. Solid State Electrochem.*

(2019), DOI: 10.1007/s10008-019-04441-z

120. Xu, Y., Zhao, W., Xu, R., Shi, Y. & Zhang, B. Synthesis of ultrathin CdS nanosheets as efficient visible-light-driven water splitting photocatalysts for hydrogen evolution. *Chem. Commun.* **49**, 9803–9805 (2013).

121. Khaselev, O. & Turner, J. A. A monolithic photovoltaic-photoelectrochemical device for hydrogen production via water splitting. *Science,* **280**, 425–427 (1998).

122. Li, Y. *et al.* Vertically aligned Ta_3N_5 nanorod arrays for solar-driven photoelectrochemical water splitting. *Adv. Mater.* **25**, 125–131 (2013).

123. Akikusa, J. & Khan, S. U. M. Photoelectrolysis of water to hydrogen in p-SiC/Pt and p-SiC/n-TiO_2 cells. *Int. J. Hydrogen Energy* **27**, 863–870 (2002).

124. Paracchino, A., Laporte, V., Sivula, K., Grätzel, M. & Thimsen, E. Highly active oxide photocathode for photoelectrochemical water reduction. *Nat. Mater.* **10**, 456–461 (2011).

125. Matula, R. A. Electrical resistivity of copper, gold, palladium, and silver. *J. Phys. Chem. Ref. Data* **8**, 1147 (1979).

126. Kuroda, H., Akeyama, K. & Kosugi, N. Cu K-edge Xanes and electronic structure of trivalent, divalent, and monovalent Cu oxides. *Jpn. J. Appl. Phys.* **32**, 98–100 (1993).

127. Pandya, K. I., Hoffman, R. W., McBreen, J. & O'Grady, W. E. In situ X-ray Absorption Spectroscopy Studies of Nickel oxide electrodes. *J. Electrochem. Soc.* **137**, 383–388 (1990).

128. Alp, E. E. *et al.* Determination of valence of Cu in superconducting $La_{2-x}(Sr,Ba)_xCuO_4$. *Phys. Rev. B* **35**, 7199–7202 (1987).

129. Deng, Y., Handoko, A. D., Du, Y., Xi, S. & Yeo, B. S. In Situ Raman Spectroscopy of Copper and Copper Oxide Surfaces during Electrochemical Oxygen Evolution Reaction: Identification of Cu^{III} Oxides as Catalytically Active Species. *ACS Catal.* **6**, 2473–2481 (2016).

130. Cervera, B. *et al.* Stabilization of copper(III) complexes by substituted oxamate ligands. *J. Chem. Soc. - Dalt. Trans.* 781–790 (1998). doi:10.1039/a706964b

131. Hanss, J., Beckmann, A. & Krüger, H.-J. Stabilization of Copper(III) Ions with Deprotonated Hydroxyiminoamide Ligands: Syntheses, Structures, and Electronic Properties of Copper(II) and Copper(III) Complexes. *Eur. J. Inorg. Chem.* **1999**, 163–172 (1999).

132. Henderson, M. A., Epling, W. S., Peden, C. H. F. & Perkins, C. L. Insights into photoexcited electron scavenging processes on TiO_2 obtained from studies of the reaction of O_2 with OH

groups adsorbed at electronic defects on $TiO_2(110)$. *J. Phys. Chem. B* **107**, 534–545 (2003).

133. Guijarro, N., Prévot, M. S. & Sivula, K. Surface modification of semiconductor photoelectrodes. *Phys. Chem. Chem. Phys.* **17**, 15655–15674 (2015).

134. Dotan, H., Sivula, K., Grätzel, M., Rothschild, A. & Warren, S. C. Probing the photoelectrochemical properties of hematite (α-Fe_2O_3) electrodes using hydrogen peroxide as a hole scavenger. *Energy Environ. Sci.* **4**, 958–964 (2011).

135. Barroso, M. *et al.* Dynamics of photogenerated holes in surface modified α-Fe_2O_3 photoanodes for solar water splitting. *Proc. Natl. Acad. Sci. U. S. A.* **109**, 15640–15645 (2012).

136. Le Formal, F., Sivula, K. & Grätzel, M. The transient photocurrent and photovoltage behavior of a hematite photoanode under working conditions and the influence of surface treatments. *J. Phys. Chem. C* **116**, 26707–26720 (2012).

137. Nellist, M. R. *et al.* Splitting Catalysts and Interfaces. *Nat. Energy* **3**, 46–52 (2018).

138. Nellist, M. R., Qiu, J., Laskowski, F. A. L., Toma, F. M. & Boettcher, S. W. Potential-Sensing Electrochemical AFM Shows CoPi as a Hole Collector and Oxygen Evolution Catalyst on $BiVO_4$ Water-Splitting Photoanodes. *ACS Energy Lett.* **3**, 2286–2291 (2018).

139. Qiu, J. *et al.* Direct in Situ Measurement of Charge Transfer Processes during Photoelectrochemical Water Oxidation on Catalyzed Hematite. *ACS Cent. Sci.* **3**, 1015–1025 (2017).

140. Laskowski, F. A. L., Nellist, M. R., Qiu, J. & Boettcher, S. W. Metal Oxide/(oxy)hydroxide Overlayers as Hole Collectors and Oxygen-Evolution Catalysts on Water-Splitting Photoanodes. *J. Am. Chem. Soc.* **141**, 1394–1405 (2019).

141. Zandi, O. & Hamann, T. W. Enhanced water splitting efficiency through selective surface state removal. *J. Phys. Chem. Lett.* **5**, 1522–1526 (2014).

142. Bediako, D. K. *et al.* Structure-activity correlations in a nickel-borate oxygen evolution catalyst. *J. Am. Chem. Soc.* **134**, 6801–6809 (2012).

143. Lyons, M. E. G. & Brandon, M. P. The oxygen evolution reaction on passive oxide covered transition metal electrodes in alkaline solution part ii - cobalt. *Int. J. Electrochem. Sci.* **3**, 1425–1462 (2008).

144. Doyle, R. L., Godwin, I. J., Brandon, M. P. & Lyons, M. E. G. Redox and electrochemical water splitting catalytic properties of hydrated metal oxide modified electrodes. *Phys. Chem.*

Chem. Phys. **15**, 13737–13783 (2013).

145. Das, S. & Jayaraman, V. SnO_2: A comprehensive review on structures and gas sensors. *Progress in Materials Science* (2014). doi:10.1016/j.pmatsci.2014.06.003

146. Sun, Y. F. *et al.* Metal oxide nanostructures and their gas sensing properties: A review. *Sensors* **12**, 2610–2631 (2012).

147. Barsan, N., Schweizer-Berberich, M. & Göpel, W. Fundamental and practical aspects in the design of nanoscaled SnO_2 gas sensors: A status report. *Fresenius. J. Anal. Chem.* **365**, 287–304 (1999).

148. Gurlo, A. Interplay between O_2 and SnO_2: Oxygen ionosorption and spectroscopic evidence for adsorbed oxygen. *ChemPhysChem* **7**, 2041–2052 (2006).

149. Gurlo, A. & Riedel, R. In situ and operando spectroscopy for assessing mechanisms of gas sensing. *Angew. Chemie - Int. Ed.* **46**, 3826–3848 (2007).

150. Vorokhta, M. *et al.* Investigation of gas sensing mechanism of SnO_2 based chemiresistor using near ambient pressure XPS. *Surf. Sci.* **677**, 284–290 (2018).

151. Wang, D. *et al.* CO_2-sensing properties and mechanism of nano-SnO_2 thick-film sensor. *Sensors actuators B* **227**, 73–84 (2016).

152. Kurganskii, S. I. *et al.* Theoretical and experimental study of the electronic structure of tin dioxide. *Phys. Solid State* **56**, 1748–1753 (2014).

153. Doh, W. H., Jeong, W., Lee, H., Park, J. & Park, J. Y. Work function engineering of SnO single crystal microplates with thermal annealing. *Nanotechnology* **27**, (2016).

154. Panaccione, G. *et al.* Advanced photoelectric effect experiment beamline at Elettra: A surface science laboratory coupled with Synchrotron Radiation. *Rev. Sci. Instrum.* **80**, (2009).

155. Tesch, M. F. *et al.* Evolution of Oxygen – Metal Electron Transfer and Metal Electronic States During Manganese Oxide Catalyzed Water Oxidation Revealed with In Situ Soft X-Ray Spectroscopy *Angew. Chem. Int. Ed.* **131**, 3464-3470 (2019),

156. Xi, L. *et al.* In Situ L - Edge XAS Study of a Manganese Oxide Water Oxidation Catalyst., *J. Phys. Chem. C* **121**, 12003-12009 (2017).

157. Edla, R., Braglia, L., Bonanni, V., Miotello, A. & Rossi, G. Study of Gaseous Interactions on Co_3O_4 Thin Film Coatings by Ambient Pressure Soft X-ray Absorption Spectroscopy. *J. Phys. Chem. C* **123**, 24511–24519 (2019).

158. Kresse, G. & Furthmüller, J. Efficient iterative schemes for ab initio total-energy calculations using a plane-wave basis set. *Phys. Rev. B - Condens. Matter Mater. Phys.* **54**, 11169–11186 (1996).

159. Kresse, G. Ab initio molecular dynamics for liquid metals. *J. Non. Cryst. Solids* **192–193**, 222–229 (1995).

160. Perdew, J. P., Burke, K. & Ernzerhof, M. Generalized gradient approximation made simple. *Phys. Rev. Lett.* **77**, 3865–3868 (1996).

161. Blöchl, P. E. Projector augmented-wave method. *Phys. Rev. B* **50**, 17953–17979 (1994).

162. Stöhr, J. *NEXAFS Spectroscopy*. (Springer-Verlag Berlin Heidelberg, 1992).

163. Bonu, V., Das, A., Amirthapandian, S., Dhara, S. & Tyagi, A. K. Photoluminescence of oxygen vacancies and hydroxyl group surface functionalized SnO_2 nanoparticles. *Phys. Chem. Chem. Phys.* **17**, 9794–9801 (2015).

164. Mamontov, E. *et al.* Dynamics and structure of hydration water on rutile and cassiterite nanopowders studied by quasielastic neutron scattering and molecular dynamics simulations. *J. Phys. Chem. C* **111**, 4328–4341 (2007).

165. Baumann, T. F., Kucheyev, S. O., Gash, A. E. & Satcher, J. H. Facile synthesis of a crystalline, high-surface-area SnO_2 aerogel. *Adv. Mater.* **17**, 1546–1548 (2005).

166. Abbate, M. *et al.* Probing depth of soft x-ray absorption spectroscopy measured in total-electron-yield mode. *Surf. Interface Anal.* **18**, 65–69 (1992).

167. Cabral Tenorio, B. N., Moitra, T., Chaer Nascimento, M.A., Braga Rocha, A. Coriani, S. Molecular inner-shell photoabsorption/photoionization cross sections at core-valence-separated coupled cluster level: Theory and examples. *J. Chem. Phys.* **150**, 224104 (2019).

168. Quaino, P. M., Chialvo, M. R. G. De & Chialvo, A. C. Hydrogen electrode reaction : A complete kinetic description. *Electrochim. Acta* **52**, 7396–7403 (2007).

169. Rau, M. S., Chialvo, M. R. G. De & Chialvo, A. C. Kinetic study of the hydrogen oxidation reaction on Pt over the complete overpotential range. *J. Power Sources* **229**, 210–215 (2013).

170. Marozzi, C. A., Chialvo, M. R. G. De & Chialvo, A. C. Criteria for the selection of the scan rate in the evaluation of the kinetic parameters of the hydrogen oxidation reaction by a potentiodynamic sweep. *J. Electroanal. Chem.* **748**, 61–69 (2015).

171. Conway, B. E. & Tilak, B. V. Interfacial processes involving electrocatalytic evolution and

oxidation of H_2, and the role of chemisorbed H. *Electrochim. Acta* **47**, 3571–3594 (2002).

172. Zeradjanin, A. R., Grote, J. P., Polymeros, G. & Mayrhofer, K. J. J. A Critical Review on Hydrogen Evolution Electrocatalysis: Re-exploring the Volcano-relationship. *Electroanalysis* **28**, 2256–2269 (2016).

173. Kucernak, A. R. & Zalitis, C. General Models for the Electrochemical Hydrogen Oxidation and Hydrogen Evolution Reactions: Theoretical Derivation and Experimental Results under Near Mass-Transport Free Conditions. *J. Phys. Chem. C* **120**, 10721–10745 (2016).

174. Watzele, S., Fichtner, J., Garlyyev, B., Schwämmlein, J. N. & Bandarenka, A. S. On the Dominating Mechanism of the Hydrogen Evolution Reaction at Polycrystalline Pt Electrodes in Acidic Media. *ACS Catal.* **8**, 9456–9462 (2018).

175. Nakamura, M., Kobayashi, T. & Hoshi, N. Structural dependence of intermediate species for the hydrogen evolution reaction on single crystal electrodes of Pt. *Surf. Sci.* **605**, 1462–1465 (2011).

176. Durst, J. *et al.* New insights into the electrochemical hydrogen oxidation and evolution reaction mechanism. *Energy Environ. Sci.* **7**, 2255–2260 (2014).

177. Stamenkovic, V., Markovic, N. M. & Ross, P. N. Structure-relationships in electrocatalysis: Oxygen reduction and hydrogen oxidation reactions on Pt(111) and Pt(100) in solutions containing chloride ions. *J. Electroanal. Chem.* **500**, 44–51 (2001).

178. Battistel, A., Fan, M., Stojadinović, J. & La Mantia, F. Analysis and mitigation of the artefacts in electrochemical impedance spectroscopy due to three-electrode geometry. *Electrochim. Acta* **135**, 133–138 (2014).

179. Tran, A. T., Huet, F., Ngo, K. & Rousseau, P. Artefacts in electrochemical impedance measurement in electrolytic solutions due to the reference electrode. *Electrochim. Acta* **56**, 8034–8039 (2011).

180. James, S. D. The Electrochemical Activation of Platinum Electrodes. *J. Electrochem. Soc.* **114**, 1113 (1967).

181. Shibata, S. The Activation of Platinum Electrodes by Preoxidation. *Bull. Chem. Soc. Jpn.* **36**, 525–527 (1962).

182. Jerkiewicz, G. Electrochemical Hydrogen Adsorption and Absorption. Part 1: Under-potential Deposition of Hydrogen. *Electrocatalysis* **1**, 179–199 (2010).

183. Conway, B. E. & Jerkiewicz, G. Relation of energies and coverages of underpotential and overpotential deposited H at Pt and other metals to the `volcano curve' for cathodic H_2 evolution kinetics. *Electrochim. Acta* **45**, 4075–4083 (2000).

184. Brug, G. J., van den Eeden, A. L. G., Sluyters-Rehbach, M. & Sluyters, J. H. The analysis of electrode impedances complicated by the presence of a constant phase element. *J. Electroanal. Chem.* **176**, 275–295 (1984).

Publications

Part of this thesis has been published in the following peer-reviewed scientific journals:

- Visibile, A., Fracchia, M., Baran, T., Vertova, A., Ghigna, P., Ahlberg, E., Rondinini, S. and Minguzzi, A., “Electrodeposited Cu thin layers as low cost and effective underlayers for Cu_2O photocathodes in photoelectrochemical water electrolysis”, *J. Solid State Electrochem.*, (2019), under press, DOI: 10.1007/s10008-019-04441-z

- Fracchia, M., Cristino, V., Vertova, A., Rondinini, S., Caramori, S., Ghigna, P. and Minguzzi, A. “Operando X-ray absorption spectroscopy of WO_3 photanodes”, *Electrochim. Acta*, (2019), 320, 134561

- Fracchia, M., Ghigna, P., Vertova, A., Rondinini, S. and Minguzzi, A. “Time-resolved X-ray Absorption Spectroscopy in (Photo) electrochemistry”, *Surfaces*, (2018), 1, 138-150

- Fracchia, M., Visibile, A., Ahlberg, E., Vertova, A., Minguzzi, A., Ghigna, P. and Rondinini, S., “α-and γ-FeOOH: stability, reversibility and nature of the active phase under hydrogen evolution”, *ACS Appl. Energy Mater.*, (2018), 1, 1716-1725

- Achilli, E., Minguzzi, A., Visibile, A., Locatelli, C., Vertova, A., Naldoni, A., Rondinini, S., Auricchio, F., Marconi, S., Fracchia, M. and Ghigna, P., “3D-printed photo-spectroelectrochemical devices for in situ and in operando X-ray absorption spectroscopy investigation”, *J. Synchrotron Radiat.*, (2016), 23, 622-628

- Baran, T., Fracchia, M., Vertova, A., Achilli, E., Naldoni, A., Malara, F., Rossi, G., Rondinini, S., Ghigna, P., Minguzzi, A. and D’Acapito, F. “Operando and time-resolved X-Ray Absorption Spectroscopy for the study of photoelectrode architectures”, *Electrochim. Acta*, (2016), 207, 16-21

- Baran, T., Wojtyla, S., Lenardi, C., Vertova, A., Ghigna, P., Achilli, E., Fracchia, M., Rondinini, S. and Minguzzi, A. “An efficient Cu_xO photocathode for hydrogen production at neutral pH: new insights from combined spectroscopy and electrochemistry”, *ACS Appl. Mater. Interfaces*, (2016), 8 (33), 21250–21260

Acknowledgments

First of all, I wish to express my deepest gratitude to my supervisor, Prof. Paolo Ghigna, for all he taught me not only during these three years of PhD, but also during my master's degree. At least 50% of all I know about physical chemistry is his merit. I would like to thank him for all his help and support, for the constant advice and for his patience in answering all my (many) questions and in enduring my (many) anxieties. Moreover, I am extremely grateful for the pleasant and friendly environment he created from the very beginning.

My special thanks go to Dr. Alessandro Minguzzi, Prof. Alberto Vertova and Prof. Sandra Rondinini from the Laboratory of Applied Electrochemistry, University of Milan, for the precious and close collaboration over all these years. I would like to especially thank Dr. Alessandro Minguzzi for clarifying all my "electrochemical doubts" and for all the advice and help he gave me over my entire PhD: he is like a second supervisor to me.

I would like to thank Dr. Daniela Meroni, Dr. Francesco Malara, Dr. Alberto Visibile, Dr. Tomasz Baran, Dr. Alberto Naldoni, Prof. Stefano Caramori and Dr. Vito Cristino for collaboration and for the provision of some samples and/or electrochemical data shown in this thesis. Thanks also to Prof. Elisabet Ahlberg and to Dr. Matthias Vandichel who provided the DFT calculations and fruitful discussion on SnO_2 nanoparticles.

I wish to express my gratitude to Prof. Fabio La Mantia, for welcoming me into his research group at the University of Bremen. Thanks for his guidance and for his help in showing me the fascinating (and let me say, rather complicated) world of dynamic impedance. Thanks to all the people in the research group for their friendship and help, especially to Dr. Doriano Brogioli, Dr. Giorgia Zampardi, Dr. Dominique Koster, Collins Erinmwingbovo, Dr. Maria Sofia Palagonia and Myriam Gutjahr.

My sincere gratitude goes to Dr. Francesco D'Acapito, the beamline scientist at LISA (BM08) at the ESRF, for his support during the experiments, and to the scientific staff of the APE-HE beamline at Elettra (Dr. Piero Torelli, Dr. Luca Braglia and Dr. Raju Edla) for their assistance during the experiments and for the recent collaboration.

I would like to thank the master's students with whom I've shared part of my path: Linda Montagna, Riccardo Montecucco and Tommaso Pozzi.

Thanks to the best work environment I could ever think of: "l'Auletta". Thanks for Briscola and Poker Polacco during the lunch break, for all our laughs, the coffees, for the improbable graphs and charts on the blackboard, for all the jokes, for the failed Instagram account. Thanks for confirming every day that no, scientists are not normal people.

A general thank goes to all the people who shared with me the time during the experiments at the synchrotron. Thanks for the gummy bears and the trash food at the vending machines, for the toothpaste tea, for the live jam sessions, the highly cultural videos and movies (ehm), for our yard hours at La Fondue.

Thanks to all my friends in Bremen, for when I will think of that period, it will be with a huge big smile. Thanks for the beer, the potatoes (everyday), the lunchinos, the German (or should I say Sicilian?) lessons, for the nights in Viertel and the days in Schlachte. Life begins out of your comfort zone, they say. Now I know that's true.

Thanks to my flatmates, old (Gioia, Tristezza, Disgusto) and new, for the most terrible cooking experiences and for the best ones, for singing trash music while washing the dishes, for predicting our deaths on the blackboards. For the travels, sometimes, when we find the right astral conjunctions. But most of all thank you because I can share everything with you, in the end of the day (or at least via Skype). Your friendship has been precious in these three years.

Finally, thanks to my parents, for all they are doing and all they have done for me. The pride I see in your eyes is my greatest reward.